CHESS Technical Memo 01-003

JLAB-ACT-01-04

Study

for a proposed

Phase I Energy Recovery Linac (ERL) Synchrotron Light Source at Cornell University

4 July 2001

Sol M. Gruner & Maury Tigner, eds.

Cornell University

Ithaca, NY 14853-2501

Ivan Bazarov [1,3], Sergey Belomestnykh [3], Don Bilderback [1,2], Ken Finkelstein [1], Ernie Fontes[1], Steve Gray[3] ,Sol M. Gruner [1,4,6], Geoff Krafft [5], Lia Merminga [5], Hasan Padamsee [3,4], Ray Helmke[3], Qun Shen [1], Joe Rogers [3,4], Charles Sinclair [5], Richard Talman [3,4], Maury Tigner, [3,4]

[1] Cornell High Energy Synchrotron Source (CHESS), Cornell University, Ithaca, NY
[2] Applied and Engineering Physics, Cornell University, Ithaca, NY
[3] Laboratory for Nuclear Studies, Cornell University, Ithaca, NY
[4] Physics Department, Cornell University, Ithaca, NY
[5] Thomas Jefferson National Accelerator Facility, Newport News, VA
[6] Laboratory of Solid State and Atomic Physics, Cornell University, Ithaca, NY

Errata

Date	Page	Comment
7/23/01	39	2nd line from bottom: Table 2.1.1 → Table 2.3.3-1
7/26/01	I	Author list error corrected
9/26/01	69	2nd paragraph: Changed "E_r=20MeV" to "E_r=100MeV". Changed "the threshold current is approximately 45 mA" to "the threshold current is approximately 225 mA"
10/1/01	114 & 115	References to Table 4.3.8-1 and Table 4.3.8-2 were removed from figure captions. These tables were in earlier draft version.
10/28/01	95	Table 4.2-1 entries changed: Longitudinal emittance, rms [keV*deg] "20" → "40" Energy spread rms [fractional] "1E-4 to 4E-3" →"1E-4 to 3E-3"
12/27/01	118	Corrected Eq. 4.3.8-5
1/17/02	77 128	2nd para. "3.8"MW" → "2.8MW" Table 5.2.1-1: "KCsSb" → "KCsTe"
2/24/02	57-59 121-122	As now noted in the footnote on pg 57, it was found that two literature references have errors in the formula for CSR. This leads to numerous small changes on pp. 57-59 and 121-122. Basically, the mistaken formula overestimates the CSR power by about x5.

List of Acronyms

ALS	Advanced Light Source
APS	Advanced Photon Source
BBU	Beam Break Up
BNL	Brookhaven National Laboratory
CEBAF	Continuous Electron Beam Accelerator Facility
CHESS	Cornell High Energy Synchrotron Source
CSR	Coherent Synchrotron Radiation
DESY	Deutsches Elektronen Synchrotron
ERL	Energy Recover Linac
ESRF	European Synchrotron Radiation facility
FEL	Free Electron Laser
HOM	Higher Order Mode
ID	Insertion Device
IRFEL	Infra-Red Free Electron Laser
JLAB	Thomas Jefferson National Accelerator Facility
LCLS	Linear Coherent Light Source
LNS	Laboratory of Nuclear Studies
MAFIA	(computer code name)
PARMELA	(computer code name)
RF	Radio Frequency
SASE	Self-Amplified Spontaneous Emission
SCHEFF	(subroutine in PARMELA)
SPring8	Super Photon ring-8
SR	Synchrotron Radiation
SRF	Superconducting RF
TDBBU	Three Dimensional Beam Break Up (computer code name)
TESLA	Tera electron volt Energy Superconducting Linear Accelerator
TTF	TESLA Test Facility
XFEL	X-ray Free Electron Laser

List of Tables

Acknowledgements

We thank Mike Billing, Ricky Campisi, David Douglas, Gerry Dugan, Steve Gray, Don Hartill, Yulin Li, Dave Rice, Stefan Simrock, Charles Strohman, and Byung Yunn for advice and help in preparing this report.

Research on accelerator physics at Cornell is supported by NSF Cooperative Agreement PHY-9809799, research on synchrotron radiation at Cornell is supported by NSF Cooperative Agreement DMR-9713424. Research at the Thomas Jefferson National Accelerator Facility is supported by the DOE under contract number DE-AC05-84ER40150.

1 Executive Summary

Synchrotron radiation (SR) has become an essential and rapidly growing tool across the sciences and engineering. World-wide, about 70 SR sources are in various stages of operation, construction, or planning, representing a cumulative investment on many billions of dollars and serving a growing research community well in excess of 10,000 scientists. To date, all major SR x-ray facilities are based on electron (or positron) storage rings. Given the expected continued growth, importance and expense of SR sources, it is important to ask if there are alternatives to the storage ring SR source which offer advantages of capability or cost. A step in this direction is being taken by the SR community with the proposed developments of linac-based x-ray free-electron lasers (XFELs) utilizing the self-amplified spontaneous emission process (SASE). However, the versatility of modern developments in accelerator physics, as applied to synchrotron radiation, is not limited to storage rings or XFELS. New developments in laser driven photoinjectors and superconducting linac technology open new and exciting possibilities for novel SR-generating machines which offer extraordinary capabilities and promise to catalyze whole new areas of SR-based science.

This is a Project Description of a SR machine technology which has been studied by a collaboration of accelerator and synchrotron light physicists at Cornell University and the Thomas Jefferson National Accelerator Facility (JLAB). We believe that SR machines based on low-emittance photoinjectors and superconducting linacs run in an energy recovery mode will significantly change the conduct and future progress of SR science. These machines, henceforth called Energy Recovery Linacs (ERLs), have captured the attention of the SR community, are the subject of a great deal of discussion and excitement within the SR community, and have already catalyzed plans for ERLs in several laboratories. Although there is no question that ERL SR sources are feasible, there are a great many open questions which have to be resolved before a large ERL machine can be built to produce x-rays beams of the projected brilliance, flux, time structure and size described in this document and in the recent literature.

We propose to construct a Phase I high current, low emittance ERL at Cornell University to experimentally test and develop ERL technology. The machine energy of 100 MeV is too low to produce x-rays; rather, the Phase I machine is designed to answer critical questions about ERL photoinjectors, characteristics and optimizations which must precede the design of a high-energy ERL. This Phase I ERL is a necessary first step towards designing a full-scale Phase II ERL hard x-ray source which we hope to build at Cornell University. The information acquired from the Phase I ERL will also be important for ERL plans at other laboratories and will serve as a vehicle for the training of accelerator physicists in ERL technology.

This Project Description is organized into 4 additional sections after this executive summary: Section 2 describes the motivation for building ERLs, their potential characteristics and the science that they enable. Section 3 paints a vision of the full-scale Phase II ERL we eventually hope to build. Section 3 includes a summary of the machine parameters of the Phase II ERL followed by detailed discussion of the accelerator and x-

ray physics and technology issues which pertain to ERLs. By the end of Section 3, it should be clear that there are many unresolved issues, which, although apparently tractable, are proscribed by uncertainties which need experimental R&D for resolution. This sets the stage for Section 4, which is a detailed discussion of the accelerator physics and technology issues for a Phase I ERL designed to perform ERL R&D. Section 5 is a technical description of the proposed Phase I ERL. The experiments to be performed during operation of the Phase I ERL are also described in this document.

It is rare that one has the opportunity to participate in the development of a technology which alters the future course of an entire community of scientists. We believe that this will be the case with ERL technology. The authors have been involved in many of the key developments which enable ERL technology. We feel we are well suited to continue this development and want to continue to serve both the accelerator physics and SR communities by making ERL x-ray sources a reality.

2. Motivation for an ERL Source

Synchrotron radiation has proven to be immensely important throughout the physical, biological, and engineering sciences. World-wide, about 70 SR sources are in various stages of operation, construction, or planning, representing a cumulative investment on many billions of dollars and serving a growing research community of more than 10,000 scientists.

The demand for SR continues to grow, with new uses opening all the time. On a global scale, the demand for new sources is immediate. Europe, with roughly the same size research community as the U.S., is in the process of building several new rings (DIAMOND in England, SOLEIL in France). Not counting Russia, Europe already has 12 SR storage rings of $\geq$1.5 GeV energy (built or under construction), and is planning at least 2 more. By contrast there are 5 such machines in the U.S. The question is not *if* the U.S. will need more SR sources in the future, but rather *when* the U.S. will need new SR resources. Given the cost and lead-time in designing a new SR machine, it is important to start preparing for this need now.

Currently, all major SR sources are based on storage rings. Given the importance of SR, it is necessary to ask:

- Are storage rings the optimal SR technology for the future?
- Are there alternatives to storage rings which enable new science?

We propose that a SR source based on closed-loop energy recovery with superconducting linacs offers significant advantages over storage ring sources, both in terms of the possible x-ray beams and, once the technology is developed, cost-effectiveness (Gruner 2000; Bilderback 2001). The basic idea behind an Energy Recovery Linac was suggested long ago (Tigner 1965) and the feasibility of operating an ERL has recently been demonstrated with a highly successful infra-red free electron laser (IRFEL) at JLAB (Neil 1998; Benson 1999; Benson 2000; Neil 2000). Our long term goal is to build a high energy (~5 - 7 GeV) SR source at Cornell, both as a development laboratory for ERL technology and as a unique user resource. As explained below in section 3, a high current, high brilliance SR machine will push ERL technology to new limits. Before committing to specific designs for a large and expensive machine, it is absolutely essential that accelerator and technology issues be explored on a brilliant, high current prototype machine. This document is a study for construction of the prototype, which is the first step in a two-phase project to a high-energy ERL SR source.

The advantages of an ERL x-ray source are best understood by first considering storage ring sources. The characteristics of the x-ray beams which may be produced by a SR source will always be limited by the qualities of the electron beams used to produce the SR. Specifically, it is desired to have

(1) Low electron beam emittance in 6 dimensions to increase the brilliance and coherence of the resultant SR;
(2) Very short electron bunches to enable fast time-resolved experiments;

(3) Ultra-small round beams;
(4) A SR output which does not decay over time; and
(5) Flexibility of operation to enable easy tailoring of x-ray beams to specific science applications.
(6) An easy upgrade path as limiting components (e.g., the electron source) improve.

Each of these electron beam characteristics is limited by the well-understood physics of storage rings (Sands 1970; Limborg 1998; Ropert 2000) . A storage ring is an equilibrium device in which the stored electron beam characteristics result from the competing factors of damping and excitation which determine the stable distribution of the electrons. Importantly, these characteristics develop slowly as equilibrium sets in during the first several thousand orbits around the storage ring, as determined by the energy, ring radius, and lattice. To choose a specific example, it is possible to use a laser photoinjector to make a round, very low emittance, sub-picosecond long bunch. If injected into a storage ring, however, by the time the beam reaches equilibrium, the ring will have imposed its own constraints on the bunch shape, emittance and length. In other words, in a storage ring, the important beam characteristics are a function of the entire ring. These characteristics are near in-principle limits in existing 3rd generation rings, such as the ESRF, APS and SPring8. Although some improvement is possible, the technology of storage rings is mature and further performance gains will be limited and will come at enormous cost. So for example, an "ultimate storage ring" has been proposed which would be 2 km in circumference (Ropert 2000) and, because of the strong Touschek effect at high particle bunch densities, would have to be refilled (or "topped off") at least each hour.

An entirely different approach is taken in an ERL machine. In an ERL, the electrons are not stored, so constraints of beam equilibrium never become limiting. As described in section 3.3, photoinjectors can produce bunches with emittances, sizes and lengths which are superior to the equilibrium bunches stored in storage rings. These bunches are then accelerated to high energy via a superconducting linac (SC linac), which can preserve the salient bunch characteristics. These superior high energy bunches are then passed though undulators to produce SR beams with unprecedented characteristics. For these reasons, ERL SR sources have recently become the focus of a number of next-generation SR source efforts (CHESS 2000a; CHESS 2000b; Ben-Zvi 2001; ESRF 2001; Padmore 2001; SRI2001 2001; Bazarov 2001b; Bazarov 2001c) .

The ERL approach has the enormous advantage that the beam quality is limited by the photoinjector, rather than by the machine as a whole. Compared to a storage ring, photoinjectors are small and relatively inexpensive. Below, we detail how present photoinjector technology can already provide electron beams with qualities superior to even the best 3rd generation storage ring sources. Moreover, photoinjectors are being intensively developed for a variety of applications and are likely to continue to be improved (Nuhn 2000).

A difficulty with any SR source is that the required beam currents carry enormous power, e.g., a 5 GeV, 100 mA electron beam carries 500 MW. Therefore, it is

economically and technically unfeasible to simply dump the electrons once they have been accelerated. In a storage ring, the power costs are kept down by reusing the energetic electrons many times, at the aforementioned cost of accepting equilibrium beam constraints.

ERLs resolve the power cost dilemma by reusing the beam energy. As schematically shown in Figure 2-1, after being used to produce SR, the electrons in an ERL are reinjected into the SC linac, but 180˚ out of accelerating phase. The bunches then decelerate and yield their energy back to the electromagnetic field in the linac. The bunches emerge from the linac with the low injector energy (minus SR losses) and are then deflected by a weak bending magnet into a beam dump. The energy recovered by the linac is used to accelerate new electrons. In other words, *an ERL differs from a storage ring in that the energy, instead of the electrons, is recirculated.*

This technology requires SC linacs because only SC linacs have sufficiently low losses for acceptable energy recovery efficiency. The JLAB IRFEL (Neil 1998; Benson 1999; Benson 2000; Neil 2000) has proven that the ERL concept works with modest currents and relatively large emittances. The estimated energy recovery of the main linac (i.e., not counting the loss due to the dumped beam, which is independent of the machine energy) exceeds 99.98%.

This document is a proposal to build a small, 100 MeV Phase I ERL to resolve outstanding accelerator physics issues, as a necessary prelude to a proposal to build a large, high-energy Phase II ERL. The document is divided into five sections. The remainder of section 2 is a more detailed explanation of ERLs, including their scientific potential, how they differ from x-ray free electron lasers (XFELs), and our vision for an eventual Phase II high energy ERL machine. Section 2 describes the motivation and Section 3 describes accelerator physics and technology issues for the Phase II ERL. Sections 4 & 5 are detailed technical descriptions of the Phase I ERL.

2.1 General Description of ERL SR Sources

The essential parts of an ERL (see Figure 2-1) are the photoinjector, the main accelerator, the SR transport loop and the spent beam dump:

- The photoinjector uses a modulated, laser-illuminated photocathode to produce bunches of electrons. These are then accelerated to relativistic energies (e.g., 10 MeV) and injected into the main accelerator. The ultimate performance of the ERL depends critically on the ability of the photoinjector to produce bunches with sufficiently low emittance and acceptable charge, energy spread and size. We propose a Phase I ERL which will operate with up to 100 mA average current and bunches in every RF bucket of a 1.3 GHz linac. This means that the photoinjector must be able to produce 77 pC bunches every 770 ps. One goal of the Phase I ERL is to demonstrate the ability to maintain 100 mA average current beam with superior bunch qualities.

- The main linac serves to both accelerate the bunches to high energy and to recover energy from bunches which have already been used to produce SR. In the simplest configuration (Figure 2-1) a single linac is used. Alternatives, such as multi-loop acceleration, in which the beam is accelerated through the linac several times, have been proposed. The advantage of multi-loop acceleration is that a shorter SC linac is required. Disadvantages include complexity and possible degradation of emittance. Most importantly, the steady state accelerating current in the linac of an N-loop machine is 2N times the injector current in the SR transport loop. Since beam break up (BBU) issues are major concerns at high currents, multi-pass ERLs require especially careful exploration of BBU limits. Although the proposed Phase I ERL uses a single pass linac, it will allow investigation of the limiting physics that would apply to a high energy multi-pass machine.

  Note that the accelerating bunches are interleaved with the decelerating bunches returning from the SR transport loop, so the actual current in the linac in even single loop ERLs is twice the current in the SR return loop.

- The SR transport loop includes the undulators and beam lines required to produce SR. Optimal use of an ERL will require undulators with a very large number of periods and will tax the capabilities of present day x-ray optics. Fortunately, undulator and beamline optics developments are being driven by the 3rd generation sources and XFEL efforts (Nuhn 2000) and are expected to evolve significantly over the next few years. The Phase I ERL will be of too low an energy to produce hard x-rays, so there is only very limited funding requested in this proposal for undulator and x-ray optical development. The transport loop also includes beam compressors to shorten bunches for science applications requiring fast timing. Because of wake-field and coherent synchrotron radiation effects, it will probably not be desirable to circulate the shortest possible bunches around the entire machine. Again, this is an important issue which will be further explored within the Phase I ERL plan. Compressed bunches will likely have to be uncompressed before being reinjected in the main linac to reduce excitation of higher order modes.

- The beam dump is a source of noticeable inefficiency. For example, a dumped current of 100 mA at 5 MeV dissipates half a megawatt of power. Fortunately, the power dissipation in the beam dump is determined by the photoinjector beam power and not the main linac. The Phase I ERL will be used to investigate the minimum required photoinjector energy. In a Phase II machine, consideration will be given to utilizing the dumped energy.

Each of the main components of the ERL machine described above require support systems, e.g., RF, cryogenics, etc., as described in subsequent sections.

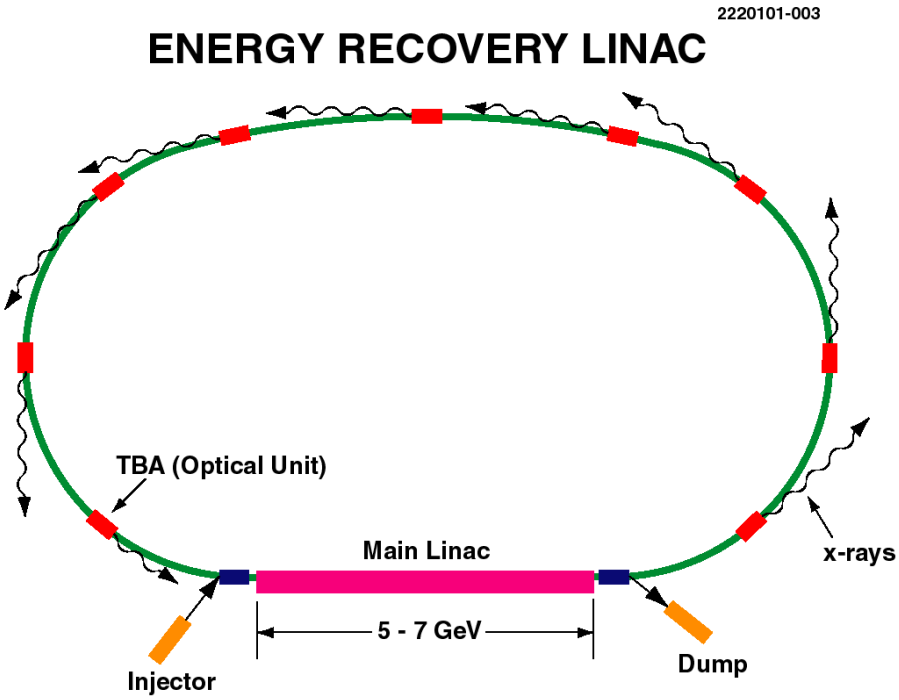

Figure 2-1. Schematic representation of a simple, single-loop ERL, consisting of the injector, the main SC linac, the SR transport loop and the energy recovered beam dump. The actual shape of the SR return transport loop can vary, depending on requirements.

2.2 Comparison of ERL, Storage Ring, and XFEL Sources

This section summarizes some of the calculated x-ray beam properties of the Phase II ERL SR source, as compared with some of the existing and proposed facilities. All calculations are performed using analytical formulae from the literature, mostly from Kwang-Je Kim (Kim 1986; Kim 1989). A more comprehensive summary (including more information on coherency and degeneracy) is given by Shen (Shen 2001). Operational differences related to the scientific usage of ERL, storage ring, and XFEL are discussed at the beginning of the next section.

The main comparisons are to APS (and projected APS upgrade), ESRF, and Spring 8 storage rings, including a 25 m long undulator. Where appropriate we also compare some selected results to the proposed 4th generation LCLS and TESLA XFELs. Representative parameters for machine design, insertion device, beamline optics, for dc vs. pulsed experiments, etc. help to compare the various types of sources for different types of x-ray experiments. Note that the beams from these sources can be improved by the use of longer undulators. Therefore, these comparisons should not be taken as the absolute upper limits of what can be obtained at the various sources shown.

The results are summarized in Table 2.2-1, and shown in Figures 2.2-1 to 2.2-5. The comparison table is based on the suggestions at the *ERL Science Workshop* held at Cornell in December 2000 (Shenoy 2000). Two options are chosen for the ERL ((Gruner 2000), with slight modifications). One is based on a machine current of 100 mA and a transverse geometric emittance in both planes of 0.15 nm. The other is based on an ultra-low geometric emittance of 0.015nm but a lower current of 10 mA. Both assume a FWHM[1] bunch duration of 300 fs, and a machine energy of 5.3 GeV (see note at the end of this section). All calculations assume perfect machine and undulator conditions, without any field errors, nor electron energy spreads. Although more complete design work needs to be done, we believe that realistic undulator field errors, energy spread, etc. will result in less than a factor of two loss in brilliance from what we have assumed here. For simplicity, the tuning curves of only the first and the third undulator harmonics are shown in Figures 2.2-1 to -5.

[1] To avoid confusion, we will be explicit about whether bunch lengths are FWHM or rms values. Assuming a Gaussian longitudinal bunch profile, the (FWHM length) = 2.354 x (rms length).

Table 2.2-1: Comparison of the Cornell ERL source with other existing and proposed synchrotron light sources.

Assuming high duty-cycle operations		ERL hi-flux	ERL hi-coh.	APS und. A	APS upgrade	ESRF U35	SPring8 5m	SPring8 25m	LCLS spont.	LCLS SASE	TESLA spont.	TESLA SASE
Machine design	Energy E_G (GeV)	5.3	5.3	7	7	6	8	8	15	15	25	25
	Avg. Current I (mA)	100	10	100	300	200	100	100	$72\cdot10^{-6}$	$72\cdot10^{-6}$	0.063	0.063
	Charge q (nC/bunch)	0.077	0.008	14	14	0.85	0.29	0.29	1	1	1	1
	ε_x (nm-rad)	0.15	0.015	8	3.5	4	6	6	0.05	0.05	0.02	0.02
	ε_y (nm-rad)	0.15	0.015	0.08	0.0035	0.01	0.003	0.003	0.05	0.05	0.02	0.02
	Bunch fwhm τ (ps)	0.3	0.3	73	73	35	36	36	0.23	0.23	0.188	0.090
	# of bunches f (Hz)	$1.3\cdot10^{9}$	$1.3\cdot10^{9}$	$7.3\cdot10^{6}$	$22\cdot10^{6}$	$2.3\cdot10^{8}$	$3.4\cdot10^{8}$	$3.4\cdot10^{8}$	120	120	56575	56575
Insertion device	Undulator L (m)	25	25	2.4	4.8	5	4.5	25	100	100	30	87
	Period λ_u (cm)	1.7	1.7	3.3	3.3	3.5	2.4	3.2	3	3	3.81	5
	# of period N_u	1470	1470	72	145	142	187	781	3300	3300	787	1740
	Horizontal β_x (m)	12.5	4.0	15.9	4.0	35	24	24	18	18	14.7	33.3
	Vertical β_y (m)	12.5	4.0	5.3	4.0	2.5	3.9	15	18	18	14.7	33.3
	Und. K (@ E_1)	1.38	1.38	1.24	1.24	0.67	2.08	1.66	3.9	3.9	2.28	4.14
	1st harmonic E_1 (keV)	8.0	8.0	8.0	8.0	8.0	8.0	8.0	8.26	8.26	10	12.4
Beamline & optics	H. div. fwhm (μrad)	9.1	6.2	54.3	70.2	26.8	38.4	37.4	4.9	1	6.7	1.76
	V. div. fwhm (μrad)	9.1	6.2	16.2	9.7	10.4	10.0	4.3	4.9	1	6.7	1.76
	H. source fwhm (μm)	103	24.5	839	277	879	892	890	82	78	60	60
	V. source fwhm (μm)	103	24.5	48.6	11.4	13.9	10.6	22.8	82	78	60	60
	Power P_0 (kW)	33.9	3.4	1.2	7.2	1	15.7	31.2	0.0027	0.003	0.070	1.6
	DP/dA @20m (W/mm^2)	2600	260	180	1080	194	1830	4568	0.45	63	336	$2\cdot10^{5}$
DC experiments	Ave. flux F_n (p/s/0.1%)	$1.5\cdot10^{16}$	$1.5\cdot10^{15}$	$7.0\cdot10^{14}$	$4.2\cdot10^{15}$	$1.3\cdot10^{15}$	$2.4\cdot10^{15}$	$9.0\cdot10^{15}$	$3.3\cdot10^{10}$	$2.4\cdot10^{14}$	$6.4\cdot10^{12}$	$4\cdot10^{17}$
	Ave. brilliance B (p/s/0.1%/mm^2/mr^2)	$1.3\cdot10^{22}$	$5.2\cdot10^{22}$	$1.5\cdot10^{19}$	$1.5\cdot10^{21}$	$3.1\cdot10^{20}$	$5.0\cdot10^{20}$	$2.2\cdot10^{21}$	$1.6\cdot10^{17}$	$4.2\cdot10^{22}$	$3.6\cdot10^{19}$	$8\cdot10^{25}$
	Coh flux F_c (p/s/0.1%)	$8.1\cdot10^{13}$	$3.1\cdot10^{14}$	$0.9\cdot10^{11}$	$9.0\cdot10^{12}$	$1.8\cdot10^{12}$	$3.0\cdot10^{12}$	$1.3\cdot10^{13}$	$9.0\cdot10^{8}$	$2.4\cdot10^{14}$	$1.4\cdot10^{11}$	$4\cdot10^{17}$
	Coh. fraction p_c (%)	0.52	20	0.013	0.22	0.14	0.13	0.14	2.7	100	2.1	100
Pulsed expts.	Photons / bunch	$1.2\cdot10^{7}$	$1.2\cdot10^{6}$	$9.6\cdot10^{7}$	$1.9\cdot10^{8}$	$5.7\cdot10^{6}$	$7.1\cdot10^{6}$	$2.7\cdot10^{7}$	$2.8\cdot10^{8}$	$2\cdot10^{12}$	$1.1\cdot10^{8}$	$7\cdot10^{12}$
	Peak brilliance (p/s/0.1%/mm^2/mr^2)	$3.0\cdot10^{25}$	$1.2\cdot10^{26}$	$2.5\cdot10^{22}$	$8.3\cdot10^{23}$	$3.3\cdot10^{22}$	$3.6\cdot10^{22}$	$1.6\cdot10^{23}$	$4.8\cdot10^{27}$	$1.2\cdot10^{33}$	$3.4\cdot10^{27}$	$7\cdot10^{33}$
	Peak flux (p/s/0.1%)	$3.9\cdot10^{19}$	$3.9\cdot10^{18}$	$1.3\cdot10^{18}$	$2.6\cdot10^{18}$	$1.6\cdot10^{17}$	$1.9\cdot10^{17}$	$7.4\cdot10^{17}$	$1.2\cdot10^{21}$	$7.2\cdot10^{24}$	$6.0\cdot10^{20}$	$3\cdot10^{25}$
	Pk coh. flux (p/s/0.1%)	$2.1\cdot10^{17}$	$7.9\cdot10^{17}$	$1.7\cdot10^{14}$	$5.6\cdot10^{15}$	$2.2\cdot10^{14}$	$2.5\cdot10^{14}$	$1.1\cdot10^{15}$	$2.7\cdot10^{19}$	$7.2\cdot10^{24}$	$1.4\cdot10^{19}$	$3\cdot10^{25}$
	Peak degen. par. δ_D	95	368	0.078	2.6	0.103	0.113	0.49	$1.3\cdot10^{4}$	$3.3\cdot10^{9}$	$4.7\cdot10^{3}$	$8\cdot10^{9}$
Nonlinear expt	Ave. coh. power (W)	0.10	0.40	$1.2\cdot10^{-4}$	0.011	0.0023	0.0038	0.017	$1.2\cdot10^{-6}$	0.32	$2.2\cdot10^{-4}$	794
	Peak coh. power (W)	269	1011	0.22	7.2	0.28	0.32	1.4	$3.8\cdot10^{4}$	$9\cdot10^{9}$	$2.2\cdot10^{4}$	$60\cdot10^{9}$
	A coh dP/dA (W/mm^2)	12.0	848	0.0029	3.5	0.19	0.40	0.84	$2.3\cdot10^{-4}$	0.0077	0.078	$2.8\cdot10^{5}$
	P coh dP/dA (W/mm^2)	$3.2\cdot10^{4}$	$2.2\cdot10^{6}$	5.4	2280	22.9	33.8	69.0	$7.2\cdot10^{6}$	$1.9\cdot10^{12}$	$7.8\cdot10^{6}$	$2.1\cdot10^{13}$
	Ave. E-field (V/m)	$1.0\cdot10^{5}$	$8.0\cdot10^{5}$	1479	$5.1\cdot10^{4}$	$1.2\cdot10^{4}$	$1.7\cdot10^{4}$	$2.5\cdot10^{4}$	416	2410	7670	$1.5\cdot10^{7}$
	Peak E-field (V/m)	$4.9\cdot10^{6}$	$4.1\cdot10^{7}$	$6.4\cdot10^{4}$	$1.3\cdot10^{6}$	$1.3\cdot10^{5}$	$1.6\cdot10^{5}$	$2.3\cdot10^{5}$	$7.4\cdot10^{7}$	$3.8\cdot10^{10}$	$7.7\cdot10^{7}$	$1.3\cdot10^{11}$

Notes for Table 2.2-1 and Figures 2.2-1 to -5:

All flux and brilliance calculations are performed at 8 keV fundamental energy except for the proposed XFEL sources LCLS and TESLA, which are at 8.26 and 12.4 keV, resp. Thus in some cases the value of the brilliance may be somewhat lower than the value at the peak fundamental energy of the undulator. This is done for the purpose of proper coherence comparisons since coherence is very sensitive to x-ray wavelength. The XFEL numbers are obtained from the (LCLS 1998) and the TESLA (Brinkmann 1997) design reports. Power density numbers at 20m for SASE are for average coherent power only and include the effects from source size and beam divergence, while all other numbers for that row are calculated using the formula listed at the end of "Flux, Brightness and Power" in (Shen 2001).

All calculated results are for high-duty cycle operations only (APS: 6+21 singlets; ESRF: 2x1/3 filling of 992 RF buckets; SPring8: 2/3 filling of 2436 RF buckets) which respresent the most common running modes at the existing storage-ring sources. The machine parameters are obtained from the respective web sites. APS parameters are obtained from http://www.aps.anl.gov/xfd/calendar/fp_2000-4.html on 1/8/01, and from e-mail communications with Dr. Dennis Mills. Upgraded parameters for APS are based on Arthur (2000). ESRF parameters are obtained from http://www.esrf.fr/machine/myweb/machine/brill.html on 12/18/00, and from communications with Dr. Pascal Elleaume (2000). SPring8 parameters are obtained from *SPring8 Annual Report 1998*, available at http://www.spring8.jp/, and from Dr. Don Bilderback's personal communication with Dr. Kitamura at SPring8.

For the purposes of the calculations, we assume β = 12.5 m in the high-flux option and β = 4 m in the high-coherence option for a 25 m undulator with segmentation. The relatively short β assumes segmentation due to focusing requirements.

One of the greatest uncertainties in Table 2.2-1 and the accompanying figures stems from a fundamental lack of knowledge about the minimum bunch length and emittances which can be simultaneously achieved. To account for this uncertainty we have inserted in the peak brilliance plot a curve that corresponds to an ERL with 0.15nm emittances at 100mA but with a more conservative 4.7ps FWHM bunch length. Furthermore, a very conservative peak brilliance value is calculated assuming 300 fs bunches but 1.5nm transverse emittances at 100 mA. This result is shown in Figures 2.2-3 and 2.2 – 6 and compared with other existing and proposed storage-ring based sources.

Resolution of these uncertainties is one of the most important objectives of the prototype ERL machine proposed in this document. Nonetheless, as Figure 2.2-6 shows, even with conservative numbers the ERL will push the synchrotron x-ray brilliance and pulse length into new territories that are completely uncharted by the existing sources.

The peak brilliance and coherence of the ERL will be greatly exceeded by the proposed XFEL sources, such as TESLA and the LCLS. Why then, one might ask, should the ERL be pursued? The answer is straightforward and compelling: Although XFEL

beams will have extraordinary properties, they will operate at relatively low duty cycle with pulses sufficiently intense to destroy most samples with each pulse. While this opens up new experimental realms about which new scientific communities will coalesce, one does not expect that XFELs will substitute any time in the foreseeable future for the vast majority of applications presently performed on storage ring sources. By contrast, ERL s are a logical evolution of 3rd generation storage ring sources. ERLs will serve essentially all existing 3rd generation applications and, therefore, can meet the expected growth in demand for SR resources. Thus, in contrast to XFELs, ERLs automatically already have a large natural constituency of users.

If ERLs only matched the performance of 3rd generation storage rings, there would be little incentive for ERL development. The limits to storage ring performance are well known, and are not far from those of existing rings. On the other hand, the ultimate performance limitations of ERLs are not known. Even the first Phase II ERL, as described in the preceding pages, already pushes well beyond the limits of existing storage rings in flux, brightness, peak brightness, coherence, and degeneracy. Each of these incremental improvements extend existing SR applications, and, for example, allow study of smaller samples, higher energy resolutions, faster XPCS time scales, more weakly scattering samples, etc. Further, in the crucial realm of fast pulses, ERLs go well beyond what may be expected from storage rings and allow study of phenomena in the much desired 100 fs range at field intensities which do not destroy many samples. Thus, ERLs naturally allow existing applications, extend existing applications to new limits and additionally open up new areas dependent on fast x-ray pulses.

The basic conclusion from this study is that the Phase II Cornell ERL will be a superlative, unique source of x-rays that will enable new science. With a long, short-period undulators in a low-β section, it can offer roughly 20 times more average brilliance and coherent flux than the best existing 3rd generation storage ring, making an ERL comparable to that of prototype 4th generation sources. The combination of its high brilliance with its short pulses in the high-duty-cycle mode would mean two-to-three-orders-of-magnitude higher peak brilliance, peak coherent flux, and peak photon degeneracy. Even with the 4th generation prototype sources due to be developed, the high-duty-cycle of the ERL makes it well balanced in all three categories of source characteristics of high flux, high coherence, and high peak brilliance.

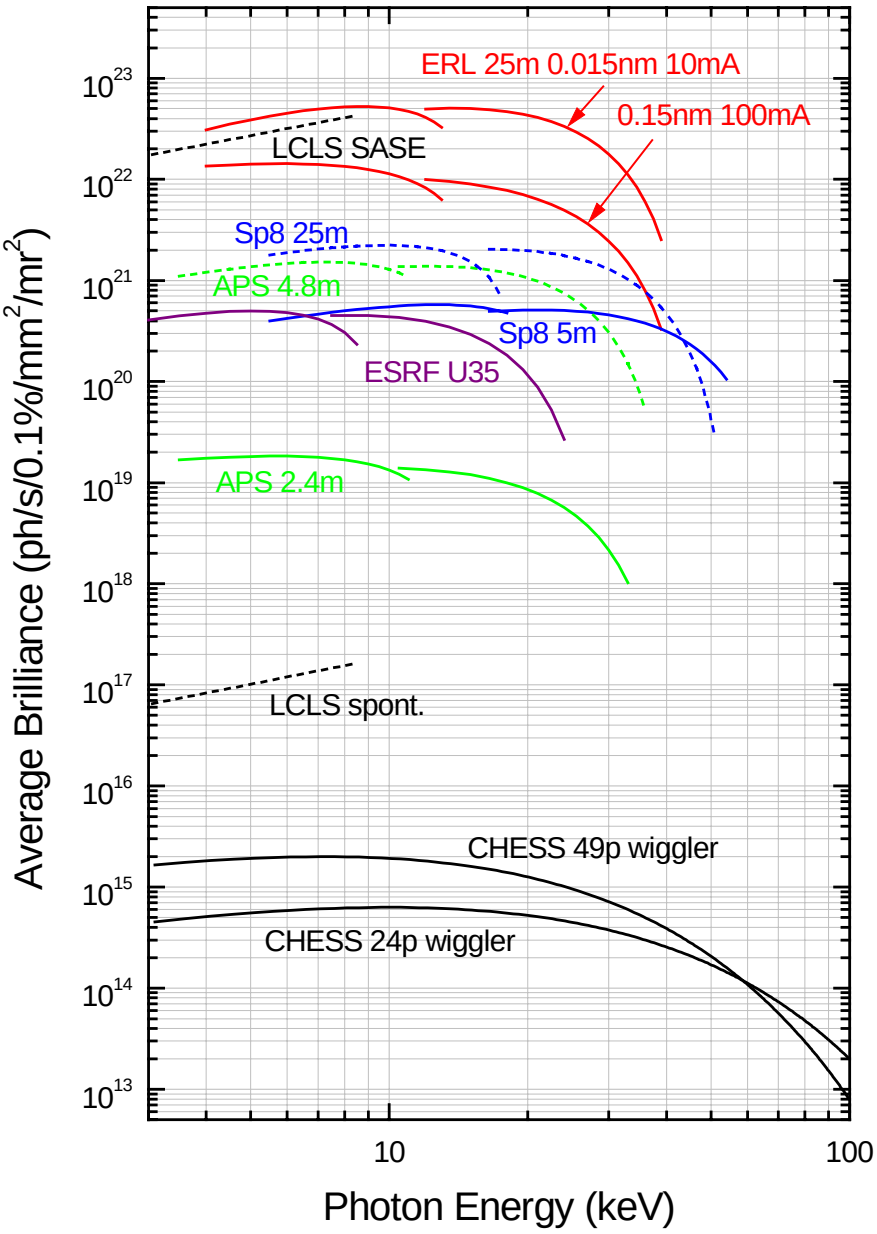

Figure 2.2-1: Comparison of calculated average spectral brilliance of the various sources. The parameters used for undulator sources are listed in Table 2.2-1. The CHESS wiggler sources assume 5.3 GeV 300 mA operation and a FWHM source size of d_x = 5.5 mm and d_y = 0.9 mm for the 24-pole wiggler at F-line and d_x = 3.3 mm and d_y = 0.85 mm for the 49-pole wiggler at A/G-line.

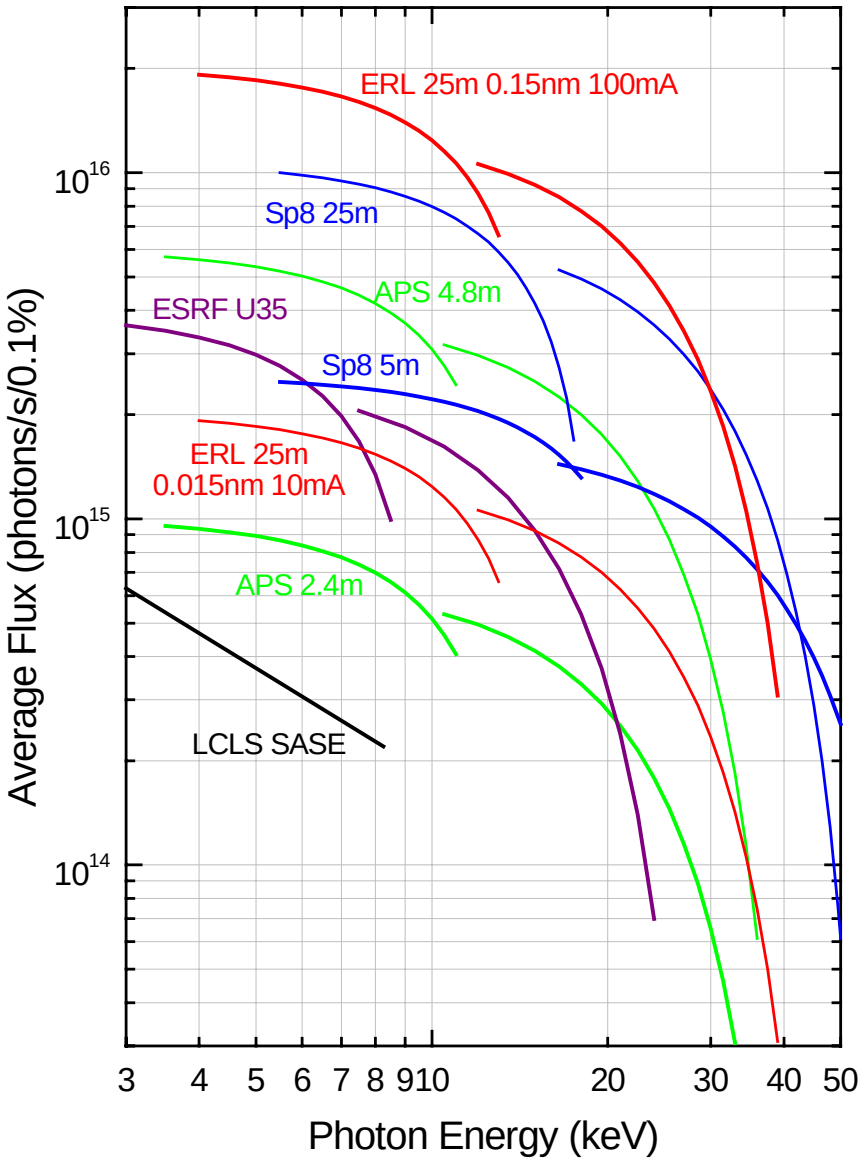

Figure 2.2-2: Comparison of calculated average photon flux of the various sources per second. The parameters used for all sources are listed in Table 2.2-1.

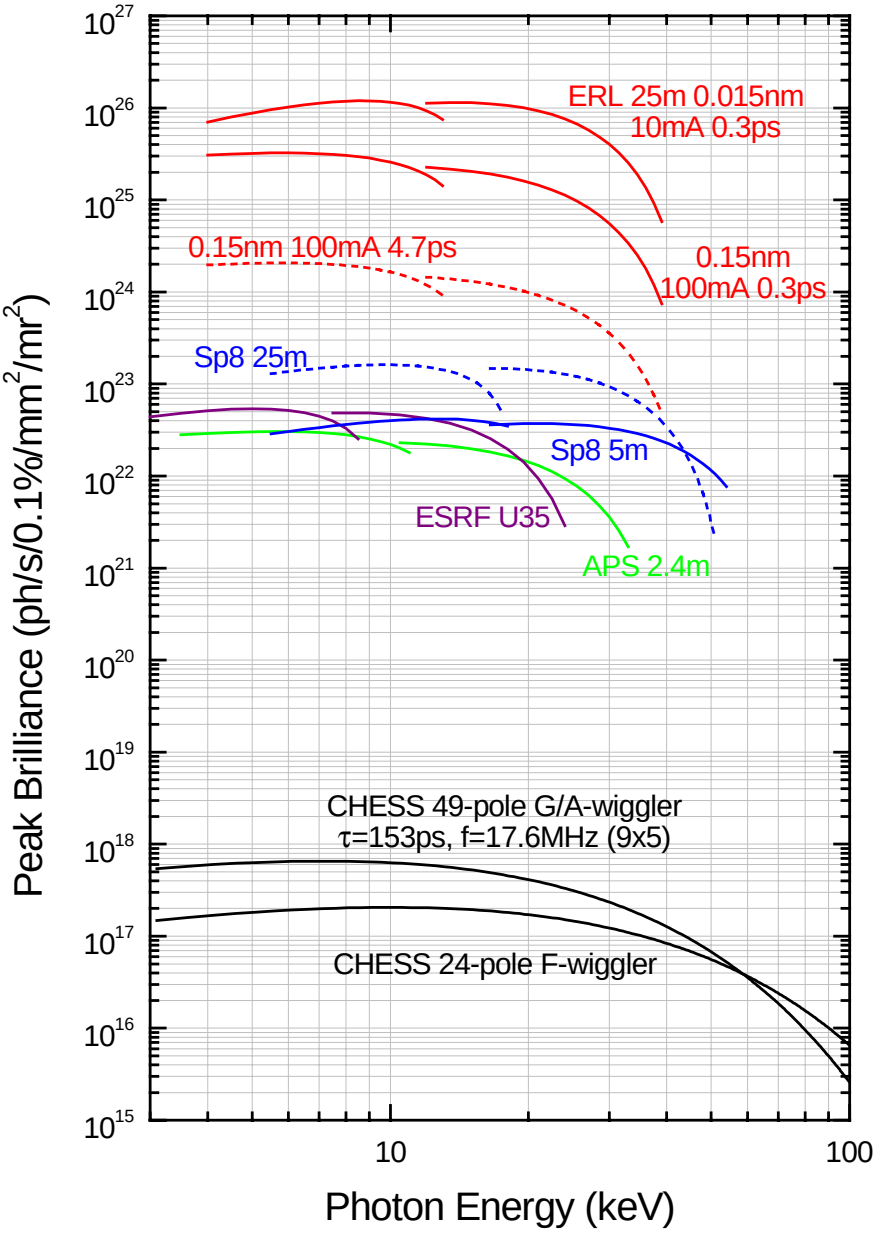

Figure 2.2-3: Comparison of the calculated peak spectral brilliance of the ERL with some existing synchrotron sources. The peak brilliance is obtained by dividing the average brilliance by the bunch length to interpulse period. The parameters used for the undulator sources are listed in Table 2.2-1. The CHESS wiggler sources assume 5.3 GeV 300 mA operation and a FWHM source size of d_x = 5.5 mm and d_y = 0.9 mm for the 24-pole wiggler at F-line and d_x = 3.3 mm and d_y = 0.85 mm for the 49-pole wiggler at A/G-line. A bunch length FWHM of 153 ps and a lattice of 9x5 in 2.56 μs revolution time, describing the present operation mode, are used for the CHESS wigglers. The LCLS curve would be, of course, well beyond the top of the graph.

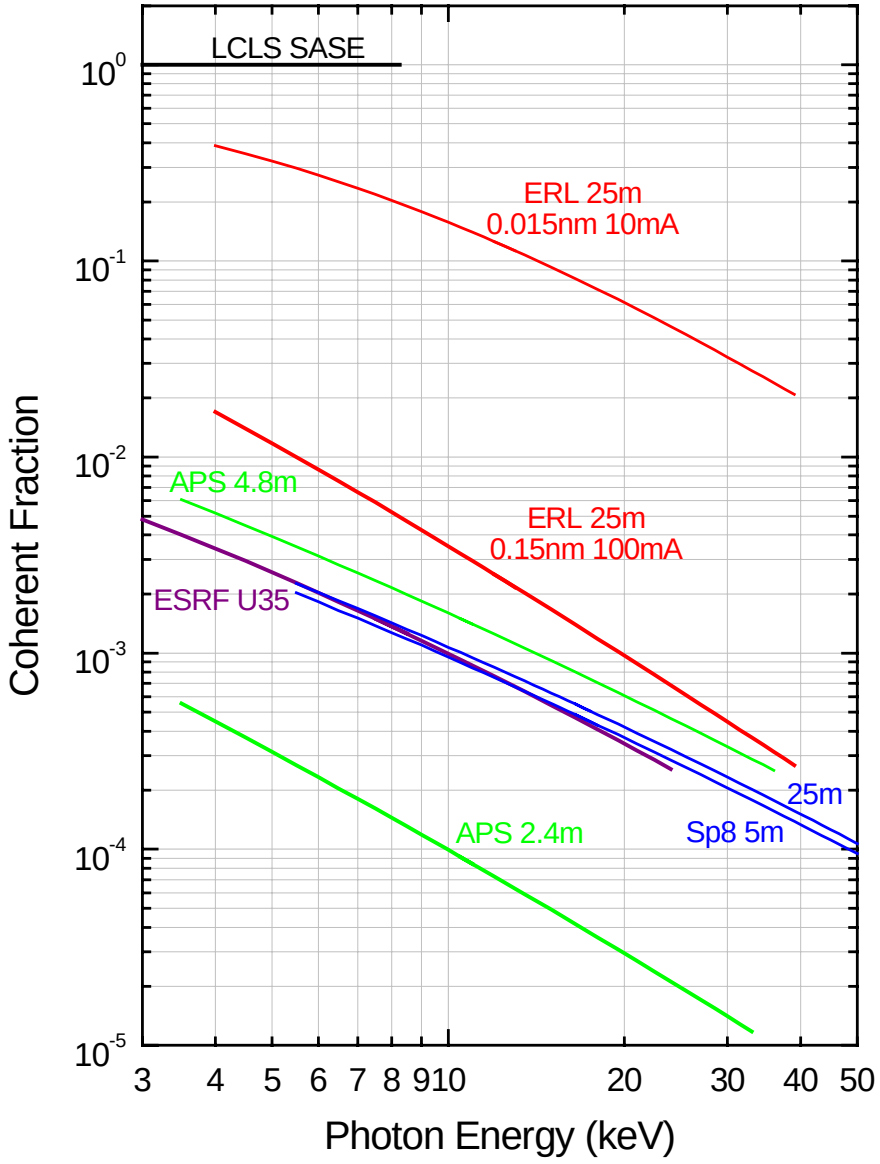

Figure 2.2-4: Comparison of calculated coherent fractions of the various sources. The parameters used for all sources are listed in Table 2.2-1. See (Shen 2001) for a more detailed discussion about coherence.

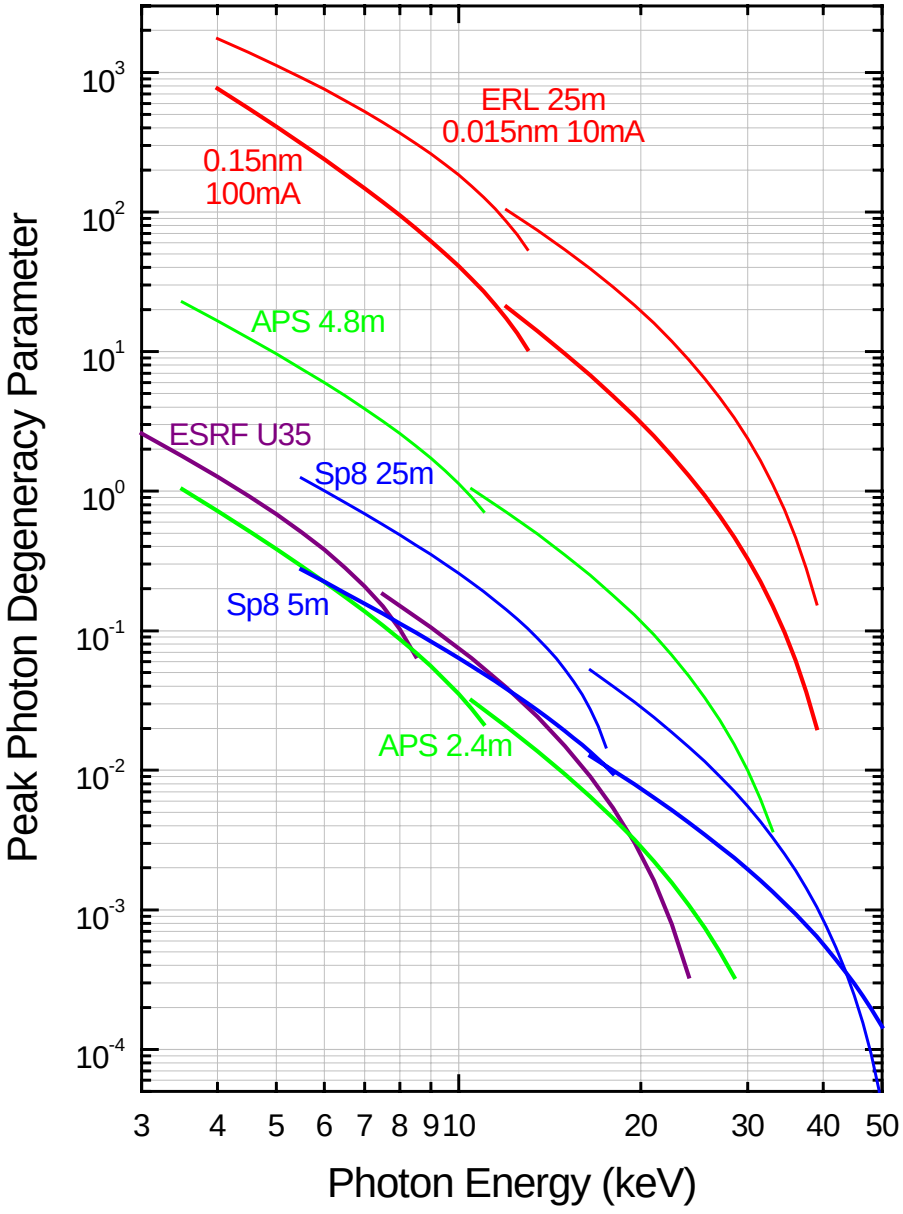

Figure 2.2-5: Comparison of the photon degeneracy parameter for the ERL and for storage ring sources. The degeneracy parameter specifies the number of photons per pulse that are in a single quantum mode, i.e., both transversely and longitudinally coherent. Note that for existing storage ring sources, the degeneracy is typically less than one for hard (> 10 keV) x-rays. Of course, none of these sources will approach the degeneracy of XFELs. The parameters used for all sources are listed in Table 2.2-1. See (Shen 2001) for a more detailed discussion about degeneracy.

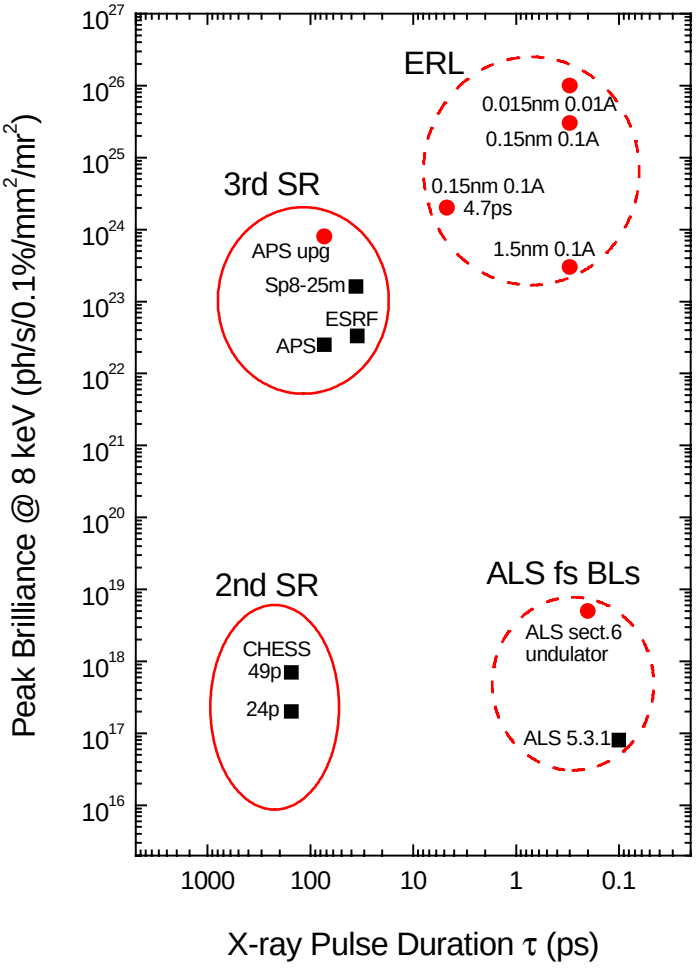

Figure 2.2-6: Comparison of peak brilliance and x-ray pulse duration of the ERL with some existing and proposed storage-ring based sources. The ERL numbers correspond to different plausible configurations of emittance, current and bunch length. All parameters for the 3rd-generation and the CHESS sources are listed in Table 2.2-1. The numbers for the ALS fs beamlines are taken from (Schoenlein 2001), which are based on fs-laser slicing of electron bunches in the ALS ring. ALS 5.3.1 is a bend-magnet beam line with 100 fs pulse slicing, and sector 6 is a proposed one-meter undulator with 2cm period and 5mm gap, and 200fs slicing. All existing sources are labeled with black squares and proposed ones with red circles in the figure. CHESS wiggler numbers represent typical existing 2nd-generation sources. The circular lines around different regions in the figure serve as rough guidelines for different types of sources.

2.3 Science Case

There are two primary scientific justifications for the ERL: The first is equivalent to the well-established scientific justifications for the 3rd generation synchrotron storage rings, namely, it should be possible to perform essentially all experiments now possible at 3rd generation machines with an ERL. This qualitatively distinguishes ERLs from x-ray free electron lasers (XFELs) now undergoing development. XFELs will provide ultra-intense, ultra-short pulses of x-rays in trains at low duty cycles (≤120 Hz) (Brinkmann 1997; LCLS 1998). The kinds of experiments which can be performed at XFELs will often differ from 3rd generation sources both because of the pulse intensity, which is so high that single pulses damage the samples, and because of the low duty cycle, which will be exacerbated by the need to multiplex the beam among different beamlines. By contrast, the ERL will deliver x-ray pulses at GHz rates to all x-ray beamlines on the transport loop with average flux and brightness exceeding the best 3rd generation storage rings. Thus, with respect to the science which can be performed, XFELs have potential to be a *revolutionary* technology, while ERLs are an *evolutionary* technology. Since ERLs have promise to be cost competitive with storage rings, this already justifies their exploration as an alternative for future synchrotron facilities.

The second scientific justification for the ERL stems from the *differences* between ERL and storage ring beams. ERL beams can be more intense, brilliant, coherent and have shorter pulses than beams at storage rings. These features enable new kinds of experiments which cannot be readily done at storage rings. In what follows, outstanding features of ERLs are summarized and examples given of x-ray science that will benefit directly from this new machine.

For perspective it is worthwhile to look back at some of the pioneering efforts of the past:

- The first synchrotron-based time-resolved x-ray diffraction experiments in the nanosecond time domain were performed by Larson and coworkers at CHESS in the early 1980s (Larson 1982). During this experiment 25 ns laser pulses melted the surface layer of a silicon crystal and structural transformations were studied with nanosecond resolution. At the time the Cornell storage ring was run in a special single-bunch mode that produced 120 ps x-ray pulses every 2.5 microseconds.
- In a seminal work in the field of protein crystallography, Rossmann and coworkers determined (Rossmann 1985) the crystal structure of the mammalian virus HRV14. The high intensity of the doubly focused CHESS A1 station beam was the critical factor in this work. The x-ray beam source size at the time was 1 mm high by 3 mm wide.

In hindsight, these results teach several lessons: First, both were done using an x-ray source far short of optimal – but it was the best available at the time. Second, both results were primary demonstrations of what could be accomplished with a bright x-ray source and have spurred subsequent fields of research and driven the development of 2nd

and 3rd generation x-ray sources. And last, it is interesting to note that neither experiment was foreseen or even hinted at in the original proposal to build the CHESS facility.

Similar experiences ring true for other x-ray sources. Major uses of sources often are not anticipated at the time the sources are designed. Thus, the prevalence of structural biology at 2nd generation sources was unexpected when these sources were built. Likewise, the rapidly growing use of microbeams was only a small part of the argument for the ESRF. Thus, in presenting a scientific case for the ERL, we must anticipate that the most exciting and important uses will emerge over time. Even so, the x-ray community now has three generations of machines under its collective belt, and knows how to optimize a dedicated machine to create a unique and useful tool. With every new machine the x-ray user community has grown enormously, in step with the machine capabilities and with new x-ray technique development. The needs are also more clearly defined now than they were 20 years ago. For example, the technological push for miniaturization and the need to design new materials with atomic and molecular precision fuel the demand for the smallest possible source sizes and divergence parameters. And, just as in the past, we expect the creativity of present and future scientists will deliver more than we plan for.

An introductory scientific case for the ERL is summarized, below. Although the x-ray community has been thinking about the possibilities presented by ERLs for only about a year, there is already considerable excitement, as evidenced by a rapid spate of publications and workshops on these machines (CHESS 2000a; CHESS 2000b; Ben-Zvi 2001; ESRF 2001; Padmore 2001; SRI2001 2001). The scientific case for ERLs will certainly continue to evolve as these workshops continue and the community begins to consider a future proposal for a Phase II ERL. Accordingly, CHESS will host an evolving web site for ERL science and applications and links to other sites about ERLs.

2.3.1 Outstanding Scientifically Usable Features of the ERL

The ERL is a natural successor to 3rd generation storage rings. It will utilize x-ray source insertion devices similar to 3rd generation storage rings but, having a single pass design, will have electron pulse size, shape and timing characteristics and flexibility similar to linear accelerators, and, in certain cases, will be preferable to XFELs. Quantitative assessment of the beam characteristics of the ERL proposed herein are given in two working documents (Gruner 2000; Shen 2001) and are summarized in Section 2.2. Qualities that matter to the x-ray user community include:

Beam size – beam shape. The ERL, with 10-50 times higher brilliance than 3rd generation sources, could produce focused beams 50 nanometer in diameter. This will benefit 3D nanoscale structure and evolution studies, local environment fracture, nucleation and growth, and fine grain mosaic materials. Whereas storage rings beams have different minimum sizes and divergences in the horizontal and vertical directions, ERL beams can be round with identical desirable properties in both the horizontal and

vertical directions. Alternatively, round beams are not required by the ERL and flat beams are possible if desired.

Short pulses. As shown in Figure 2.2-6, one of the outstanding qualities of the Phase II ERL will be to provide high-brilliance, short x-ray pulses that will open up entirely new areas of time-resolved structural and electronic studies of condensed matter. Pioneer studies in this area are already being intensively pursued at the ALS (Schoenlein 2001) where sub-ps x-ray pulses are produced by slicing the electron bunches by a fs-laser. The 5 to 7 orders of magnitudes increase in peak brilliance expected at the ERL will dramatically improve these ultrafast timing experiments which range from studies of atomic disordering on the time scales of an atomic vibrational period, to investigations of acoustic and optical phonons, and photochemical reactions in biological systems.

Short pulses – CW operation. The bunches in a linac-based x-ray source can be much shorter than the bunches in a storage ring (Krafft 1998; Wang 1998). Because of their flexibility and inherently shorter bunch lengths, linac-based sources are being intensively studied at LBNL for the generation of very short x-ray pulses (Zholents 1999). The minimum bunch lengths which are feasible in an ERL are not yet known and will depend on factors such as wake-field and coherent synchrotron radiation effects. Measurement of these effects, which are discussed at length in this document, are an important part of the experimental program of the Phase I ERL. It is likely that bunches ~1 ps long are feasible through the full transport return arc and bunches as short as a hundred fs rms, using bunch compression and decompression, will be feasible through part of the arc. Further x-ray pulse compression may be possible using techniques described by Zholents et al. (Zholents 1999). Short x-ray pulses allow study of atomic disordering on the time scales of a vibrational period, acoustic phonons, and photochemical reactions.

Coherence[2]. The low current, high coherence option of the Phase II ERL will be a diffraction-limited coherent source for 8 keV photons and will provide two-orders-of-magnitude more time-averaged coherent flux than the existing APS and ESRF sources. Such beams will extend x-ray photon correlation spectroscopy studies to shorter time scales and to higher spatial resolutions that have not been exploited at the currently available facilities Highly coherent beams will also benefit phase-contrast hard x-ray microscopy and microtomography experiments, and may make it possible to perform coherent diffraction measurements on non-crystalline biological samples, e.g. proteins and macromolecule assemblies that are difficult to crystallize.

Photon degeneracy[2]. Photon degeneracy refers to the number of photons in a single quantum mode of an electromagnetic wave. For all existing x-ray sources, this number is well below unity. With the Phase II ERL, the peak photon degeneracy number is expected to be on the order of 10^2, which may open up new research areas of x-ray science that involve nonlinear interactions of x-ray photons with materials. Potential new applications may include multi-photon spectroscopic imaging, and nonlinear x-ray scattering for valence electron structural determinations.

[2] In this design report we do not explore the obvious possibility of using an ERL as a FEL driver.

Flux – brilliance – bandwidth. The enhanced brilliance of the ERL aides many experimental techniques and pushes the envelop of high energy resolution. Inelastic x-ray scattering spectroscopy, microfluorescence, and microtomography need extreme fluxes to help compensate for narrow bandwidth optics or wavelength dispersive high-resolution detectors. As an example, the practical flux available from existing sources limit experiments to energy resolutions on the order of a meV, which is adequate to explore some aspects of the phonon spectrum of materials. The increased brilliance of the ERL will enable practical resolutions on the order of 100 μeV, thereby significantly broadening the range of materials which may be studied by inelastic scattering (Alp 2000).

Infinite lifetimes – stability – flexibility. The beam current in the ERL will be constant, yielding ideal normalization characteristics and translating into stability in x-ray beamline and optical components because of the absence of the periodic heating cycles associated with storage ring fills. The ERL is extremely flexible; the injector can run over a wide range of current, pulse shapes, timing and bunch structures. However, it is important to realize that not all ERL features may be possible simultaneously. For example, it may not be possible to maintain the maximum brilliance values simultaneously with the maximum flux or minimum bunch length. Exploration of the limits of simultaneous machine parameters is an important function of the Phase I ERL program.

2.3.2 X-ray Optics Frontiers and Challenges

Just as with all past SR sources, the technology of delivering the x-ray beam to the researcher requires beamline and optical components that do not degrade the brilliant short-pulsed beams. The power and x-ray beam heat loads produced by the ERL on the x-ray optics will be comparable to 3rd generation sources and we expect, therefore, that past designs for apertures, beam position monitors and crystal optics can be utilized. The enhanced coherence and ultra-short pulses, however, require new approaches. For example, the intrinsic short x-ray pulse width coming from the ERL would be lengthened considerably if the response time of the diffracting monochromator crystal were longer than 100 fs. Also, with 3rd generation machines it was discovered that semi-transparent x-rays windows can act as refractive "phase-retarders" and can spoil photon coherence. Resolution of these technical challenges will certainly be among the first tasks for a full-scale ERL light source. More information on x-ray optical challenges may be found in Sections 3.1.11 and 3.1.12.

2.3.3 X-ray Microbeams

Micro-focused x-ray beams 0.3 to 1 micron in size have been one of the real success stories (Riekel 2000) of 3rd generation synchrotron x-ray machines such as the APS, ESRF, and SPring8. One of the limitations of storage rings, though, is that the

horizontal size of beams is much larger that the vertical size. To achieve the highest spatial resolution, the most useful beams for microbeam experimentation are round in shape. The ERL will produce round beams with rms sizes of 3 - 11 microns in diameter (Table 2.3.3-1). With suitable brilliance-preserving optics, the ERL should provide focused beams of 50 nanometer size. This will have an immediate benefit to all measurements on small specimens. Two examples of microbeam research follow:

Microbeam High-Pressure Research: Advances in maximum pressure-temperature capabilities have opened new research opportunities in the studies of physics, chemistry, material sciences, and Earth-planetary sciences. Because most high-pressure work involves the very small volumes of the diamond anvil cells, *in-situ* microprobe capabilities are essential for measurements of properties of microscopic samples at ultrahigh pressures and temperatures and for reducing the effects of gradients across the specimens in these variables. The present state-of-the-art measurements utilize 10 micron beams at the NSLS and ~1 micron beams at 3rd generation ID beam lines. By providing smaller, ultra-high quality microbeams, the ERL will be able to make a significant impact, especially for those situations where it can reduce measurement times from days to hours.

Microbeams in Materials Science: Most metals are polycrystalline and the size, structure, and interfaces between the grains control the properties of the material. Recently developed techniques like Three Dimensional X-ray Diffraction Microscopy (3DXDM) at the ESRF use 1 micron-sized beams to study the dynamics of structure evolution on a minute time scale with 40 to 80 keV x-rays (Margulies 2001; Poulsen 2001). Microbeams in conjunction with micron-wide tungsten shadow wires are being used at the APS to study strain and orientation of individual micron-sized grains in the bulk of polycrystalline metal samples (Ice 2000). In both of these examples, present experiments are limited by the beam size and flux. Impressive picosecond and sub-picosecond experiments have been performed on large size samples, but they have been limited by source intensity, resolution, triggering and/or detection capabilities (Raksi 1996; Rischel 1997; ALS ; Cavalleri, et al. 2000; Lindenberg 2000). The enhanced brilliance and time structure of the ERL will be needed for Pulsed Laser Deposition and film growth diffraction studies in order to resolve the crystallization phase (Larson 2000). Microbeam focusing with a brilliant ERL beam can provide enough intensity for single-terrace surface studies.

Table 2.3.3-1. Horizontal and vertical beam sizes for ESRF, APS, and ERL sources designed for microfocusing. For the calculation in this table, the 25 meter long ID is assumed to have a beta of 4 meters in segmented form, and a 1m beta for the 2 m long ID, i.e. half its length. The comparison is for 10 mA (low emittance) and 100 mA (higher emittance) ERL running. Sigma(=rms) values are given.

	Sigma x (μm)	Sigma x' (μrad)	Sigma y (μm)	Sigma y' (μrad)
ESRF microfocus ID13	57	88.5	10.3	7.2
APS(APS 1999)	359	24	21	6.9

ERL, ID=25m, 100 mA normal focus	24.5	6.1	24.5	6.1
ERL, ID=2m, 10mA, microfocus	3.2	3.2	3.2	3.2

Powerful x-ray methods have been often limited because of available microbeam intensities. For example, x-ray standing wave analysis has become a very important tool for characterization of materials and surfaces (Zegenhagen 1993; Daillant 1997; Wang 1998). Typically, standing wave analysis requires relatively large dynamically diffracting substrates. The use of very brilliant microbeams opens the possibility of extending this technique to microcrystals, which often are sufficiently perfect to act as dynamical scatterers. The extension of the standing wave technique to microcrystalline substances would have an enormous impact on materials analysis. It would be necessary, however, to produce a parallel wave front, which places stringent conditions on the way the microbeam is produced.

Another area of interest is in using ERL microbeams for microfluorescence, microspectroscopy and microtomography applications. The increased brilliance from an ERL source can potentially increase the flux in a 1 micron size by a factor of 100 over APS (1 micron size) to 1000 (if full brilliance can be utilized) or to reduce the spot size to 100 nm or less (Rivers 2000). The flux can be used to compensate for the low efficiency of wavelength dispersive high-energy resolution detectors that employ crystals on a Roland circle, which will be very important for heterogeneous samples with many nearby fluorescent lines.

2.3.4 Time-resolved X-ray Diffraction and Scattering

Since the earliest pioneering time-resolved diffraction measurements in the 1970s the brightness, brilliance and coherence of a single bunch have been increased by many orders of magnitude with subsequent generations of SR sources. However, the time structure during these two decades has not changed much: the typical pulse length of the APS is 65 ps, and 35 ps at the ESRF. This is in striking contrast with the needs of the scientific community to explore the femtosecond time domain.

X-ray machines with pulses of 300 fs and shorter include plasma sources based on focusing a femtosecond laser pulse on a solid target (Murnane 1991), sources based on Thomson scattering of laser pulse on a relativistic electron beam (Schoenlein 1996) and, more recently, on the laser modulation of the electron bunch inside an insertion device (Schoenlein 2000). Sub-picosecond x-ray pulses cannot be produced directly in storage rings due to electron bunch instabilities (Limborg 1998), but can be achieved in a recirculating linac arrangement (Krafft 1999), because in contrast with storage rings, the bunch length out of the injector is already short (~1-2 ps), and, given the absence of constraints on bunch storage, may be used to produce even shorter x-ray pulses by a variety of means (Garoby 1998; Zholents 1999; Leemans 2000). X-ray pulses of 100 fs rms may be feasible; indeed, 200 fs bunches are used at CEBAF routinely (Kazimi 2000; Krafft 2000b) and bunches below 100 fs rms have been observed (Wang 1995; Wang 1998; Kazimi 2000).

The very strong science case for sub-picosecond x-ray pulses has been described in detail in a LBNL proposal for an ultrafast x-ray science facility at the ALS (ALS 2000). An ERL would provide x-ray pulses many orders of magnitude more intense than possible at the ALS (Figure 2.2-6); indeed, this realization is motivating consideration of a linac-based ultrafast x-ray source at LBNL (Padmore 2001). Given the ALS documents (Schoenlein 1996; ALS 2000; Schoenlein 2000), the science case for sub-picosecond x-ray pulses will only be touched upon here.

Vibrations and rotations of atoms in single molecules and molecular ensembles occur on a time scale of 10^{-15}-10^{-12} second. This means that, in principal, with sub-ps x-ray pulses such fundamental structural transformations on molecular level as breaking and formation of chemical bonds can be accessible. Several pioneering experiments have been performed in recent years. In time-resolved protein crystallography (Moffat 1989) 1 ns time structural response has been measured in experiments on photolysis in myoglobin (Srajer 1996) and experiments on energy transfer in photoreceptor (photoactive yellow protein)(Perman 1998). Both experiments were performed at the ESRF using fast Laue techniques and x-ray pulses of 50-150 ps. The limitations toward shorter times are both the bunch length and the degree of photolysis in the relatively large crystals which were used at the ESRF. These limitations will be lifted with the shorter x-ray pulses and more brilliant microbeams (enabling use of 2—25 μm crystals) from an ERL (Wulff 1996).

Perhaps one of the most exciting uses of fast x-ray pulses is to help elucidate the details of transition states. Macromolecular crystallography has given us detailed information about the time-averaged structures of active sites in enzymes, but the details of the transition states on which the enzymes actually depend are, in most cases, very much unknown. Many, if not most, aspects of the transition state theory formulated by Eyring and colleagues in the 1930's (Glasstone 1940) have never been structurally verified because of the short lives of transition states. Recent work using ultra-fast (e.g., 1 ps) electron diffraction of laser-driven gas-phase reactions (Ihee 2001) has shown that the time-resolved radial distribution functions can be used to verify the detailed transition paths of chemical reaction. The ultimate impact of elucidation of the transition-state structures of analogs of the active sites of enzyme may well turn out to be comparable in importance to structural biology as the enzyme structures themselves.

Yet another broad areas for study by fast x-ray pulses which may have enormous impact on biology is elucidation of the dynamics of ion hydration. Biology occurs in water. Yet the critical steps of hydration dynamics are still very poorly understood. It is now believed, for example, that ion selectivity in membrane protein channels involves the selective dehydration of ions. Hydration dynamics may be studied by examination of the time-resolved EXAFS spectra of atoms in water after laser-photoneutralization or photo-ionization (Kloepfer 1998). This is but one of many examples of optical pump/x-ray probe type experiments which have the promise to revolutionize our understanding of basic processes.

Ultra-short ERL electron bunches can be periodically diverted and also be used to enable new experiments. An example is the recent use of picosecond-long laser-generated electron pulses to elucidate the detailed structure of the transition states of gas phase reactions (Cao 1999; Ihee 2001). The electron pulses available from the ERL will be both shorter and more intense, allowing study of primary reactions. Although the scattering cross-sections of electrons in these experiments are higher than for x-rays, the ERL x-ray pulses are sufficiently intense that they might allow similar experiments using the x-rays alone.

As another example, intense coherent, broad-band THz radiation (Blum 1991; Lai 1994) has been produced and measured on both the CEBAF accelerator (Wang 1995), and on the IRFEL accelerator (Krafft 1998; Piot 1999). Even with the Phase I accelerator, the photon fluxes will be increased by roughly a factor of 20 beyond what is presently available. It has been suggested that this radiation could be used to generate intrinsic localized modes in solids, akin to vibrational solitons, arising from the anharmonic part of the molecular interaction potential (Rossler 1997). The observation of these localized modes would be a remarkable verification of a theoretical prediction of a state of matter which has not yet been observed.

2.3.5 Non-linear X-ray Spectroscopy

A focused ERL beam will produce electric-field amplitudes similar to those from conventional pulsed lasers. This "perturbative regime", where the electric susceptibility must include higher order terms in the E-field, is normally the domain of visible-light laser research (Figure 2.3.5-1). Using x-rays allows study of nonlinear effects on a much shorter length scale, and possibly combining nonlinear x-ray optical studies with atomic-scale structural analysis. Inside matter, a "non-linear" response refers to time dependent displacements of charge from equilibrium positions (*i.e.* electric polarization) that depend on powers of the electric field greater than one. In addition, when the incident frequencies are near a resonance, these effects can become very much larger.

By way of contrast, the proposed XFEL sources will provide the peak E-field strengths comparable to or exceeding the static Coulomb fields in atoms and are therefore limited to studying the strong-field nonlinear regime. This regime is dominated by stripping of electrons from atoms and subsequent creation of dense plasmas.

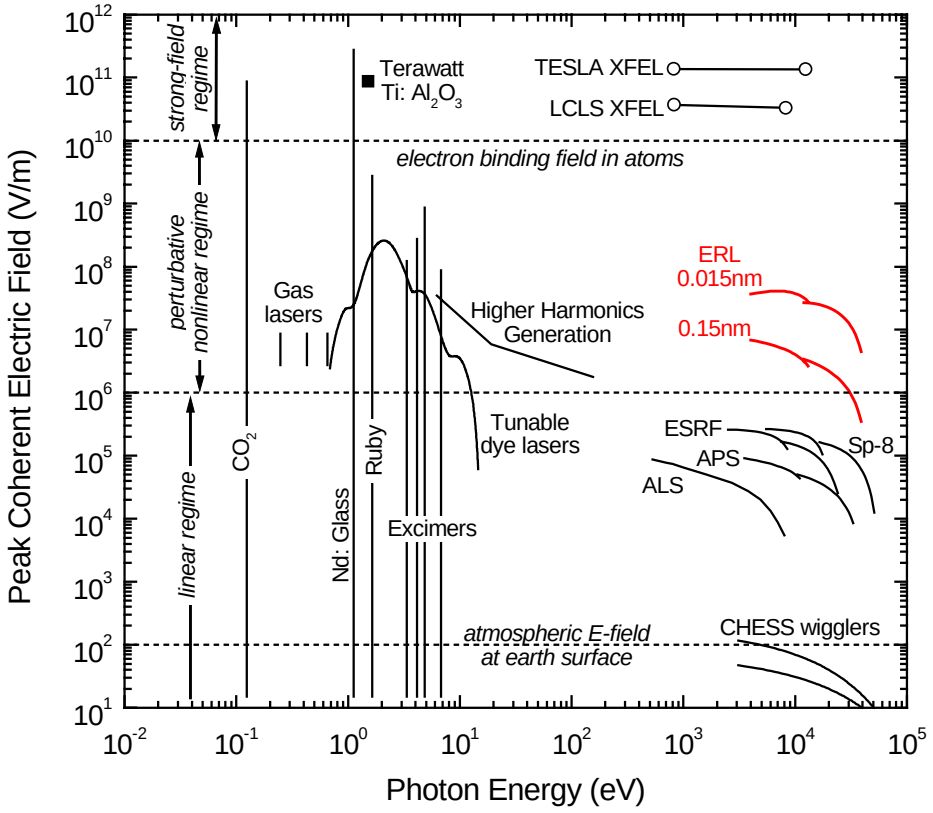

Figure 2.3.5-1. Peak coherent electric field strength vs. photon energy of various radiation sources, showing the possibility that the Phase II ERL will open up a new area for nonlinear optical research even with the XFEL projections. Different regimes of nonlinear photon-matter interactions are based on knowledge of nonlinear laser materials (Fejer 1994; Garmire 1994). Laser sources are based on (Kim 1992; Fejer 1994; Garmire 1994; Levy 1994). Note that the frontier advances in petawatt lasers and strong focusing (Brabec 2000) will make $>10^{13}$ V/m fields, which are not included in this figure. All field values for accelerator based sources assume 1:1 focusing except that a typical 4:1 focal ratio is used for CHESS wigglers. The parameters for ERL, APS, ESRF, and Spring-8 (25m) undulators are listed in Table 2.2-1, and those for the ALS undulator are listed in Figure 2.2-6 but without bunch-slicing.

Non-linear x-ray scattering: A useful area of application would be to determine valence electron charge distributions by non-linear x-ray diffraction (Eisenberger 1971; Freund 1972). The idea is to use parametric down conversion, where the energy of an incident x-ray photon (or pump) is split to create two photons inside a crystal; one at a slightly lower x-ray energy (the signal) and the second (the idler) with energy just below the lowest energy absorption edge for atoms in the crystal. Momentum conservation between these photons and the selected reciprocal lattice vector determine the scattering geometry. The diffraction structure factor can be broken into separate contributions from the atomic core and valence electrons (Freund 1972). The scattering geometry selects the

idler photon frequency and when its energy is near that of the highest valence edge (and therefore well below core level excitations) the scattering is dominated by the charge distribution of valence electrons. A probe that is sensitive to valence electrons allows one to probe chemical bonding, exchange interactions and other areas of significant interest in materials science. This technique needs a clear proof of principle and significant development, but it has the potential to become an important compliment to traditional x-ray crystallography.

Multi-photon spectroscopy: During a two-photon absorption process the atom (or molecule) is excited through two steps (Xu 1996; Xu 1997); a transition from the ground to an intermediate state, followed by a transition from intermediate to excited state. This 2-photon excitation will not violate energy conservation if the second photon arrives within the lifetime of the intermediate state. Several aspects of these transitions are novel and interesting in the x-ray regime: the type of 2-photon transition, the intermediate state lifetime associated with typical x-ray transitions, the photon degeneracy and pulse width of ERL generated beams. Because the lifetime for the core level excitations is short, the two-photon process dictates that the two photons must arrive within about $3x10^{-16} \geq \Delta\tau \geq 6x10^{-15}$ seconds of each other. This condition can be satisfied by the ERL because the beams are so intense that one quantum mechanical mode at 8 KeV contains >300 photons. Therefore there is a reasonable probability for such a 2-photon transition.

Once multi-photon scattering cross-sections are well understood, it would be natural to try to develop 2-photon excitation fluorescent microscopy, similar to the optical wavelength applied in biological imaging (Xu 1997). Multi-photon (non-linear) microscopy takes advantage of two essential factors: a) it occurs only in an extremely limited spatial volumes (Williams 2001) where the E-field intensity is high enough to permit the excitation and b) the signal to background can be very high as the multi-photon fluorescence signal occurs at an energy well above that of the incident beam and its parasitic scattering. With these characteristics the microscope might have very high spatial resolution and high selectivity to atomic species.

2.3.6 Coherent Flux and Hard X-ray Microscopy

The ERL offers high coherent flux and focused coherent flux density in the hard x-ray regime (Figure 2.3.6-1). Compared to the 3rd generation synchrotron sources, the average coherent flux per unit area from the ERL can be 10^3–10^4 times higher, offering many opportunities for new sciences in this area. Compared to the proposed 4th generation XFEL sources, the ERL provides competitive time-averaged coherent flux densities but much less (10^5–10^6 less) coherent photons in each pulse. Consequently the science that can be done at the ERL would defer significantly from science proposed at the XFEL, both in experimental measurement techniques and in fundamental regimes of how x-ray photons interact with matter.

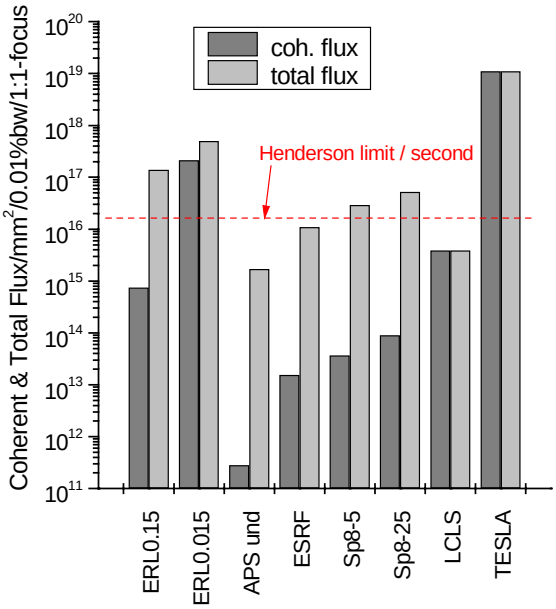

Figure 2.3.6-1. Coherent and total flux from various x-ray sources

The ERL offers high coherent flux and focused coherent flux density in the hard x-ray regime (Figure 2.3.6-1). Compared to the 3rd generation synchrotron sources, the average coherent flux per unit area from the ERL can be 10^3–10^4 times higher, offering many opportunities for new science in this area. Compared to the proposed 4th generation XFEL sources, the ERL provides competitive time-averaged coherent flux densities but much less (10^5–10^6 less) coherent photons in each pulse. Consequently the science that can be done at the ERL will defer significantly from science proposed for the XFEL, both in experimental measurement techniques and in fundamental regimes of x-ray interactions with matter.

What experiments make use of coherence and how much coherent flux is usable? The next few sections highlight several measurement techniques that gain with increased coherence. Some measurements have fundamental limits that prevent any simple extension of their technique. For instance, it has been known for some time that radiation damage is a fundamental limit in detecting weak scattering signals from biological specimens using intense x-ray beams (Henderson 1990; Henderson 1995). Based on the "Henderson limit" biological molecules would be destroyed by a single pulse of $2\text{x}10^{12}$ photons coming from an XFEL source such as the LCLS. Thus only single-shot experiments are possible at the XFEL sources (Hajdu 2000), and high resolution structural data would require the development of techniques to handle molecular samples and to combine data from many shots. With the ERL source, on the other hand, while the average coherent flux density (assuming 1:1 perfect focusing with zone plates) can be as high as the XFEL sources, the coherent photons in a single pulse are several orders of magnitude smaller. This makes the ERL radiation in a single pulse well below the conventional radiation damage limit for biological specimens, but at or just above that limit (if focused) for continuous-wave experiments. Therefore one could perform coherent scattering experiments averaging over many pulses, or even continuous measurements using slightly defocused beams, similar to the present-day crystallography experiments performed at the 3rd generation sources. Ultimately, of course, techniques to

combine data from many samples will be needed with any x-ray source if the sample volume shrinks to too low a value. Thus, the ERL would be most useful for samples which are too small to be analyzed by present 3rd generation sources, but still consist of many molecules. Examples include protein microcrystals, small 2-dimensional rafts of membrane crystals, nanocrystals, and molecular clusters.

One technique that could benefit greatly from an ERL source is x-ray microscopy. X-ray microscopes can be categorized into five classes: transmission x-ray microscopy, scanning x-ray microscopy, contact microradiography, Gabor in-line holography, and diffraction microscopy (Kirz 1995). The first three types do not generally require a coherent illumination of the specimen if only amplitude contrast is desired. However, a coherent incident beam would allow certain types of optics such as zone plates be used to create a small beam or to magnify an object image (projection microscope). In the hard x-ray regime at synchrotron sources, the most widely adopted method so far is x-ray microscopy using a scanning micro-probe. But in recent years, due to the availability of highly collimated beams from 3rd generation undulator sources, phase-contrast imaging in transmission x-ray microscopy has received considerable attention (Snigirev 1995). This is an area that will benefit greatly by the highly coherent x-rays at the ERL source.

Of all types of x-ray microscopes, most are based on measuring variations of the electric susceptibility at low angles around the direct beam. Therefore their spatial resolution is ultimately determined by the size of the incident beam, which had been pushed down to ~50nm for hard x-rays before the ERL (Bilderback 1994). With the ERL as a diffraction-limited source, the potential exists to build a microscope based on diffraction that measures the interference among the atoms in the far-field regime. A primary example of this, of course, is x-ray crystallography, which provides structural images on an atomic length scale. The ERL has the potential to extend the method of x-ray crystallography to microscopic crystals and to non-crystalline materials by using coherent scattering and diffraction.

2.3.7 X-ray Photon Correlation Spectroscopy (XPCS)

The dynamics of domain wall ordering in a binary alloy was the first application of coherent x-ray scattering. Alloys like FeAl or CuAu have an ordered phase below a critical temperature, T_c. Above T_c, the sublattices have random occupation. In the temperature regime where critical scattering is observed, clusters of the low-temperature phase are beginning to form and fluctuate in space and time. In this regime, typically a few degrees above T_c, a dynamic speckle pattern appears due to these short-lived ordered domains. XPCS reveals the important time constants of these fluctuations as a function of temperature and length scale (Sutton 1991; Brauer 1995; Grubel 1995; Dufresne 1996).

Making direct use of a coherent incident beam, the x-ray speckle dynamics can be used to study a wide variety of phenomena including dynamics at surfaces (diffusion, step flow, adatom diffusion) (Libbert 1997), lattice defects and disordered systems, and

ultrasoft vibrational modes in biological systems (fluctuations at liquid surfaces, protein folding and fluctuations). Recently first observations of magnetic speckles have been reported (Yakhou 1999). These demanding experiments are flux starved due to very small magnetic cross sections.

A more brilliant x-ray source is needed to go beyond current limits and extend the application of coherent dynamic scattering. All of the improved operating parameters of the ERL will be advantageous for XPCS: large lateral coherence lengths are optimized by small, symmetrically-shaped beams, and longitudinal coherence will be achieved by designing 0.1% bandwidth undulator sources. The time structure of the source determines directly the accessible time and frequency domains. The high repetition rate of 1.3 GHz makes the ERL a quasi-CW photon source, which should allow measurement of photon correlations in the sub-microsecond regime.

The time structure is also the largest difference between an ERL and the presently planned XFEL sources. The XFEL delivers pulses or pulse trains at low overall duty cycle. This limits the time scales of the XPCS experiment, whereas an ERL would cover a wider range of time scales. Another concern for XPCS experiments at an XFEL is the extremely high photon flux during each bunch. The specific intensity is so high that the sample may suffer photoelectron ejection loss and subsequent Coulomb explosion damage with each pulse. The ERL delivers lower intensity pulses over longer period, a potential advantage for this kind of experiment.

Compared to the coherent flux from current insertion devices, the ERL provides intensity gains of a factor of more than 100. The expected flux gain may make previously unexplored regions in q-ω space accessible, at low ω and large q to extend the probed region to shorter length scales (1-30 nm) or at low q and large ω to probe dynamics on short time scales below 10 μsec. Both areas have not been accessible previously, mainly for reasons of insufficient coherent flux. Note also that bandwidth and time structures have to be optimized simultaneously. The envisioned parameters for the ERL would make it the ideal machine for XPCS. Also, the extreme coherent flux at high photon energies (50 keV and above) would open the field for applications studying high-Z materials.

2.3.8 Coherent Scattering from Non-crystalline Materials

The enormous success of structural biology in the past ten years can be attributed largely to the availability of present-day synchrotron sources and advances in isolating and crystallizing proteins. Yet this success has been limited to the small portion of biological specimens that form crystals of sufficient size. There are many biological systems that cannot form crystals and only a limited number of techniques are available for structural studies of non-crystalline materials.

Coherent x-ray scattering has the potential (Sayre 1980) to change this situation dramatically. Instead of using crystals, for which only Bragg diffraction intensities at

discrete reciprocal lattice points are measured in x-ray crystallography, one can in principle measure the intensities of the continuous Fourier transform from a single unit cell or non-crystalline sample. The continuous Fourier transform has an advantage in recovering phase information due to a technique called "oversampling". Miao *et al.* used this recently to invert a soft x-ray diffraction image and recover an object image to 75 nm resolution (Miao 1999). The best resolution to date is ~20 nm in recorded soft-x-ray diffraction image but no reconstructed or phased object image at that resolution has been achieved. It would be of enormous interest to extend these resolutions to below a few nanometers and ultimately to atomic resolution. This would be most useful for study of non- or weakly- periodic cellular structures. A good example is the chloroplast. This will require an ultra-brilliant hard x-ray source, such as the ERL.

Substantial technical developments are needed to achieve this ultimate goal: (i) production of a highly coherent beam in a sub-micron focal spot, (ii) specimen handling, positioning, and cryoprotection from radiation damage, and (iii) phasing with a large number of volume elements or atoms. One of the key issues is the proper balance among the number of atoms in an unknown structure in a given illuminated volume, the amount of material needed to provide a measurable scattering signal to a desired resolution, and the amount of radiation damage suffered by the specimen for a given incident beam intensity.

In addition to the ultimate goal of atomic structure determination without crystals, several intermediate types of experiments can be performed and developments along these lines could pave the way for future more advanced coherent scattering experiments. These include (i) coherent scattering from nanocrystalline biological materials, (ii) two-dimensional crystal arrays of nanofabricated templates, (iii) single macromolecule or macromolecular assemblies at low resolution (e.g. 5-10nm), and (iv) differential partial structural analysis focusing only on certain diffraction features that may change during e.g. a chemical reaction.

2.4 Section 2 References

Alp, E. (2000). "How an ERL Might Benefit Our Understanding of Elementary Excitations in Condensed Matter". Energy Recover Linac (ERL) Science Workshop, Cornell University, Ithaca, NY 14853, 2-3 Dec 2000 http://erl.chess.cornell.edu/papers/X-rayScienceWorkshopDec2000.htm.

ALS (2000). Workshop on Femtosecond X-ray Science, ALS Users Meeting, Advanced Light Source, Lawrence Berkeley National Laboratory, Berkeley, CA, Oct 17-18, 2000 http://xraysweb.lbl.gov/esg/meetings/umfemto/index.html.

APS (1999). "APS Undulator A Specifications", http://www.aps.anl.gov/aod/params/xunda.pdf.

Bazarov, I. V., Bilderback, D.H., Gruner, S.M., Padamsee, H.S., Talman, R., Tigner, M., Krafft, G.A., Merminga, L. and Sinclair, C. (2001b). "The energy recovery linac (ERL) as a driver for x-ray producing insertion devices". 2001 PAC, Argonne Nat. Lab, Argonne, IL: (submitted).

Bazarov, I. V., Krafft, G.A., and Merminga, L. (2001c). "Linac optics for energy recovery linac". 2001 PAC, Argonne Nat. Lab, Argonne, IL: (submitted).

Benson, S., Biallas, G., Bohn, C., Douglas, D., Dylla, H.F., Evans, R., Fugitt, J., Hill, R., Jordan, K., Krafft, G., Legg, R., Li, R., Merminga, L., Neil, G.R., Oepts, D., Piot, P., Preble, J., Shinn, M., Siggins, T., Walker, R., Yunn, B. (1999). "First lasing of the Jefferson Lab IR Demo FEL.", Nuclear Instruments and Methods in Physics Research A **429**: 27-32.

Benson, S. V., Biallas, G., Bohn, C.L., Douglas, D., Dylla, H.F., Evans, R., Fugitt, J., Grippo, A., Gubeli, J., Hill, R., Jordan, K., Krafft, G., Li, R., Merminga, L., Neil, G.R., Piot, P., Preble, J., Shinn, M., Siggins, T., Walker, R., Yunn, B. (2000). "Jefferson Lab Free-Electron Laser Starts Operation with Sustained Lasing at the Kilowatt Level.", Synchrotron Radiation News **13**(4): 13-17.

Ben-Zvi, I., and Krinsky, S. (2001). "Future light sources based upon photo-injected energy recovery linacs.", Synchrotron Radiation News **14**(2): 20-24.

Bilderback, D., Bazarov, I., Finkelstein, K., Gruner, S., Krafft, G., Merminga, L., Padamsee, H., Shen, Q., Sinclair. C., Tigner, M., and Talman, R. (2001). "New energy recovery linac source of synchrotron x-rays.", Synchrotron Radiation News **14**(3): 12-21.

Bilderback, D. H., Hoffman, S.A. and Thiel, D.J (1994). "Nanometer spatial-resolution achieved in hard x-ray-imaging and Laue diffraction experiments.", Science **263**: 201-203.

Blum, E. B., Happek, U. and Sievers, A.J. (1991). "Observation of Coherent Synchrotron Radiation at the Cornell Linac.", Nuclear Instruments & Methods in Physics Research Section A **307**(2-3): 568-576.

Brabec, T., and Krausz, F. (2000). "Intense few-cycle laser fields: frontiers of nonlinear optics.", Rev. Mod. Phys. **72**: 545-591.

Brauer, S., Stephenson, G. B., Sutton, M., Bruning, R., Dufresne, E., Mochrie, S. G. J., Grubel, G., Alsnielsen, J., and Abernathy, D. L. (1995). "X-Ray-Intensity Fluctuation Spectroscopy Observations of Critical-Dynamics in Fe_3Al.", Physical Review Letters **74**(11): 2010-2013.

Brinkmann, R., Materlik, G., Rossbach, J. and Wagner, A. (1997), "Conceptual Design of a 500GeV e+e- Linear Collider With Integrated X-ray Laser Facility", DESY, Hamburg, Germany, http://www.desy.de/~schreibr/cdr/cdr.html.

Cao, J. M., Ihee, H. and Zewail, A. H. (1999). "Ultrafast electron diffraction and direct observation of transient structures in a chemical reaction.", Proceedings of the National Academy of Sciences of the United States of America **96**(2): 338-342.

Cavalleri, A., C. W. Siders, F. L. H. Brown, D. M. Leitner, C. Toth, J. A. Squier, C. P. J. Barty, K. R. Wilson, K. Sokolowski-Tinten, M. H. von Hoegen, D. von der Linde and M. Kammler (2000). "Anharmonic lattice dynamics in germanium measured with ultrafast x-ray diffraction.", Physical Review Letters **85**: 586-589.

CHESS (2000a). Energy Recovery Linac (ERL) Machine Workshop, Cornell Univ., Ithaca, NY, 11-12 Aug 2000 http://erl.chess.cornell.edu/papers/ERLMachineWorkshopAgenda.htm.

CHESS (2000b). Energy Recovery Linac (ERL) Science Workshop, Cornell University, Ithaca, NY 14853, 2-3 Dec 2000 http://erl.chess.cornell.edu/papers/ScienceWorkshopAgenda.htm.

Daillant, J. (1997). "Some recent Techniques using x-rays for the investigation of condensed matter.", Comptes Rendus De L Academie Des Sciences Serie Ii Fascicule B- Mecanique Physique Chimie Astronomie **324**(4): 239-255.

Dufresne, E. (1996), Intensity fluctuation spectroscopy with coherent x-rays, (Ph.D. Thesis, Dept. of Physics, McGill University, Montreal, Canada).

Eisenberger, P. M., and McCall, S.L. (1971). "Mixing of X-Ray and Optical Photons.", Physical Review A **3**: 1145.

ESRF (2001). Future applications of science with synchrotron radiation and free electron lasers in Europe., ESRF, Grenoble, France., 16-17 Mar 2001 http://www.esrf.fr/news/FEL-SR.html.

Fejer, M. M. (1994). "Nonlinear optical frequency conversion.", Physics Today **47**(5): 25-32.

Freund, I. (1972). "Nonlinear X-Ray-Diffraction - Determination of Valence Electron Charge Distributions.", Chem. Phys. Letter **12**: 583.

Garmire, E. (1994). "Special Issue: Nonlinear Optics.", Physics Today **47**(5): 23-24.

Garoby, R. (1998). RF gymnastics in a synchrotron. Handbook of Accelerator Physics and Engineering. A. W. Chao, and Tigner, M. (World Scientific, NJ. pp. 557-559).

Glasstone, S., Laidler, K.J., and Eyring, H. (1940). Theory of Rate Processes. NY, McGraw-Hill, NY.

Grubel, G., et al (1995). ESRF Newsletter (23): 14.

Gruner, S., Bilderback, D. and Tigner, M. (2000), "Synchrotron radiation sources for the future", Sept., 2000, CHESS, Cornell University, Ithaca, NY, http://erl.chess.cornell.edu/papers/WhitePaper_v41.pdf.

Hajdu, J., et al. (2000), "Strucutral studies on single particles and biomolecules, in LCLS: The First Experiments", Sept., 2000, SLAC, Stanford, CA, http://www-ssrl.slac.stanford.edu/lcls/papers/LCLS_experiments_2.pdf.

Henderson, R. (1990). "Cryoprotection of Protein Crystals against Radiation-Damage in Electron and X-Ray-Diffraction.", Proc. R. Soc. B **241**: 6-8.

Henderson, R. (1995). "The potential and limitations of neutrons, electrons, adn X-rays for atomic resolution microscopy of unstained biological molecules.", Quart. Rev. Biophys. **28**(2): 171-193.

Ice, G. (2000). "Frontiers of x-ray microdiffraction". Energy Recovery Linac (ERL) Science Workshop, Cornell University, Ithaca, NY, 2-3 Dec 2000 http://erl.chess.cornell.edu/papers/X-rayScienceWorkshopDec2000.htm.

Ihee, H., Lobastov, V. A., Gomez, U. M., Goodson, B. M., Srinivasan, R., Ruan, C. Y., and Zewail, A. H. (2001). "Direct imaging of transient molecular structures with ultrafast diffraction.", Science **291**(5503): 458-462.

Kazimi, R., Sinclair, C.K. and Krafft, G. (2000). "Setting and measuring the longitudinal optics in the CEBAF injector". Proc. of the Int. LINAC Conf.: 125.

Kim, K.-J. (1986). Characteristics of Synchrotron Radiation. X-ray Data. (Lawrence Berkeley Laboratory, Berkeley. pp. CH 4-1).

Kim, K.-J. (1989). "Characteristics of Synchrotron Radiation". AIP Conference Proceedings**189**: 565-632.

Kim, K.-J. (1992). Accelerator Technology for Bright Radiation Beam. Coherent Radiation Generation and Particle Acceleration. J. M. Buzzi, Sprangle, P. and Wille, K. (AIP, New York. pp. 107-115).

Kirz, J., Jacobsen, C.,and Howells, M. (1995). "Soft-X-Ray Microscopes and Their Biological Applications.", Quarterly Review of Biophysics **28**: 33-130.

Kloepfer, J. A., Vilchiz, V.H., Lenchenkov, V.A., and Bradford, S.E. (1998). "Femtosecond dynamics of photodetachment of the iodide anion in solution: resonantexcitation into the charge-transfer-to-solvent state.", Chem. Phys. Lett. **298**: 120-128.

Krafft, G., et al. (2000b). "Measuring and Controlling Energy Spread at CEBAF". 2000 International LINAC Conference: 721.

Krafft, G. A. (1999). "Short Pulse Synchrotron Light from Jefferson Lab's Nuclear Physics Accelerator". Proc. of the 1999 Part. Accel. Conf.: 2448.

Krafft, G. A., Piot, P., Jordan, K. and Song, J. (1998). "Measuring and characterizing ultrashort bunches in the Jefferson Lab free electron laser". 1998 European Part. Accel. Conf., Stockholm, 22 -26 June 1998: 1580-1582.

Lai, R., Happek, U., and Sievers, A. J. (1994). "Measurement of the Longitudinal Asymmetry of a Charged-Particle Bunch from the Coherent Synchrotron or Transition Radiation Spectrum.", Physical Review E **50**(6): R4294-R4297.

Larson, B. (2000). "Impact of ERL pulse-length and brilliance on structure and evolution investigations". Energy Recover Linac (ERL) Science Workshop, Cornell University, Ithaca, NY, 2-3 Dec 2000 http://erl.chess.cornell.edu/papers/X-ray%20Science%20Proceeding%20Papers/LarsonERL.pdf.

Larson, B. C., White, C.W., Noggle, T.S. and Mills, D.M. (1982). "Synchrotron X-ray diffraction study of silicon during pulsed-laser annealing.", Phys. Rev. Lett. **48**: 337-340.

LCLS (1998), "Design Study Report", http://www-ssrl.slac.stanford.edu/lcls/design_report/e-top.html.

Leemans, W., Chattopadhyay, S., Esarey, E., Zholents, A., Zolotorev, M., Chin, A., Schoenlein, R., and Shank, C. V. (2000). "Femtosecond X-ray generation through

relativistic electron beam-laser interaction.", Comptes Rendus De L Academie Des Sciences Serie Iv Physique Astrophysique **1**(3): 279-296.

Levy, D. H. C. C. (1994), "Free electron lasers and other advanced sources of light: scientific research opportunities", National Academy Press, Washington, DC, http://books.nap.edu/books/NI000099/html/R1.html#pagetop.

Libbert, J. L., Pindak, R., Dierker, S. B., and Robinson, I. K. (1997). "Speckle in coherent x-ray reflectivity from Si(111) wafers.", Phys. Rev. B **56**: 6454-6457.

Limborg, C. (1998). "Present time structure properties of storage ring based X-ray sources.", SPIE **3451**: 72-81.

Lindenberg, A. M., Kang, I., Johnson, S. L., Missalla, T., Heimann, P. A., Chang, Z., Larsson, J., Bucksbaum, P. H., Kapteyn, H., Padmore, H. A., Lee, R. W., Wark, J. S. and Falcone, R. W. (2000). "Bragg diffraction study of coherent acoustic phonons.", Physical Review Letters **84**: 111-114.

Margulies, L., Winther, G., and Poulsen, H.F. (2001). "In-situ Measurement of Grain Rotation During Deformation of Polycrystals.", Science **291**: 2392-2394.

Miao, J., Charalambous, P., Kirz, J. and Sayre, D. (1999). "Extending the methodology of x-ray crystallography to allow imaging of micrometer-sized non-crystalline specimens.", Nature **400**: 342-344.

Moffat, K. (1989). "Time-resolved macromolecular crystallography.", Ann. Rev. Biophys. Chem. **18**: 309-332.

Murnane, M. M., Kapteyn, H.C., Rosen, M.D. and Falcone, R.W. (1991). "Ultrafast X-ray pulses from laser-produced plasmas.", Science **251**: 531-536.

Neil, G. R., Bohn, C.L., Benson, S.V., Biallas, G., Douglas, D., Dylla, H.F., Evans, R., Fugitt, J., Grippo, A., Gubeli, J., Hill, R., Jordan, K., Li, R., Merminga, L., Piot, P., Preble, J., Shinn, M., Siggins, T., Walker, R., Yunn, B. (2000). "Sustained Kilowatt Lasing in a Free-Electron Laser with Same-Cell Energy Recovery.", Phys. Rev. Lett. **84**(4): 662.

Neil, G. R., Jefferson Lab FEL Team (1998). "Industrial applications of the Jefferson Lab high-power free-electron laser.", Nuclear Instruments and Methods in Physics Research B **144**: 40-49.

Nuhn, H. D. (2000). "Technological challenges to X-ray FELs.", Nuclear Instruments & Methods in Physics Research Section A **445**(1-3): 149-154.

Padmore, H. A., Schoenlein, R.W., Zholents, A.A (2001). "A recirculating linac for ultrafast x-ray science.", Synchrotron Radiation News **14**(2): 26-31.

Perman, B., Srajer, V., Ren, Z., Teng, T., Pradervand, C., Ursby, T., Bourgeois, D., Schotte, F., Wulff, M., Kort, R. Hellingwert, K. and Moffat, K. (1998). "Energy transduction on the nanosecond time scale: early structural events in a xanthopsin photocycle.", Science **279**: 1946-1950.

Piot, P., Kraft, G.A., Jordan, K., Grippo, A., and Song, J. (1999). "Performance of the Electron Beam Diagnostics at Jefferson Lab's High Power Free Electron Laser". Proc. of the 1999 IEEE Part. Acc. Conf.**3**: 2229-2231.

Poulsen, H. F., Neilson, S.F., Lauridsen, E.M., Schmidt, S., Suter, R.M., Lienert, U., Margulies, L., Lorentzena, T., and Juul Jensen (2001). "Three-Dimensional Maps of Grain Boundaries and the Stress-State of Individual Grains.", J. Appl. Cryst. (submitted):

Raksi, F., Wilson, K. R., Jiang, Z. M., Ikhlef, A., Cote, C. Y. and Kieffer, J. C. (1996). "Ultrafast x-ray absorption probing of a chemical reaction.", Journal of Chemical Physics **104**(15): 6066-6069.

Riekel, C. (2000). "New avenues in x-ray microbeam experiments.", Rep. Prog. Phys. **63**: 233-262.

Rischel, C., Rousse, A., Uschmann, I., Albouy, P. A., Geindre, J. P., Audebert, P., Gauthier, J. C., Forster, E., Martin, J. L., Antonetti, A. (1997). "Bragg peak monitoring of laser breakup of metal bonding in Cd arachidate Langmuir-Blodgett Film (~600 fs).", Nature **390**: 490-492.

Rivers, M. (2000). "Microfluorescence, Microspectroscopy and Microtomography Application". ERL Science Workshop, Cornell University, Ithaca NY, December 2-3, 2000 http://erl.chess.cornell.edu/papers/X-rayScienceWorkshopDec2000.htm.

Ropert, A., Filhol, J.M., Elleaume, P., Farvacque, L., Hardy, L, Jacob, J., Weinrich, U. (2000). "Towards the ultimate storage ring-based light source". Proceedings of EPAC: 83.

Rossler, T., and J. B. Page (1997). "Creation of intrinsic localized modes via optical control of anharmonic lattices.", Physical Review Letters **78**(7): 1287-1290.

Rossmann, M. G., Arnold, E., Johnson, J.E., Mosser, A.G., Rueckert, R.R., Sherry, B. (1985). Nature **317**(9): 145-153.

Sands, M. (1970), "The physics of electron storage rings. An introduction", November 1970, SLAC, Stanford, CA, SLAC-121.

Sayre, D. (1980). "Imaging Processes and Coherence in Physics.", Lecture Notes in Physics **112**: 229-235.

Schoenlein, R. W., Chattopadhyay, S., Chong, H.H.W., Glover, T.E., Heinmann, P.A., Leemans, W.P., Shank, C.V., Zholents, A. and Zolotorev, M. (2000). "Generation of femtosecond X-ray pulses via laser-electron beam interaction.", Applied Physics B **71**: 1-10.

Schoenlein, R. W., Chin, A.H., Chong, H.H.W., Falcone, R.W., Glover, T.E., Heimann, P.A., Johnson, S.L., Lindenberg, A.M., Shank, C.V., Zholents, A.A, and Zolotorev, M.S. (2001). "Ultrafast x-ray science at the Advanced Light Source.", Synchrotron Radiation News **14**(1): 20-27.

Schoenlein, R. W., Leemans, W.P., Chin, A.H., Volfbeyn, P., Glover, T.E., Balling, P., Zolotorev, M., Kim, K.-J., Chattopadhyay, S. and Shank, C.V. (1996). "Femtosecond x-ray pulses at 0.4 angstrom generated by 90 degrees Thomson scattering: A tool for probing the structural dynamics of materials.", Science **274**: 236-238.

Shen, Q. (2001), "X-ray Flux, Brilliance and Coherence of the Proposed Cornell Energy-Recovery Synchrotron Source", Cornell University, Ithaca, NY, 01-002, http://erl.chess.cornell.edu/Papers/ERL_CHESS_memo_01_002.pdf.

Shenoy, G., and Arthur, J. (2000). "Comparison of Storage Rings, ERL, and XFEL X-ray Sources". ERL Science Workshop, Cornell University, Ithaca NY, December 2-3 http://erl.chess.cornell.edu/papers/ScienceWorkshopAgenda.htm.

Snigirev, A., Snigireva, I., Kohn, V., Kuznetsov, S. and Schelokov, I. (1995). "On the possibilities of x-ray phase contrast microimaging by coherent high-energy synchrotron radiation.", Rev. Sci. Instrum. **66**: 5486-92.

Srajer, V., Teng, T., Ursby, T., Pradervand, C., Ren, Z., Adachi, S., Schildkamp, W., Bourgeois, D,. Wulff, M. and Moffat, K. (1996). "Photolysis of the carbon monoxide complex of myoglobin: nanosecond time-resolved crystallography.", Science **274**: 1726-1729.

SRI2001 (2001). "Energy recover linac source of synchrotron radiation, Workshop at SRI2001"., Madison, WI, 21 Aug 2001 http://www.src.wisc.edu/SRI2001/workshops.html.

Sutton, M., Mochrie, S. G. J., Greytak, T., Nagler, S. E., Berman, L. E., Held, G. A. and Stephenson, G. B. (1991). "Observation of Speckle by Diffraction with Coherent X-Rays.", Nature **352**: 608-610.

Tigner, M. (1965). "A Possible Apparatus for Electron Clashing-Beam Experiments.", Nuovo Cimento **37**: 1228-1231.

Wang, D. X., et al. (1995). "A Fast Coherent Synchrotron Radiation Monitor for the Bunch Length of the Short CEBAF Bunches". Proc. of the Microbunches Workshop, AIP Conf. Proceedings **367**: 502.

Wang, D. X., Krafft, G.A., and Sinclair, C.K. (1998). "Measurement of Femtosecond Electron Bunches Using a RF Zero-phasing Method.", Phys. Rev. E **57**: 2283.

Wang, J. (1998). "Characterizing surfaces and interfaces using X-ray standing waves.", Current Opinion in Colloid & Interface Science **3**(3): 312-320.

Williams, R. M., and Zipfel, W. (2001). Personal Communication.

Wulff, M., Schotte, F., Naylor, G., Bourgeois, D., Moffat, K. and Mourou, G. (1996). "Single-pulse Laue diffraction, stroboscopic data collection and femtosecond flash photolysis on macromolecules". 17th International Conference, Hamburg, Germany, AIP **389**: 267-293.

Xu, C., and Webb, W.W. (1997). Multiphoton Excitation of Molecular Fluorophores and Nonlinear Laser Microscopy. Topics in Fluorescence Spectroscopy, Vol 5. J. Lakowicz. (Plenum Press, NY.

Xu, C., Zipfel, W., Shear, J.S., Williams, R.M. and Webb, W.W. (1996). Proceedings of the National Academy of Sciences of the United States of America **93**: 10763.

Yakhou, F., et al. (1999). ESRF Newsletter **32**: 12.

Zegenhagen, J. (1993). "Surface-Structure Determination with X-Ray Standing Waves.", Surface Science Reports **18**(7-8): 199-271.

Zholents, A., Heimann, P., Zolotorev and M., Byrd, J. (1999). "Generation of subpicosecond X-ray pulses using RF orbit deflection.", Nuclear Instruments & Methods in Physics Research Section A **425**(1-2): 385-389.

3.0 Vision & Parameters of a Phase II ERL Facility

The purpose of this document is to identify the accelerator issues which must be resolved before a full-scale Phase II ERL can be designed, and to propose a small-scale prototype Phase I ERL to explore and test these issues experimentally. Identification of these issues requires an overall vision of a Phase II ERL. Although many aspects of a Phase II ERL have yet to be determined, enough is already certain to be able to sketch the overall picture of a Phase II facility able to meet the scientific needs described above, in sections 2.2 and 2.3, respectively. Section 3 details the technical requirements and challenges of a Phase II ERL facility.

A Phase II ERL facility would be built around a machine with sample specifications given in Table 3-1. As detailed below, we believe these parameters to be achievable based on very reasonable extensions of existing technology. Note, however, that in many cases it is still unclear as to the optimum strategy to achieve the best performance – this, in fact, is a prime reason for the proposed Phase I ERL program.

We envison a Phase II ERL facility at Cornell which serves three simultaneous, interwoven missions:

1. First, it serves as a vehicle for the development of ERL technology and the continued training of accelerator and x-ray physicists. Cornell has a long tradition of hands-on training of both accelerator physicists and synchrotron x-ray scientists who have gone on to contribute to high energy physics and x-ray synchrotron x-ray facilities around the world. The mechanism for this training is through the development of new accelerator and x-ray technology. A consequence of the growth in the size and scope of storage rings for both high energy physics (HEP) and x-ray applications has been the migration of accelerators from universities to national laboratories, where the machines are built by professional scientific staffs. The result has been a dramatic decrease in the number of graduate students who are trained to build accelerators and beam lines. The work force skilled in building machines and x-ray facilities is aging and soon will suffer large-scale retirements. This is a world-wide problem: The consensus of a recent European conference on future x-ray sources was that the bottleneck in future SR source development will not be funding as much as a dearth of skilled personnel (ESRF 2001). An important aspect of our both Phase I and II ERL plans is to continue and enhance Cornell's educational service as a provider of skilled personnel in these areas.

2. A Phase II ERL will provide beams with characteristics that will challenge the state-of-the-art of undulator development, x-ray optics, and many science applications for many years. We fully expect that ERLs will become the SR technology of choice and will be duplicated around the world as SR needs continue to grow. As with any new technology, there will be a learning curve which must be climbed and which will be steepest for the first ERL machines. A second mission of both the Phase I and II ERLs will be to provide a development laboratory for ERL technology to help the world community climb this learning curve.

3. The third mission of the Phase II ERL will be to provide a user facility with unique x-ray beams for new scientific applications, as touched upon in section 2.3. We see this laboratory as complementing larger facilities in the national laboratories in being able to maintain the advantages of a university environment.

Table 3-1. Sample Phase II ERL Parameter List

(Note: Many parameters of the Phase II ERL depend on the outcome of experimental measurements on the Phase I ERL. Other parameters depend on choices and optimizations which have not yet been decided, e.g., the radiated power will depend on the number and length of the undulators chosen, the dipole radii, etc. The sample parameter list given below serves the purpose of providing a plausible set of parameters with which to examine the machine issues discussed in this report.)

Parameter	Value	Unit
Energy[1]	5	GeV
Macropulse Current	100	mA
Bunch Charge	77	pC
Transverse Emittance (norm. rms)[1]	≤2	mm mrad
Longitudinal Emittance (rms)	40	keV deg
Bunch Length after compression (rms)	0.1-1	psec
Energy Spread (fractional; rms)	1E-4 to 3E-3	
Beam Power	500	MW
Beam Loss	<1	μA
Number of Accelerating Cavities	240	
Cavity frequency	1.3	GHz
Cavity length	1.04	m
Accelerating Gradient	20	MV/m
cavity energy gain	21	MeV
Power/cavity	4.7	kW
Cells/cavity	9	
Q_0	1.00E+10	
Q_{ext}	2.60E+07	
Impedance (r/Q)	9.00E+02	Ohms
Static heat loss/cavity	3	W
Dynamic heat losses	49	W
Lorentz detuning	1	Hz/MV^2
Microphonic Detuning	25	Hz rms
Number of Klystrons	240	
Amplitude Control	1.00E-04	rms
Phase Control	0.1	deg rms
Refrigerator power	16.4	MW
Total power radiated (typical)	400	kW
RF drive power	1.1	MW
Injector beam power	1000	kW
Magnets	700	kW
Undulator 1 period	2.5	cm
Undulator 1 length	25	m
Undulator 2 period	1.7 to 3.3	cm
Undulator 2 length	2	m
Undulator source size (see Table 2.1.1)	24	Microns rms
Photon flux	1E+16	/sec/ 0.1%BW

Brilliance	1E+22	/sec/mm^2/mrad^2/ 0.1%BW
Injector Output/RF		
Energy	10	MeV
Macropulse Current	100	mA
Bunch Charge	77	pC
Longitudinal Emittance (rms)	10	keV deg
Bunch Length	2	psec
Beam Power	1000	kW
Number of Accelerating Cavities	4	
Power/cavity	150	kW
Voltage/cavity	1.5	MV
Cells/cavity	1,3	
Accelerating Gradient	4.3	MV/m
Q_0	1E10	
Q_{ext}	1.40E+05	
Photocathode Gun		
Voltage	500 to 750	kV
Average Current	100	mA
Bunch Charge	77	pC
Thermal Emittance (norm. rms)	< 0.5	mm mrad
Bunch Length	20	psec
Repetition Rate	0.02-1.3	GHz
Beam Pulse Length	2	msec to CW
Cathode Peak Field	10 to 15	MV/m
Drive Laser Power	10	W
Max. Cathode Spot Diameter	5	mm

[1] These values differ slightly from those used to calculate Table 2.2-1. Even so, both tables use values that may be reasonably anticipated in a Phase II ERL

3.1 Phase II ERL Accelerator Physics & Technology Issues

3.1.1 Design Principles

To achieve maximally brilliant x-ray beams, it is important that the ERL be designed so that the photoinjector emittance is as small as possible and that emittance growth during beam acceleration and during beam transport to the undulators is minimized. Another important requirement is that the beam remain stable against transverse and longitudinal multibunch instabilities, which are somewhat analogous to the multibunch instabilities that afflict storage rings at high current. It is also required that beam loss is small during beam recirculation, for both cryogenic efficiency and machine protection reasons, and that the RF beam loading from the two beam passes is efficiently compensated in order to minimize the RF power draw. Finally, because the accelerator contains only a few passes, the longitudinal phase space of the accelerated beam can be preserved and manipulated, yielding extra degrees of freedom in design, but also extra degrees of complication. Each of these issues will be treated briefly in this section, and in more depth in sections 4 and 5, when we discuss the details of the Phase I ERL. In this section, however, we discuss general issues (e.g., Phase II) ERL issues.

It is necessary to decrease the electron beam emittance as much as possible in order to maximize the brilliance out of the undulators. Because 3rd generation SR storage ring sources already have very bright beams, the first requirement is to design the machine with an average beam brightness that exceeds that possible in an equivalent energy storage ring. This requirement places a severe limit on the parameter choices possible in the machine. In particular, the requirement tends to drive one to a design with low charge-per-bunch and more frequent bunches, just the opposite of the case with XFELs. One would like the normalized emittance at the undulator to remain as close to the emittance generated at the injector as possible. The emittance from the injector should be minimized by space charge compensation techniques discussed in the sections 2.4.3.1 and 3.3.8, with the goal of approaching the lower limit of thermal emittance from the photocathode.

Supposing for the moment, as shown below, that an injector can be designed with an average brightness better than an equivalent ring. Then one must take steps to assure that the beam emittance is not degraded on acceleration and delivery to the undulators. The approach taken here involves:

(1) Choosing the single bunch charge low enough that typical single bunch emittance growth mechanisms (e.g. transverse single bunch beam breakup, wakes, non-inertial space charge, and coherent synchrotron radiation), do not result in much emittance growth. This is helped by the fact that superconducting accelerating cavities are being used, thereby permitting large apertures.

(2) Designing the beam optics such that the single particle sources of emittance growth, in particular that generated by the synchrotron emission in the turn-around arcs, is minimized. The approach is very similar to that taken in storage rings where a minimum emittance lattice design is employed.

(3) Because the beam average current in the ERL will be high, it is necessary to take care that the beam is stable against multibunch instabilities. The threshold for instability depends strongly on two design parameters, the once around beam optics and the properties of the High Order Modes (HOMs) of the accelerating cavities. By proper linac and arc beam optics designs that keep the beta functions small (60 m and smaller) throughout the linac, we have performed simulations that show that a 5 GeV accelerator should be stable at an operating current of 100 mA, assuming the HOMs are damped as well as they have been for the TESLA test facility cavities at DESY.

The high energy beam loss tolerable in the ERL accelerator is already partially understood through the experience at JLAB on the CEBAF 6 GeV superconducting nuclear physics accelerator. Machine protection requirements in this accelerator dictate that the CW beam loss be held under 1 μA. Additional confidence that losses can be kept low comes from the experience at the JLAB IRFEL (Neil 1998; Neil 2000), where better than 99.98% of the beam current is recovered, indicates that low losses are possible. The beam loss at the JLAB IRFEL may well be better than 99.98%, but has not been

measured to the required accuracy. One of the goals to be demonstrated by the prototype is that losses can be kept under 1 μA for the full beam current of 100 mA. (See also the Beam Loss subsection of section 3.1.9)

As discussed previously in Section 2, in any recirculating accelerator that has only a few passes it is possible to accelerate beams with short pulse lengths by suitable manipulation of the longitudinal phase space of the beam in the injector. Because of this possibility, the ERL provides a way of providing brilliant x-ray beams of short temporal duration. It is still uncertain whether it is possible to simultaneously supply x-ray beams with sub-picosecond duration and greater than 10^{22} photons/s/0.1% bw/mm^2/mrad^2 brilliance, because single bunch collective effects, in particular emittance growth generated by non-inertial space charge and coherent synchrotron radiation, can act to increase the emittance and reduce the brilliance. These effects are worse at higher bunch charge and shorter bunch length. Given a desired pulse length and machine design, there is an optimal charge-per-bunch for producing maximum brilliance. Both theory and experiment on CSR and non-inertial space charge effects are still uncertain, which is a prime motivation for making a Phase I ERL to experimentally explore these effects. As the design of the Phase II ERL matures, we expect to incorporate and take advantage of any methods developed on the Phase I ERL to combat effects which cause the emittance to grow.

As shown in Section 3.1.9, small beam losses at the 10^{-5} level will have no effect on the beam acceleration systems in the energy recovery loop. However, phase shifts between the phases of the first and second pass beams will be easily discerned even when the phase shifts are as low as 0.5 degrees of RF phase, because of the increased load on the RF systems. For the high brilliance running at ps bunch lengths, when it is possible to design the longitudinal optics to minimize such phase shifts, there should be only small effects on machine stability. Some of the most exciting scientific applications will require bunches on the order of 100 fs in length. This will make it necessary to tune the turnaround arcs in ways that are relatively error sensitive, requiring development of active controls.

3.1.2 Electron Source

The electron source must provide a high average-current bunched beam with small transverse and longitudinal emittances. The highest bunch repetition frequency will match the accelerator fundamental frequency of 1300 MHz. Flexible bunch patterns must also be practical over a wide range of possibilities, from simple reduced repetition rate bunch trains to well-separated groups of bunches at various repetition rates, in order to match specialized experimental needs. For a 100 mA average beam current at the 1300 MHz bunch repetition rate, the charge per bunch is 77 pC.

The normalized transverse emittance in each plane is specified to be no greater than 2 μm at the full accelerator energy. The thermal emittance from the photocathode will be no greater than 0.5 mm-mrad, and emittance compensation will be employed to

minimize the space-charge driven correlated emittance growth in the early part of the injector. With reduced average beam current, even smaller emittance values should be achievable, as required for certain applications.

Both RF and DC photoemission guns are potential sources for an ERL. Considerable experience with both types has been acquired world-wide. Possible application of a normal conducting RF gun to an ERL is discussed in (Ben-Zvi 2001). DC sources have been much used in practice at JLAB (Engwall 1997) and elsewhere. In the future, it will be important to pursue R&D on superconducting RF guns in the drive to yet lower emittances.

There are advantages and disadvantages of each gun approach. RF guns use positive affinity cathodes, which require very challenging laser systems to deliver 100 mA for an ERL. The DC guns use negative affinity electron emitter materials, such as GaAs, which are more efficient, but easily degraded.

We plan to meet the electron source requirements with a 500 kV DC electron gun incorporating a negative electron affinity GaAs photoemission cathode. The photocathode will be illuminated by light from a mode-locked Ti:sapphire laser operating at 780nm. The Ti:sapphire laser will have a fundamental frequency of 260 MHz, and will be locked to the fundamental accelerator RF by an RF gain switched diode laser. This laser can provide bunch trains at multiples of its 260 MHz fundamental frequency up to 1300 MHz.

No photoemission cathodes have been operated at the requisite performance levels of simultaneous lifetime, current and emittance. A key issue is the operational lifetime of the cathode in the above conditions. The quantum efficiency of the photocathode typically degrades during operation. Based on present experience at JLAB with GaAs photocathodes, it is possible to regenerate the quantum efficiency of a degraded cathode *in situ*, by cleaning and re-activation. This process requires several hours to complete. At CEBAF, this is accomplished via the use of two side-by-side photoguns, so that one may be in use while the other is being regenerated. Since the regeneration is *in situ*, switching from one gun to the other requires only a momentary pause in machine operations. Alternatively, one could construct a load-locked gun that would allow degraded cathodes to be removed and replaced with fresh cathodes. In either case, a long cathode operational lifetime is required to permit extended operation of the full accelerator with infrequent, scheduled interruptions to regenerate or exchange the cathode. Demonstration of acceptable cathode lifetimes at full beam current will be a key issue to be addressed with the Phase I ERL.

GaAs photocathodes have produced beams with measured thermal emittances below the values required for the ERL project. There is good reason to believe that cooling the GaAs photocathode will reduce the thermal emittance further. We will explore the beam emittance provided by a GaAs cathode over a range of parameters during the development of the Phase I ERL.

There is a high degree of correlation between the emittance growth caused by space charge effects in the electron gun and in the beam line immediately after the gun. With careful attention to the beam optics, it has proven possible to "recover" much of this emittance growth, and obtain a final emittance much closer to the natural thermal emittance from the cathode. This process is known as space charge compensation. How well space charge compensation works depends on details such as the transverse and longitudinal profile of the initial electron bunch. These conditions will be explored for optimal space charge compensation with the injector for the Phase I ERL.

Various codes are used to model the performance of the electron gun and injector. With the Phase I ERL, we will make sufficiently detailed measurements to benchmark these codes. This will allow the codes to be used with confidence to develop further improvements to the electron sources and injectors for the Phase II ERL.

There are additional issues such as dark current resulting from thermionic and/or field emission from the photocathode, and the level of beam halo present on the main beam, which will be explored with the electron gun and injector for the Phase I accelerator. If the level of dark current and halo are unacceptable, we will develop means to reduce or eliminate them before they reach the main accelerator. This might be done with the use of apertures to form an emittance filter, or beam scrapers at locations of high dispersion, for example.

3.1.3 General Observations about Linac Optics for the Phase II ERL

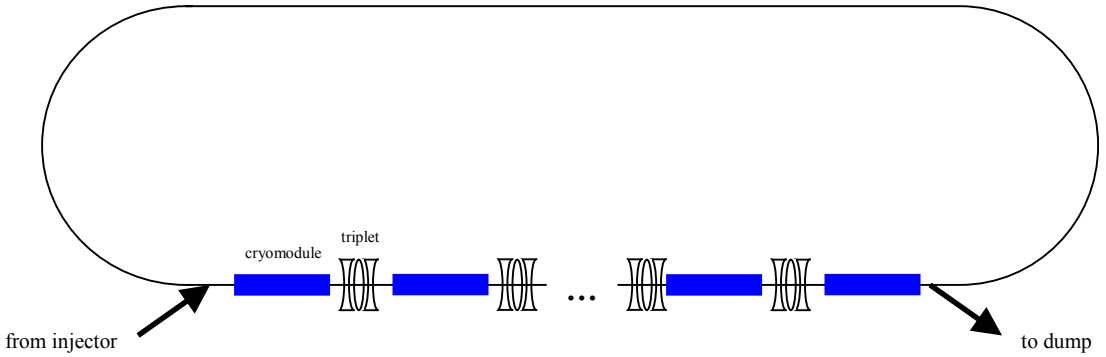

Fig. 3.1.3-1. ERL Conceptual layout.

A conceptual layout for a full-scale ERL is shown in Fig. 3.1.3-1. A 10 MeV electron beam with small normalized transverse emittance from the photoinjector is introduced into the main linac. The linac superconducting RF (SRF) structure accelerates the electrons to 5-7 GeV. Subsequently, the beam is taken through the recirculating transport loop where it performs its role as a source of x-rays and then is returned to the linac with a 180^{o} RF phase offset for energy recovery. In the linac the recirculated electrons yield most of their energy so that it can be used for the acceleration of successive bunches. Finally, the low energy beam exits the linac and is dumped.

Key issues concerning the linac include the development of linac optics which avoids electron beam instabilities. At either end of the linac, very low and very high energy bunches are interleaved only centimeters apart, necessitating consideration of linac electron optics which are stable over a wide range of simultaneous bunch energies. Since the linac operates at 2K, each watt of power lost in the linac requires the expenditure of almost 800 watts of refrigeration wall-plug power for its removal. Hence, it is essential to minimize all sources of heat loss into the linac.

Since the SRF structure of the Phase II ERL is several hundred meters long, external quadrupole focusing is introduced between the cryomodules which make up the linac. External focusing in the linac is also critical to suppress Beam Break Up (BBU) instability. Quadrupole triplets between the SRF cryomodules will be used, allowing good flexibility. The fact that the bunches with two different energies are found along the linac introduces a major constraint on the focusing optics in the SRF structure since electrons with different magnetic rigidity pass through the same quadrupoles. The constraint becomes especially important near the ends of the linac where the energy ratio of the accelerating and decelerating beams may be as high as 1000 (or about as high as 30 for the outer triplets[1]).

This concern has led to the suggestion that the maximum energy ratio of two beams in the linac should not exceed 10 (Ben-Zvi 2000; Douglas 2000a). This would require splitting a 5 GeV linac into two (or more) parts so that early stages of acceleration and late stages of energy recovery would take place in a section different from the longer SRF structure where most of the acceleration / energy recovery occurs, e.g., (Ben-Zvi 2000). Nevertheless, we have found upon simulation that such a "split linac" scenario produced no noteworthy advantages over a single long linac structure in terms of either BBU suppression or the ability to propagate a beam envelope with small β-functions through the linac.

Adiabatic damping/antidamping is another important reality to keep in mind when designing the linac optics. Consider the beam-transport matrix ($i \to f$) for the drift with a uniform acceleration/deceleration (the matrix can be worked out from the transverse momentum conservation):

$$\begin{pmatrix} x_f \\ x'_f \end{pmatrix} = \begin{pmatrix} 1 & \frac{\gamma_i}{\gamma'} \ln \frac{\gamma_f}{\gamma_i} \\ 0 & \frac{\gamma_i}{\gamma_f} \end{pmatrix} \begin{pmatrix} x_i \\ x'_i \end{pmatrix}, \qquad (3.1.3\text{-}1)$$

where γ and γ' are the normalized energy (divided by the rest energy mc^2) and the accelerating gradient, respectively, and x is the transverse position. $R_{12} = \frac{\gamma_i}{\gamma'} \ln \frac{\gamma_f}{\gamma_i}$ can be interpreted as an effective length since $x_f - x_i = x'_i R_{12}$ (Helm 1969); The **R** matrix is

[1] The "outer triplets" are located after the first cryomodule and before the last one. The ratio of the energies at those locations is (5000-166.4)/(10+166.4) = 27.5 for 5 GeV linac, 10 MeV injection energy, and a 166.4 MeV energy gain per cryomodule, assuming a gradient of 20 MV/m in the SRF cavities.

defined in TRANSPORT notation in (Brown 1977). Thus, the effective length of the linac is contracted when the beam is accelerated ($R_{12} = 5$ m with an actual 400 m linac) and elongated when the beam is decelerated ($R_{12} = 2.5$ km if the beam is decelerated down to 10 MeV). This illustration indicates that special care must be taken in the late stages of the energy recovery where adiabatic antidamping is especially prominent.

3.1.4 Transverse Beam Break Up Stability

Multipass, multi-bunch BBU has been long known to be a potential limiting factor in the operation of high current linac-based recirculating accelerators (Rand 1980; Bisognano 1987). Consider the first orbit of recirculation. The first-pass beam may be perturbed by the transverse magnetic fields of a dipole higher order mode (HOM). Transverse beam displacement on successive passes will feed energy into this mode by interaction with its longitudinal electric field. This can lead in turn to further displacement of the beam, driving it into instability, if the rate with which the energy is supplied to the HOM by this mechanism is greater than the rate of the mode's decay. Thus, BBU can limit the maximum current that a linac-based recirculating accelerator can support. Obviously, the effect can be significant in SRF cavities because of the potentially higher Q's of the HOMs. BBU transverse instability is also exacerbated in long RF structures of several hundreds of meters length. The Phase II ERL envisioned will have to deal with both of these complications, since a long (~400 m) superconducting RF structure will be at the heart of the machine.

The ERL will operate in quasi-continuous wave (CW), as opposed to pulsed mode, by which we mean that most, if not all RF buckets in the linac will be filled. There has never been an experimental demonstration of a high current (~0.1 A) CW beam in a high energy ERL. The result of calculations of the BBU threshold current which were performed for the JLAB IRFEL Upgrade (Campisi 1999) is indicative of the seriousness of the problem. The BBU threshold current obtained by numerical simulations was 75 mA for a 170 MeV recirculating SRF structure. Therefore, it is evident that the design of a 5 GeV, several hundred meter long recirculating SRF structure needs careful exploration.

Analytical solution for single-recirculation-single-HOM case

Important insights into the problem can be gained by studying a simple case of single-loop recirculation and only one HOM. In this case, an analytical solution for BBU threshold current I_{th} exists (Krafft 1988):

$$I_{\text{th}} = -\frac{1}{e}\frac{2\omega_\lambda}{(R/Q)_\lambda Q_\lambda k_\lambda^2 m_{12} \sin(\omega_\lambda t_r)} \qquad (3.1.4\text{-}1)$$

where e is the electron charge; $(R/Q)_\lambda$, Q_λ are the geometric shunt impedance and quality factor of the mode, respectively, $\omega_\lambda = k_\lambda c$ is the mode's frequency, c is the

speed of light, t_r is the total recirculation time, and m_{12} is the recirculation transfer matrix element (momentum to transverse position) for conjugate transverse phase-space coordinates. It can be readily shown that $m_{12} = R_{12}/p_i \cong R_{12}/(E_i/c)$, where p_i (E_i) is the total initial momentum (energy) and R_{12} is the beam-transport matrix element in the classical TRANSPORT notation (Brown 1977).

Inspection of (3.1.4-1) suggests (Krafft 1988), there are several things one can do to mitigate the instability. The most obvious suggestion is to increase the energy of the beam injected into the recirculating RF structure. However, to make an ERL power efficient will require adopting as low an injection energy as possible to minimize the amount of beam power that goes to the dump. The injection energy is determined primarily by the lowest possible energy at which an electron beam of sufficiently high quality can be produced and transported to the main linac without diluting its high transverse phase-space density. Another important solution to lessen the BBU instability involves lowering Q's for the HOM. HOM damping is of fundamental importance and has been incorporated into the SRF cavity design (TESLA 2000) From the results of BBU simulations, it is also clear that HOM damping, while being very significant, cannot substitute for intelligent lattice design for the ERL as a whole. The latter can be reduced in part to an optimization problem of the pass-to-pass horizontal and vertical beam-transport matrix elements R_{12} and R_{34} along the SRF structure.

An analytical solution for the value of the BBU threshold current exists only for very simple cases similar to the one just presented above. It is necessary to use computer simulation codes to determine the BBU threshold for an actual machine configuration. Such a two-dimensional simulation code (TDBBU) has been developed at JLAB (Krafft 1987). The problem of lattice optimization also allows analytical solution for only a limited number of cases (Rand 1980) that did not include an ERL. Computer optimization routines were used in this work to obtain the desired lattice parameters by adjusting the strength of quadrupoles in the SRF structure. These two simulation tools have been extensively used to obtain optimal linac optics design, and to test the suggested simple guidelines (discussed below) for choosing linac and recirculating transport line optics that should allow for a sufficiently high BBU threshold current in the ERL. These simulations will be experimentally tested in the Phase I ERL machine.

RF focusing in standing-wave cavities

In order to correctly simulate the transverse dynamics of the particles in the linac, it is important to include the RF focusing that an electron experiences when it traverses an RF cavity operated in an axisymmetric TM mode. The RF focusing effect was originally studied by Chambers (Chambers 1968) and later by Krafft (Krafft 1991) and by Rosenzweig and Serafini (Rosenzweig 1994). Following (Rosenzweig 1994), the transport matrix for a pure π-mode standing-wave cavity for a particle run on RF-wave crest is given by

$$\begin{pmatrix} x_f \\ x'_f \end{pmatrix} = \begin{pmatrix} \cos(\alpha) - \sqrt{2}\sin(\alpha) & \sqrt{8}\frac{\gamma_i}{\gamma'}\sin(\alpha) \\ -\frac{3}{\sqrt{8}}\frac{\gamma'}{\gamma_f}\sin(\alpha) & \frac{\gamma_i}{\gamma_f}\left[\cos(\alpha) + \sqrt{2}\sin(\alpha)\right] \end{pmatrix} \begin{pmatrix} x_i \\ x'_i \end{pmatrix}, \quad (3.1.4\text{-}2)$$

where $\alpha = \frac{1}{\sqrt{8}} \ln \frac{\gamma_f}{\gamma_i}$. The expression (3.1.4-2) also describes the focusing (defocusing) kick that the particle experiences at the entrance (exit) of the cavity due to RF fringe field regions. The sign of the focusing radial force due to RF edges is reversed when the particle goes through energy recovery (running in the RF-wave trough). We compared the analytical expression (3.1.4-2) with numeric simulations for electrons on RF crest (in trough) and found good agreement for beam energies higher than 5 MeV. The RF focusing effect was implemented into the TDBBU simulations.

The effect of RF focusing on the BBU threshold current was found to be significant. The net effect of the SRF cavities on the transverse motion of the particles is always focusing for both acceleration and energy recovery. As a result, this additional focusing facilitates the design of the linac optics and helps to suppress BBU instability.

Linac optics solution to suppress BBU instability

As discussed earlier, the analytical solution for the BBU threshold current in a simple case of one recirculation and one HOM (3.1.4-1) suggests that if the ERL optics can be designed so as to have the pass-to-pass matrix elements R_{12} and R_{34} small everywhere in the SRF cavities then BBU instability will be suppressed. As pointed out below, this statement represents a necessary, but not sufficient requirement for maximum instability suppression in an actual recirculating accelerator. Here, the pass-to-pass matrix is defined as the beam-transport matrix from a given point in the linac to the same point after recirculation. In general, the ideal condition ($R_{12} = R_{34} = 0$) cannot be satisfied everywhere in the linac except in the limit of no acceleration (Rand 1980). Yet, we have found that it is possible to produce an ERL configuration which will have small values of R_{12} and R_{34} (< 10 m) for a long SRF structure of several hundred meters. It is interesting to note that absolutely no external focusing is required in the linac to achieve small values of R_{12} and R_{34} in this case, which corresponds to large β-functions in the linac (the maximum value is approximately equal to the total length of the SRF structure). An example of the β-function in such a configuration, as well as R_{12} values along the linac, is shown in Fig. 3.1.4-1 (the vertical β_y- and horizontal β_x-functions, and R_{12} and R_{34} were chosen to match since the RF focusing in the linac is radially symmetric). The injection energy was 410 MeV and the full energy was 5.01 GeV. The SRF structure was about 300 m long and consisted of 23 cryomodules, each providing 200 MeV of energy. To obtain small values of R_{12} (R_{34}), the pass-to-pass phase advance, $\Delta\psi$, has to be an integer multiple of π throughout the linac. This can be achieved by adjusting optics in the turnaround arc.

Despite the fact that the obtained R_{12} (R_{34}) values are small (≤ 9 m) throughout the SRF structure, TDBBU simulations in the case shown in Fig. 3.1.4-1 for HOM data

taken from 9-cell 1.3 GHz TESLA cavities (Sekutowicz 1994) yielded an instability threshold current of less than 25 mA (all values of BBU current cited here are the current in SR transport loop unless otherwise stated). Such a low BBU threshold current can be explained if one considers that small values of R_{12} (R_{34}) for the pass-to-pass matrix do not guarantee suppression of the instability since the same matrix elements may be quite large for a transport matrix from cavity to cavity. In other words, although the condition discussed above may, indeed, suppress the coupling of a HOM in the same cavity on successive passes it does not preclude the HOMs of two cavities in different parts of the SRF structure to "talk" to each other, either on the same or on successive passes, thus rendering the system unstable. Indeed, one can write the following expression for R_{12} in terms of the β-function and phase advance

$$R_{12}(i \to f) = \gamma_i \sqrt{\frac{\beta_i}{\gamma_i}\frac{\beta_f}{\gamma_f}} \sin \Delta\psi \,. \qquad (3.1.4\text{-}3)$$

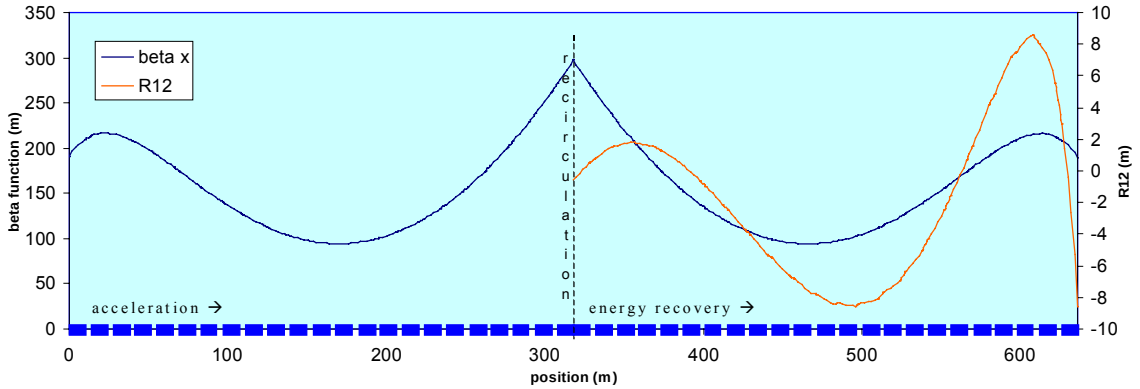

Fig. 3.1.4-1. β-function in the linac for the case of a small R_{12} of pass-to-pass matrix (note a different scale for R_{12} plotted against the other ordinate axis on the right). The injection energy is 410 MeV; the SRF structure is over 300 m long, providing 4.6 GeV of acceleration to the beam.

According to (3.1.4-3) the R_{12} of the transport matrix between different cavities can be very large (on order of the β-function or even bigger). For the example under consideration, the phase advance in the SRF structure changes rather slowly and, consequently, the absolute value of R_{12} between the first cryomodule on acceleration and other cryomodules along the linac during energy recovery increases slowly, reaching about 150 m in the last cryomodule.

These observations suggest the following guidelines for choosing focusing optics in the linac:

1) Minimize the β-function in the linac by adjusting the strength of the quadrupoles and by matching the envelope of the injected beam.
2) Set the phase advance of the recirculating arc to minimize R_{12} and R_{34} of the pass-to-pass matrix.

Because of all the earlier mentioned complexities of transverse particle dynamics in the ERL, the first task of minimizing the β-function in the linac is best achieved by numeric optimization methods (for example, by employing a quasi-Newton method (Gill 1972)).

The results of such optimization for a 5 GeV ERL with a cavity gradient of 20 MV/m are presented in Figures 3.1.4-2 and -3. The injection energy is 10 MeV. The 5 GeV SRF structure contains 30 cryomodules, and its length is about 400 m. The strength, $|k|$ (where $k = (\partial B/\partial x)/(B\rho)$ [m^{-2}] and B and $(B\rho)$ are magnetic field and rigidity, respectively), of a middle quadrupole of all 29 triplets (- ½ k, k, - ½ k; quadrupoles are of the same 50-cm-length) is shown in Figure 3.1.4-3. It can be seen from this figure that triplets are set in such a way as to produce a nearly constant focusing length for the quadrupoles in the end of the linac during the final stage of energy recovery. In Figure 3.1.4-3 an output of a TDBBU simulation is shown approximately at the instability threshold current of 205 mA, using the HOM data of Table 3.1.4-1.

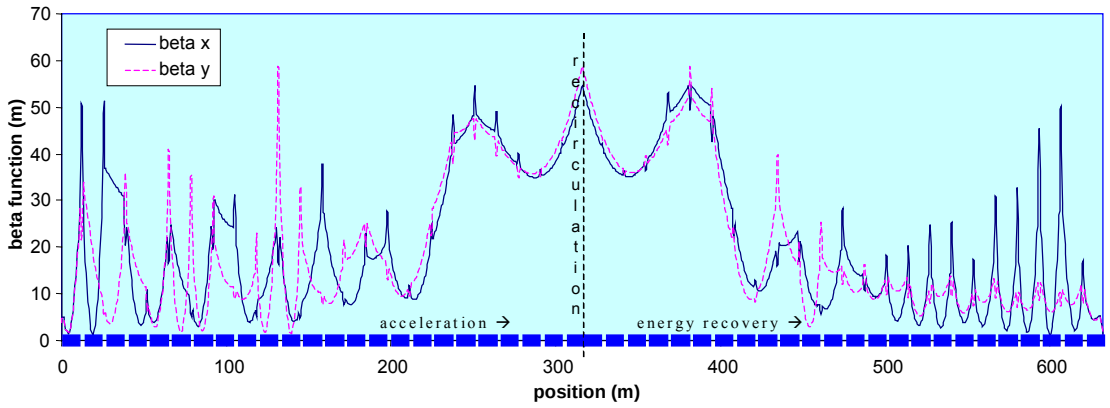

Fig. 3.1.4-2. β-functions in the linac for the case of a BBU threshold current of 230 mA. SRF structure consists of 24 cryomodules; injection energy is 10 MeV; energy after acceleration is 5002 MeV; dumped beam energy is 5 MeV.

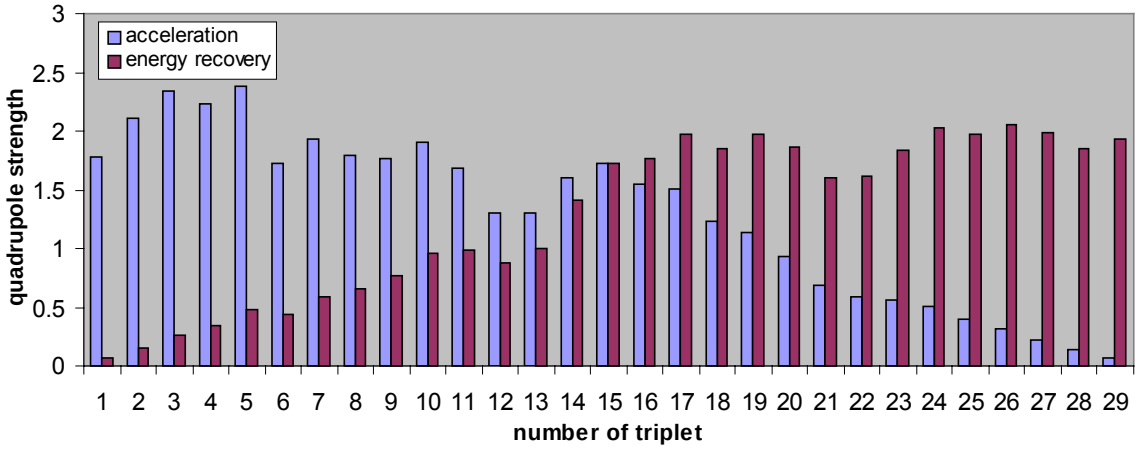

Fig. 3.1.4-3. Strength $|k|$ in [m^{-2}] of the middle quadrupole in a triplet along the SRF structure corresponding to Fig. 3.1.4-5.

HOM effect and frequency randomization

The parameters of ten HOMs included in the simulations are shown in Table 3.1.4-1 (Sekutowicz 1994). Note that this table presents computed values. Measured values of some HOM Q's of nine-cell TESLA cavities are ten times higher and would limit ERL beam currents. HOM coupling and polarization control (see Section 5.2.3) will be early development priorities for the Phase II ERL. That such improved coupling is feasible is shown by the performance of the LEP and HERA cavities, e.g., see pg 373 of (Padamsee 1998).

No.	f (MHz)	polarization	R/Q [Ω]	Q
1	1734	x	116.7	3400
2	1734	y	116.7	4500
3	1865	x	42.4	50600
4	1865	y	42.4	26500
5	1874	x	56.8	50200
6	1874	y	56.7	51100
7	1880	x	11.8	95100
8	1880	y	11.8	85500
9	1887	x	1.2	633000
10	1887	y	1.2	251000

Table 3.1.4-1. TESLA cavity HOM parameters used in TDBBU simulations.

Using Table 3.1.4-1, the BBU threshold is primarily determined by two modes with the highest product of $(R/Q)\cdot Q$ (table entries 5 and 6). Including the other modes into the simulations did not change the BBU threshold current by more than 5 mA, which is the approximate accuracy with which the BBU threshold current was determined. This result suggests that these two modes are the ones that go unstable and that the coupling of the other modes with these two is small.

All the instability threshold values cited earlier were determined for resonance frequencies of the HOMs chosen to be random between f and f + 1 MHz to mimic the expected frequency spread in the actual cavities. It was also found that by increasing frequency spread of the HOMs (random between f and $f + A$ MHz, where A is the frequency spread from cavity to cavity) in the cavities it is possible to increase the BBU threshold current by a hundred mA or more (see Fig. 3.1.4-4).

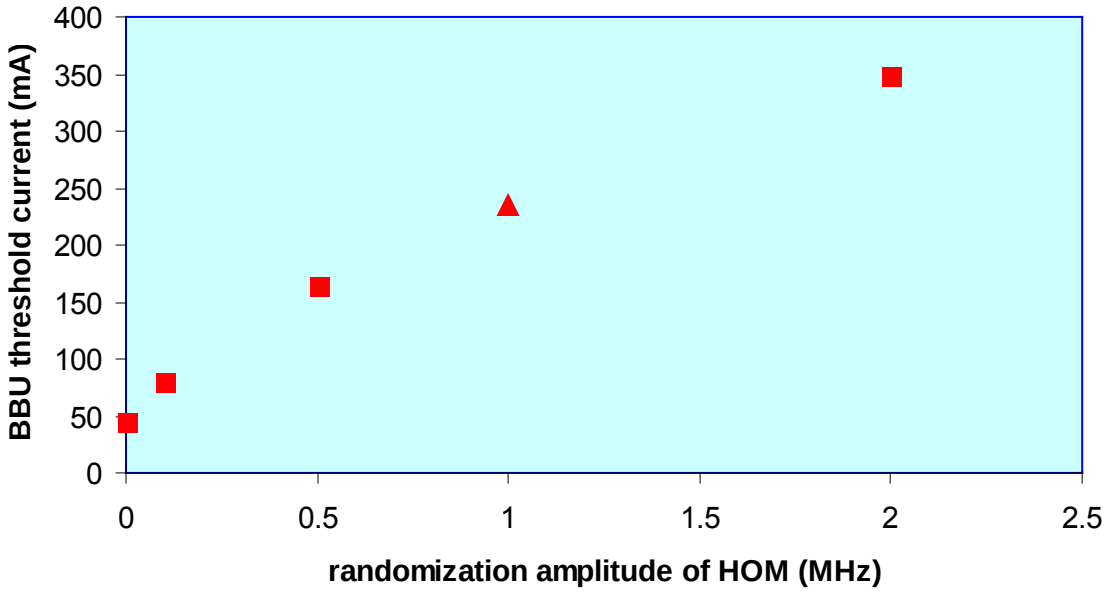

Fig. 3.1.4-4. BBU threshold current vs. randomization amplitude A of HOM frequencies.

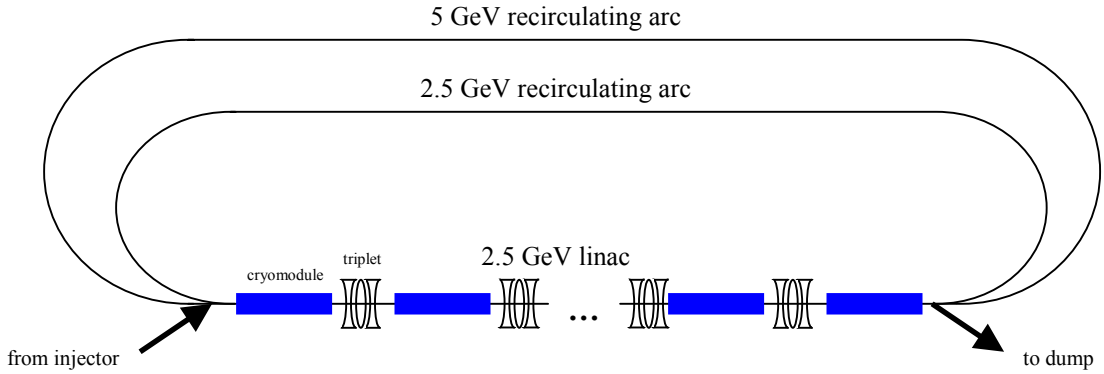

Fig. 3.1.4-5. Conceptual layout of a two-pass 5 GeV ERL.

Multipass ERLs

It may be desirable for cost optimization reasons to design a multipass ERL. For a two-pass ERL (Fig. 3.1.4-5) each electron bunch traverses the 2.5 GeV linac twice on crest before it is introduced with 180^o offset in RF phase for two recirculations of energy recovery. Of course, the total length of SRF structure that a particle sees is the same as in the case of one-pass ERL, assuming the same gradient for both scenarios. While the half-energy recirculating arc seems to provide additional leverage to transverse particle dynamics, there is a serious additional constraint on the linac optics in the case of two-pass ERL because the same optics in the linac section will have to provide adequate focusing for electron bunches of four different energies. Besides, a two-pass ERL must be designed to have twice as high a BBU threshold current as in one-pass ERL to provide the same beam current in SR transport loop.

Attempts to design two-pass ERL optics able to support 100 mA beam were made by following the same guidelines as in the case of one-pass ERL, but with an additional requirement of minimizing elements R_{12} and R_{34} of the pass-to-pass transport matrix for each successive recirculation, for two recirculations separated by another one, etc. The optimized linac optics allowed propagation of the beam envelope with a relatively small β-function (< 70 m) in the SRF structure. Nevertheless, the simulated BBU threshold current was only 20 mA (actual current in the linac is four times that). This low threshold is thought to be a consequence of the additional constraint on the linac optics to support particles of four different energies, namely, that the quadrupole focusing turns out to be limited in such a way that it allows slow variations of rather large β-function (50-60 m) over almost the whole length of the SRF structure on two of the passes (second pass of acceleration and first pass of energy recovery). A slowly changing large β-function suggests a small phase advance, and as a result, R_{12} and R_{34} of the beam-transport matrix from a particular cavity may become large over extensive distances in the SRF structure, allowing strong interaction between the HOMs.

With a small SRF structure, such as the one in the envisioned 100 MeV Phase I ERL, the BBU instability for a two-pass scenario is less threatening. In this case, the best obtained BBU threshold current was 85 mA.

Summary

Numerical simulations have shown that a sufficiently high (twice the considered ERL current) multipass BBU threshold can be achieved in a one-recirculation, one-linac ERL scenario, provided that HOMs suppression is adequate to ensure their parameters in the same range as specified for TESLA 9-cell cavities. The comparison of a two-pass ERL vs. one-pass ERL indicates that a higher BBU threshold current can be achieved in a one-recirculation, one-linac configuration.

3.1.5 Transport Loop Design

The Phase II ERL is expected to be in the range of 5 – 7 GeV. However, for the sake of calculation, the following discussion assumes a 5 GeV machine. This may be done with little loss of generality. A conceptual layout of a 5 GeV ERL for a single linac, one-recirculation scenario is presented in Fig. 3.1.5-1. At this stage we will not be concerned with the exact shape of the machine nor with details such as whether the insertions devices (IDs) all point off to one side or to alternate sides of the ring.

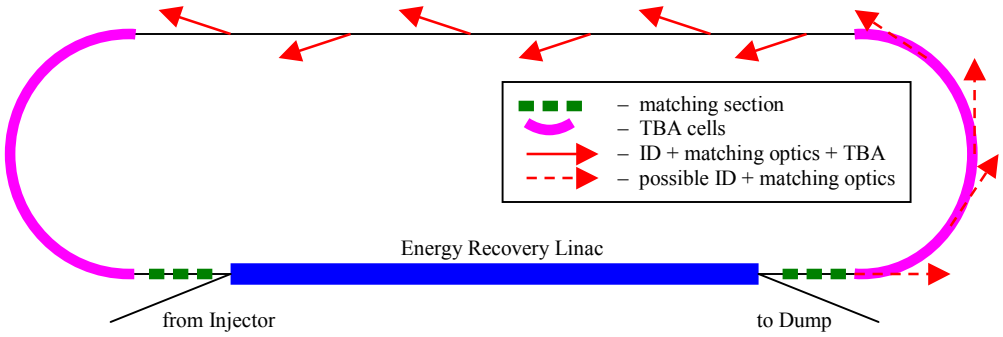

Fig. 3.1.5-1. Conceptual layout of 5 GeV ERL source.

The transport loop is the part of the ERL which transports the bunches from the output of the linac back to the linac input. The transport loop performs the function of hosting the SR IDs, dipoles and beam lines and returns the electron bunches to the linac 180^{o} out accelerating phase. In addition, the transport loop has to meet the following specifications:

1) For a given injection energy, energy losses due to SR from both the bending dipoles and the IDs must be kept acceptably small, e.g., ≤5 MeV energy loss per particle or 500 kW total power at beam current of 100 mA. If the losses are too high, the bunches will have insufficient energy when recirculated through the linac for energy recovery.
2) The transport loop has to be optimized so that the transverse emittance dilution is small in comparison with emittance of the beam from the injector (≤2 mm mrad).
3) The energy spread growth in the dipoles, due to radiative processes, has to be small enough to enable operation of IDs with a narrow photon spectral bandwidth. The spectral bandwidth, $\Delta\lambda/\lambda$, of an N_p-period undulator is given by $\Delta\lambda/\lambda = 1/N_p$. Thus, the maximum tolerable beam energy spread for $\Delta\lambda/\lambda$ = 0.1 % is estimated to be 0.05 % for a 1000-period undulator, since radiation wavelength from an ID is inversely proportional to squared energy of the beam, cf. (3.1.5-4).
4) It is desirable to have adjustable R_{56} in the turnaround arcs so as to perform bunch compression / decompression, and to be able to preserve bunch length (R_{56} is an element of the beam-transport matrix **R** in TRANSPORT notation).

5) From a BBU suppression point of view, an additional requirement for the whole transport line (see section 3.1.4) , which is not difficult to meet, is that the betatron phase advance, $\Delta\psi$, of the recirculating arc has to be fixed to some value determined by BBU simulations.
6) Since short pulses are desired, it is important to understand the effects of the Coherent Synchrotron Radiation (CSR) which is produced when short bunches traverse the arcs.

These concerns are addressed below. Examples of the building blocks for the first-order optics are also presented.

SR energy losses

Incoherent synchrotron radiation. Radiative losses due to incoherent SR will determine the minimum permissible bending radius of dipoles in the transport loop. The instantaneous radiation power, P_{incoh}, and energy, U_{d}, radiated by one electron in one revolution for an isomagnetic ring are given by (Sands 1970)

$$P_{\text{incoh}} = \frac{1}{4\pi\varepsilon_0}\frac{2}{3}\frac{ce^2\gamma^4}{\rho^2}, \qquad (3.1.5\text{-}1)$$

$$U_{\text{d}} = \oint P_{\text{incoh}}\,dt = \frac{1}{3\varepsilon_0}\frac{e^2\gamma^4}{\rho}. \qquad (3.1.5\text{-}2)$$

Here c is the speed of light; $E = mc^2\gamma$ is the electron energy, m is the electron mass; $\varepsilon_0 = 8.8542\times10^{-12}\ \text{F m}^{-1}$ is the dielectric constant, and ρ is the bending radius of the dipoles. In more practical units, U_{d} and the total radiation power, $P_{\text{d, tot}}$, for a circulating beam current, I, due to incoherent SR from dipole magnets are

$$U_{\text{d}}\left[\text{eV}\right] = 88463\frac{E[\text{GeV}]^4}{\rho[\text{m}]},$$

$$\text{and } P_{\text{d, tot}}\left[\text{W}\right] = U_{\text{d}}[\text{eV}]I[\text{A}].$$

For undulators of total length L_{u}, the radiated energy, U_{ID}, per electron is (Wiedemann 1995)

$$U_{\text{ID}} = \frac{\pi}{3}\frac{e^2}{\varepsilon_0}\frac{\gamma^2}{\lambda_{\text{p}}^2}K^2L_{\text{u}}, \qquad (3.1.5\text{-}3)$$

where λ_{p} is the undulator period length and K is the dimensionless undulator strength

parameter: $K = 0.934 B_0[\mathrm{T}]\lambda_\mathrm{p}[\mathrm{cm}]$, where B_0 is the undulator magnetic field strength and λ_p is the magnetic period. In practical units, U_ID and the total radiation power from IDs are given by

$$U_\mathrm{ID}[\mathrm{eV}] = 725.69 \frac{E[\mathrm{GeV}]^2 K^2}{\lambda_\mathrm{p}[\mathrm{cm}]^2} L_\mathrm{u}[\mathrm{m}],$$

$$\text{and } P_{\mathrm{ID,\,tot}}[\mathrm{W}] = U_\mathrm{ID}[\mathrm{eV}] I[\mathrm{A}].$$

To estimate the total radiation power from IDs, the following parameters will be used: $K = 1.22$ and $\lambda_\mathrm{p} = 1.7\,\mathrm{cm}$. The photon energy, E_1, at the fundamental frequency emitted in the forward direction from an undulator is given by

$$E_1 = \frac{2hc}{\lambda_\mathrm{p}} \frac{\gamma^2}{1 + \frac{1}{2}K^2}, \qquad (3.1.5\text{-}4)$$

where h is Planck's constant. In practical units,

$$E_1[\mathrm{eV}] = 949.63 \frac{E[\mathrm{GeV}]^2}{\lambda_\mathrm{p}[\mathrm{cm}]} \frac{1}{1 + \frac{1}{2}K^2}.$$

Thus, $K = 1.22$ and $\lambda_\mathrm{p} = 1.7\,\mathrm{cm}$ correspond to $E_1 = 8\,\mathrm{keV}$. Furthermore, let us assume a total length of undulators, $L_\mathrm{u} = 200\,\mathrm{m}$ (or about half the size of 5 GeV superconducting RF structure with 20 MV/m gradient in RF cavities). Then, the total incoherent SR power in IDs is $P_{\mathrm{ID,\,tot}} = 187\,\mathrm{kW}$. It seems reasonable to require that the radiation power $P_{\mathrm{d,\,tot}}$ from dipole magnets should be approximately the same as $P_{\mathrm{ID,\,tot}}$. For a bending radius $\rho = 30\,\mathrm{m}$, the power of radiative losses in the bends is $P_{\mathrm{d,\,tot}} = 184\,\mathrm{kW}$. The total incoherent SR power from bends and IDs becomes 371 kW. Obviously, larger radius arcs would reduce the loss even further and more undulator length will increase the radiated power.

Coherent synchrotron radiation. Formula (3.1.5-1) gives the instantaneous radiation power due to incoherent SR in the dipoles. There is also coherent SR (the wavelength of CSR is $\lambda_\mathrm{CSR} \geq \Delta z$, where Δz is a bunch length) in addition to incoherent SR if the electrons are not uniformly distributed along the orbit. Strictly speaking, expression (3.1.5-1) is true only for a uniform circular current, which does not radiate coherently (Saldin 1997). However, if the electron bunch length is close to or greater than the transverse dimensions of the conducting beam pipe (such being the case in many storage rings), or if the number of electrons, N, in the bunch is sufficiently small, CSR becomes negligible. The bunches in the ERL are short (the rms bunch length for the beam after

the main linac is $\sigma_l = 0.7\,\text{mm}$ or $\sigma_t = 2.3\,\text{ps}$ -- see Section 4.2) and the number of electrons in the bunch is large ($N = 4.8\times10^8$); therefore, CSR may be significant.

Schwinger (Schwinger 1945) found an expression for the instantaneous coherent radiation power, $P_{\text{coh}}^{(N)}$, from N electrons uniformly distributed over the length, l, in free space (i.e. in the case of no shielding by the conducting beam pipe, meaning that the bunch length is much smaller than the beam pipe dimensions):

$$P_{\text{coh}}^{(N)} = \frac{1}{4\pi\varepsilon_0}\frac{N^2e^2c}{\rho^2}\left(\frac{\sqrt{3}}{\alpha}\right)^{4/3}, \qquad (3.1.5\text{-}5)$$

where $\alpha = l/\rho$ is the angular interval occupied by the bunch. In contrast, incoherent radiation is given by

$$P_{\text{incoh}}^{(N)} = P_{\text{incoh}}N, \qquad (3.1.5\text{-}6)$$

where P_{incoh} is the incoherent radiation power of one electron given by expression (1).

Schiff (Schiff 1946; Nodvick 1954; Derbenev 1995[2]) found an expression for $P_{\text{coh}}^{(N)}$ of an electron bunch with a Gaussian distribution:

$$P_{\text{coh}}^{(N)} = \frac{1}{4\pi\varepsilon_0}\frac{N^2e^2c}{\rho^2}\left(\frac{\sqrt{3}}{\sigma_\alpha}\right)^{4/3}\times\frac{1}{2\pi\sqrt{3}}\left[\Gamma(2/3)\right]^2 \qquad (3.1.5\text{-}7)$$

where $\sigma_\alpha = \sigma_l/\rho$, $\Gamma(2/3)\cong 1.35412$, and σ_l is the rms bunch length. The ratio of $P_{\text{coh}}^{(N)}$ (3.1.5-7) to incoherent $P_{\text{incoh}}^{(N)}$ (3.1.5-6) is

$$\frac{P_{\text{coh}}^{(N)}}{P_{\text{incoh}}^{(N)}} = \frac{3N}{2\gamma^4}\left(\frac{\sqrt{3}}{\sigma_\alpha}\right)^{4/3}\times\frac{1}{2\pi\sqrt{3}}\left[\Gamma(2/3)\right]^2, \qquad (3.1.5\text{-}8)$$

or in practical units for a bunch with charge q_{bunch}:

$$\frac{P_{\text{coh}}^{(N)}}{P_{\text{incoh}}^{(N)}}[\%] = 0.2237\frac{q_{\text{bunch}}[\text{pC}]}{E[\text{GeV}]^4}\left(\frac{\rho[m]}{\sigma_l[\text{mm}]}\right)^{4/3}.$$

Estimates for an rms bunch length of 0.7 mm, 77 pC bunch charge, and a bending radius of 30 m show that coherent radiation power from the dipoles is 4 % of the incoherent SR

[2] Saldin, 1997, has pointed out that Nodvick, 1954, and Derbenev, 1995 contain an error in their expression for the instantaneous CSR power from a Gaussian bunch.

power. For compressed electron bunches with a rms bunch duration $\sigma_t = 100\,\text{fs}$ this ratio becomes 3, i.e., the instantaneous radiation power is greater than the one determined by expression (3.1.5-1) and is mostly due to CSR. Shielding and limiting the length of transport of short bunches will ameliorate some of the CSR. Additionally, the assumptions used in deriving the formula for CSR may not be strictly applicable for the case at hand (e.g., see Sections 4.3.1 and 4.3.8). Experimental determination of the CSR effect will be a primary goal of Phase I. These estimates do suggest that extreme care will be needed in transporting short bunches. Further, the extent of short bunch transport may need to be limited, via use of compressors and decompressors, to only part of the transport arc.

Shielding by a conducting beam pipe reduces CSR. Schwinger (Schwinger 1945) studied the shielding effect of two plane sheets of metal placed parallel to the plane of the orbit. He found that the shielding effect from such two metal sheets will reduce CSR from a bunch with a uniform distribution by a factor of

$$k_{\text{shielding}} = \left(\frac{\alpha}{\sqrt{3}}\right)^{1/3} \frac{a}{2\rho\alpha}, \qquad (3.1.5\text{-}9)$$

where a is the distance between the sheets. Expression (3.1.5-9) is obtained under the assumption that the size of the bunch is at least of the order of the plate separation. If this condition is not satisfied, i.e., $l << a$ (as it is in the case of sup-picosecond bunches), then the shielding effect becomes very small and is not of significance. For the 0.7 mm bunches, assuming a = 2 cm the shielding factor of CSR $k_{\text{shielding}} = 0.34$. Thus, the correction to the incoherent radiation power estimated using (3.1.5-1) and (3.1.5-2) becomes $0.34 \times 4\,\% = 1.4\,\%$ for 0.7 mm bunches.

Energy spread and emittance growth due to quantum excitation

As an electron bunch travels through any bend (either a dipole magnet or an ID), it emits photons, which in turn causes energy fluctuations and excitation of betatron motion in the sections with nonzero dispersion. The result of such quantum excitation is energy spread and transverse emittance growth in the system. In storage rings, the presence of energy supplementing RF structures result in damping of both energy and betatron oscillations caused by radiation fluctuations so that the ultimate energy spread and emittance are determined by equilibrium between quantum excitation and its damping. In transport systems without energy feedback quantum excitation will lead to steady growth in both longitudinal and transverse (predominantly in the plane of bending) phase space area occupied by the bunch. Quantum excitation rates for energy spread and transverse emittance were first studied by Sands (Sands 1970; Sands 1985) and are well known. In all expressions given in this section only the quantum excitation due to incoherent SR is taken into account.

Energy spread.

An expression for the energy spread can be derived by noting that in the case of

SR the emission of successive quanta is a purely random process, which satisfies a Poisson distribution (or a Gaussian distribution in the limit of a high number of photons emitted per second). The increase in rms energy spread, σ_E, is given by[3]

$$\Delta\sigma_E^2 = \int dt \int E_{\text{ph}}^2 \dot{N}_{\text{ph}}\left(E_{\text{ph}}\right) dE_{\text{ph}}, \qquad (3.1.5\text{-}10)$$

where $\dot{N}_{\text{ph}}\left(E_{\text{ph}}\right)dE_{\text{ph}}$ is the rate of photon emission with energies $\left(E_{\text{ph}}, E_{\text{ph}} + dE_{\text{ph}}\right)$.

1) Energy spread in dipole magnets. Performing an integration of (3.1.5-10) over the SR spectrum from a bend one can find energy spread along the path of length L (Wiedemann 1995):

$$\Delta\sigma_{E,\text{d}}^2 = \frac{55\hbar c e^2}{96\sqrt{3}\pi\varepsilon_0}\gamma^7 \int_0^L \left(\frac{1}{|\rho_x|^3} + \frac{1}{|\rho_y|^3} \right) ds, \qquad (3.1.5\text{-}11)$$

where ρ_x and ρ_y are bending radii in the horizontal and vertical planes ($1/\rho_y = 0$ for our case). For an isomagnetic ring ($\rho_x = \rho = \text{const}$) with total bend angle Θ ($\Theta = 2\pi$ for one recirculation), the energy spread becomes

$$\Delta\sigma_{E,\text{d}}^2\left[\text{GeV}^2\right] = 2.5964\times10^{-10}\,\frac{E[\text{GeV}]^7}{\rho[\text{m}]^2}\,\frac{\Theta[\text{rad}]}{2\pi}.$$

Estimates show that for a transport arc made of dipoles with $\rho = 30\,\text{m}$, the energy spread increase due to incoherent SR quantum excitation becomes $\sigma_E^2 = 2.25\times10^{-8}\ \text{GeV}^2$ after a full loop.

2) Energy spread in IDs. To obtain the energy spread from IDs one would have to integrate (3.1.5-11) over the radiation spectrum from an undulator. Instead, for purposes of estimation, let us assume that all photons are emitted with the same energy E_1 given by (3.1.5-4) (i.e. only the fundamental frequency is important, which is generally true only for $K << 1$). With this assumption, incoherent SR-induced energy spread is given by a simple expression

$$\Delta\sigma_{E,\text{ID}}^2 = N_{\text{ph}} E_1^2. \qquad (3.1.5\text{-}12)$$

We will estimate the number of photons as $N_{\text{ph}} = U_{\text{ID}}/E_1$, with U_{ID} given by (3.1.5-3). Therefore, the energy spread can be estimated by using the following formula

[3] There is no factor of ½ in formula (3.1.5-10) as appears in the expression for the energy spreading rate due to quantum excitation in storage rings. This is because there are no synchrotron oscillations in the ERL turnaround arc (cf. pg. 416 of Lee, S. Y. (1999). Accelerator Physics. NJ, World Scientific, NJ.).

$$\Delta\sigma^2_{E,\mathrm{ID}}\left[\mathrm{GeV}^2\right] = 6.8914\times10^{-13}\,\frac{E[\mathrm{GeV}]^4}{\lambda_\mathrm{p}[\mathrm{cm}]^3}\,\frac{K^2}{1+\frac{1}{2}K^2}\,L_\mathrm{u}[\mathrm{m}].$$

For undulators with K = 1.22 and $\lambda_\mathrm{p} = 1.7\,\mathrm{cm}$ with a total length of 200 m, the energy spread induced by incoherent SR is estimated to be $\Delta\sigma^2_{E,\mathrm{ID}} = 1.50\times10^{-8}\ \mathrm{GeV}^2$.

Thus, the energy spread due to quantum excitation by incoherent SR is estimated to be very small. The total energy spread from both dipole magnets and IDs is estimated to be $\Delta\sigma^2_{E,\mathrm{incoh}} = 3.75\times10^{-8}\ \mathrm{GeV}^2$ ($\Delta\sigma_{E,\mathrm{incoh}} = 194\,\mathrm{keV}$ or $\Delta\sigma_{E,\mathrm{incoh}}/E = 3.9\times10^{-5}$; to obtain the final energy spread one has to add these values in quadrature with the energy spread from other sources).

Emittance growth.

The geometric emittance growth, $\Delta\varepsilon$, due to quantum excitation is given by (Wiedemann 1995)

$$\Delta\varepsilon = \frac{1}{2cE^2}\int ds \int E_\mathrm{ph}^2\,\dot{N}_\mathrm{ph}\left(E_\mathrm{ph}\right)H(s)\,dE_\mathrm{ph}\,, \qquad (3.1.5\text{-}13)$$

where the so-called "curly-H" is given by $H = \frac{1}{\beta}\left[\eta^2 + (\beta\eta' + \alpha\eta)^2\right]$ with Twiss parameters β, α, dispersion function η, and its derivative $\eta' = d\eta/ds$. Emittance growth takes place in the horizontal plane (the bending plane); vertical emittance growth is a second order effect (that is $\Delta\varepsilon_y/\Delta\varepsilon_x = 1/\gamma^2$) and therefore will be ignored.

1) <u>Emittance growth in dipole magnets</u>. Emittance growth due to quantum excitation in the bends along a distance, L, is given by (Sands 1970; Sands 1985):

$$\Delta\varepsilon_{x,\mathrm{d}} = \frac{1}{4\pi\varepsilon_0}\,\frac{55\hbar ce^2}{48\sqrt{3}\left(mc^2\right)^2}\,\gamma^5\int_0^L \frac{H_x}{\left|\rho_x\right|^3}ds\,. \qquad (3.1.5\text{-}14)$$

In practical units for isomagnetic dipoles with total bend angle Θ, the emittance growth can be written as

$$\Delta\varepsilon_{x,\mathrm{d}}\left[\mathrm{m\,rad}\right] = 2.0661\times10^{-11}\,\Theta[\mathrm{rad}]\,\frac{E[\mathrm{GeV}]^5}{\rho[\mathrm{m}]^2}\left\langle H\right\rangle[\mathrm{m}],$$

where $\left\langle H\right\rangle = \left(\frac{1}{L}\right)\int_{\mathrm{bends}} H(s)\,ds$ is the average of the H-function in the dipoles. For an

optimized double bend achromat (DBA) lattice, also known as the Chasman-Green lattice, the average of the *H*-function in the limit of small bending angle, θ, of each dipole is given by

$$\langle H \rangle = \frac{1}{4\sqrt{15}} \rho \theta^3, \quad \theta << 1. \qquad (3.1.5\text{-}15)$$

$\langle H \rangle$ is given by the same expression for an optimized triple bend achromat (TBA) (or quadruple bend achromat, etc. (Lee 1996)) with θ being the bending angle of either outer dipole. By relaxing the achromaticity requirement, one is able to design a lattice with $\langle H \rangle$ being equal to $\frac{1}{3}$ of its value given by (3.1.5-15). That additional factor of $\frac{1}{3}$ is of importance for storage rings, where $\langle H \rangle$ determines the equilibrium emittance, whereas in the ERL it only determines emittance growth due to quantum excitation. Therefore, in an ERL machine a TBA is a reasonable choice for a basic cell in the turnaround arc. Thus, in order to keep the emittance growth small after a full recirculation loop (i.e., to 10 % of the proposed 1.5×10^{-10} m rad geometric emittance), $\langle H \rangle$ should be equal to 0.033 m, which can be easily achieved.

2) Emittance growth in IDs. Instead of performing the integration in (3.1.5-13) we will follow the same simple model we used earlier to obtain the energy spread from IDs. With this assumption, the emittance growth in the IDs is given by

$$\Delta\varepsilon_{x,\mathrm{ID}} = \frac{1}{2}\frac{E_1^2}{E^2} N_{\mathrm{ph}} \langle H \rangle = \frac{1}{2}\frac{\sigma_{E,\mathrm{ID}}^2}{E^2}\langle H \rangle. \qquad (3.1.5\text{-}16)$$

By noting that the dispersion function in an undulator with a sinusoidal magnetic field $B(z) = B_{\mathrm{u}} \cos k_{\mathrm{p}} z$ (here $k_{\mathrm{p}} = 2\pi/\lambda_{\mathrm{p}}$, and z is the longitudinal coordinate) behaves like

$$\eta(s) = \frac{1}{k_{\mathrm{p}}^2 \rho_{\mathrm{u}}}\left(1 - \cos k_{\mathrm{p}} z\right) + \eta_0,$$

with η_0 introduced here to account for a possible departure from achromaticity in the section where the undulator is located and ρ_{u} is the minimum bending radius in the undulator $\rho_{\mathrm{u}} = \gamma/(k_{\mathrm{p}} K)$, one can find by straightforward calculation that

$$\langle H \rangle = \frac{\beta^*}{2k_{\mathrm{p}}^2 \rho_{\mathrm{u}}^2}\left(1 + \frac{L^2}{12\beta^{*2}} + \frac{2\eta_0^2 k_{\mathrm{p}}^2 \rho_{\mathrm{u}}^2}{\beta^{*2}} + \frac{8\eta_0 \rho_{\mathrm{u}}}{\beta^{*2}} + \frac{11}{2\beta^{*2} k_{\mathrm{p}}^2}\right).$$

Here β^* is the betatron function at the beam waist which is assumed to be exactly in

the middle of undulator with length *L*. If r_0 is on the order of a millimeter and β^* is on the order of ten meters, $\langle H \rangle$ can be estimated as $\langle H \rangle \approx \frac{\beta^* K^2}{\gamma^2}$. For the case under consideration $\langle H \rangle = 3 \times 10^{-7}$ m, and the corresponding emittance growth in the undulators is $\Delta\varepsilon_{x,\mathrm{ID}} \approx 10^{-16}$ m rad, which can be ignored.

Quantum excitation due to the incoherent SR does not significantly dilute the 6-D phase space density of the beam in an ERL. The situation changes when CSR can no longer be neglected, as it is the case with sub-picosecond bunches.

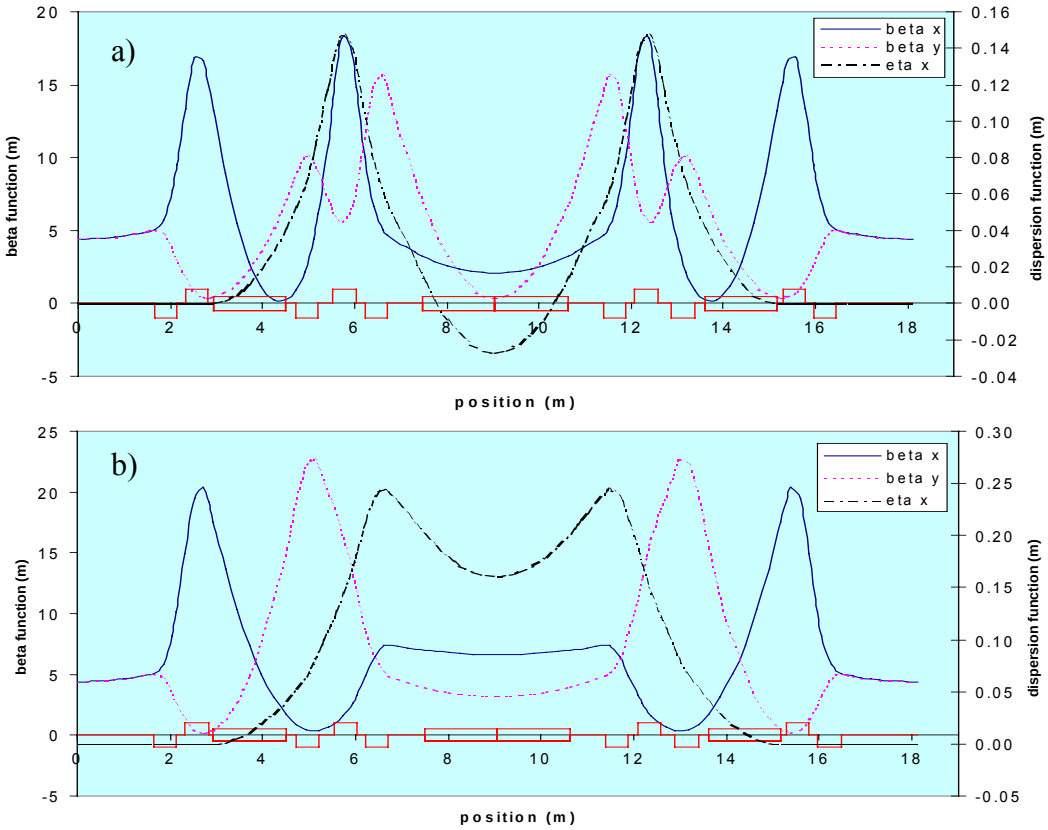

Fig. 3.1.5-2. A TBA cell for an ERL recirculating arc: a) $R_{56} = 0$; b) $R_{56} = 2\,\mathrm{cm}$.

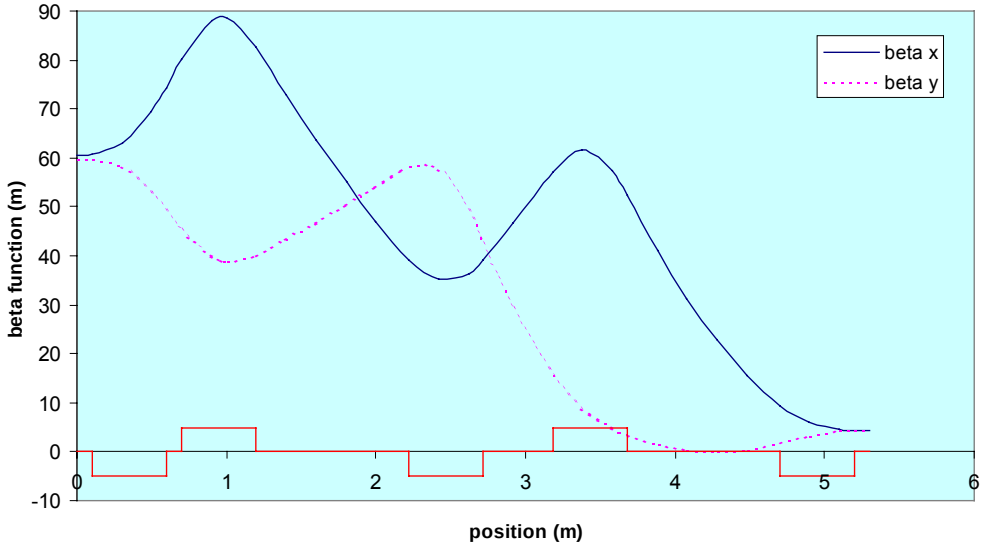

Fig. 3.1.5-3. Matching of the β-functions from the linac to the TBA cell.

Examples of optics for the turnaround arc in ERL

Fig. 3.1.5-2 shows a possible TBA cell for the ERL turnaround arc. Each dipole has a bending angle of $3°$, $\rho = 30\,\text{m}$, and thus, the total bending angle per cell is $12°$. The cell length is 18.1 m, which corresponds to a radius of the recirculating arc of $R_{\text{arc}} = L_{\text{TBA}}/\theta_{\text{TBA}} \approx 86.4\,\text{m}$. The cell is isochronous. By changing settings of quadrupoles one can change R_{56} (Fig. 3.1.5-2b). The $\langle H \rangle$ value for such cell is $\langle H \rangle = 0.0036\,\text{m}$, which is much smaller than needed. For different quadrupole settings $\langle H \rangle$ changes, but within the acceptable range. For example, $\langle H \rangle = 0.0091\,\text{m}$ for the case of Fig. 3.1.5-2b.

The matching of the betatron functions is achieved with a series of quadrupoles. An example of matching β-function from the linac (Bazarov 2001) to TBA is shown in Fig. 3.1.5-3. Similar matching sections, but with fewer quadrupoles, will be used with undulators to optimize their performance.

CSR effect on emittance and energy spread in the bends

This section presents preliminary estimates of emittance and energy spread due to CSR in the bends. From expression (3.1.5-8) one can conclude that the effect is worse for short bunches with high charge. The choice of charge per bunch for the ERL (77 pC) should alleviate the problem of CSR-induced emittance growth that one has to deal with in most FEL projects with charge per bunch values ≥ 1 nC. On the other hand, CSR-induced emittance growth can constrain the production of bright sub-picosecond X-ray pulses.

To illustrate the nature of the forces that arise in a bend let us consider the analytical result for the electric field along the direction of motion found for a short, uniform density line of charge undergoing circular motion (to the lowest order in x/ρ) (Carlsten 1996):

$$\frac{\lambda}{4\pi\varepsilon_0}\frac{1}{r_{\text{ret}} - \mathbf{r}_{\text{ret}}\mathbf{u}_{\text{ret}}/c}\left(\frac{1}{\gamma^2} - \beta^2\frac{x}{\rho} + \beta^2\left[1-\cos(\zeta')\right]\right)_{\zeta_{\text{r}}}^{\zeta_{\text{f}}}, \quad (3.1.5\text{-}17)$$

here λ is the current density; β is the azimuthal velocity divided by the speed of light (not to be confused with β-function used elsewhere in this note), x is the transverse displacement of the observer location in the bend plane relative to the trajectory of the source line, $\mathbf{r}_{\text{ret}}$ is the vector from the source point (presently at angular position ζ) at the retarded time to the observer location, $r_{\text{ret}} = |\mathbf{r}_{\text{ret}}|$, $\mathbf{u}_{\text{ret}}$ is the retarded velocity of that point at the retarded time, ζ' is the retarded angle of the source point's azimuthal position, and ζ_{f} and ζ_{r} are the present azimuthal angles of the front and rear of the bunch respectively. While the first term represents the "usual space charge" force ($\propto \gamma^{-2}$) the second and third terms are independent of energy. The second term is known as "noninertial space-charge" term (Carlsten 1996), and the third one as CSR term.

Alternatively, in Ref. (Derbenev 1995; Derbenev 1996) this radiative interaction is treated separately in its effect on longitudinal dynamics (radiative tail-head interaction (Derbenev 1995) and transverse dynamics (radiative focusing (Derbenev 1996)). Normally, one would have to use numerical computation in order to calculate the effect on emittance and energy spread resulting from radiative microbunch interaction (for example, see (Carlsten 1997; Dohlus 2000)). We will use simple arguments here to obtain rough estimates of the effect.

Longitudinal radiative interaction leads to an energy loss gradient along the bunch, so that the bunch head particles get some excess of energy while the tail and center part mostly lose the energy. For a bunch consisting of N electrons with Gaussian linear density distribution $\lambda(s) = \left(1/\sqrt{2\pi}\sigma_l\right)e^{-s^2/2\sigma_l^2}$, rms induced energy difference after passing through a dipole magnet of length L_d is given by (Derbenev 1995)

$$\frac{\Delta E_{\mathrm{CSR}}}{mc^2} \approx 0.22\frac{Nr_eL_\mathrm{d}}{\left(\rho\sigma_l^2\right)^{2/3}}, \qquad (3.1.5\text{-}18)$$

r_e is classical electron radius. Since this energy spread and energy loss originate inside the bends where the dispersion function and its derivative are not zero, there is a change of particle angle (and transverse position) due to induced energy spread, which can be estimated as $\Delta x' \sim \theta_\mathrm{d}\left(\Delta E_{\mathrm{CSR}}/E\right)$, with ΔE_{CSR} being either CSR-induced energy spread (3.1.5-18). The increase in normalized emittance ($\varepsilon_{x,n} \cong \gamma\varepsilon_x = \gamma\sqrt{\left\langle x^2\right\rangle\left\langle x'^2\right\rangle - \left\langle xx'\right\rangle^2}$) can be estimated by using

$$\Delta\varepsilon_{x,n}^{\mathrm{long}} \sim \sigma_r\frac{\Delta E_{\mathrm{CSR}}}{mc^2}\theta_\mathrm{d}, \qquad (3.1.5\text{-}19)$$

here $\sigma_r = \sqrt{\left\langle x^2\right\rangle}$ is rms transverse bunch radius. Expression (3.1.5-19) generally overestimates the emittance growth, but it will be used here to represent the worst case scenario.

The effect of transverse radiative microbunch interaction results in defocusing of the particles at the head of the bunch and focusing of other particles. The minimum focusing length due to this effect is given by (Derbenev 1996)

$$f_x^{\mathrm{rad}} \cong \frac{\gamma\rho^{4/3}\sigma_l^{5/3}}{1.3Nr_eL_\mathrm{d}3^{1/3}}, \qquad (3.1.5\text{-}20)$$

with ratio of this focusing radiative force F_x^{rad} and the "usual space charge" force $F_{\mathrm{s.c.}}$ being equal to

$$\frac{F_x^{\mathrm{rad}}}{F_{\mathrm{s.c.}}} \cong 0.65 \frac{\gamma^2 \sigma_r^2}{\rho^{4/3} \sigma_l^{2/3}}. \qquad (3.1.5\text{-}21)$$

As this focusing force depends on the position along the bunch, the resultant normalized emittance growth $\Delta\varepsilon_{x,n}^{\mathrm{tr}}$ is of the order of:

$$\Delta\varepsilon_{x,n}^{\mathrm{tr}} = \gamma\beta_x\theta_{\mathrm{d}}^2 \left(\frac{r.m.s.\, B_c}{B_{\mathrm{d}}} \right)^2, \qquad (3.1.5\text{-}22)$$

here $r.m.s.\, B_c = 0.28 B_c^{\max}$, with maximum centripetal field $B_c^{\max}$ due to transverse radiative microbunch interaction calculated as $B_c^{\max} = -\frac{\mu_0 c}{4\pi} \frac{2Ne}{\sqrt{2\pi}\rho\sigma_l}$; B_{d} is dipole field.

These formulae are obtained with the assumption that the bunch length c_l satisfies conditions of a "thin" bunch and absence of beampipe shielding (*b* is beampipe radius):

$$\sigma_r \sqrt{\sigma_r / \rho} << \sigma_l << b\sqrt{b/\rho}. \qquad (3.1.5\text{-}23)$$

We use these results as well as previously found CSR power losses to make some estimates. First, we notice that the energy spread due to CSR from *a single dipole* given by (3.1.5-18) for our choice of parameters ($N = 4.8\times10^8$, $\rho = 30$ m, $L_{\mathrm{d}} = 1.57$ m) is very small; namely, for $c_z = 0.7$ mm energy spread becomes $\Delta E_{\mathrm{CSR}} = 0.4$ keV, and for $c_z = 0.03$ mm (100 fs rms bunches) $\Delta E_{\mathrm{CSR}} = 26.6$ keV. This is to be compared with CSR energy losses per dipole that are about 1.4 keV for $c_z = 0.7$ mm, and 269 keV for $c_z = 0.03$ mm (incoherent SR losses per dipole are 15.4 keV, and energy spread is 13.7 keV). The emittance growth due to CSR-induced energy spread is correlated with a slice position within the bunch and, thus, in principle can be minimized by proper optics design (Emma 1997). Crude estimates show that the emittance growth caused by energy spread due to CSR is negligible for longer bunches ($c_l = 0.7$ mm), whereas for 100 fs rms bunches the worst case scenario is estimated by (3.1.5-19) to be 0.13 mm mrad normalized emittance increase per dipole. Furthermore, we estimate the radiative focusing force by using (3.1.5-20) and (3.1.5-21). $f_x^{\mathrm{rad}} = 1.3\times10^6$ m for 0.7 mm bunches, and $f_x^{\mathrm{rad}} = 6.6\times10^3$ m for 0.03 mm bunches. The ratio $F_x^{\mathrm{rad}} / F_{\mathrm{s.c.}}$ is 0.2 and 1.6 for 0.7 mm and 0.03 mm bunch length respectively. This indicates that the radiative focusing is very small for the longer bunches, becoming the same order of magnitude effect as the "usual space-charge" force for sub-picosecond bunches, – the force, which is negligible at 5 GeV.

The CSR-induced effects for a case with lower beam energy, such as 5 MeV injector for the Phase I ERL or 10 MeV injector for the full size machine, are likely to be

more deleterious because of the smaller bending radii, larger bending angles and bigger transverse bunch size. The latter, however, may result in the breaking of condition (3.1.5-23) where the model (Derbenev 1995) is no longer valid. It was found that the emittance growth due to CSR for short bunches with very large aspect ratio A_x ($A_x = \langle x \rangle / \sigma_l$) is not as severe as for the bunches of the same short length but with smaller aspect ratio, as has been the experience at the IRFEL at JLAB (Douglas 2000). The estimates of these effects at lower energies are presented in section 4.3.8.

To complete this brief discussion on microbunch radiative interaction, we evaluate the effect in undulators. First, let us estimate CSR-induced energy spread from undulators. We do so by using the results of (Saldin 1999). For the same undulator parameters that were used earlier, we find for the worst case scenario (i.e. $c_t = 100\,\mathrm{fs}$, total undulator length 200 m) that the energy spread due to CSR is $\Delta E_u^{CSR} / E = 5.5 \times 10^{-7}$. The energy spread is very small and can be ignored. As a result, the emittance growth due to CSR-induced energy spread in undulators is expected to be small too, even in the case of the short sub-picosecond bunches.

3.1.6. Single Bunch Dynamics

An intense bunch of particles traveling through an accelerating structure, excites wakefields, which act back on the bunch itself. The longitudinal wakefields affect the energy of the particles along the bunch, inducing a correlated energy spread. When a bunch travels off-axis in a cavity, the transverse wakefields will deflect the tail of the bunch away from the axis, resulting in an increase of the total transverse phase space area occupied by all the particles in the bunch. Next we obtain estimates of the energy spread and emittance degradation due to short-range wakefield effects.

Longitudinal dynamics

The energy spread within a bunch, induced by longitudinal wakefields, is approximately equal to twice the average energy loss of a particle in the bunch: $\Delta E = 2eQk_{\parallel}$, where $k_{\parallel}$ is the loss factor of the accelerating structures. To correctly determine the steady-state wake for a long periodic array of cavities in the linac, the longitudinal wakefields for the TESLA 9-cell cavities were calculated for up to 2 TESLA modules, each containing eight 9-cell cavities, bellows and beam pipes (Novokhatski 1999). The calculated loss factor as function of bunch length shows a dependence which is much weaker than $1/\sqrt{\sigma_z}$, characteristic of the single-cell behavior in the high frequency regime. Therefore, the condition of an infinite periodic structure appears to be relatively well fulfilled for the TESLA linac. For a Gaussian bunch of length σ_z =0.3 mm, the calculated loss factor is 12.78 V/pC per cavity (L_{cav} = 1.038 m), and the induced rms energy spread at 5 GeV is approximately $\sigma_E/E \approx 3.76 \times 10^{-5}$.

This correlated energy spread can be reduced by running the bunch at the optimal rf phase. This is demonstrated to work well for the TESLA collider parameters (σ_z=0.3 mm), but it becomes less efficient for shorter bunches (TELSA 2001). Finally for the ERL, one needs to ensure that the optimum RF phase for energy spread reduction is

consistent with the RF phasing requirements imposed by longitudinal gymnastics needed to obtain minimum bunch length at the undulators.

Transverse dynamics

When a bunch is injected off-axis, it performs a betatron oscillation about the central trajectory. The particles in the tail of the bunch are resonantly driven by wakefields excited by the particles in the head of the bunch. As a result, the amplitude of the oscillation grows rapidly as the beam travels down the linac. This effect leads to a tolerance on the allowed amplitude of the betatron oscillation. A simple estimate of the effect may be obtained using the amplification parameter η(Chao 1980). For a bunch with rectangular charge distribution and in the linear wakefield approximation, $\eta$is given by,

$$\eta = \frac{L r_e N_e W_0}{k_0(\gamma_f - \gamma_0)} \ln\left(\frac{\gamma_f}{\gamma_0}\right),$$

where k_0 is the betatron wavenumber, W_0 is the transverse wake function, r_e the classical radius of the electron, L is the linac length and N_e is the number of electrons per bunch. The wake function W_0 can be expressed in terms of the transverse loss factor $k_\perp$, as $W_0 = 4\sqrt{\pi}\, k_\perp / L_{cav}$ and provides a measure of the slope of the wake in the linear approximation. The loss factor is equal to 18 V/pC/m for a 1 mm bunch (Edwards 1995), and scales according to $\sigma_z^{-1/2}$. For an rms bunch length of 0.3 mm, W_0 is equal to $7.7\text{x}10^{-3}$ cm^{-3}. For betatron wavelength of 50 m and $4.8\text{x}10^{8}$ electrons per bunch, $\eta$is equal to $1.3\text{x}10^{-2}$.

In the limit of small η, the emittance degradation r_e, defined by $\varepsilon_f = \varepsilon_0 r_e$, where ε_0 and ε_f are the emittances at the linac entrance and exit respectively, can be approximated by (Bisognano 1999)

$$r_e = 1 + \frac{x_0 \eta}{2\pi} \sqrt{\frac{\gamma_0}{\beta \varepsilon_n}}$$

where x_0 is the beam offset, β is the betatron function and ε_n is the normalized emittance. Assuming that the beam offset is equal to the rms beam size at the linac entrance (which is a rather pessimistic assumption), then the emittance degradation is approximately 0.2% for the value of ηcalculated above.

3.1.7 Longitudinal Stability

Energy recovered linacs and recirculating linacs in general, may also exhibit longitudinal multibunch instabilities. Such instabilities may be classified into two broad categories: (1) High average current instabilities that result from the interaction of the beam with the longitudinal Higher Order Modes (HOMs) in the cavity, and (2) Beam loading-type instabilities that result from the interaction of the beam with the fundamental accelerating mode. Both types of instabilities can arise from energy fluctuations, which can couple either to energy apertures and cause beam loss, and/or to non-zero momentum compaction of the recirculator and cause phase oscillations. Both classes of instabilities have been studied previously (Bisognano 1988; Merminga 1996c; Merminga 1999). Instabilities of the latter category have been observed experimentally in the energy recovery experiment performed at Los Alamos (Wang 1987).

Longitudinal multipass beam breakup can result from the following mechanism (Bisognano, 1988): Suppose there is an initial excitation of some longitudinal HOM. Let the bunches enter the cavity on the first pass perfectly spaced. On exiting the cavity, the energy of the bunches will be modulated by the mode. If the isochronicity of the recirculation optics on the second pass through the cavity is not perfect, either by design or due to an error, the energy modulation will be translated into a spacing modulation. This modulation will generate a side-band current whose frequency matches that of the exciting HOM. Thus, on the second pass, the resulting current can enhance the excitation of the HOM that created it. A feedback loop analogous to that which generates multipass transverse beam breakup is formed. A model for the instability for a simple one-cavity, two-pass configuration has been developed and a worst-case estimate of a threshold current has been derived:

$$I_{th} = \frac{2E_r}{eR_{56}(R/Q)_m Q_m k_m} ,$$

where E_r is the first-pass energy, R_{56} is the momentum compaction of the recirculation arc, $(R/Q)_m$, Q_m and k_m are the shunt impedance, quality factor and wavenumber of the longitudinal HOM. Assuming R_{56}=0.5m, E_r=100MeV and one of the strongest monopole modes of the TESLA cavities at frequency 2.4517 GHz, R/Q=142.488 Ω and Q=2.5x10^5 (TELSA 2001), the threshold current is approximately 225 mA. Note that this estimate provides only a magnitude of the effect due to the simplifications of the model. It does however point out that more detailed studies that involve all the cavities and the most important modes and their interaction should probably be carried out. The result of this study will be a specification on the damping of longitudinal HOMs and/or on the magnitude of the R_{56} of the arc.

The second class of instabilities can arise from fluctuations of the cavity fields in the linac and can cause beam loss on apertures and phase oscillations. Beam loss can originate from an energy error, which shifts the beam centroid off its central trajectory and leads to beam scraping on apertures. Phase shifts can originate from an energy error coupled to the finite momentum compaction factor R_{56} of a non-isochronous arc. Both effects – beam loss and phase shifts – change the beam-induced voltage in the cavities

through the recirculating beam. Depending on the RF feedback characteristics (gain, bandwidth) these changes can lead to unstable variations of the accelerating fields.

Stability analysis for small perturbations from the equilibrium has been performed and a threshold current has been derived (Merminga 1996c),

$$I_{th} = \frac{E_r}{e(R/Q)Q_L[R_{56}kS - (\eta_x / L)C]}$$

where $S=sin(\psi_1-\psi_2)$ and $C=cos(\psi_1-\psi_2)$, ψ_1 and ψ_2 are the phases of the accelerating and decelerating beams respectively, with respect to the cavity voltage, η_x is the horizontal dispersion of the arc and L is a loss coefficient which characterizes the amount of beam loss. $L=1$ implies that 1 mm offset produces beam loss at the 10^{-3} level. Finally (R/Q), Q_L and $k=\omega/c$ refer to the accelerating mode, and E_r is the energy of the recirculating beam. Note the similarity of this expression with the equivalent expressions for the longitudinal and transverse HOM instabilities.

The analysis has been extended to include a detailed model for the RF feedback controls, a more refined model for the beam loss mechanism, and details of some of the cavity performance characteristics (Merminga 1999). This self-consistent model has been solved numerically for the JLAB IRFEL and has been compared to experimental data (Merminga 2000b), where quantitative agreement was established between the model and the data. For the JLAB IRFEL parameters (5 mA of average current), the model predicts that this interaction is unstable open loop, however, modest gains (DC gain of ~50) at reasonable frequencies (1–3 kHz) are sufficient to stabilize the system. Clearly, at some operating current the instability threshold is so exceeded that even the RF controls can not stabilize the system. Equivalent simulations will be possible for designing the main ERL accelerator, given the prior work. It is especially important to get a good understanding of the beam loss mechanisms in an energy recovered linac from the Phase I ERL work in order to make a final assessment of the instability in the Phase II ERL.

3.1.8 Higher Order Modes, Cryomodules, and Refrigeration

Higher Order Modes

High average current and short bunch length beams in superconducting cavities can excite Higher Order Modes (HOMs) which, in addition to beam stability consequences, could result in increased cryogenic load due to power dissipation in the cavity walls. The power in HOMs, primarily longitudinal, depends on the product of bunch charge, q, and average current, $I_{ave,}$ and it is equal to $2qk_{\parallel}I_{\mathrm{ave}}$ where $k_{\parallel}$ is the loss factor of the superconducting cavity and the factor of 2 accounts for the two beams in the main linac (accelerating and decelerating). The total power depends on the bunch length through the loss factor. For the TESLA 9-cell cavities, the calculated loss factor is 10.5 V/pC per cavity for 1 ps bunch (TELSA 2001), therefore the power dissipated by the beam for average current of 100 mA and 77 pC per bunch is 162 W per cavity. This

amount of power is a factor of ~100 higher than the present specifications of the TESLA cavities during collider operation. Modifications in the extraction of HOM power are required in order to accommodate the increased power load.

The fraction of the total power that is dissipated in the cavity walls, P_c, is of primary relevance as it can potentially limit the peak and average current due to finite cryogenic capacity. The excitation of high frequency HOMs by the short bunches can degrade the cavity's quality factor Q_0, as $Q_0 \sim f^2$ according to BCS theory, and result in increased power dissipation. An analytic model has been developed (Merminga 2000a) to estimate the amount of power dissipated on the walls. The model, which includes the BCS scaling of Q_0 with frequency and uses an analytic expression for the cavity impedance in the high frequency limit, suggests that:

1. For 1 psec bunches, >90% of the power lost by the beam is in modes below 100 GHz, although frequencies in the THz range are excited. (Recall that bunch compressors and decompressors will be used to produce the shortest bunches in part of the transport arc, but the shortest bunches will not be allowed in the linac.)
2. The amount that is dissipated on the walls is a strong function of bunch length, $\sigma_t^{-5/2}$.
3. An effective Q_{ext} <2000, due to all coupling mechanisms, is adequate to ensure that P_c remains a small fraction of the fundamental mode load.

Moreover, a "multiple reflection model" was developed, valid in the geometric optics limit, where much of the relevant spectrum belongs. This model suggests that the effective coupling due to beam-pipe openings has a Q_{ext} of order 100, suggesting that most of the power will propagate along the structure and will be reflected at normal and superconducting surfaces. A "photon diffusion model" developed at DESY (Joestingmeier 2000) arrives at the same conclusion. In order to reduce the losses at normal conducting surfaces at 2K and 4K, a special HOM absorber is foreseen in the TESLA cavities (Joestingmeier 2000; TELSA 2001), which operates at 70K, where the cooling efficiency is much higher. The absorber consists of a pipe of absorbing material mounted in a cavity-like shielding and integrated into the connection between two modules. As the inner surface area of this absorber is small compared to that of all the normal conductors on one cryomodule, the absorber has to absorb a significant part of all the rf power incident upon it. Field propagation studies have shown that an absorber with a reflectivity below 50% is sufficient for the TESLA operating conditions (Joestingmeier 2000; TELSA 2001). Theoretical and experimental studies carried out at DESY have suggested that the required absorption may be obtained with ceramics like MACOR (Joestingmeier 2000; Joestingmeier 2000) or with artificial dielectrics (Mikijeli 1993).

Finally the effect of losses in the frequency range beyond the threshold for Cooper pair breakup (about 750 GHz) in superconducting niobium has been investigated in (Brinkmann 2000). It was concluded that in a string of 9-cell cavities the temperature rise of the inner cavity surface and the resulting Q_0 drop are negligible.

In summary, a modified HOM power extraction scheme is required in the TESLA cavities of the main linac that can handle the increased HOM power levels of the ERL compared to TESLA operation. In addition, cooled photon absorbers placed between modules or perhaps between cavities will be needed to absorb the fraction of HOM power that propagates along the structures. Evaluation of designs to accommodate these needs will be a primary goal of the Phase I ERL.

Cryomodules

Extensive work on developing cryomodules for superconducting linacs has been carried out as part of the TESLA development (TELSA 2001). We propose to use that design with minor modification in the Phase I and II ERLs. Figures 3.1.8-1 and –2 illustrate the TESLA developments.

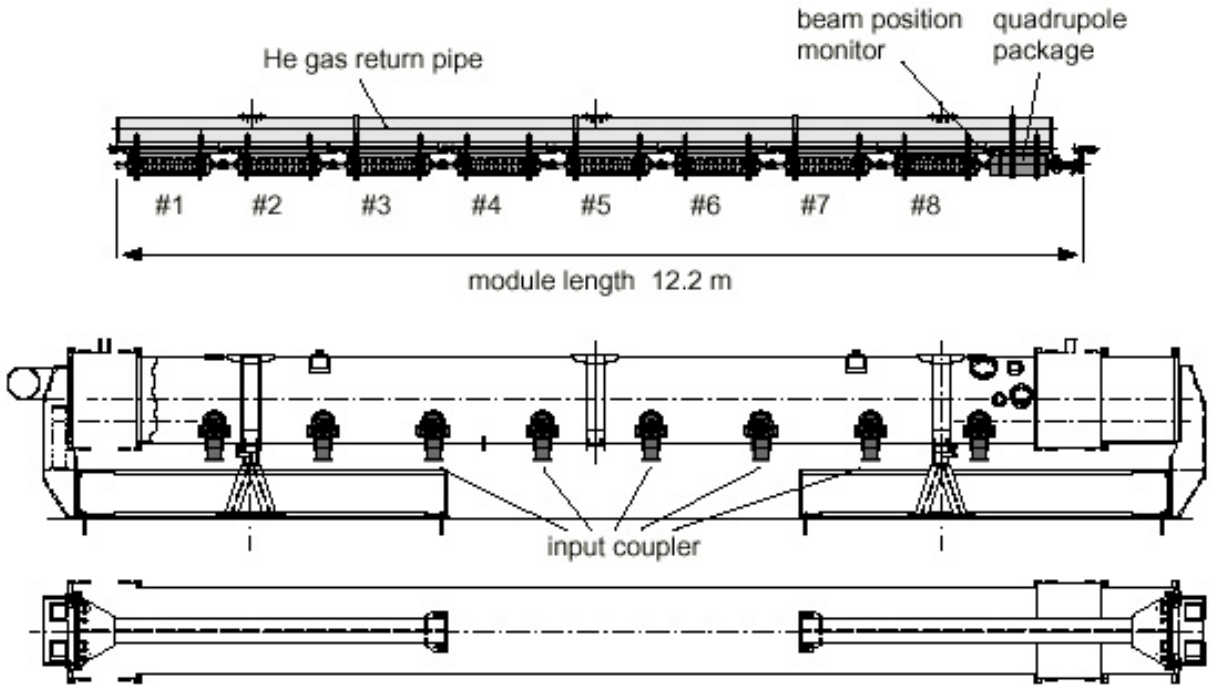

Fig. 3.1.8-1. TTF cryomodule (with permission from DESY).

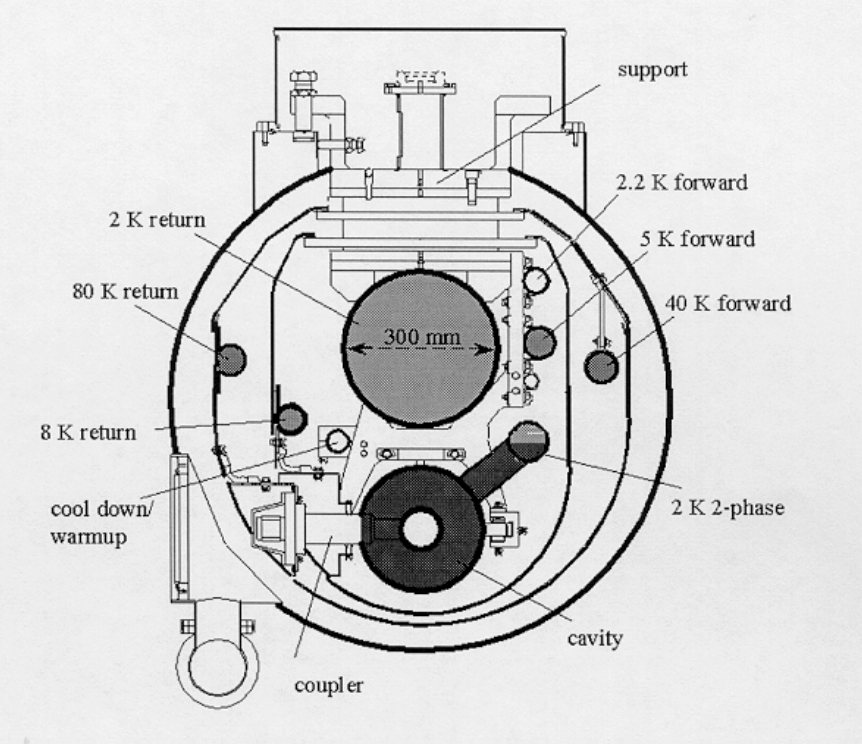

Fig. 3.1.8-2. TTF Cryomodule Cross-Section (with permission from DESY).

Refrigeration

Using currently achieved TESLA parameters and projected needs for the Phase II ERL, the refrigeration power required at 2 K will be on the order of 10 kW, and 5 kW at 4.2K. Optimization of the overall design taking capital and operating costs into account will be required for final determination of this number. The optimization process may involve one or more recirculations. For comparisons the refrigeration plant for the 6 GeV CEBAF accelerator is about 5 kW (at 5 recirculations).

3.1.9. RF Power, Coupling Optimization, and Stability

Efficient use of RF power and excellent stability of the beam are essential for a successful ERL. Here we discuss these matters quantitatively beginning with the basic dependencies of the linac cavity voltages.

The equation for the cavity voltage is (Krafft 1990)

$$\left[\frac{d^2}{dt^2}+\frac{\omega_c}{Q_L}\frac{d}{dt}+\omega_c^2\right]V_c=\frac{\omega_c}{Q_0}2\eta\beta\frac{dV_+}{dt}-\omega_c\frac{R}{Q}\frac{dI_B}{dt},$$

where V_c is the cavity voltage, a_c is the angular frequency of the cavity resonance, Q_L and Q_0 are the cavity loaded and unloaded quality factors, V_+ is the voltage of the

forward going wave to the cavity, $\imath$ is the transformer ratio, β is the coupling factor, R/Q is the cavity shunt impedance, and I_B is the beam current. Calculating the incident power utilizing the relation $\beta = (R/Q)Q_0/(2\eta^2 Z_0)$,

$$P = \frac{|V_+|^2}{2Z_0} = \frac{|V_c|^2}{(R/Q)Q_0}\frac{(1+\beta)^2}{4\beta}\left\{\left[1+\frac{R}{Q}\frac{Q_L I_{B1}}{|V_c|}\cos\psi_1 + \frac{R}{Q}\frac{Q_L I_{B2}}{|V_c|}\cos\psi_2\right]^2 + \left[\tan\psi + \frac{R}{Q}\frac{Q_L I_{B1}}{|V_c|}\sin\psi_1 + \frac{R}{Q}\frac{Q_L I_{B2}}{|V_c|}\sin\psi_2\right]^2\right\},$$

where $|V_c|$ is the magnitude of the cavity voltage, I_{B1} and I_{B2} are the beam current on the first and second passes through the cavity, ψ_1 and ψ_2 are the phases of the beam referenced to maximum acceleration at $\psi_i = 0$, and $\tan\psi = Q_L\left(\frac{\omega}{\omega_c} - \frac{\omega_c}{\omega}\right)$ is the detuning angle.

It can be shown that the optimized coupling and detuning are (Merminga 1996a)

$$\beta^2 = (1 + k_{c1}\cos\psi_1 + k_{c2}\cos\psi_2)^2 + I$$

and

$$Q_0\left(\frac{\langle\omega\rangle}{\omega_c} - \frac{\omega_c}{\langle\omega\rangle}\right) = -k_{c1}\sin\psi_1 - k_{c2}\sin\psi_2$$

for a total average power of

$$\langle P\rangle = \frac{P_0}{2}\left[1 + k_{c1}\cos\psi_1 + k_{c2}\cos\psi_2 + \sqrt{[1 + k_{c1}\cos\psi_1 + k_{c2}\cos\psi_2]^2 + I}\right],$$

where $P_0 = \frac{|V_c|^2}{(R/Q)Q_0}$ is the power dissipated in the cavity walls and $k_c = \frac{R}{Q}\frac{Q_0 I_B}{|V_c|}$ is the cavity multiplication factor (Krafft 2000c). In these equations I is an *rms* frequency fluctuation integral giving the microphonic fluctuation amplitude

$$I = \left\langle Q_0^2\left(\frac{\omega' + \langle\omega\rangle}{\omega_c} - \frac{\omega_c}{\omega' + \langle\omega\rangle}\right)^2\right\rangle - \left\langle Q_0\left(\frac{\omega' + \langle\omega\rangle}{\omega_c} - \frac{\omega_c}{\omega' + \langle\omega\rangle}\right)\right\rangle^2 \approx Q_0^2\left(\frac{1}{\omega_c} + \frac{\omega_c}{\langle\omega\rangle^2}\right)^2\omega_{rms}^2$$

and it is assumed in this calculation that the distribution of microphonic fluctuations does not depend on the detuning choice.

The equation for the optimal β is understood as the condition leading to minimal average reflected power. The first term gives the matching of the power to the beam load and the second term gives the extra average power needed to control the microphonic fluctuations. Clearly, $\beta - 1$ if $\alpha_{rms} - 0$ and there is no beam load, because only P_0 in power is needed to establish the field in the cavity. For finite α_{rms}, there is no benefit in making β smaller than the optimum, because additional power would be needed to provide control against the increased sensitivity to microphonic oscillations at larger loaded Q.

Using the parameters in Table 3-1, above, assuming that the energy recovered beam is exactly 180 degrees out of phase with respect to the accelerating beam, and assuming the microphonic detuning amplitude is 25 Hz rms, we find that the total average power delivered by the klystrons must be 9.4 kW/cavity at a Q_{ext} of 2.6×10^7, as summarized in Table 3.1.9-1. More interestingly, this analysis may be used to estimate the power needed to overcome imbalances due to
(a) continuous beam loss between the first pass and second pass through the machine, and
(b) path length changes of the second pass beam away from 180 degrees.

The results are again summarized in Table 3.1.9-1. In order to stay within a klystron power tolerance of 15 kW, it is necessary for the beam loss to be less than 0.3%, and the path length error to be less than 0.5 degrees. There is good evidence at JLAB that such path length stability can be achieved (Krafft 2000b). As a novel path length setup diagnostic, it may be that it will be easiest, and most accurate, to determine the 180º phase point of the second pass beam by RF power measurements. Accuracy at the 0.1º level is possible, representing the best measurements done presently with the diagnostics at JLAB.

Case	Detuning	$\Delta I/I$	Ψ_1	Ψ_2	P
Nominal	0	0	0	180	9.4
Current Error	0	0.0025	0	180	12.4
Phase Error	0	0	0	179.5	13.8

Table 3.1.9-1: RF system power requirements (kW/cavity)

The cavity fields will be amplitude and phase stabilized by RF control modules as described below. A reasonable model for the requirements on the RF controls is provided by the CEBAF at JLAB, whose beams are long-term stable to several times 10^{-5} in relative energy error. The requirements on the individual cavity field fluctuations and amplitude fluctuations is given in Table 3.1.9-2 (Krafft 1987), where the corrected energy drift is specified to be less than 10^{-4}, somewhat less stringent than in the CEBAF accelerator.

Quantity	Correlated	Uncorrelated
Amplitude	1.1e-5	2e-4
Fast Phase	0.1	0.3
Slow Phase	NA	2

Table 3.1.9-2: Amplitude and Phase Fluctuation Tolerances

Given a microphonic fluctuation level of 25 Hz (to be compared to a measured fluctuation level of 3 Hz in the CEBAF cavities and around 7 Hz for TESLA cavities), the overall gain of existing RF control modules should be sufficient to obtain the requisite stability. See Section 5.2.5.2 **.**

Beam Loss

As noted previously in this section, the pass to pass beam loss must be under 0.3% in order that there be small additional load on the klystrons powering the accelerator. In fact, because of machine protection issues, the beam loss should be restricted to around 1 μA, based on CEBAF operations experience at several GeV. The CEBAF Beam Loss Accounting system, is set up to turn the beam off if more than 2 μA beam loss is detected (measured electrically) between the experimental halls and the injector (Ursic 1996). A continuous loss of several kW (2 μA at several GeV) can be very damaging to machine vacuum elements if the loss is concentrated, a circumstance that may sometimes be unavoidable. A 1 μA beam loss specification was taken over to the JLAB IRFEL, where beam trip monitors were calibrated to abort beam at 1 μA beam loss. Because the IRFEL operates without tripping at a beam current of 5 mA, it is known that 99.98% of the beam current is energy recovered in that device (Neil 2000). Another factor of 20 is needed to ensure that 99.999% of the beam current is recovered in the ERL.

There are isolated pieces of evidence that this accuracy in energy recovery has been achieved in the JLAB IRFEL already, although a detailed measurement has not yet been performed with the requisite accuracy (Neil 2001). A 1.1 mA beam was run for 1 hour followed by low duty factor beam for one half hour into an insertable dump. Afterwards, a radiation survey was completed of both the beam dump and the beamline around the energy recovered linac. The ratio of the dump activation to the integrated residual beamline activation was about 20:1. If the beamlines were saturated by the high duty factor beam, and one assumes that the dump activation is primarily from the low duty factor beam, the ratio between the induced activity measured from 1.1 mA loss, and that measured at the dump, had the beam been CW, is less than 1 part in 40,000. The continuous beam loss would have to be less that 25 parts per million, within a factor of 2 of the requirement. It is felt that there are many occasions when the IRFEL runs with beam losses far below the 10 ppm requirement.

The beam loss is directly related to the efficiency of energy recovery (Krafft 2000c). In the general case where recirculation phases may be set up so that the injected

beam actually delivers net power to the RF cavities, it is not clear *a priori* how the efficiency should even be defined. This problem has been analyzed in some detail with the following conclusions:

(1) A facility multiplication factor can be defined, which is the ratio of the beam power after acceleration to the power needed to accelerate this beam. For an energy recovered linac the multiplication factor can be larger than one.
(2) As calculated above, beam losses in an ERL tend to cause an increase in the required RF power.
(3) The ratio of the power required without losses to the power required with losses defines an efficiency with the correct behaviors.

To illustrate the arithmetic, consider an ERL with the following parameters: V_{gun} = 500 keV, I_{beam} = 0.1 A, $\eta_{DC,inj}$ = 0.5, N_{inj} = 4, $\eta_{DC}\eta_{DC-RF}$ = 0.35, $R/Q = 900\ \Omega$, V_{inj} = 2 MV, $Q_{L,inj} = 22{,}000$, $P_{0,inj}$ = 50 kW, $k_{c,inj}$ = 1, $V = 26$ MV, $Q_L = 2.6\times10^7$, P_0 = 7.2 kW, k_c = 90, N =184, and all the ψ s = 0. Then P_{in} = 5.1 MW, 2.3 MW from the injector RF and 2.8 MW from the linac, and P_{beam} = 500 MW. The multiplication factor is 98. A 10^{-4} current error on recirculation yields a 1.3% reduction of the multiplication factor. Our canonical 1 μA loss would give 99.87% "energy recovery efficiency".

It is advantageous to concentrate on ERL designs that maximize the system multiplication factor. Such a design is achieved by the obvious expedients of increasing the component efficiencies as much as possible, by minimizing the injector power needed, by choosing as low injector energy as possible, and by putting most of the energy gain on the most energy efficient converters in the injector. Also, it is clear that superconducting designs are to be preferred to normal conducting designs because the multiplication factor will be higher; P_0 for superconducting cavities is much lower than for normal conducting cavities.

3.1.10. Ion Effects

As the quasi-continuous electron beam in the ERL has negative average space charge, positive ions generated by ionization of the background gas in the beam vacuum enclosure by the electron beam will tend to collect inside the electron beam, acting to neutralize the average space charge. There are electron beam dynamical effects associated with the collected ions, and such ion trapping phenomena have been studied in electron storage rings for a number of years. In storage rings, a primary effect of the accumulated ions is the betatron tune shift resulting from the accumulated ion space charge. Such ion effects become significantly more important in storage rings as the beam current approaches and exceeds 100 mA.

Ion trapping effects must be anticipated when the continuous duty design current of the ERL approaches values of 100 mA. In an ERL, the collected ions affect the beam in a way somewhat different that in a storage ring, as there is no parameter equivalent to the betatron tune shift. Instead, the beam transverse match will tend to wander away from

the design values as the ions accumulate, leading to beta-function and spot size changes, most particularly, in the undulators producing the end-use x-rays (Raubenheimer 1995). Because the undulators will be in places where the beta-function is minimum, largely independent of the beam matching conditions coming into the undulators, the time-dependent effects observed by the end users as the ions accumulate are expected to be small. Because the electron beam resides in the accelerator for a time small compared to typical growth times, and because the electron beam is dumped after a single pass, the possibility of ion cloud instability is small (Raubenheimer 1995). Therefore, it is anticipated that ion effects will have less deleterious effects in the ERL as compared to a storage ring. As additional evidence, it is a fact that in both the JLAB CEBAF machine, and in the JLAB ERL-driven IRFEL, it has never been necessary to correct any machine optical elements due to the presence of ions, or to implement any ion clearing scheme, even though it is known that ions should accumulate in both of these beams.

There have been two basic methods of combating ion trapping effects in storage rings, both of which are available for use in an ERL, should the need arise: high voltage electrodes for clearing away the accumulated ions, and the imposition of "clearing gaps" in the beam current of the circulating beam. In the former solution, the ions are not allowed to accumulate within the beam path because they are drawn away physically, whereas the second solution relies on the fact that a positively charged ion cloud is unstable in itself without the presence of the electron beam. It is shown in Section 4.3.2 below that ion clearing in the injector, the most difficult case, can be accomplished with a several microsecond beam gaps spaced at one second intervals, a beam current pattern that it is straightforward to implement on the laser. The resulting RF transient can be controlled by feed forward. For more detail see section 4.3.1.

3.1.11 Insertion Devices

X-ray undulators are the insertion device of greatest interest for the ERL machine as they are the technology of choice for making ultra-high brilliance x-ray beams. They have been generally fabricated from permanent magnets and can be built with low phase error so that even long arrays are practical. The technology of making and tuning undulators is well developed and we plan to take advantage of current developments in the field at the time of actual ERL machine construction.

In the next sections we briefly review

1. the types of undulators needed for the ERL, and
2. the current progress in relevant undulator design for storage rings and FELs that is related.

Types of undulators need for ERL

Short period and short gap permanent magnet based undulators will be the natural choice of ID for the ERL machine. Most of the x-ray interest is in the 5 to 25 keV region, so undulator periods of several cm length are relevant. Although one can imagine many types of specialty undulators, two IDs that seem to be suitable for much of the suggested

science of a Phase II ERL are an undulator of 25 meter length (segmented, 1470 periods of 1.7 cm) and a 2 meter undulator (1.7 to 3.3 cm period length of 118 to 61 periods respectively). The 25 m long ID is picked in order to significantly increase the brilliance and flux of the ERL when compared with conventional storage rings (see section 2.2).

The second, shorter length ID is of particular interest to the x-ray microprobe community where transverse electron beamsizes can be less than 7.5 microns FWHM in both planes perpendicular to the electron trajectory. By highly demagnifying this source, a fantastic microbeam of ultra small dimension can be obtained.

The rms transverse beam size in the ERL for the 2 m long undulator is 3.2 microns (see Table 2.3.3-1). Having a small round beam in the ID will be highly desirable for further demagnification by optics to reduce the image of the source by factors of 500 to 1000. This is the basis of hoping to reach x-ray beam sizes in the few nm range, if perfect enough optics can be obtained. For instance, with a perfect zone plate, a 7.5 nm FWHM beam could be made.

One of the important related design issues for IDs is the appropriate machine energy. The ERL source naturally makes lower emittance beams (inversely proportional to energy) as the machine energy goes up. But higher machine energies involve higher capital and operating costs. The appropriate machine energy for a Phase II ERL will therefore depend on the emittance which can actually be achieved out of the photogun and maintained in the ERL. Determination of the achievable emittance is, again, a prime motivation for the Phase I ERL R&D program.

Current progress in undulator design

Three areas of recent insertion device developments have been identified by Ingold (Ingold 2000) :

1) Short period devices with gaps below 10 mm may be used to enhance the brilliance and to increase the emitted photon energy.
2) Variable polarization devices may be used to address science requiring specially polarized x-ray beams.
3) Long, segmented undulators with strong focusing are important for single pass, high gain FELs.

It is particularly developments in (1) and (3) that are most relevant for ERL machines.

The status of IDs for high energy storage ring sources such as the APS, ESRF, and SPring 8 can be found in references (Chavanne 1996; Chavanne 1998; Gluskin 1998; Kitamura 2000). The progress at these machines has recently led machine designers to lower energies for new machines such as DIAMOND and SOLEIL with very high performance undulators. Methods have been found to quantify and control phase errors to less than 2.5 degrees rms so that nearly theoretical performance can be obtained on the higher harmonics. Undulators can operate in the vacuum as well if needed to reach to higher energies. The Swiss Light Source will be depending on the 9^{th} or 11th harmonic

of a small gap in vacuum undulator to reach 13 keV for x-ray crystallography (Ingold 1999).

Segmented undulators are in use at SPring8 and on the Tesla Test Facility (Pfluger 2000) and have been designed for the LCLS XFEL (Tatchyn 1998). Segmentation gives better control of conventional manufacturing methods and allows for installation of beam position monitors and focusing between the segments. This technology is evolving quickly as well and looks very promising for the Phase II ERL machine. Other technologies that may be important are vacuum chambers with 5 mm gap, such as have been developed by APS, and possibly far into the future: superconducting undulators with very short periods.

Although these developments in undulator design are promising, considerable design work needs to be done well in advance of specifying a Phase II ERL. For instance, the precision in the construction of undulators will have to improve to fully take advantage of the high brilliance electron beams that the ERL machine will be able to produce. At first look, one might say that the Spring8 undulators are 25 m long and so are the ones for the ERL, so just use Spring8 technology. But the phase errors of the undulators that are tolerable for Spring8 are of the order 8 to 10 degrees. Most likely - and this is where a sensitivity study needs to be made - the phase errors will have to come down to 1 to 2 degrees on each pole, similar to what is specified for the Swiss Light Source. But the Swiss Light Source undulators are relatively short. There will need to be considerable R&D on reducing the phase errors of long undulators to optimally utilize the beams possible from an ERL source.

Another area which will require attention during Phase I is methods of producing long in-vacuum undulators at reasonable cost. Precision undulators of many thousands of poles will be very expensive unless new technologies can be brought to bear on ID design. Cost will be a key issue. In the absence of well thought through demonstration projects, there is concern that the largest single cost component of a Phase II facility might be the undulators. It will be important in setting vendor specifications to quantitatively specify how ideal the periodic B fields of the undulators must be and to figure out how to reasonably achieve these specifications. This part of the R&D will require close collaboration during the Phase I period with scientists at current 3rd generation machines, such as APS, ESRF, and Spring8, to refine these methods to make them work on an ERL machine. A cost analysis study should be undertaken to identify the most economical approach to this problem. As part of the engineering work, magnetic designs (peak field, period length, tolerable quadrupole and sexupole field errors) will be determined. Engineering work will also proceed on design of a magnetic unit cell with computer codes which will be verified in stages of prototype construction followed by experimental measurement of the as-produced field properties. Long, in-vacuum undulators will almost certainly be segmented, and advance design work on the best way to assemble and phase segmented undulators will need to part of the design work.

A further area requiring considerable advance design work is to determine what kind of IDs will be needed for optimal use of the properties of an ERL as the feasibly attainable machine characteristics become clear during the course of the Phase I development. This will involve use of programs like SXW from the ESRF to critically examine tradeoffs between brilliance, undulator length, source size, etc. For instance, a 2 m long undulator with a 1 m beta may be close to the design of an optimal source for microdiffraction, but other experiments that desire brilliance and a lot of flux may prefer the 25 m long undulators with a larger source size. These preferences are evident now, but they need to be placed on a firmer scientific and engineering footing before specifying a final ID plan for a Phase II ERL.

One further idea should be noted with regards to undulators in an ERL machine. As discussed by J. Als-Nielson at the ERL Science Workshop (Als-Nielson 2000) with a round (as opposed to a pancake shaped) source one is no longer limited to diffracting in the vertical plane as we currently do in storage ring sources, but we can diffract horizontally as is currently done for neutron diffraction. Beam lines can be built on a "spokes around a hub" model and heavy apparatus such as furnaces and dewars can more easily be scanned in angle without having to work against gravity. All that is required is to rotate the ID magnets 90 degrees to what is currently done on storage rings. This, again, points to the need to think though the design of a Phase II ERL well ahead of time and to avoid the temptation to simply extrapolate from existing storage ring designs. Design workshops involving the larger x-ray community will be key to developing the new ideas needed for a Phase II ERL facility. Hosting these workshops will be an essential task during the Phase I period.

3.1.12 Design Considerations for ERL X-ray Optics

We divide the discussion on ERL x-ray optics into three broad categories:

1) heat load specific issues,
2) preserving the intrinsic brilliance and transverse coherence, and
3) challenges associated with temporal properties of ERL beams.

Heat load tolerant optics design

The concerns about heat loads on the x-ray optics are also concerns for the existing 3rd generation machines and, certainly, for the planned 4th generation machines. Table 3.1.12-1 gives a comparison of heat loads expected from the ERL and from undulators now installed at SPring-8, both at 8 keV.

Table 3.1.12-1 Heat Loads at ERL and SPring-8

	25m ERL undulator @ 5.3GeV operation: 100 mA	10 mA	**SPring8 undulators** @ 8GeV&100mA ID length: 25 m	4.5 m
Power (kW)	33.9	3.4	31.2	15.7
Power/Area (W/mm^2) @ 20 meters	2600	260	4568	1830

Based on the time-averaged power and heat load tolerance, optics designs that work successfully at SPring8 should also work at the Phase II ERL. At present, published reports (Yabashi 1999; Ishikawa 2001) are available on the performance of the SPring8 standard high heat load (asymmetric-inclined) crystal monochromator and 4.5 meter undulator, where measurements indicate a specific flux of $5x10^{10}$ photons/second/mm^2 at 10 keV and 1 km from the source. This is about 25% of the flux expected for perfect optics. Assuming that the deviation is due to heat loading implies that the heat load issue is far from completely solved.

One should also consider "non-thermal" effects on optics associated with instantaneous power. Mills (Mills 1999) has examined such concerns by comparing expected pulse width and fluence from FEL sources to results obtained in studies of lattice damage in short pulse laser experiments. The LCLS XFEL is predicted to produce $2x10^{12}$ photons at 8 keV per 230 fsec. pulse. Given the source parameters (see Table 3.1.12-2), this corresponds to a fluence of 40.3 Joules/cm^2 at 50 meters. After factoring in x-ray absorption, Mills (Mills 1999) concludes that non-thermal damage should not occur in diamond optics and may not occur for silicon. In comparison, the ERL would produce 300 fs pulses with a fluence at 50 meters of 7.2(1.6) $x10^{-6}$ Joules/cm^2 in high flux (high coherence) mode. This much lower value is however not the whole story since Mills considered pulses from the FEL operating at 120Hz, while the ERL duty cycle is planned to be higher then the LCLS by 10^7. However, if non-thermal damage can be ignored, as anticipated, then we need consider only thermal (equilibrium) effects of power and then it is safe to return to our comparison with SPring8.

We are unaware of published reports on the optical performance of components on the SPring-8 25 meter undulator beam line. This is not surprising, since this undulator only recently went into operation. The magnitude of the problem will become clearer after more operating experience is gained with this device.

Preserving x-ray beam brilliance and transverse coherence.

Transverse coherence is preserved by eliminating the distortion of the wave-front in passing through beamline components, such as x-ray windows, monochromators, and focusing devices (mirrors, refractive lenses, phase plates, etc.) An upper bound on wave front distortion can be estimated by reference to beam characteristics for the ERL (along with comparable sources) listed in Table 3.1.12-2.

In high coherence mode the Phase II ERL beam spot size at 50 meters is dominated by the angular size of the source. If portions of this beam deviate in angle, the spot size will enlarge. For instance, an average slope error on reflecting surfaces of 3 microradians should add angular size, in quadrature, enlarging the beam by √2 from 311 to 440 microns. State-of-the-art slope errors (rms) in mirror manufacture stand at or below 2 microradians (Freund 1999) (surface roughness is now also below 2Å rms); however, thermal distortions can cause considerably larger slope variation.

A second, closely related criterion of perfection for x-ray optics involves preserving transverse coherence. The source size and wavelength together define an angle (see (Shen 2001), pg. 5) within which the wave front has a well defined phase (points on the wave front have a definite phase relation). At 8 keV for the ERL this angle is 5.3 microradians, so distortions on this order will render the beam incoherent.

25m ERL undulator @ 5.3GeV			**SPring8**	**ESRF, 200mA,6GeV**	**LCLS/SASE,15 GeV**
operation:	100mA	10mA	ID length: 25m	5m undulator	100m undulator
source size (μm)					
horizontal	103	24.5	890	879	78
vertical	103	24.5	22.8	13.9	78
source diverg. (μrad)					
horizontal	9.1	6.2	37.4	26.8	1
vertical	9.1	6.2	4.3	10.4	1
beam size at 50 m (μm)					
horizontal	466.5	311	2071	1603	93
vertical	466.5	311	216	520	93
average brilliance p/s/.1%bw/mm^2/mrad^2	1.3e22	5.2e22	2.2e21	3.1e20	4.2e22
% beam coherence	0.52	20	0.14	0.14	100

Table 3.1.12-2 shows that the horizontal source properties of the ERL in high coherence (10mA) mode result in a beam smaller than storage ring sources, and comparable to the XFEL. (In contrast to these sources, horizontally flattened storage ring sources require that for maximum brilliance the optics operate in vertical scattering geometry. The ERL can have round electron beams which allow the undulator and/or scattering plane for the optics to be rotated by any angle about the beam direction without loss of brilliance. (Polarization factors alter this slightly.) Assuming beam divergence orthogonal to the scattering plane is preserved through optics, then brilliance preserving optics for SPring8 with the 25m undulator should also work at the ERL. Another way of saying this is, based on source phase space, the level of perfection (in terms of slope error) for the ERL optics is comparable to that for SPring8.

Early results from measurements at the SPring8 1 km long beamline BL29XU give a practical indication that transverse coherence can be preserved through beamline optics. First reports on diffraction enhanced imaging and topography (Yabashi 1999) dramatically illustrate two facts: problems with storage ring stability affect these measurements, and if monochromatic images are taken through a fast shutter (to mitigate beam motion) excellent phase contrast is visible over an area as large as 10 mm by 10mm. This implies that the x-ray beam transport has preserved the expected beam coherence. (Note that the coherence angle for the SPring8 4.5m undulator, which is the source in question, should produce a coherent spot at 10 KeV and 1 km that is 5.85mm high by 0.07mm wide. The fact that good phase contrast is observed in diffraction enhanced images suggests that the "coherence angle" is not the limitation for this technique.)

Challenges associated with the ERL temporal properties

What is known on how x-ray optics preserve the temporal properties of ERL beams and conversely how do very short pulses affect the throughput of optics? There are several aspects to the question. The first concerns a relation between pulse length and Bragg reflectivity. When the x-ray pulse length (in space) is smaller than the extinction length in a perfect crystal (or the absorption length in mosaic crystals) simulations (Wark 1994) predict that integrated reflectivity will be reduced from conventional values. This effect, if true, would be very significant for mosaic crystal optics and for perfect crystal near-back reflection analyzers used in high resolution inelastic scattering. A 300 fs pulse from the ERL is about 90 micron long and this may be compared to perfect crystal extinction lengths that range from 5 to 100 microns, but the pulse is measured along the incidence beam direction while extinction is measured normal to the Bragg planes, so reflectivity reduction may be sensitive to angle of incidence.

This effect can be thought of as a "response time" of the crystal to x-rays. It is being studied as a means to filter out extremely short fluctuations in source intensity, but may ultimately limit the delivery of short pulses (Shastri 2001). For a practical set of 111 silicon optics, Shastri and Mills calculate the added temporal spread to be less than 5 fs. For higher order reflections and narrower energy bandwidths, this number can stretch out to many 10s of femtoseconds. The situation for mosaic crystals can be much worse because reflectivity is limited by absorption in the material.

Another issue that will need to be addressed when optimizing x-ray optics for short pulse beams concerns the distortion, in space and time, of pulse shape in the process of scattering (Tatchyn 1999). If a beam wavefront is not specularly reflected by an x-ray optic, then the shape of the front (and pulse) will emerges from the reflection having suffered a linear transformation (mixing of position and time) in shape. This will tend to broaden the time width of pulses and would be particularly significant when time resolution is paramount and for optics such as asymmetric-inclined crystal monochromators and zone plates. Issues pertaining to the x-ray optical effects of very short x-ray pulses are an area of great current interest for which the community at large has practically no experience. It will begin to be explored in the next few years by the

appearance of ways of generating fast (if relatively low intensity) x-ray pulses (Schoenlein 2001) and by the R&D efforts of the XFEL activities. We plan to be involved in these new developments and to collaborate with colleagues doing experimental work at other facilities in order to gain expertise in this emerging area.

To summarize, considerable advance development work on x-ray optics will be needed to make optimal use of ERL beams. The slope errors on the current generation of cryogenically cooled silicon optics are barely adequate for 3rd generation sources (Bilderback 2000). Most likely slope errors will have to be improved by factors of 2-10. Mirror optics will need a similar improvement. The very high specific heat loads expected from an ERL are also beyond the present state of the art. One possibility is to develop cryogenically cooled diamond crystals of higher perfection than are presently available. Another is to investigate fabricating isotopically pure top layers of some of the silicon optics to obtain a 60% higher thermal conductance than the current generation of optics (Ruf 2000). Extensive computer modeling of thermal loading will be needed to develop x-ray optical components to deal with the very high specific heat loads expected from long undulators on a Phase II ERL. Another area which will require considerable thought and planning is optimal optics to preserve the temporal characteristics of very short x-ray pulses. Since all of these x-ray optical developments will take time and will affect the projected cost of a Phase II ERL facility, it is important to begin this advance planning during the Phase I period.

3.2 Section 3 References

Als-Nielson, J. (2000). "Vertically Polarized Undulators". Energy Recovery Linac (ERL) Science Workshop, Cornell University, Ithaca, NY, 2-3 Dec 2000 http://erl.chess.cornell.edu/papers/X-ray%20Science%20Proceeding%20Papers/JensAlsNielsenERL%20Workshop.pdf ,.

Bazarov, I. V. (2001), "Transverse beam break-up stability or linac optics for Energy Recovery Linac", CHESS, Cornell University, Ithaca, NY, ERL-Prototype-TN-01-001.

Ben-Zvi, I., and Krinsky, S. (2001). "Future light sources based upon photo-injected energy recovery linacs.", Synchrotron Radiation News **14**(2): 20-24.

Ben-Zvi, I., Kewisch, J., Murphy, J. and Peggs, S. (2000). "Accelerator physics issues in eRHIC". Proc. 2nd eRHIC Workshop, Yale University, New Haven, CT, April 2000.

Bilderback, D. H., Freund, A. K., Knapp, G. S., and Mills, D. M. (2000). "The historical development of cryogenically cooled monochromators for third-generation synchrotron radiation sources.", Journal of Synchrotron Radiation **7**: 53-60.

Bisognano, J. J. (1999). Personal Communication.

Bisognano, J. J., and Fripp, M.L. (1988). "Requirements for longitudinal HOM damping in superconducting recirculating linacs". Proc. 1988 LINAC Conf., Newport News, VA.

Bisognano, J. J., Gruckstern, R.L. (1987). "Multipass beam breakup in recirculating linacs". Particle Acceleration Conference, IEEE Proc.: 1078-1080.

Brinkmann, R., et al (2000). "THz Wakefields and their Effect on the Superconducting Cavities in TESLA". Proc. of 7th EPAC, Vienna.

Brown, K. L., Rothacker, F., Carey, D.C., and Iselin, F.C. (1977), "TRANSPORT - a computer program for designing charged particle beam transport systems", May 1977, SLAC, Stanford, CA, SLAC-91, http://www.slac.stanford.edu/spires/hep/.

Campisi, I. E., Douglas, D., Merminga, L. and Yunn, B.C. (1999). "Beam breakup simulations for the Jefferson Lab FEL upgrade". Particle Accelerator Conference, IEEE Proc.: 1180-1182.

Carlsten, B. E. (1996). "Calculation of the noninertial space-charge force and the coherent synchrotron radiation force for short electron bunches in circular motion using the retarded Green's function technique.", Phys. Rev. E. **54**: 838-845.

Carlsten, B. E., and Goldstein, J.C. (1997). "Emittance growth of a short electron bunch in circular motion.", Nuc. Instr. Meth. Phys. Res. A **393**: 490-493.

Chambers, E. (1968), "Summer Study on Superconducting Devices and Accelerators", Stanford University, Stanford, CA, BNL 50155 and HEPL TN-68-17.

Chao, A. W., Richter, B., and Yao, C.-Y. (1980). "Beam Emittance Growth Caused by Transverse Deflecting Fields in a Linear-Accelerator.", Nuclear Instruments & Methods in Physics Research Section A **178**: 1-8.

Chavanne, e. a. (1996). Proc. 1996 European Particle Conf.: 220.

Chavanne, J., Elleaume, P. and Van Vaerenbergh, P. (1998). "The ESRF insertion devices.", Journal of Synchrotron Radiation **5**: 196-201.

Derbenev, Y. S., and Shiltsev, V.D. (1996), "Transverse effects of microbunch radiative interaction", May 1996, Fermi Lab, FERMILAB-TM-1974, SLAC-Pub 7181.

Derbenev, Y. S., Rossbach, J., Saldin, E.L. and Shiltsev, V.D. (1995), "Microbunch radiative tail-head interaction", September, DESY, Hamburg, Germany, TESLA-FEL 95-05.

Dohlus, M., Kabel, A. and Limberg, T. (2000). "Numerical calculation of coherent synchrotron radiation effects using TRAFIC4.", Nuc. Instr. Meth. Phys. Res. A **445**: 338-342.

Douglas, D. (2000a), "Injector linac optics for a high current srf driven electron accelerator", February 2000, Thomas Jefferson Nat. Accel. Facility, Newport News, VA, JLAB-TN-00-005.

Douglas, D. (2000d). Personal Communication.

Edwards, D. A. (1995), "TESLA test facility linac - Design Report", DESY, Hamburg, Germany, TESLA 95-01, March 1995.

Emma, P., and Brinkmann, R. (1997), "Emittance dilution through coherent energy spread generation in bending systems", May 1997, SLAC, Stanford, CA, SLAC-PUB-7554.

Engwall, D., Bohn, C., Cardman, L., Dunham, B., Kehne, D., Legg, R., Liu, H., Shinn, M. and Sinclair, C. (1997). "A high-DC-voltage GaAs photoemission gun: Transverse emittance and momentum spread measurements". Proceedings of 1997 PAC, Vancouver, Canada: 2693.

ESRF (2001). Future applications of science with synchrotron radiation and free electron lasers in Europe., ESRF, Grenoble, France., 16-17 Mar 2001 http://www.esrf.fr/news/FEL-SR.html.

Freund, A. (1999). "Summary of Group V". ICFA Workshop on Future Light Sources, Argonne National Lab, Argonne, IL, April 6-9. 1999.

Gill, P. (1972). "Quasi-Newton methods for unconstrained optimization.", Journal of the Institute of Mathematics and Its Applications **9**: 91-108.

Gluskin, E. (1998). "APS insertion devices: Recent developments and results.", Journal of Synchrotron Radiation **5**: 189-195.

Helm, R. H., Miller, R. (1969). "Particle Dynamics". Linear Accelerators, North-Holland, Amsterdam.

Ingold, G. (1999). Proc. ICFA 1999 Workshop on Future Light Sources, Argonne Nat. Lab., Argonne, IL.

Ingold, G. (2000). "Insertion devices: new concepts and performance". Proc. EPAC 2000, paper TUZF102, Vienna, Austria, 26-30 June 2000: 222-226.

Ishikawa, T., et al (2001). Proc. SPIE **4145**

Joestingmeier, A., Dohlus, M. and Cramer, C. (2000), "Photon Diffusion Model for TTF2", DESY, Hamburg, Germany, DESY TESLA-00-11.

Joestingmeier, A., Dohlus, M., Wendt, M. and Cramer, C. (2000), "Theoretical and Practical Investigations Concerning the Design of a HOM Broadband Absorber for TESLA", DESY, Hamburg, Germany, DESY TESLA-00-11.

Kitamura, H. (2000). "Recent trends of insertion-device technology for X-ray sources.", Journal of Synchrotron Radiation **7**: 121-130.

Krafft, G., and Bisagnano, J. (1987). "Two dimensional simulations of multipass beam breakup". Particle Accel. Conference, IEEE Proc.: 1356-1358.

Krafft, G., et al. (2000b). "Measuring and Controlling Energy Spread at CEBAF". 2000 International LINAC Conference: 721.

Krafft, G. A. (1991), "More on the Transfer Matrix for a Cavity", Jefferson Laboratory, CEBAF TN-91-80.

Krafft, G. A., and L. Merminga (2000c). Personal Communication.

Krafft, G. A., Bisagnano, J.J. and Laubach, S. (1988), "Beam breakup in Superconducting Linear Accelerators", Thomas Jefferson Natl. Accel. Facility, Newport News, VA.

Krafft, G. A., S. N. Simrock, and K. L. Mahoney (1990). "Beam Loading Studies at CEBAF". Proc. of the 1990 Int. LINAC Conf: 300.

Lee, S. Y. (1996). "Emittance optimization in three- and multiple-bend achromats.", Phys. Rev. E **54**: 1940-1944.

Lee, S. Y. (1999). Accelerator Physics. NJ, World Scientific, NJ.

Merminga, L., Alexeev, P., Benson, S., Bolshakov, A., Doolittle, L., Neil, G. (1999). "Analysis of the FEL-RF interaction in recirculating, energy- recovering linacs with an FEL.", Nuclear Instruments & Methods in Physics Research Section A **429**(1-3): 58-64.

Merminga, L., Bisognano, J. J., and Delayen, J. R. (1996c). "Energy stability in recirculating, energy-recovering linacs.", Nuclear Instruments & Methods in Physics Research Section A **375**(1-3): ABS39-ABS41.

Merminga, L., Delayen, J. (1996a), "On the Optimization of Under Heavy Beam Loading and in the Presence of Microphonics", Jefferson Laboratory, CEBAF-TN-96-022.

Merminga, L., et.al. (2000b). "First experimental data on the FEL-RF interaction at the Jefferson Lab IR FEL.", Nuc. Instr. Meth. Phys. Res. A **445**: II-3.

Merminga, L., Krafft, G.A., Leemann, C.W., Sundelin, R.M., Yunn, B.C. and Bisognano, J.J. (2000a). "Specifying HOM-Power Extraction Efficiency in a High Average Current, Short Bunch Length SRF Environment". Proceedings of the 2000 Linac Conference, Monterey, August: 13.

Mikijeli, B., Campisi, I. (1993). "Development of an Artificial Dielectric Ceramic for the use at CEBAF". Proceedings of the Workshop on Microwave-Absorbing Materials for Accelerators, CEBAF, Newport News, VA.

Mills, D. (1999). "Group V". ICFA Workshop on Future Light Sources, Argonne Nat. Lab, Argonne, IL, April 6-9.

Neil, G. R. (2001). Personal Communication.

Neil, G. R., Bohn, C.L., Benson, S.V., Biallas, G., Douglas, D., Dylla, H.F., Evans, R., Fugitt, J., Grippo, A., Gubeli, J., Hill, R., Jordan, K., Li, R., Merminga, L., Piot, P., Preble, J., Shinn, M., Siggins, T., Walker, R., Yunn, B. (2000). "Sustained Kilowatt Lasing in a Free-Electron Laser with Same-Cell Energy Recovery.", Phys. Rev. Lett. **84**(4): 662.

Neil, G. R., Jefferson Lab FEL Team (1998). "Industrial applications of the Jefferson Lab high-power free-electron laser.", Nuclear Instruments and Methods in Physics Research B **144**: 40-49.

Nodvick, J. S., and Saxon, D.S. (1954). "Suppression of coherent radiation by electrons in a synchrotron.", Phys. Rev. **96**: 180-184.

Novokhatski, A., Timm, M., and Weiland, T. (1999),,, DESY, Hamburg, Germany, DESY-TESLA-99-16.

Padamsee, H., Knobloch, J., and Hays, T. (1998). RF Superconductivity for Accelerators. NY, John Wiley & Sons, NY.

Pfluger, J. (2000). "Undulators for SASE FELs.", Nuclear Instruments & Methods in Physics Research Section A **445**(1-3): 366-372.

Rand, R. E., Smith, T.I. (1980). "Beam optical control of beam breakup in a recirculating electron accelerator.", Particle Accelerators **11**: 1-13.

Raubenheimer, T. (1995). Particle Accel. Conf.: 2752.

Raubenheimer, T., Zimmermann, F. (1995). "Fast Beam-Ion Instability .1. Linear-Theory and Simulations.", Phys. Rev. E **52**: 5487-5498.

Rosenzweig, J., Serafini, L. (1994). "Transvers particle motion in radio-frequence linear accelerators.", Phys. Rev. E **49**: 1599-1602.

Ruf, T., Henn, R.W., Asen-Palmer, M., Gmelin, E., Cardona, M. and Pohl, H.-J. (2000). "Thermal conductivity of isotopically enriched silicon.", Solid State Comm. **115**: 243-247.

Saldin, E. L., Schneidmiller, E.A. and Yurkov, M.V. (1997). "On the coherent radiation of an electron bunch moving in an arc of a circle.", Nuc. Instr. Meth. Phys. Res. A **398**: 373-394.

Saldin, E. L., Schneidmiller, E.A., Yurkov, M.V. (1999). "Growth of the energy spread due to the radiative interaction in a short electron bunch moving in an undulator.", Nuc. Instr. Meth. Phys. Res. A **429**: 41-45.

Sands, M. (1970), "The physics of electron storage rings. An introduction", November 1970, SLAC, Stanford, CA, SLAC-121.

Sands, M. (1985), "Emittance growth from radiation fluctuations", December, SLAC, Stanford, CA, SLAC-47.

Schiff, L. (1946). Rev. Sci. Instrum. **17**: 6.

Schoenlein, R. W., Chin, A.H., Chong, H.H.W., Falcone, R.W., Glover, T.E., Heimann, P.A., Johnson, S.L., Lindenberg, A.M., Shank, C.V., Zholents, A.A, and Zolotorev, M.S. (2001). "Ultrafast x-ray science at the Advanced Light Source.", Synchrotron Radiation News **14**(1): 20-27.

Schwinger, J. (1945). On radiation by electrons in a betatron. LBNL-39088/CBP Note-179, July 1996. T. b. M. A. Furman

Sekutowicz, J. (1994), "Higher order mode coupler for TESLA", February, DESY, Hamburg, Germany, TESLA 94-07.

Shastri, S. D., Zambianchi, P. and Mills, D.M. (2001). "Femtosecond x-ray dynamical diffraction by perfect crystals.", Proceedings of the SPIE **4143**: 69-77.

Shen, Q. (2001), "X-ray Flux, Brilliance and Coherence of the Proposed Cornell Energy-Recovery Synchrotron Source", Cornell University, Ithaca, NY, 01-002, http://erl.chess.cornell.edu/Papers/ERL_CHESS_memo_01_002.pdf.

Tatchyn, R. (1998). "Field design studies of a planar hybrid/permanent magnet undulator with strong planar permanent magnet focusing.", Nuclear Instruments & Methods in Physics Research Section A **407**(1-3): 454-458.

Tatchyn, R. (1999). Proc. SPIE **3773**: 188.

TELSA (2001), "Technical Design Report", March, 2001, DESY, Hamburg, Germany, DESY 2001-011, http://tesla.desy.de/new_pages/TDR_CD/start.html.

TESLA (2000). “Superconducting TESLA cavities.”, Physical Review Special Topics-Accelerators and Beams **3**(9)

Ursic, R., et al (1996). 2000 Int. LINAC Conf., AIP Conf. Proc. **390**: 405.

Wang, T.-S., and Takeda, H. (1987). "RF stability in the Los Alamos free-electron laser energy recovery experiment". Proc. 1987 Particle Accel. Conf.: 1102.

Wark, J. S., He, H. (1994). “Subpicosecond X-Ray-Diffraction.”, Laser and Particle Beams **12**(3): 507-513.

Wiedemann, H. (1995). Particle Accelerator Physics II, Springer, Berlin

Yabashi, T., et al (1999). “Proc. SPIE.”, **3773**

4. Motivation for the Phase I ERL

4.1 Why is a Phase I ERL Needed?

Considerable investigation of the accelerator physics issues involved will be required and technological advancements attained in order to achieve the flux, brilliance, and time structures that appear to be possible with the ERL. Accelerator physics issues revolve largely around emittance production and preservation and have implications for all parts of the accelerator, from the laser to the gun itself to the capture section, the main linac and the transport lines and undulators. Technological issues center on cathode longevity and high gradient CW operation of superconducting cavities well beyond current standards and the very high efficiency energy recovery demanded for economical and stable operation. In addition, diagnostics and beam control for such a bright and high power beam will also be significant challenges. Given the large number of parameters needing to be pushed beyond current levels, a prototype in which most of these parameters can be demonstrated is essential. Fig. 5.1-1 shows the prototype concept which we are hereby putting forward to make this demonstration.

Accelerator Physics Challenges

In order to achieve the goal of 2 μm normalized emittance or less in the undulators for x-ray production in a robust manner, it will be necessary to achieve 1.5 μm or less out of the injector and less than that from the gun. Thus, space charge emittance compensation (Carlsten 1989) of a high order must be achieved at the low energy end where the beam is most vulnerable and effects of RF focusing, non-inertial space charge and coherent synchrotron radiation emittance dilution (Rosenzweig 1994; Carlsten 1995; Braun, et al. 2000) must be strictly minimized. These are matters under active research in the accelerator community and no completely reliable computer codes for calculating these effects are as yet available. Measuring these effects and benchmarking codes will be an essential feature of the accelerator physics program of the Phase I ERL herein proposed. Wake fields in the cavities and beam lines will also present a challenge to emittance preservation and are also, but to a lesser extent, still research topics in the field to be explored in the Phase I study.

Another topic of great importance, related to the above, is that of halo formation on the beam and how to control and remove it. With such a high power beam, halo and its loss to the walls will be inimical to stable operation and high efficiency of the energy recovery. Prediction and measurement of halos at various positions in the loop will be an important datum in design of a full scale facility.

Accelerator Technology Challenges

The photoinjector source is at the heart of the facility since it determines the maximum achievable flux and brilliance. Various source technologies are being studied for their potential suitability for an ERL aimed ultimately at x-ray production. Initial surveys and calculations (see sections, below) convince us that the DC, laser excited photocathode is the most likely to be successful. Selecting the optimum cathode material and assuring adequate operating life under high current operating conditions present significant challenges that must be surmounted early on. Minimization of dark current while permitting operation at the highest possible cathode voltages will require developments in insulators, corona ring materials and forms and the maintenance of extreme vacuum conditions.

The superconducting capture section of the photoinjector will also require much development. The need to minimize emittance-diluting asymmetries while coupling 500 kW to the beam in a flexible way so that RF focusing and RF bunching can be accomplished without destroying space charge compensation are far more demanding than in any existing system. The Phase I ERL must demonstrate robust operation of this element of the system.

The main linac posited for the Phase II ERL works at levels far beyond existing technology. The economic optimum seems to indicate that 20 MV/m or less is a desirable operating gradient. This gradient has been routinely achieved in pulsed operation and relatively small average beam currents. It must be demonstrated that the needed gradients and Q values can be maintained under the needed CW, high current operating conditions. Further, in order to avoid emittance dilution from beam break up driven by higher order modes in the cavities, one will have to achieve heavier higher mode damping than is now the case in superconducting linear accelerator structures, yet this must be done without compromising the achievable Q and gradient. Not only must the higher modes be more heavily damped but, because of the CW operation and the consequent significant power in these modes, they must be extracted from the low temperature with high efficiency. This demands not only innovations in the off-beam-line HOM couplers but also development of on-line absorbers to catch the HOM power that propagates down the beam line, i.e., absorbers that have the absorbing element operating at a relatively high aperture. Careful measurements, using the prototype, will be needed to assure that these criteria can be met and maintained under operating conditions. Economy of operation in the main linac will also be helped by being able to operate at very high external Q values, thereby minimizing the reserve klystron power needed. The challenge here is the microphonics inevitably present in the system. Development of an active feedback tuning system that can operate under the full dynamic range of beam currents and cavity gradients must therefore be a priority for development with the Phase I ERL as well. The degree of required vibration isolation must also be determined.

An important feature of the ERL is the possibility of providing sub-picosecond bunches to the undulators. Avoiding the severe wake field consequences of such short bunches in the injector and linac requires that the short bunches be obtained at the highest energy by magnetic compression. The accelerator physics and technology of effecting this without undue damage to the beam properties is beyond today's state-of-the-art and will require exploration on the Phase I ERL before one can design the needed system for a full scale facility with confidence.

Measuring the beam properties with the accuracy needed in the face of the enormous flowing beam power will require non-intercepting methods that are robust and easily read out for tuning and feedback control. Optical methods analyzing incoherent and coherent synchrotron radiation picked up at various stations around the loop are promising (Lai 1998; Shintake 1998) but will need demonstrating in this very low normalized emittance context. Likewise, measuring halo in the presence of such high power flow will be difficult. Easily repeated methods for doing so must be developed as tuning and diagnostic tools.

Phase I ERL Parameter Goals

To achieve the above goals it will be necessary to prototype the source and other injector components at full scale, given the uncertainties, the accelerator physics considerations, and the

several technological demands beyond today's state-of-the-art. Demonstration of acceptable energy recovery efficiency requires a full ERL configuration. Beyond that, one must be able to probe the beam break up threshold for the type of cavities planned for the facility and this requires sufficient length of cavity that build up of any instability can be seen. With these considerations in mind we propose a Phase I ERL prototype with full beam power from the injector, 100 mA CW at 5 MeV, to avoid excessive space charge dilution during the bunching process. A 100 MeV energy for the main linac of the Phase I ERL appears adequate for a good evaluation of the BBU, as discussed in sections 3.1.4 and 4.3.5. Demonstration of sub-picosecond bunch lengths also needs to be an important goal of the prototype and magnetic compression and de-compression sections are a feature. As achievement of 20 MV/m gradient and possible periodic restoration of the gradient capability are also essential. A pulsed power processing capability will be a part of the Phase I ERL, as will the instruments needed to verify achievement of the important desiderata and to serve as control elements where required. We estimate that designing and developing of components and operating the Phase I ERL for measurements and demonstrations will be a 4 – 5 year process.

It is worth noting that most of the challenges which would be resolved on the Phase I machine cannot be resolved at existing machines. Thus, for example, no photoinjector exists anywhere which is adequate to investigate the crucial issues of emittance preservation at the requisite emittance and currents. Likewise, the merging sections of the ERL cannot be adequately emulated without first constructing a suitable photoinjector and superconducting linac operating at higher gradients than is now the practice. The stringent HOM couplers and absorbers do not exist and will require extensive use of a superconducting linac, which, itself, has to be custom made. And thus it goes for most of the other parts of the Phase I ERL as well. And, of course, the most important lessons will be learned from the interactions of the various parts of the ERL. In conclusion, adequate exploration of the challenges presented by ERL technology will require the construction of a machine specifically for this purpose.

4.2 Phase I ERL Parameters

In order to address the above issues a prototype (e.g., the Phase I ERL) is required. Its design must accommodate demonstrations and measurements of the needed beam qualities and phenomena of concern. Accordingly we propose to construct a full energy recovery circuit including injector, linac and return transport line together with the beam manipulation and measurement equipment necessary for exploration of all anticipated operating modes of an eventual facility. The proposed injector is essentially that required for a full scale facility to be able to demonstrate the needed current, lifetime and emittance capabilities. The linac is likewise intended to be a short section of the linac structure needed for a full facility, allowing evaluation of all the relevant technologies and long enough to explore instability thresholds and anticipated adiabatic damping of the emittance adequately. A module consisting of 5, 1m sections and capable of producing 100 MeV total has been selected. The reason for selecting 100 MeV is to verify that adequate energy recovery and beam stability are possible with bunches whose energies differ by a large factor. A 100 MeV linac and a 5 MeV injector provide an energy ratio of 20, which was deemed large enough to investigate beam physics issues. The optics of the return transport are modeled after the optics scheme appropriate for the full facility. In the prototype each focusing element is individually powered for full flexibility in the optics as

needed to investigate the important dependencies of emittance and BBU phenomena. The resulting physical object is described in chapter 5 with the planned layout displayed in Fig. 5.1-1

In laying down the appropriate parameters for a prototype aimed at exploring the important accelerator issues it is useful to make reference to the recent energy recovery linac driver for the JLAB IRFEL.

The JLAB IRFEL has demonstrated energy recovered beam recirculation at the highest average current to date, 5 mA (Neil 1998, Neil 2000). This is the first in a series of devices intended ultimately to achieve 1 MW IR beam power. 25 – 100 MW of circulating electron beam power will likely be required thereby necessitating use of SRF technology.

The technology used for the IRFEL builds on that used for the JLAB main high energy accelerator, CEBAF with the additional complexity that the recirculation transport optics must accommodate several percent energy spread in the beam emerging from the IRFEL wiggler. The main beam parameters for the Jefferson Lab IRFEL driver are 40 MeV, 5 mA average current, 67 pC bunch charge and 75 MHz bunch repetition rate with a normalized emittance of 5 – 8 mm-mrad.

Table 4.2-1 provides detailed parameters for the Phase I ERL. Points in common with the IRFEL:

(1) Most importantly, the charge per bunch is very comparable to that in the IRFEL. The higher average current in the Phase I ERL derives from filling every RF bucket in the accelerating wave. Therefore, one would expect that the single bunch collective effects will be similar to those in the IRFEL.
(2) The SRF accelerating frequencies are very comparable.
(3) A single accelerating and single decelerating pass is used on both devices, and a similar low energy electron injection scheme is used in both devices.
(4) The energy and physical size (of several 10s of meters) of the two devices are very similar; the Phase I ERL achieves roughly twice the beam energy of IRFEL, and roughly one-half the energy of the next IRFEL being built at JLAB, the IRFEL upgrade.

Points of departure for the Phase I ERL are:

(1) Significantly enhanced cavity performance. The expected gradients and unloaded Qs are roughly a factor of 2-3 beyond the performance in the IRFEL. This situation is partly the result of improvements in cavity production since the IRFEL was completed.
(2) The higher average current yields a larger excitation of the High Order Modes (HOMs) of the accelerating cavities. This situation has implications both for beam stability against multipass BBU instability and for cooling of the HOMs.
(3) For higher brilliance, the beam emittance must be smaller for ERL than in the IRFEL. This has necessitated a distinctly different design for the ERL injector.
(4) Because there is no IRFEL interaction, the beam energy spread in the Phase I ERL should be smaller than in the IRFEL (IRFEL interaction increases energy spread in the IRFEL by about factor of 5 (Douglas 2000)). The maximum energy spread in the Phase I ERL will be

comparable to that of the IRFEL energy spread when the FEL is turned off (rms 0.2 %) to allow for a bunch compression. Therefore, an adequate momentum acceptance of the transport loop required for the Phase I ERL will be a factor of 4-5 smaller than that of the IRFEL.

(5) In order to push the RF efficiency up, it is advantageous to run the loaded quality factor of the fundamental mode up to around 2.6E7 for the cavities within the energy recovered loop. The RF control problem becomes more difficult as the frequency tuning width of the fundamental mode is reduced.

(6) The injector RF systems will operate on such wide resonances ($Q_{ext} = 10^4$), that it is planned to run all non-recovered injector cavities from a single klystron.

(7) The Phase I ERL beam dump is an order of magnitude larger than that for the IRFEL.

Table 4.2-1. Phase I ERL Parameters

Parameter	**Value**
Main Linac	
Max beam energy [MeV]	100
Max average beam current [mA]	100
Bunch charge [pC]	77
Max bunch rep. Rate [MHz]	1300
Operating frequency [MHz]	1300
Transverse emittance (normalized, rms) [mm-mrad]	≤ 2
Longitudinal emittance, rms [keV deg]	20
Bunch length range, rms [ps, post compression]	0.1 – 1
Bunch length in linac, rms [ps]	3.2
Energy spread rms [fractional]	1E-4 to 4E-3
Beam loss goal [microamp]	<1
Number of cavity units	5
Cavity length [m]	1.04
Number of cells per cavity	9
Number of HOM couplers	4
Operating gradient [MV/m]	20
Power per cavity to fields [kW]	8.0
Q_o [goal]	10^{10}
Q_{ext}	$2.6 \cdot 10^7$
R/Q, fundamental, per cavity unit [ohm]	1036
R/Q, HOM s	See Table 3.1.4-1.
BBU threshold, calculated [mA]	<200>
$k_{\|\|}$ [V/pC] @ 0.7 mm rms bunch length	10.3
HOM power per cavity at 100 mA beam current [W]	162
HOM extraction efficiency goal [%]	95
Linac cryomodule dynamic heat load [W @ 2K]	240.4
Linac cryomodule dynamic heat load [W @ 4K]	10
Linac cryomodule dynamic heat load [W @ 77K]	135
Static heat load of cryomodule [W @ 2K]	29

Static heat load of cryomodule [W @ 4K]	10
Static heat load of cryomodule [W @ 77K]	29
Distribution heat load [W@2K]	2W
Distribution heat load [W@77K]	20W
Refrigerator peak power [W@2K]	500
Refrigerator duty factor for peak power delivery	8 hours continuous/day
Lorentz detuning [$\mathrm{Hz}/(\mathrm{MV}/\mathrm{m})^2$]	1
Microphonic detuning [Hz rms]	25
Number of klystrons	5
Power rating per klystron [kW]	13
Amplitude control [fractional, rms]	$1\cdot 10^{-4}$
Phase control [deg., rms]	0.5
Injector	
Beam Energy [MeV]	5-7
Max average beam current [mA]	100
Bunch charge [pC]	77
Longitudinal emittance, rms [keV deg] (correlated)	40
Bunch length, rms [ps]	2.3 to 3.2
Beam power [kW]	500
Number of accelerating cavity units	5
Number of cells per cavity unit	3
Power per cavity [kW]	100
Number of power couplers per cavity	1
Number of HOM couplers per cavity	2
Voltage per cavity [MV]	1
Amplitude control [fractional]	$5\ 10^{-3}$
Phase control [deg. rms]	0.5
Q_o	$5\cdot 10^{9}$
Q_{ext}	$3\cdot 10^{4}$
Dynamic heat load 5 cavities [W @ 2K]	13.2
Dynamic heat load for all injector cavities [W @ 4K]	18
Dynamic heat load for all five cavities [W @ 77K]	300
Static heat load of injector cryomodule [W @ 2K]	11.4
Static heat load of injector cryomodule [W @ 4K]	2.5
Static heat load of injector cryomodule [W @ 77K]	18
Distribution heat load [W@2K]	2W
Distribution heat load [W@77K]	20W
Alpha x, alpha y	–5, -5
Beta x , beta y [m]	3, 3
Injector beam dump capability [kW]	500
Photocathode Gun	
Voltage [kV]	500

Max average beam current [mA]	100
Bunch charge [pC]	77
Transverse emittance, norm., at cathode, rms [mm-mrad]	0.5
Longitudinal emittance, rms [keV deg]	4
Bunch length, rms [ps]	17
Bunch rep rate at 100 mA [MHz]	1300
Bunch rep rate at reduced beam current [MHz]	Multiples of 260 up to 1300
Beam pulse length range [ms]	2 - ∞
Drive laser power, 780 nm [W]	10
Modulation frequency [MHz]	up to 1300
Cathode spot size, rms [mm]	1-3
Gun beam dump capability [kW]	50
Return Transport System	
Energy range [MeV]	50 – 100
Continuous path length adjustment range [cm]	8
Clear physical aperture, beam chamber [inch]	1.88
Clear physical aperture, magnets [inch]	2.25
Multipole content of magnetic fields (integrated), each multipole*	$<10^{-3}$
Average residual gas pressure at full beam [Torr]	10^{-8}
Residual gas pressure outside cryomodule ends, valves closed [Torr] See "Vacuum Equipment"	10^{-9}
Residual gas pressure in insulation vacuum space, warm [Torr] See "Vacuum Equipment"	10^{-4}
Magnetic strengths and lengths	"Optics Parameter List"
Regulation of magnetic element currents (except steering correctors)	10^{-4}
Regulation of steering corrector currents	10^{-3}
Linac exit beam dump capability [kW] see"RF Beam Dump Scheme"	600
H,V correctors 0.2 m long, [T]	10^{-2} max
Infrastructure	
Electric Substation addition [MVA]	2
Evaporative cooling unit [MW]	2
Demineralized water evaporation rate [kg/s]	.75
LCWS circulation rate @ 20 ° F rise [GPM]	600

* Measured at 2/3 radius of the magnet aperture. In the case of a dipole, measured on a circle of diameter = magnet gap, centered on the central axis of the dipole.

4.3 Phase I ERL Accelerator Physics & Technology Issues and Experiments

4.3.1 Coherent Synchrotron Radiation and Non-inertial Space Charge

When a beam is bent in a dipole magnet, it radiates electromagnetic radiation. At wavelengths longer than the bunch length, the electrons in the bunch radiate coherently, i.e. with a power proportional to the total charge in the bunch squared, as opposed to the linear growth with charge for the incoherent radiation. Because of the fact that the energy loss within the bunch is not uniform for realistic bunch distributions for this coherent synchrotron radiation (CSR), and because the radiation occurs at positions where the transverse dispersion function does not vanish, it is possible for an effective emittance growth to arise in going through a beam bend (reviewed in (Li 2000)).

Similarly, it has been known for a number of years that the space charge interaction from a bending beam can be a source of emittance growth in a bending beam (Talman 1986; Lee 1990; Carlsten 1995). Estimates based on these references indicate that the CSR effect is greater than this effect for the anticipated Phase I ERL parameters. Estimates of the emittance growth due to the effects of CSR are discussed in detail in Section 4.3.8 below. In this section we concentrate on the prototype experiments that should be done to quantify the effect of CSR.

In the Phase I ERL, there are two primary bending regions where CSR might occur: the injector merge and the 180 degree bends. For the injector merge, because there are beam diagnostics already planned for characterizing the injector, there will be a measurement placing an upper limit to the emittance growth generated by the CSR effect in the injector merge. A much more quantitative measurement, which addresses the CSR effect in a more isolated way, is to measure the beam emittance before and after the first 180 degree bend, and measure the dependence of the emittance growth on such parameters as bunch length and beam charge. Likewise, for diagnostic purposes, one will directly observe the long wavelength emission and correlate the intensity and spectrum of this radiation with changes in the beam parameters (Krafft 1995; Krafft 1997; Wang 1997)

Such measurements and correlation studies have been attempted previously (Braun, Chautard, et al. 2000), but with agreement with theory at the factor-of-two level only. Re-examining this problem in the ERL prototype will provide information not only useful to designing the subsequent Phase II machine, but may provide better answers on the CSR emittance growth measurement problem. The reasons are that the starting emittance in the ERL should be much smaller than in the other measurements to date, and because confusing space charge effects will be minimized, thereby making for a cleaner experimental situation.

4.3.2 Ions in the Phase I ERL Injector

Ions generated by beam-gas collisions can become trapped in the negative potential of the beam. The ion density in the beam increases until it is stabilized by neutralization in the beam potential. These trapped ions can cause beam emittance increases, betatron phase shifts, and a broadening of betatron phase distributions, and collective instabilities and lifetime reductions in storage rings. Linear theory is used to estimate:

a) the minimum atomic mass expected to be trapped in the ERL 5 MeV, 100 mA injector,
b) the ionization time for H_2, and
c) the induced change in the focusing of the electrons. If gaps in the bunch train are to be invoked as a clearing mechanism, the gap length is estimated as $2/f_p$, where f_p is the ion plasma frequency.

The condition for trapping in the linear theory is (Baconnier 1985):

$$(A_{trap})_{x,y} \geq \frac{1}{2}\frac{m_e}{m_p}\frac{I}{I_A}\frac{(\Delta L)^2}{\sigma_{x,y}(\sigma_x+\sigma_y)},$$

where A_{trap} is the minimum atomic mass that is trapped, I is the average current, ΔL is the separation between bunches, $\sigma_{x,y}$ the rms beam sizes, m_e and m_p the electron and proton mass respectively and $I_A = (r_e/ec)^{-1} \approx$ 17045 Amperes is the Alfven current.

In the ERL injector with average beam current I=100 mA, bunch separation ΔL=23 cm, σ_x=670 μm and σ_y= 950 μm, the minimum atomic mass that is trapped is $(A_{trap})_x = 7\text{x}10^{-5}$ and $(A_{trap})_y = 5\text{x}10^{-5}$. In a typical vacuum, ions can be found with atomic masses ranging from 1 to 44. Therefore ions, in particular ionized background hydrogen, will be trapped in the prototype injector.

The accumulation of ions continues until the defocusing force due to ion space charge in the drift region is strong enough for the stability limit to be reached. The limiting ion density d_i at the center of the bunch in this equilibrium accumulation limit is given by (Baconnier 1985):

$$d_i = \frac{1}{r_e}\frac{I}{I_A}\frac{1}{2\pi\sigma_x\sigma_y},$$

where r_e is the classical radius of the electron. For the ERL injector parameters, $d_i = 5.24\text{x}10^8$ cm^{-3} .

The time to reach equilibrium is given by the neutralization time:

$$\tau_n = \beta\tau_m,$$

where τ_m is the ionization time (time it takes for one electron to create one ion), given by

$$\tau_m = \frac{1}{d_m(\beta c)\sigma_m},$$

where d_m is the residual molecular density (m^{-3}), σ_m the ionization cross section for molecule m (m^2) and βc is the velocity of the electron beam. The number density of the residual gas molecules, d_m, is related to the gas pressure P and temperature T via the ideal gas law:

$$d_m = \frac{1}{R_g}\frac{P[\text{Torr}]}{T[^\circ\text{K}]} = G\frac{P}{T},$$

where $G=R_g^{-1} = 9.656\text{x}10^{24}$ is the inverse of the ideal gas constant, R_g.

The ionization cross section depends on the molecule of the residual gas and on the velocity of the ionizing particle. A theoretical expression for the ionization cross section has been derived by Bethe and is given by (Baconnier 1994),

$$\sigma_i = 4\pi\left(\frac{\hbar}{m_e c}\right)^2\left\{M^2\left[\frac{1}{\beta_e^2}\ln\left(\frac{\beta_e^2}{1-\beta_e^2}\right)-1\right]+\frac{C}{\beta_e^2}\right\},$$

where

$$4\pi\left(\frac{\hbar}{m_e c}\right)^2 = 1.87\times10^{-24}\ \mathrm{m}^2,$$

and M^2 and C are experimentally determined coefficients. For H_2 , M^2 = 0.5 and C = 8.1, at 5 MeV (γ=9.7847) the ionization cross section for H_2 is $19\text{x}10^{-24}$ m^2. For P=10^{-10} Torr, d_m = $3.3\text{x}10^{12}$ m^{-3} (at 20^o C) and the neutralization time for H_2 is 50.5 sec.

The accumulated ions will introduce extra focusing forces on the electron bunches and they will change the total effective transverse betatron phase advance of the electrons. The phase advance change caused by the accumulated ions in the full-neutralization limit is given by:

$$(\Delta\nu_{x,y})_{\text{ions}} = \frac{r_e}{\gamma}d_i\int_0^{2\pi R} ds\frac{\beta_{x,y}(s)}{\left[1+\frac{\sigma_{x,y}(s)}{\sigma_{y,x}(s)}\right]}\ .$$

A simpler formula, valid for the case of a round beam with $\varepsilon_x = \varepsilon_y$ and $\beta_x = \beta_y$ averaged over the lattice, is:

$$\left(\frac{\Delta\nu}{\nu}\right)_{\text{ions}}^{\text{round beam}} = \frac{I}{I_A}\frac{\beta_x}{2\varepsilon_N}\ .$$

For the ERL injector, assuming an injector length of 3 m and an rms normalized emittance of ε_N=1.5 mm mrad, yields $\Delta\nu/\nu = 5.8$. Requiring that the phase advance change be under 0.1 as the neutralization builds up means that the time between the clearing gaps should be 50 sec/58, or 0.86 sec.

If gaps in the bunch train are used as a clearing mechanism, one can conservatively estimate the needed gap length by setting it equal to $2/f_p$ where f_p is the ion plasma frequency. From the expression,

$$\omega_p^2 = \frac{4\pi e^2 n}{m}\ ,$$

where n is the maximum ion density $d_i = 5.24\text{x}10^8$ cm^{-3}/58, and m is the mass of the ion equal to $2\text{x}1.6661\text{x}10^{-24}$ gr for H_2, one finds that $\omega_p = 2.8\text{x}10^6$ rad/sec or f_p = 0.45 MHz. Therefore, the

gap length should be approximately equal to 4.5 μsec. This beam modulation can only be applied to the photoinjector.

4.3.3 Gun Performance

There are two key electron gun issues to be addressed in the Phase I accelerator. The first is a demonstration that we can achieve the anticipated photocathode operational lifetime in high average current operation at full gun voltage. The second is a demonstration that the beam emittance is as small as indicated by the modeling codes and the calculation of the thermal emittance at the operating wavelength.

Experience at JLAB indicates that the cathode operational lifetime is limited only by ion back bombardment. This implies that a reduction in the vacuum pressure in the cathode-anode gap region would give a corresponding increase in the cathode operational life. This correlation has been observed in the JLAB electron guns, but their average current is significantly below the 100 mA requirement of the ERL. The vacuum pressure in the JLAB guns is close to the measurable limit with present technology. We plan to demonstrate a cathode lifetime at the full 100 mA average current which is as good as presently achieved in the best JLAB electron guns – above 2 x 10^5 coulombs/cm^2 for a 1/e reduction in the cathode quantum efficiency. The gun design will incorporate the very best vacuum practices to achieve the lowest practical base pressure. We will also include measures to reduce the field emission from the cathode electrode and its support structure to a very low level, so that any vacuum pressure rise caused by electron stimulated desorption by the field emitted electrons is negligible at the full gun voltage.

The thermal emittance of the cathode is a calculated number, based on the results measured by Dunham (Dunham 1995). The growth of this emittance under the influence of space charge forces is modeled. We will conduct emittance measurements to verify that the modeling code (Young 2000) correctly predicts this space charge emittance growth, and to verify the Dunham results in the small space charge limit. Emittance measurements at low space charge will be made by observing the electron beam size at three different locations downstream of the gun anode. These measurements will be made in a dedicated beam line setup, prior to connecting the gun to the remainder of the injector. For the full average current emittance measurements, the duty factor of the beam will be reduced to 1.0% or lower by controlling the laser beam incident on the photocathode. We will use the “pepper pot” or multislit method to measure this emittance. We will also verify that the measured emittance does not depend on the duty factor over the range used for these measurements.

We will also measure the dark current from the unilluminated photocathode. This dark current may result from some combination of thermionic and field emission from the cathode. When illuminated, the cathode may produce halo electrons from regions at larger radius than the illuminated spot. If the magnitude of this dark current or the halo is problematic for operation of the full accelerator, we will eliminate it through the use of scrapers.

There are other issues that may be investigated as time and resources permit. These issues are primarily relevant to future ERL applications, rather than the Phase I accelerator. For

example, if a suitable gun high voltage power supply is available, we will explore the emittance with higher gun voltage and/or higher cathode field strength. The effects of cathode cooling on the basic thermal emittance may be investigated, though this might be more easily done with a smaller, dedicated test gun. We may investigate the issue of the optimal cathode electrode shape to provide focusing which would ease the use of multiple beam spots at the photocathode. This latter problem could likely be resolved with a code like MAFIA (MAFIA, v4.00), however.

We emphasize that the primary issues for gun tests with the Phase I accelerator are to establish the cathode operational lifetime at full average current and gun voltage; to verify that the thermal emittance is in agreement with the Dunham experiment; and to benchmark the code describing the space charge related emittance growth.

4.3.4 Injector Performance

The emittance and bunch length are the key beam parameters provided by the full injector. As in the case of the gun tests, measurements of these key properties will be conducted in a dedicated beam line, prior to connection of the injector to the main accelerator. The emittance will be determined either by measuring the beam size at three suitable locations, or by a "pepper pot" or "multislit" method. In these latter types of measurement, a small, emittance dominated beamlet is extracted from the space charge dominated beam for measurement. For high average current emittance measurements, the beam duty factor will be reduced below 1% by modulating the laser beam illuminating the photocathode. We will verify that the measured emittance does not depend on the duty factor over the range used for these measurements. The correct focusing conditions to accomplish optimal emittance compensation will be explored. We plan to illuminate the cathode with a laser beam having a Gaussian transverse profile truncated at $\pm 1\sigma$, and a Gaussian longitudinal profile. We will verify by measurement the improvement that transverse truncation at $\pm 1\sigma$ provides. We will also verify the absence of dark current and/or halo at unacceptable levels.

Methods for measuring emittance and bunch length at full average current are discussed in Section 5.2.5.3.

4.3.5 Linac Transverse Stability

BBU instability in the Phase I ERL

The accuracy of the predicted BBU instability thresholds for a Phase II 5 GeV ERL is contingent upon the trustworthiness of the TDBBU codes. One of the important tasks to be accomplished with the 100 MeV, 100 mA Phase I ERL is exhaustive calibration of the TDBBU simulated results against experimentally obtained instability threshold data. Therefore, it is desirable to design the Phase I ERL with the capability of changing the instability threshold to verify the code's predictions.

Because the linac in the Phase I ERL will consist of only one cryomodule with five 9-cell TESLA cavities, and because the RF focusing at a 5 MeV injection energy is very significant,

no external focusing in the linac is either possible or needed. Instead, the turnaround arc can provide the necessary leverage to manipulate the properties of the pass-to-pass matrix properties in the linac.

Results of TDBBU simulations for experimentally obtained values of Q's of the nine cell TESLA cavities (TELSA 2001) indicate that BBU threshold for Phase I ERL will be in convenient range to enable BBU experiments. By adjusting the betatron phase advance of the recirculating arc, the threshold can be varied from 220 mA to 70 mA.

Multibunch BBU Experiments

A series of beam experiments is proposed for the Phase I ERL in order to

a) Study multipass beam breakup instabilities,
b) Verify the predictions of the numerical code TDBBU (Krafft 1987), and
c) Uncover any trapped modes in the RF cavities.

The tests are extensions of previously performed or proposed experiments (Campisi 1999) and will be considerably more sensitive in the present configuration.

Three experiments are proposed. In the first experiment we will attempt to induce BBU instabilities in the accelerator by lowering the final beam energy, and varying the optics in the recirculation arc.

In the second experiment we plan to measure the beam transfer functions in the recirculating mode. These measurements can be performed at beam currents lower than the threshold current, yet lead to clear if indirect estimates of the instability threshold in the event that the first experiment does not yield a direct observation of the onset of instability. Such measurements require modulation of the current moment $I\Delta x$ (or Δy) at the HOM frequencies or subharmonics. The modulation can be achieved in several different ways. We plan to employ four separate techniques, to achieve independent confirmation of the threshold estimates.

The first method, employs modulation of beam displacement at constant current (Sereno 1994). The basic RF measurements use a broadband RF kicker to excite the beam. The detection of the modulation can either be done with one of the SRF cavities' field probe, or by a dedicated broadband pickup beam position monitor.

The second method consists of injecting RF power at selected HOM frequencies in an unpowered cavity with an external broadband generator and exciting a TE_{111} mode around 1.6-1.7 GHz, as described by Lyneis (Lyneis 1983).

The third method uses beam current modulation at static displacement and the fourth requires tuning of the relevant HOM frequencies of an unpowered cavity to match a resonance condition with the bunch repetition frequency (Fartoukh 1998; Fartoukh 1998b; Fartoukh 1998c).

In the third experiment, we plan to measure the spectrum of the RF power emerging from the linac cavities as a function of charge-per-bunch and bunch length. Such measurements will proceed in parallel with the wakefield studies discussed next.

Effects of Wakefields on Beam Quality

To independently confirm the effect of longitudinal and transverse wakefields on beam quality, we propose to vary the bunch length and charge per bunch and measure the energy spread and emittance growth after the main linac. In addition to obtaining direct experimental evidence on the beam quality degradation due to wakefield effects, we will also be able to benchmark the numerical code (Krafft 1989) we use to calculate the magnitude of these effects.

4.3.6 RF Stability

The purpose of these experiments is to measure the effect of beam loading on the quality of cavity gradient and phase regulation and to verify that RF controls are stable under heavy beam loading (injector) or nearly no beam loading (main linac). Further, direct measurements of the amplitude and frequency content of the microphonic noise present in the system will be conducted. An external Schottky diode with DC-block may be used to measure gradient fluctuations independently of noise generated in the electronics of the control modules (Merminga 1993). The spectra of the gradient fluctuations will be obtained at different beam currents (0, 25, 50, 75, 100 mA) and compared. Furthermore, the integral of the rms gradient error signal will be calculated and the relative rms amplitude error will be extracted. This measurement can then be compared to the required specification for gradient stability.

4.3.7 Higher Order Mode Cooling

HOM Measurements in the ERL

Higher Order Mode frequencies and Q's up to twice the fundamental mode's frequency will be measured in all the injector and linac cavities, after their final installation in the accelerator. The data will be compared with bench measurements and with the results of simulations.

Measurements of HOM power dissipation

Several experiments will be performed in order to

a) Experimentally determine the loss factor of the TESLA cavities;
b) Experimentally study the dependence of the HOM power dissipated on beam parameters; and
c) Identify the fraction of dissipated power that is extracted by a filter to room temperature, the fraction of power that propagates down the beam pipe and the fraction of power that is dissipated in the cavity walls.

The fraction of power that is dissipated in the cavity walls is of greatest concern, because it could potentially impose limitations on the maximum average and peak currents due to finite cryogenic capacity. As shorter bunches excite modes of higher frequency, and the surface

resistance of the superconducting cavities varies quadratically with frequency, according to BCS theory, the quality factor Q of the cavity could deteriorate and the amount of power dissipated in the walls would increase (Merminga 2000a). Therefore, it is of importance for this amount of power to be quantified and its dependence of beam parameters determined.

TESLA cavities have filters to extract the HOM power to a load at room temperature, therefore the total integrated power can be measured with a bolometer, and its spectrum, up to tens of gigahertz, can be measured with a spectrum analyzer at the room temperature output of the HOM filter cable. Furthermore, one might be able to identify the amount of power the beam loses in selected, individual modes by measuring the external Q of the filter for those modes.

Calorimetry may be used to measure temperature rise of the He bath, by measuring the increase in the He-mass flow. However, this method is not very sensitive (sensitivity of a few Watts) and may only be used in extreme circumstances.

To measure the amount of power that propagates down the beam pipe, thermometers will be used in absorbing ceramic materials placed between cavities to dissipate HOM power. One can increase the sensitivity of this measurement by thermally floating the ceramic (no thermal ground) and measuring its temperature rise (diagnostic mode). During operation the ceramic can be thermally anchored to the appropriate temperature, by reconnecting the thermal ground.

All the measurements described above will be repeated at different values of charge per bunch, bunch repetition rate and bunch length. A number of scaling relations should be verified experimentally. These include the high frequency behavior of the longitudinal loss factor and the dependence of power dissipated in the walls.

Increased sensitivity of these measurements may be obtained by enhancing the Q_{ext} of selected modes. There are various ways to achieve this, for example, by modifying the HOM filters, or by directly injecting power in the frequency of the mode (Lyneis 1983). In fact, in the case of TESLA cavities, this can be done in a straightforward way because the HOM filters can be used as the input device as well. Provisions should be made that some of the filters should be equipped with high power rating cables, so they can also be used to inject power into a mode, in addition to extracting power.

4.3.8 Emittance Preservation in the Phase I ERL

As the ERL will depend critically on the emittance of the electron beam out of the photoinjector, it will be essential to numerically model and then experimentally measure the emittance that might be achieved. In this section, initial numerical injector simulations are presented and longitudinal phase space manipulations are discussed. Coherent synchrotron radiation (CSR) effects on the transverse emittance in the ERL prototype are also estimated. The section is lengthy, but understanding emittance preservation is absolutely key to the ERL concept.

In the first part of this section the simulations of particle dynamics performed with PARMELA (Young 2000) are presented. Of course, numerical simulations are always subject to assumptions and limitations. In our case, the simulations of the injector were performed without the envisioned sextupole / linearizer correction of the particle distribution in longitudinal phase space. A final design incorporating these second order corrections will require several iterations.

In the second part of this section simulations of longitudinal dynamics of the whole machine with a simple model are presented. Longitudinal dynamics here is treated separately from transverse dynamics, and corrections to the transverse emittance resulting from the CSR effect in dipole magnets for short bunches are made *a posteriori*. Independent treatment of longitudinal dynamics is well justified for the bunches with the aspect ratio *A* small: $A/\gamma << 1$ (γ is relativistic Lorentz factor; $A = c_r / c_z$ with c_r and c_z being the transverse and longitudinal rms dimensions of the bunch). This is, indeed, the case everywhere in the Phase I ERL with the exception of the gun's photocathode, so the effect of transverse particle dynamics on longitudinal dynamics is generally small. The transverse motion exhibits a more dramatic dependence on longitudinal bunch parameters, in particular, on the bunch length at picosecond lengths. At low energies in the injector, short bunch lengths influence transverse motion (via the "usual space-charge" force -- radial repulsive force acting on a bunch moving along a straight line – which is proportional to $\sim \frac{q/\sigma_z}{\gamma^2 \sigma_r}$, where *q* is a charge per bunch), the CSR microbunch interaction, and CSR energy losses. Although some estimates of transverse emittance dilution due to CSR are presented, a more rigorous treatment of the effect by using particle tracking codes that include radiative processes is desirable, and will be one of the early Phase I tasks.

In principle, resistive-wall wakefields and CSR change the particle distribution in the longitudinal phase space. These effects may become important, especially if one is striving to obtain very small longitudinal emittance (on the order of ten keV-deg), which requires cancellation of correlated longitudinal emittance growth. CSR and wakefields produce correlated changes in the longitudinal phase space particle distribution, or change the "curvature" of phase space distribution, which can be locally removed by using nonlinear momentum compaction, T_{566}, or a third harmonic linearizer. In the simple model used in this work to represent evolution of the longitudinal phase space in the ERL machine only the most important effects are taken into account: 1) RF standing wave curvature; 2) momentum compaction, R_{56}; and 3) nonlinear momentum compaction, T_{566}. CSR and wakefields effects on longitudinal dynamics are ignored.

Units

The quoted normalized transverse rms emittance is in mm-mrad. The longitudinal rms emittance is in keV-deg, where "deg" stands for 1 RF degree. The relations between different units for longitudinal coordinate of a particle are as follows: 1 RF deg = $1/(360\, f_{\rm rf})$ = 2.14 ps = $-(\beta/360)\lambda_{\rm rf}$ = - 0.64β mm with $\beta = v/c$ being the ratio of particle velocity, *v,* and the speed of light, *c*, $\lambda_{\rm rf} = c/f_{\rm rf}$, $f_{\rm rf} = 1.3$ GHz; where a minus sign represents the fact that the front particles have smaller values of the longitudinal coordinate in units of ps or RF deg than the particles at the back of the bunch, as opposed to a longitudinal coordinate in mm.

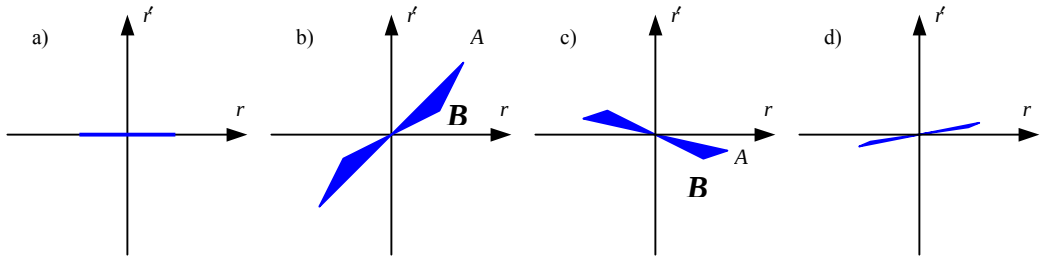

Fig. 4.3.8-1. Transverse phase space plots schematically showing the emittance compensation technique (Carlsten, 1989). a) initial phase space with small emittance at the gun; b) phase space after transport to the solenoid lens, showing the growth of the projected emittance due to the different space charge defocusing force at the bunch center (*A*) and the tails (*B*); c) the phase space distribution has been rotated by an external focusing kick; d) phase space after a drift behind the lens, showing the projected emittance reduction due to the different expansion rates of points *A* and *B*.

Transverse emittance compensation in the injector

The understanding of the emittance compensation technique has evolved from Carlsten's original paper on the subject (Carlsten 1989) to the so-called "invariant envelope" concept of (Serafini 1997). To understand the idea of emittance compensation (Fig. 4.3.8-1) one should notice that the resultant transverse emittance is, in fact, a *projection* of the phase space areas occupied by each slice (of length small compared to the total bunch length) along the bunch. While the emittance of each slice is essentially a constant (determined by thermal emittance from the photocathode), the projection of the phase space area occupied by all such slices can grow significantly because each slice experiences different repulsive space charge forces.

The beam is space charge dominated in the gun, where the projected emittance grows quickly due to different expansion rates of various slices. The growth of a slice is a function of space charge density, which is greater in the center of the bunch than in the tails of the bunch. Most of this emittance growth is correlated and can be removed by introducing a focusing kick with a properly tuned solenoid lens which will, after a drift of proper length, cause different slices of the bunch to line up in the transverse phase space due to space charge forces, resulting in a small projected emittance of the whole bunch. To avoid further dilution of the projected emittance one has to follow the solenoid with an accelerating structure (booster), so that the minimum emittance is reached at a higher energy where the space charge force is sufficiently suppressed.

The best emittance compensation results are achieved when one is able to meet the following conditions:

1) A uniform transverse particle distribution (and consequently a uniform laser light intensity profile on the cathode) yields better result than a non-uniform distribution, for the reason that the radial space charge force in this case exhibits linear dependence with radial coordinate *r*. This condition, leads to a better cancellation of the correlated emittance growth due to the space charge. A truncated Gaussian distribution ($\pm 1\sigma$) was found to be adequate for an effective emittance compensation.
2) It is important for the beam to be fairly laminar in the transverse plane. This implies that

in the transverse plane trajectories do not cross each other. Such crossovers (see Fig. 4.3.8-2a) lead to bifurcations, which result in increased emittance and halo formation.

3) It is desirable that in the longitudinal dimension different slices do not mix with each other (longitudinal crossover, see Fig. 4.3.8-2b). Longitudinal crossovers may happen when a bunch that has a curved longitudinal phase space distribution undergoes magnetic compression. The longitudinal mixing of the slices, if it happens at low energies, can considerably affect transverse motion and hinder emittance compensation.

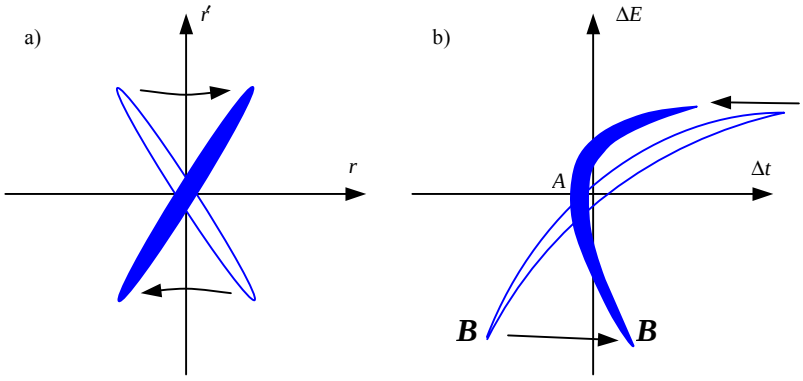

Fig. 4.3.8-2. Transverse and longitudinal crossovers. a) transverse phase space diagram showing crossover being formed when converging particles cross the r' axis while transforming to diverging particles; b) longitudinal phase space diagram showing the mixing of different slices as the bunch with curved longitudinal phase space distribution undergoes compression.

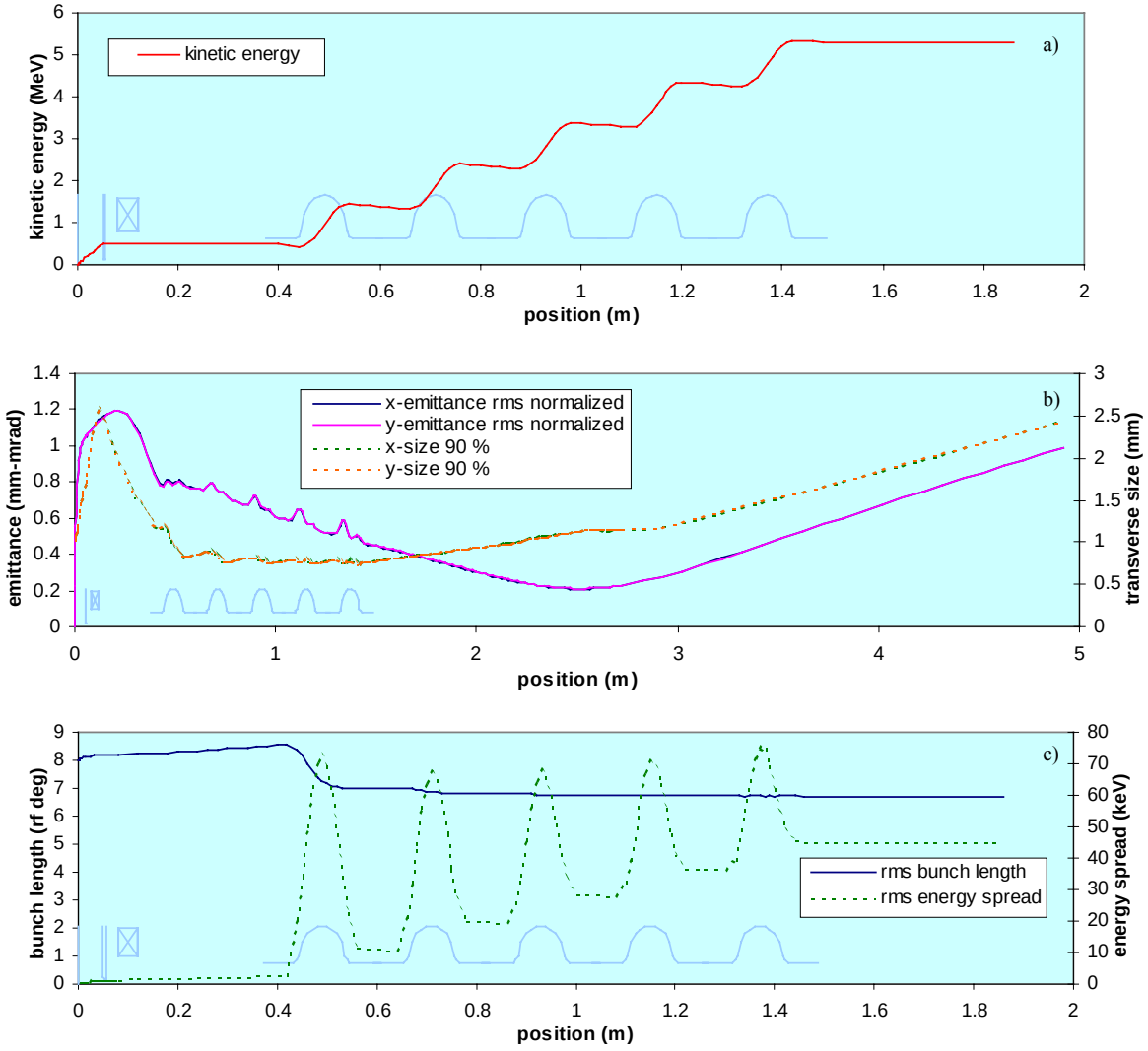

Fig. 4.3.8-3. Various parameters vs. longitudinal position in the injector with 5 one-cell SRF capture cavities. Locations of cathode, anode, solenoid and cavities are shown. a) kinetic energy; b) transverse emittance and bunch size (the envelope includes 90 % of the particles); c) bunch length and energy spread. The ripply line at the bottom shows the RF cavity positions.

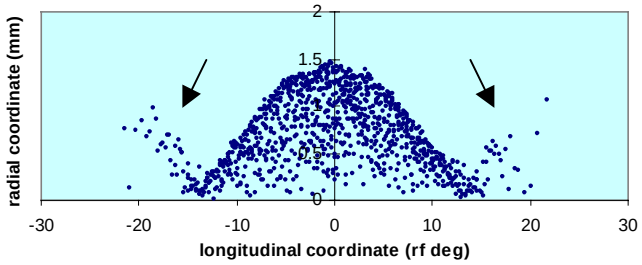

Fig. 4.3.8-4. Formation of the halo at the entrance of the first cavity. The arrows show overfocused particles in the tails of the bunch.

Fig. 4.3.8-3 shows an example of PARMELA simulations for a 5 MeV injector. The laser pulse is assumed to be of Gaussian shape with $\sigma_\phi = 8$ RF deg or $\sigma_t = 17$ ps (σ_ϕ and σ_t stand for bunch length in units of RF deg and time respectively). The transverse profile of laser light intensity on the cathode is a truncated Gaussian ($\pm 1\sigma_r$) with $\sigma_r = 1$ mm. The charge per bunch is 77 pC which corresponds to 100 mA average current at a 1.3 GHz repetition rate. The DC gun provides 500 kV, with the anode being 5 cm away from the cathode, the electric DC field at the photocathode is 10 MV/m. Thermal emittance in these simulations is set to zero (thermal emittance for GaAs photocathodes, assuming a uniform transverse laser light intensity distribution, is given by $\varepsilon_{\text{th}} = \frac{r}{2}\sqrt{\frac{E_{\text{GaAs}}}{mc^2}}$, where r is the spot radius, E_{GaAs} is thermal energy for GaAs: $E_{\text{GaAs}} < 50$ meV (Sinclair 2000), mc^2 is the electron rest energy; for a spot size radius r = 1 mm, the rms thermal emittance is $\varepsilon_{\text{th}} = 0.16$ mm-mrad). In our case the correlation between the thermal and the space charge induced emittances is small (verified by simulations), so the total emittance is given by $\varepsilon = \sqrt{\varepsilon_{\text{s.c.}}^2 + \varepsilon_{\text{th}}^2} \approx \varepsilon_{\text{s.c.}}$ for $\varepsilon_{\text{s.c.}} \geq 2\varepsilon_{\text{th}}$.

As can be seen in Fig. 4.3.8-3, most of the space charge induced emittance growth is removed at about 2.5 m from the photocathode ($\varepsilon_{\text{s.c.}} \approx 0.3$ mm-mrad)[1]. One could argue that by changing the solenoid setting it should be possible to move the minimum in the dependence of emittance vs. position further downstream, to the entrance of the main 100 MeV linac, to circumvent further emittance degradation after the minimum shown in Fig. 4.3.8-3. However, it was found that the high accelerating gradient of one-cell cavities (about 8 MeV/m) precludes one from doing so without the beam being overfocused due to strong RF focusing (Helm 1969), especially from a transverse kick at the entrance of the first cell due to RF fringing fields. The focusing length of this kick (both in vertical and horizontal) can be estimated as $2\gamma/\gamma' \approx 25$ cm, where γ' is accelerating gradient in the cavity divided by electron rest energy. To avoid a transverse crossover, the bunches have to be tightly focused at the entrance of the first cavity so that the repulsive forces due to the space charge partially counteract RF focusing. If the solenoid field is decreased so as to move the minimum in the dependence of emittance vs. position further downstream, the bunch radius at the entrance of the booster is increased, the beam becomes overfocused, and the halo forms. Besides, the halo forms at the tails of the bunch even in the case of Fig. 4.3.8-3 because the tails experience the same amount of external focusing but a weaker space charge repulsive force to counteract its action than the center of the bunch (see Fig. 4.3.8-4). It is possible to reduce the fraction of the particles, which form the halo, by 1) making the longitudinal particle distribution more uniform, 2) applying weaker external focusing to the beam in the injector. The first solution suggests stacking laser pulses to produce a more uniform temporal laser profile at the photocathode, while the second option suggests a lower accelerating gradient in the capture cavities.

[1] In principle, by increasing the energy gain from the booster one can "seal" this small emittance and decrease considerably space charge forces so that the crossovers discussed here become unimportant.

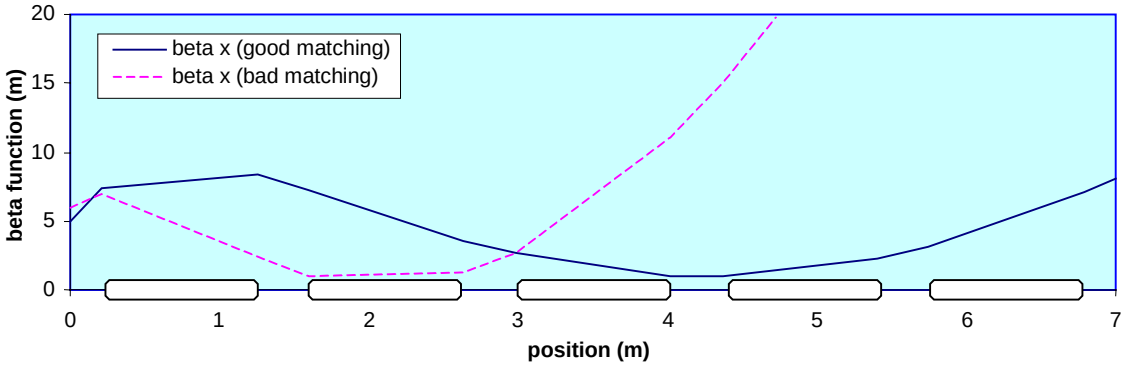

Fig. 4.3.8-5. Betatron functions in the main linac during acceleration. Locations of the SRF cavities are shown. Here, "good matching" corresponds to Twiss parameters from the injector $\beta_x = 5$ m, $\alpha_x = -5.2$, and "bad matching" corresponds to $\beta_x = 6$ m, $\alpha_x = -2$ (the betatron function is about 60 m at the exit of the linac).

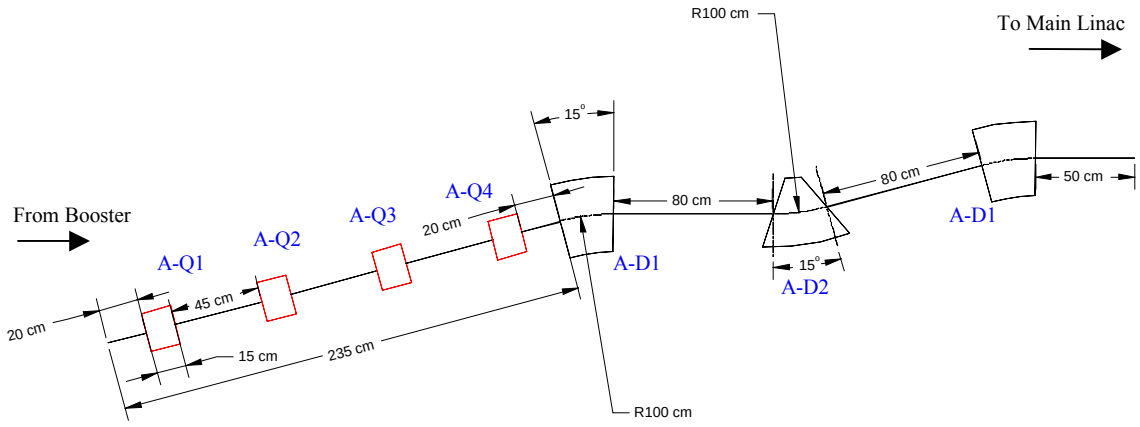

Fig. 4.3.8-6. The section of injector between the booster and the main linac. A-Q1, A-Q2, A-Q3, A-Q4 are quadrupoles, A-D1 is sector magnet, A-D2 is magnet with pole-face rotation (-21° for both planes).

Injector and merger simulations

The injector and merger design has to perform the following functions: transverse emittance compensation, longitudinal phase space manipulations, and matching of betatron functions to the entrance of the main linac. SRF cavities in the main linac operate at a high accelerating gradient (20 MeV/m); therefore, a 5 MeV bunch experiences strong RF focusing in the beginning of the linac. To keep the betatron function small in the linac, it is necessary to introduce quickly diverging bunches with a small beam envelope at the entrance of the main linac (see Fig. 4.3.8-5). It is also possible to run the first cavity in the linac at lower gradient to mitigate RF focusing.

One possible version of the merger is shown in Fig. 4.3.8-6. The section of four quadrupoles provides the matching of the betatron function. Three 15° -dipole magnets serve to introduce the beam to the main linac. The bending section is achromatic. Two outer dipoles are identical sector magnets and the center dipole has a pole-face rotation (-21° for both planes). It is possible to construct an achromat from three identical sector magnets; however, the distance between the magnets would have to be 3.6 m for 15° -dipole magnets, i.e. pole-face rotation introduces additional focusing and allows a more compact bending section.

Space charge forces are not negligible for tightly focused bunches at 5 MeV. Therefore, space charge has to be taken into account in order to determine correctly the required quadrupole strengths for matching of the betatron functions.

The accelerating gradient in the cavity is 2.89 MV/m, which corresponds to an energy gain of 1 MeV per cavity for ultrarelativistic electrons. The cavity geometry and axial electric field profile are shown in Fig. 4.3.8-7.

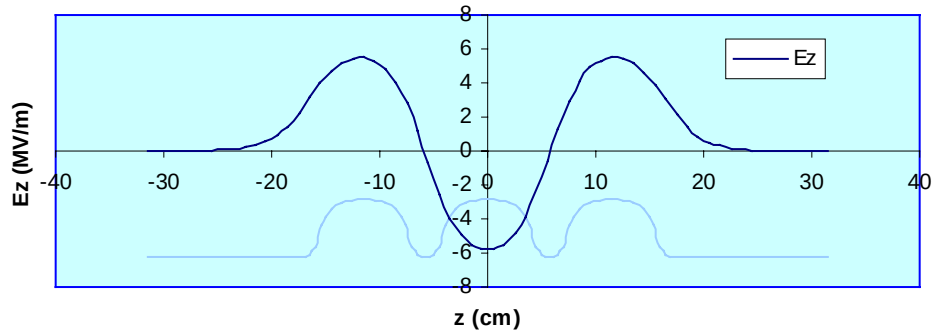

Fig. 4.3.8-7. Axial electric field profile in a 3-cell cavity.

PARMELA simulation results and the injector layout are shown in Fig. 4.3.8-8 and 4.3.8-9, where the charge per bunch is 77 pC. In the case of no compression (Fig. 4.3.8-8) the emittance at the entrance of the main linac is $\varepsilon_x = 0.9$ mm-mrad and $\varepsilon_y = 0.5$ mm-mrad. With bunch compression (Fig. 4.3.8-9) the calculated emittance after the injector is $\varepsilon_x = 2.4$ mm-mrad and $\varepsilon_y = 1.2$ mm-mrad. The longitudinal emittance is 330 keV-deg and 100 keV-deg without and with compression, respectively. The longitudinal phase space distribution after the injector for both cases is shown in Fig. 4.3.8-10. Note the deformation of the phase space distribution due to substantial bunch compression at 5 MeV in Fig. 4.3.8-10b.

It is worthwhile making the following comments about these PARMELA simulations:

1) It was found that point-to-point space-charge calculations in PARMELA do not correctly represent emittance compensation processes for a moderate number of macroparticles (≤

5000). Mesh space-charge calculations in PARMELA seem to represent transverse dynamics more correctly.

2) The SCHEFF subroutine in the version of PARMELA used here assumes that the electron bunch cross-section is nearly circular, which may become a poor approximation in the sections with nonzero dispersion and with realistic β variation. A better routine should include the possibility of calculating space-charge for bunches with elliptical cross-section (Koltenbah 1999). It is indicated in (Koltenbah 1999) that PARMELA with this circular algorithm of the SCHEFF subroutine overestimates the emittance growth due to space-charge in the bend plane by 30-40 %.

3) The optimization of external focusing settings of the simulations presented in Fig. 4.3.8-8 and 4.3.8-9 is by no means exhaustive. The solenoid setting was optimized with fixed values of the laser-irradiated spot size at the cathode, position of the solenoid, position of the booster, etc. According to emittance compensation theory (Serafini 1997), matching the beam into the accelerating structure to "invariant envelope flow" condition assures (normalized) emittance damping in the accelerating structure. One can notice that it is, in fact, the case of Fig. 4.3.8-3b, but not that of Fig. 4.3.8-9b. The condition of such correct matching requires that a beam entering the booster should have initial beam size given by $\sigma_r = (2/\gamma')\sqrt{I/3I_0\gamma}$ with vanishing divergence, where I is the peak bunch current, $I_0 = 17$ kA, and γ' and γ are the normalized booster gradient and energy at the entrance of the booster, respectively.

4) There is no chopping of the bunch tails – such chopping will improve both transverse and longitudinal emittances, since the particles in the tails of the bunch are scattered considerably in the phase space in comparison with the particles in the center of the bunch.

The presented simulation results, although still being far from optimal, indicate that a bunch of desired high quality from the injector should be possible with DC gun. Exploring these computations experimentally will be the first priority for the Phase I ERL project.

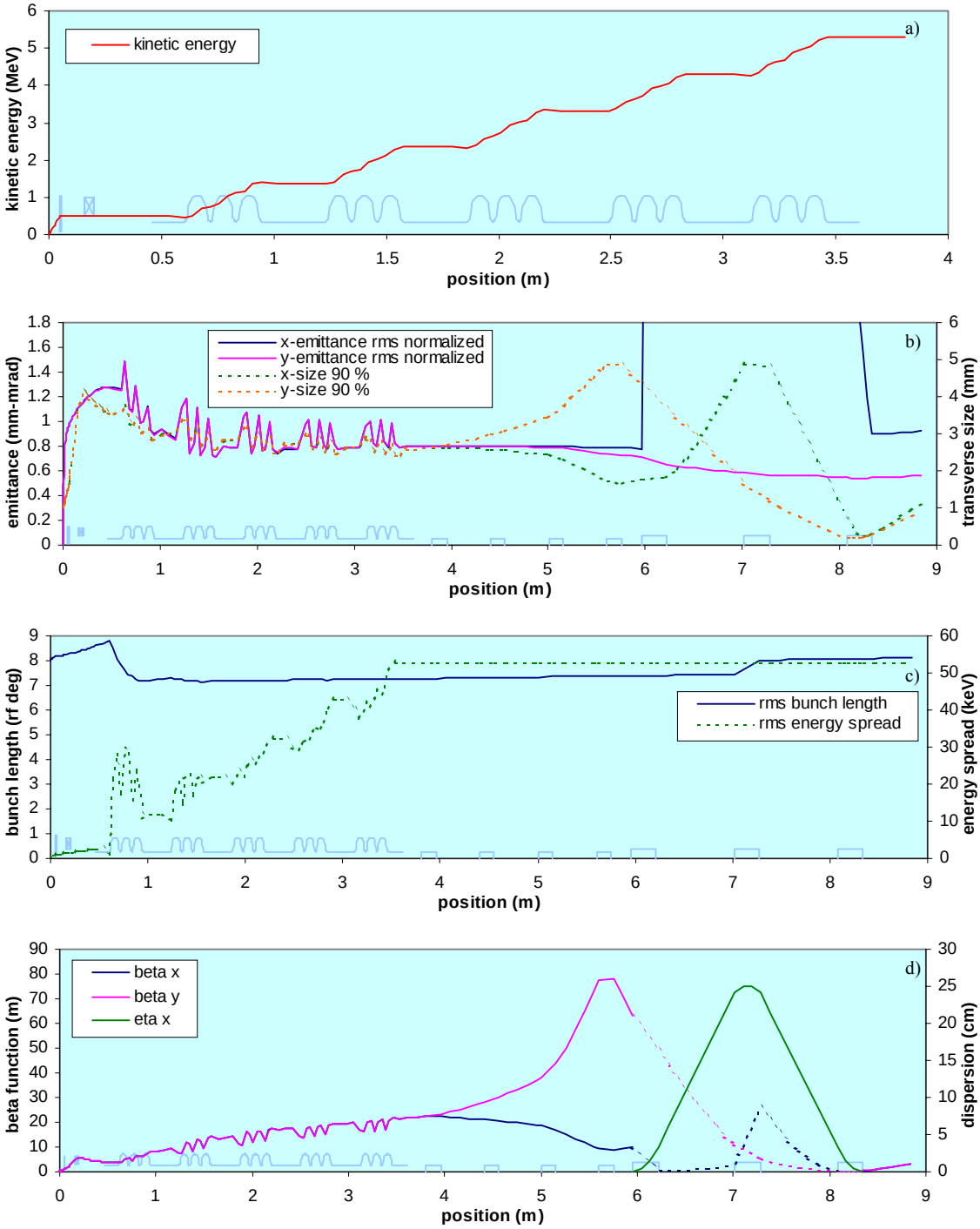

Fig. 4.3.8-8. Various parameters vs. longitudinal position in the injector with 5 three-cell SRF capture cavities (no compression). Locations of cathode, anode, solenoid, cavities, quadrupoles and dipoles are shown. a) kinetic energy; b) transverse emittance and bunch size (the envelope includes 90 % of the particles); c) bunch length and energy spread; d) betatron and dispersion functions (dashed lines show betatron functions in the achromat section).

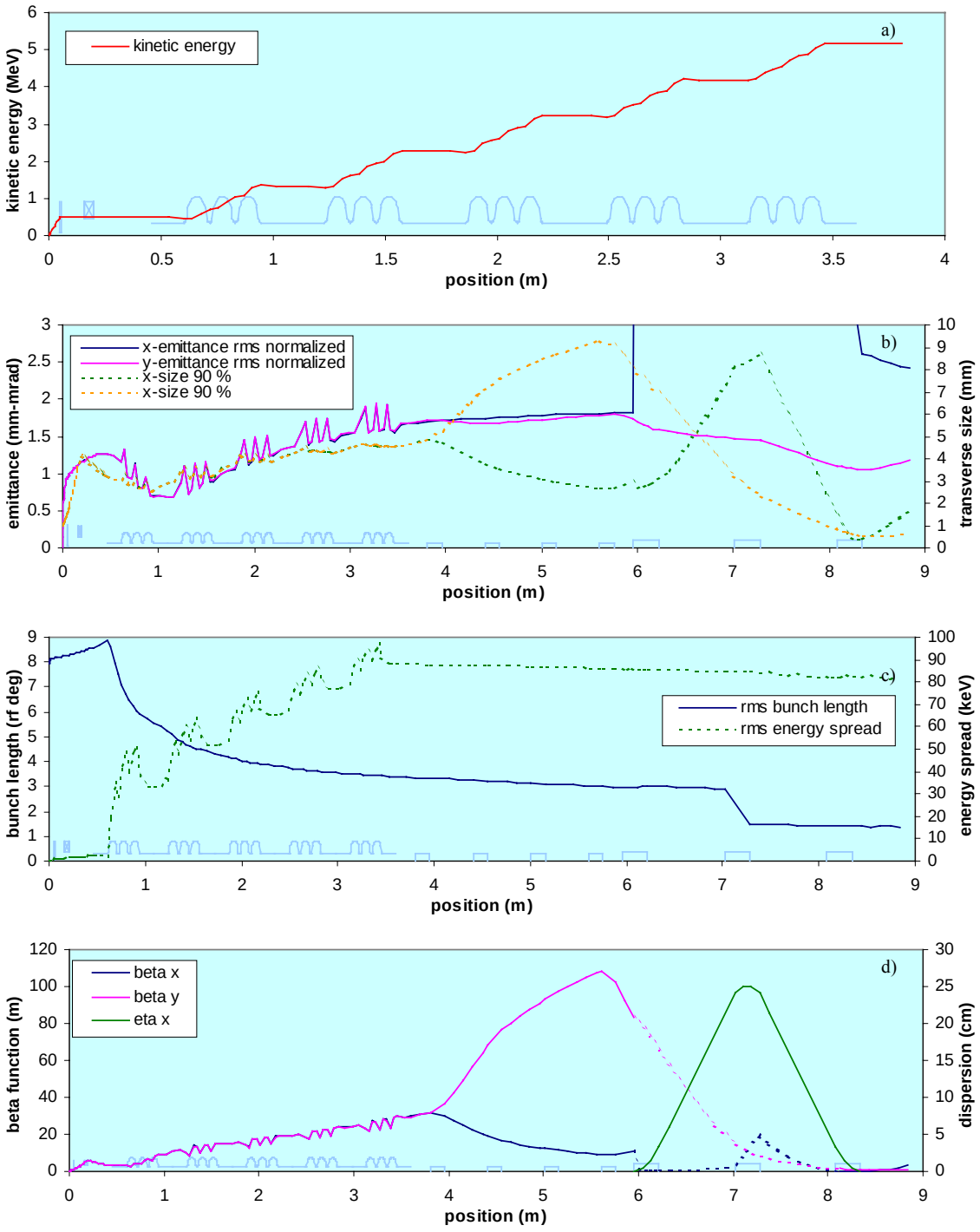

Fig. 4.3.8-9. Various parameters vs. longitudinal position in the injector with 5 three-cell SRF capture cavities (compressed by a factor of 6). Locations of cathode, anode, solenoid, cavities, quadrupoles and dipoles are shown (see Table 4.3.8-2). a) kinetic energy; b) transverse emittance and bunch size (the envelope includes 90 % of the particles); c) bunch length and energy spread; d) betatron and dispersion functions (dashed lines show betatron functions in the achromat section).

Longitudinal phase space manipulations

Achieving small longitudinal emittance presents no lesser challenge than achieving small transverse emittance, especially when both are to be achieved at the same time. The following simple model was adopted to represent longitudinal phase space evolution: The beam from the gun was considered to be essentially monoenergetic (zero longitudinal emittance), so that the resultant longitudinal emittance is completely correlated (i.e. can be removed in principle) and arises from "curvature" of an infinitely thin distribution in the phase space. "Active" elements that change the longitudinal phase space distribution are drift (for nonrelativistic electrons), the accelerating structure, and linear and nonlinear momentum compaction (R_{56}, T_{566}). The SRF cavity is treated as a sequence of finite-length monoenergetic drifts (half the RF wavelength) interleaved with impulsive kicks in energy (Douglas 1999). The energy kicks are intended to simulate the effect on the beam of a single cell of the cavity. The bunch itself is represented by 19 macroparticles, which at the cathode have different phases from $-3\sigma_\phi$ to $+3\sigma_\phi$ with a step of $\sigma_\phi/3$ (here σ_ϕ is the laser pulse rms duration in RF deg) with each having a statistical weight proportional to $\exp\left(-\phi_i^2/2\sigma_\phi^2\right)$, where ϕ_i is the phase of a macroparticle at the cathode (Gaussian distribution). The rms longitudinal emittance, ε_z, is determined as usual:

$$\varepsilon_z = \sqrt{\left\langle \phi^2 \right\rangle \left\langle W^2 \right\rangle - \left\langle \phi W \right\rangle^2}\,, \tag{4.3.8-1}$$

where ϕ and W are macroparticle phase and kinetic energy, and $\langle \ldots \rangle$ represents the average over the ensemble of macroparticles. Each macroparticle is traced individually according to the following transformation rules for longitudinal phase space coordinates ϕ and W:

1) <u>In a drift</u> of length L, coordinates after the drift ϕ_2, W_2 are related to those before the drift ϕ_1, W_1 as

$$\begin{aligned} \phi_2 &= \phi_1 + \frac{L}{v}\omega_{\mathrm{rf}}\,, \\ W_2 &= W_1\,, \end{aligned} \tag{4.3.8-2}$$

where v is the macroparticle velocity, and ω_{rf} is the fundamental angular frequency.

2) <u>In an energy kick</u> from a cell with energy gain amplitude ΔE and phase offset $\Delta\phi$

$$\begin{aligned} \phi_2 &= \phi_1\,, \\ W_2 &= W_1 + \Delta E \cos(\phi_1 - \bar{\phi} + \Delta\phi)\,, \end{aligned} \tag{4.3.8-3}$$

where $\bar{\phi}$ is the phase of central macroparticle.

3) In a bending system with path length L for the central macroparticle and nonzero values of R_{56} and T_{566}, the transform is given by

$$\phi_2 = \phi_1 + \frac{\omega_{\mathrm{rf}}}{v}\left(L + R_{56}\delta + T_{566}\delta^2\right),$$
$$W_2 = W_1, \tag{4.3.8-4}$$

where $\delta = (p - \bar{p})/\bar{p}$ is the momentum deviation of the trajectory from that of the central trajectory.

All other processes that may influence longitudinal dynamics are presumed to be small and are neglected (space charge, CSR, wakefields). It appears from PARMELA simulations that space charge becomes significant in longitudinal dynamics for shorter bunches ($\sigma_\phi \leq 2$ RF deg) in a 5 MeV merger (cf. Fig. 4.3.8-10 b). However, this simple model will be used here to illustrate longitudinal beam dynamics in the machine. Quantitative agreement of this simple model with PARMELA simulations is within a factor of 1-2 for the injector (the model overestimates longitudinal emittance), which is primarily due to a crude representation of the first three-cell cavity with only 3 kicks while the beam is not yet ultrarelativistic.

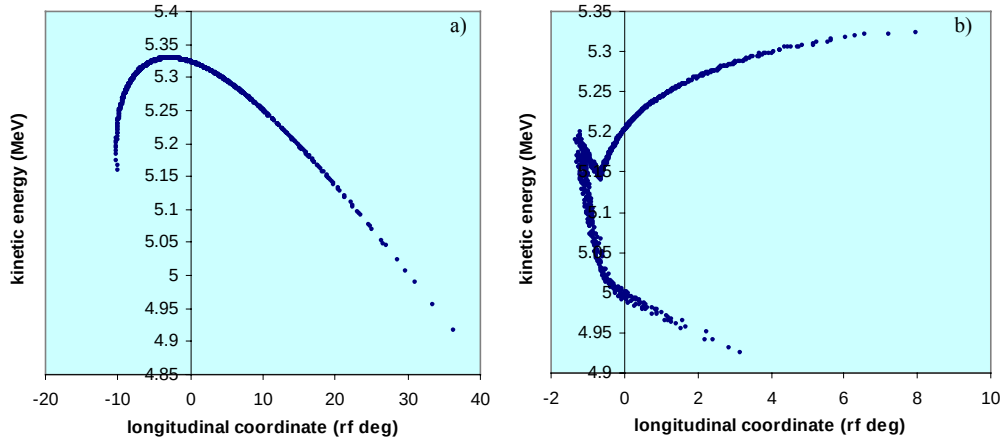

Fig. 4.3.8-10. Longitudinal phase space distribution after the injector. a) no compression (see Fig. 4.3.8-8), rms longitudinal emittance is 331 keV-deg; b) compression to 1.4 RF deg rms bunch length (see Fig. 4.3.8-9), rms longitudinal emittance is 98 keV-deg. (Note horiz. scale change.)

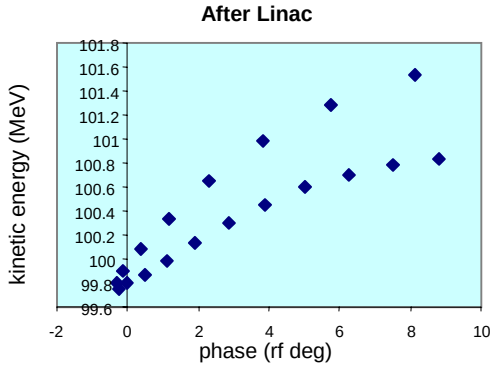

Fig. 4.3.8-11. Example of longitudinal phase space after the main linac. The linac is run -10º off-crest. Estimated emittance based on PARMELA results is 120 keV-deg.

RF-induced curvature in the longitudinal phase space

When a monoenergetic beam goes through a linac, longitudinal phase space adopts a cosine-like shape according to (4.3.8-3), and the longitudinal emittance ε_z is no longer zero. It is straightforward to calculate emittance growth due to the RF curvature for an ultrarelativistic bunch with Gaussian longitudinal distribution after a linac run off-crest with phase offset $\Delta\phi$:

$$\Delta\varepsilon_{z,\mathrm{rf}} = \frac{\Delta E}{\sqrt{2}}\sigma_\phi\sqrt{1-e^{-\sigma_\phi^2}[1+\sigma_\phi^2-(\cos 2\Delta\phi)(e^{-\sigma_\phi^2}-1+\sigma_\phi^2)]}\,, \qquad (4.3.8\text{-}5)$$

where σ_ϕ is the bunch length in rad, ΔE is energy gain from the linac when run on crest. For $\Delta\phi = 0$ (on crest operation) and $\sigma_\phi << 1$, the expression becomes

$$\Delta\varepsilon_{z,\mathrm{rf}} \cong \frac{\Delta E}{\sqrt{2}}\sigma_\phi^3\,, \qquad (4.3.8\text{-}6)$$

or in more practical units

$$\Delta\varepsilon_{z,\mathrm{rf}}\,[\mathrm{keV\ deg}] = 0.2154\cdot\Delta E[\mathrm{MeV}]\sigma_\phi[\mathrm{deg}]^3\,.$$

For example, the emittance growth due to RF-induced curvature for a bunch with 1.4 RF deg rms length (the case of Fig. 4.3.8-9) will be 59 keV-deg. The phase space distribution after the injector has C-shape, while the main linac tends to introduces "the top of cosine"-shape. In this case the resultant emittance can be found by adding injector emittance (100 keV-deg) and RF-induced emittance from the main linac (59 keV-deg) in quadrature, i.e. 116 keV-deg. The longitudinal phase space distribution will assume the form depicted in Fig. 4.3.8-11 (space charge effects seen on Fig. 4.3.8-10 b are not shown).

Correction of longitudinal phase space

Since longitudinal emittance is proportional to the bunch length it is beneficial to have as short bunches in the linac as possible. The lower limit on the bunch length appears to be 1-1.5 RF deg for a 10 MeV injector and 1.5-2 RF deg for a 5 MeV injector. The reasons for these limitations are the space charge and the shortest allowable bunch in the linac, given the higher order modes excitation problem. Thus, the emittance increase due to RF-induced curvature is about 70 – 170 keV-deg in the Phase I ERL and 1100 – 3600 keV-deg in the Phase II 5 GeV machine. It is possible to remove most of this emittance growth by 1) nonlinear momentum compaction T_{566} (sextupole correction), or 2) an RF structure that operates on the third harmonic frequency – 3.9 GHz (linearizer). Calculations made with the simple model and possible scenarios of longitudinal phase space manipulations are presented next.

Sextupole correction

If the curvature of the longitudinal phase space distribution was not removed after the booster and the bunch was consequently compressed in the injector, the phase space will look similar to that of Fig. 4.3.8-11 and sextupole correction in the recirculating arc of the prototype will not remove most of the emittance growth. This implies that sextupole correction has to be introduced in the injector (at least for the Phase I machine; in the Phase II machine most of longitudinal emittance growth will be from the main linac and not the injector). Also, by looking at (4.3.8-4) one notices that the T_{566} correction requires energy-position correlation in the bunch, i.e., off-crest running (which is also required for further bunch compression in the recirculating arc). Such off-crest running produces a rms energy spread ($\sigma_\phi[\text{rad}] << 1$) of

$$\sigma_{E,\text{rf}} = \frac{\Delta E}{\sqrt{2}}\sigma_\phi\sqrt{(1-\cos 2\Delta\phi(1-\sigma_\phi^2)}\,. \qquad (4.3.8\text{-}7)$$

The larger the phase offset $\Delta\phi$ in the accelerating structure, the smaller the value of T_{566} which will be needed to correct longitudinal phase space distribution, but the greater the energy spread, $\sigma_{E,\text{rf}}$, will be. In practical units for small angles $\Delta\phi\,[\text{rad}] << 1$, the energy spread can be written as

$$\sigma_{E,\text{rf}}\,[\text{keV}] = 0.2154\cdot\Delta E[\text{MeV}]\sigma_\phi[\text{deg}]\sqrt{\sigma_\phi[\text{deg}]^2 + 2\Delta\phi[\text{deg}]^2}\,.$$

Thus, for the Phase I machine ($\sigma_\phi = 1.5$ RF deg), the smallest rms energy spread from the main linac, which corresponds to its operation on crest (no longitudinal phase space correction), is 50 keV; if the linac is run 7° off-crest energy, the spread becomes 320 keV. For the Phase II 5 GeV machine, the smallest rms energy spread ($\sigma_\phi = 1$ RF deg in the linac) is 1.1 MeV for an on-crest operation, and 15.2 MeV for a 10° phase offset.

100 MeV Phase I Machine. Fig. 4.3.8-12 depicts a possible scenario of longitudinal phase space evolution for the prototype obtained with the simple model outlined earlier. Here, the T_{566} correction is sufficient when applied only in the merger. Because of this fact, operating the main linac off-crest does not significantly change the longitudinal emittance. The longitudinal emittance after the main linac is estimated to be 20 keV-deg. The required values of R_{56} and T_{566} in the injector for the length of merger corresponding to the design of Figure 4.3.8-6 are 3.5 cm and 64.7 cm, resp. The needed value of R_{56} will be produced through adequate control of the dispersion function in the bends, or, alternatively, by adjusting the path length in the merger. T_{566} may be introduced by either sextupoles or by pole-face shaping of the dipole magnets. The particular final design issues require further studies.

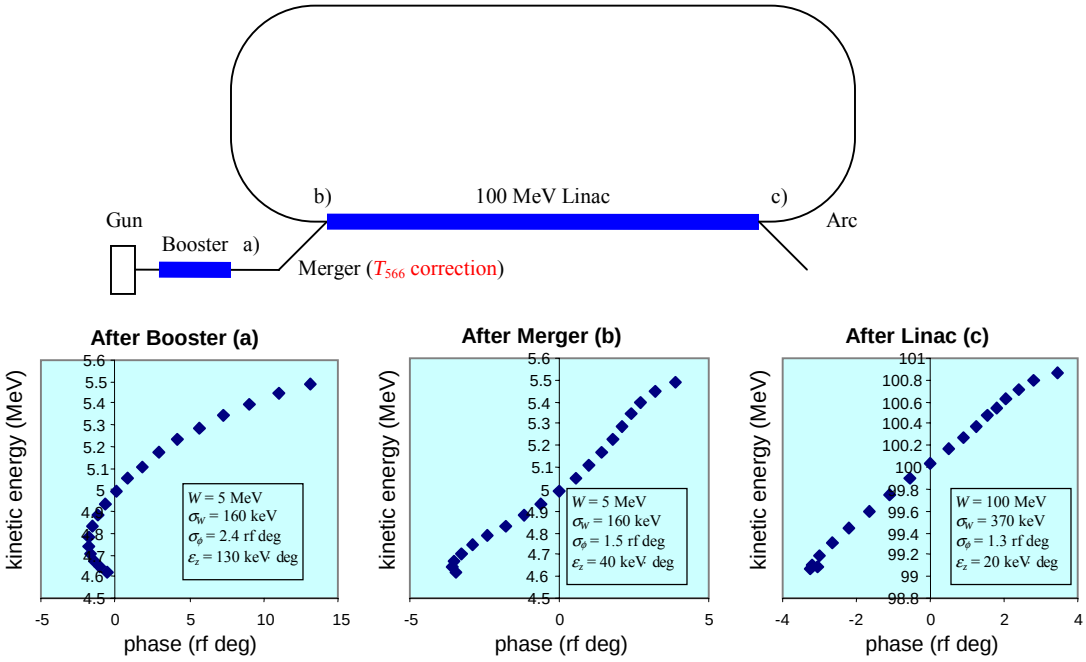

Fig. 4.3.8-12. Possible longitudinal phase space evolution in the prototype with T_{566} correction in the injector. The booster is run -28° off-crest, the main linac is run -5° off-crest. In the merger L = 5.2 m, R_{56} = 3.5 cm, T_{566} = -64.7 cm. Average bunch kinetic energy W, energy rms spread σ_W, bunch rms length σ_ϕ and emittance ε_z values are given.

CSR in thePhase I ERL

Incoherent synchrotron radiation in the Phase I ERL is very small and does not effect particle dynamics in the machine. CSR, on the other hand, is independent of beam energy and its effect on the machine performance has to be studied. The CSR energy loss, U_d, per electron in a dipole magnet of length, L_d, and bending radius, ρ, the energy spread, ΔU_d, due to the tail-head radiative microbunch interaction for a bunch with a Gaussian temporal distribution are estimated using the following formulae (Nodvick 1954; Derbenev 1995):

$$U_d\,[\mathrm{eV}] = 198\frac{q[\mathrm{pC}]}{\sigma_z[\mathrm{mm}]^{4/3}}\rho[\mathrm{m}]^{1/3}\frac{\theta_\mathrm{d}[\mathrm{deg}]}{360^\circ}, \qquad (4.3.8\text{-}10)$$

$$\Delta U_d\,[\mathrm{eV}] = 19.8\frac{q[\mathrm{pC}]}{\sigma_z[\mathrm{mm}]^{4/3}\rho[m]^{2/3}}L_\mathrm{d}[\mathrm{m}],$$

where q is the charge per bunch, and θ_d is the dipole bending angle. The total CSR power loss is given by $P_\mathrm{CSR}\,[\mathrm{W}] = U_\mathrm{d}[\mathrm{eV}]\cdot I[\mathrm{A}]$. The formulae are correct in the absence of beampipe shielding:

$$\sigma_z << a\sqrt{a/\rho}\,,$$

Where a is the beampipe aperture. The beampipe shielding coefficient can be crudely estimated by the following formula

$$k_\mathrm{shielding} = \left(\frac{\alpha}{\sqrt{3}}\right)^{1/3}\frac{a}{2R\alpha}, \qquad (4.3.8\text{-}11)$$

which was obtained by Schwinger for two parallel infinite conducting metal sheets separated by distance a (Nodvick 1954). The formula for the CSR-induced energy spread also assumes "thin" bunches and that the dipole length, L_d, is greater than a so-called "overtaking length" L_o:

$$\sigma_z >> \sigma_r\sqrt{\sigma_r/\rho}\,, \qquad (4.3.8\text{-}12)$$

$$L_\mathrm{d} \geq L_\mathrm{o}\,,$$

where the "overtaking length" is given by $L_\mathrm{o} \sim \left(24\sigma_z\rho^2\right)^{1/3}$. If $L_\mathrm{d} < L_\mathrm{o}$, then the energy spread is lower than that of expression (4.3.8-10) by the additional factor of $\left(L_\mathrm{d}/L_\mathrm{o}\right)^2$ (see (Carlsten 1995; Derbenev 1995) for details).

To correctly estimate the effect of CSR on transverse emittance one has to calculate the variance of transverse coordinate Δx and divergence $\Delta x'$ according to (Emma 1997) :

$$\left\langle \Delta x^2 \right\rangle_\mathrm{CSR} = \left(\int R_{16}(s)\frac{d\sigma_\delta}{ds}ds\right)^2,\ \left\langle \Delta x'^2 \right\rangle_\mathrm{CSR} = \left(\int R_{26}(s)\frac{d\sigma_\delta}{ds}ds\right)^2$$

where the $R_{16}(s)$ and $R_{26}(s)$ transfer matrix elements are from the point of energy loss to the end of the bending system, and $d\sigma_\delta$ is the energy spread increment due to CSR at a given location in the bending system. Deferring this kind of calculation to the actual design activities of the Phase I machine, here we estimate the CSR emittance using the conservative formulae of

(Carlsten 1995; Derbenev 1995), despite the arguments made in (Emma 1997) that such treatment may overestimate the CSR-induced emittance in the bending system. The direct transverse effects of the microbunch radiative interaction (Derbenev 1996) are found to be small in the prototype and are neglected here. Table 4.3.8-3 shows rough estimates of the CSR-induced transverse emittance growth.

It can be seen that for $a = 2$ cm, $\rho = 1$ m there is no effective suppression of CSR due to beampipe shielding for bunches with $\sigma_z \le 0.8$ mm. For the bunch length $\sigma_z = 0.7$ mm, we find that the energy loss by one electron per recirculation would be 31 keV or 3.1 kW of radiation power. The numbers for a 1.5 RF deg rms bunch is 20 keV and 2 kW, respectively. Table 4.3.8-4 summarizes CSR power losses in the Phase I ERL. Please note that these estimates assume that the condition (4.3.8-12) of "thin" bunches is met. In reality, this condition may be easily broken in the Phase I ERL dipoles, where the dispersion function has large values and the bunch has large horizontal size because of energy spread (Shibata 1994; Douglas 2000a; Douglas 2000b). In this case the results of Tables 4.3.8-1 and 4.3.8-2 may significantly overestimate the effect of CSR on transverse emittance and energy loss. Quantitative measurement of these effects and their functional dependences will be a major priority of the Phase I ERL study.

Table 4.3.8-1. Estimates of CSR emittance growth in different parts of the Phase I ERL, assuming no beampipe shielding and "thin" bunch (4.3.8-12).

Machine Part	W (MeV)	θ_d (deg)	ρ (m)	σ_z (mm)		$\Delta\varepsilon_{x,n}$ (mm-mrad)	
Merger	5	15	1	0.96	0.7	0.4	0.6
Arc TBA	100	60	1	0.96	0.7	1.4	2.1
Chicane	100	20.5	1	0.03		16	

Table 4.3.8-2. CSR power in different parts of the prototype, assuming no beampipe shielding and "thin" bunch (4.3.8-12).

Machine Part	W (MeV)	σ_z (mm)		P_{CSR} (kW)	
Merger	5	0.96	0.7	0.1	0.2
Arc TBAs	100	0.96	0.7	1.6	2.4
Chicanes	100	$0.96 \rightarrow 0.03$		2×14	

4.4 Section 4 References

Baconnier, Y. (1985). "Neutralization of Accelerator beams by ionization of the residual gas". Proceedings of CERN Accelerator School, CERN 85-19.

Baconnier, Y., Poncet, A. and Tavares, P.F. (1994). "Neutralization of Accelerator Beams by Ionization of the Residual Gas (CERN 94-01)". Proceedings of CERN Accelerator School, CERN, Geneva **Vol 2**.

Braun, H., F. Chautard, R. Corsini, T. O. Raubenheimer and P. Tenenbaum (2000). "Emittance growth during bunch compression in the CTF-II.", Phys. Rev. Lett. **84**: 658-661.

Campisi, I. E., Douglas, D., Hovater, C., Krafft, G.A., Merminga, L., Yunn, B.C. (1999). "Beam Current Limitations in the Jefferson Lab FEL: Simulations and Analysis of Proposed Beam Breakup Experiments". Proceedings of 1999 PAC, New York, March: 1177.

Carlsten, B. E. (1989). "New photoelectric injector design for the Los Alamos National Laboratory XUV FEL accelerator.", Nuc. Instr. Meth. Phys. Res. A **285**: 313-319.

Carlsten, B. E., and Raubenheimer, T.O. (1995). "Emittance growth of bunched beams in bends.", Phys. Rev. E **51**: 1453.

Derbenev, Y. S., and Shiltsev, V.D. (1996), "Transverse effects of microbunch radiative interaction", May 1996, Fermi Lab, FERMILAB-TM-1974, SLAC-Pub 7181.

Derbenev, Y. S., Rossbach, J., Saldin, E.L. and Shiltsev, V.D. (1995), "Microbunch radiative tail-head interaction", September, DESY, Hamburg, Germany, TESLA-FEL 95-05.

Douglas, D. (1999), "Modeling of longitudinal phase space dynamics in energy-recovering ERL drivers", Thomas Jefferson Nat. Accel. Facility, Newport News, VA, JLAB-TN-99-002.

Douglas, D. (2000a), "Injector linac optics for a high current srf driven electron accelerator", February 2000, Thomas Jefferson Nat. Accel. Facility, Newport News, VA, JLAB-TN-00-005.

Douglas, D. (2000b), "Preliminary estimate of CSR effects in the IR upgrade FEL driver", 29 Aug 2000, Thomas Jefferson National Acclelerator Facility, Newport News, VA, JLAB-TN-00-017.

Dunham, B. M., Cardman, L.S. and Sinclair, C.K. (1995). "Emittance measurements for Illinois/CEBAF polarized electron source". Particle Accelerator Conference, Dallas, IEEE, New York: 1030-1032.

Emma, P., and Brinkmann, R. (1997), "Emittance dilution through coherent energy spread generation in bending systems", May 1997, SLAC, Stanford, CA, SLAC-PUB-7554.

Fartoukh, S. (1998), "A New Method to Detect the High Impedance Dipole Modes of TESLA Cavities", Saclay, France, CEA/DAPNLA/SEA-98-18, Saclay.

Fartoukh, S. (1998b), "RF Steering Experiments on TTF", Saclay, France, CEA/DAPNIA/SEA-98-02.

Fartoukh, S. (1998c), "Multibunch Experiments on TTF", Saclay, France, CEA/DAPNIA/SEA-98-02.

Helm, R. H., Miller, R. (1969). "Particle Dynamics". Linear Accelerators, North-Holland, Amsterdam.

Koltenbah, B. E. C., and Parazzoli, C.G. (1999). "Space charge calculations of elliptical cross-section electron pulses in PARMELA.", Nuc. Instr. Meth. Phys. Res. A **429**: 281-286.

Krafft, G. A. (1997). "Diagnostics for Ultra-short Bunches". Proc. 3rd European Workshop on Beam Instrumentation: 48.

Krafft, G. A., and Bisognano, J.J. (1989). "On Using a Superconducting Linac to Drive a Short

Wavelength FEL". Proceedings of the 1989 PAC, Chicago, March: 1256.
Krafft, G. A., Bisognano, J.J. (1987). "Two Dimensional Simulations of Multipass Beam Breakup". Proceedings of 1987 PAC: 1356.
Krafft, G. A., et al. (1995). "Coherent Synchrotron Radiation Detector for Non-invasive Subpicosecond Bunch Length Monitor". Proceedings of 1995 Particle Accelerator Conference: 2601.
Lai, R., Schneider, G. and Sievers, A.J. (1998). Measuring longitudinal distribution of electron bunches with coherent synchrotron radiation. Handbook of Accelerator Physics and Engineering. A. W. Chao, and Tigner, M. (World Scientific, NJ. pp. 557-559).
Lee, E. P. (1990). Particle Accelerators **25**: 241.
Li, R. (2000). "Progress on the Study of CSR Effects". Proc. of 2nd ICFA Advanced Accelerator Workshop: 369.
Lyneis, C. M., Rand, R.E., Schwettman, H.A. and Vetter, A.M. (1983). "Standing Wave Model of Regenerative Beam Breakup in Recirculating Electron Accelerators.", Nuc. Instr. Meth. Phys. Res. A **204**: 269-284.
MAFIA (v 4.00) MAFIA User's Guide Version 4.00, 4.00. (CST GmbH, Darmstadt, Germany).
Merminga, L., Bisognano, J.J., Hovater, C., Krafft, G.A., Simrock, S.N. and Kubo, K. (1993). "Operation of the CEBAF Linac with High Beam Loading". Proceedings of 1993 PAC, Washington, D.C.: 3515.
Merminga, L., Krafft, G.A., Leemann, C.W., Sundelin, R.M., Yunn, B.C. and Bisognano, J.J. (2000a). "Specifying HOM-Power Extraction Efficiency in a High Average Current, Short Bunch Length SRF Environment". Proceedings of the 2000 Linac Conference, Monterey, August: 13.
Nodvick, J., and Saxon, D. (1954). "Suppression of coherent radiation by electrons in a synchrotron.", Phys. Rev. **96**(180-184)
Rosenzweig, J., Serafini, L. (1994). "Transvers particle motion in radio-frequence linear accelerators.", Phys. Rev. E **49**: 1599-1602.
Serafini, L., and Rosenzweig, J.B. (1997). "Envelope analysis of intense relativistic quasilaminar beams in RF photoinjectors: a theory of emittance compensation.", Phys. Rev. E **55**: 7565-7590.
Sereno, N. (1994), Experimental studies of multipass beam break-up and energy recovery using the CEBAF injector linac, (Ph.D. Thesis, University of Illinois at Urbana-Champaign, Urbana-Champaign).
Shibata, Y., Ishi, K., Takahashi, T., Kanai, T., Arai, F.,Kimura, S., Ohsaka, T., Ikezawa, M., Kondo, Y., Kato, R., Urasawa, S., Nakazato, T., Niwano, S., Yoshioka, M., and Oyamada, M. (1994). "Coherent transition radiation in the far-infrared region.", Phys. Rev. E **49**: 785.
Shintake, T. (1998). Laser Interference Methods. Handbook of Accelerator Physics and Engineering. A. W. a. T. Chao, M. (World Scientific, NJ. pp. 557-559).
Sinclair, C. K. (2000). Personal Communication.
Talman, R. (1986). "Novel Relativistic Effect Important in Accelerators.", Phys. Rev. Lett. **56**: 1429-1432.
TELSA (2001), "Technical Design Report", March, 2001, DESY, Hamburg, Germany, DESY 2001-011, http://tesla.desy.de/new_pages/TDR_CD/start.html.
Wang, D. X., Krafft, G.A, Price, E., Wood, P.A.D., Porterfield, D.W. and Croew, T.W. (1997). "A noninvasive bunch length monitor for femtosecond electron bunches.", Appl. Phys.

Lett. **70**: 529-531.
Young, L. M. (2000) PARMELA, Revised Jan 2000, (Los Alamos Natl. Lab., LA-UR-96-1835, Los Alamos, NM).

5 Technical Description of the Phase I ERL

5.1 Overall Machine Layout

An overall layout of the Phase I ERL is shown in Figure 5.1-1. A more detailed drawing is available at http://www.lns.cornell.edu/~draft/colleague-access.html. Technical discussion of the various subsystems and components of the machine are described in the next sections, below.

The layout is based on a minimal arrangement necessary to accomplish the experimental investigations intended for the Phase I ERL, as described in Section 4. It consists of a photoinjection stage which inserts bunches into the main linac at a slight angle. The remainder of the machine is designed with flexible optics for the study of emittance preservation, coherent synchrotron radiation effects, magnetic compression to very short bunches, etc. Overall considerations were that the legs of the loop must be long enough to accommodate the merging in and out of the injected and spent beams and the matching optical elements that go with this function. The joining legs needed to be long enough for the Triple Bend Achromat (TBA) optics with flexibility for manipulating the transport matrix elements for the various needed studies. While it is possible to fold the spent beam line with a U-turn as the emittance preservation is no longer an issue, calculations needing to be verified indicate that one must bend the input beam only very gently to avoid CSR degradation of the emittance. The latter extends the footprint of the machine considerably.

Figure 5.1-1. (next page) Overview of the Phase I ERL.

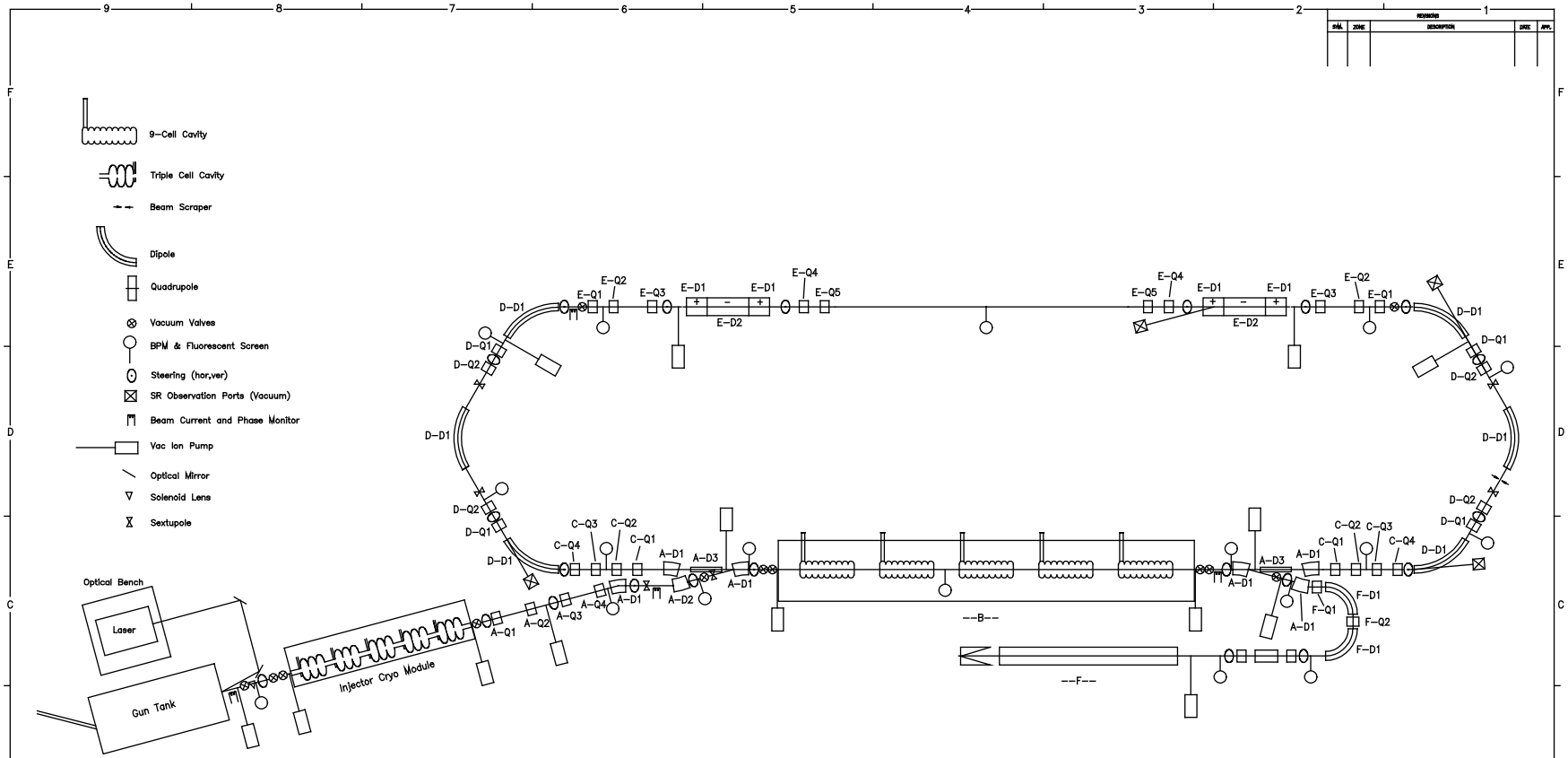

Un-Issued LNS Drawing, Last revised 4/25/01

ITEM	DWG. NO.	DESCRIPTION	QUANTITY G1 G2 G3	REMARKS	REV.

PRINT DISTR. D

PLOT DATE APRIL 30, 2001
CAD FILE NAME D-6040-288-02

UNLESS OTHERWISE SPECIFIED
DIMENSIONS ARE IN INCHES
TOLERANCES ON
.XX ±.010
.XXX ±.005
FRACTIONS ±1/64
ANGLES ±0.5°
ALL SURFACES 63

CR-1

Cornell University
Floyd R. Newman Laboratory of Nuclear Studies - Ithaca, NY 14853

HIGH VOLT LAB.
ENERGY RECOVERY LINAC LAYOUT
(LINAC DETAIL)

CHECKED BY	DRAWN BY	DRAWN FOR	DATE	SCALE	SIZE	DWG. NO.	REV.
APPROVED BY	J. LACEY	M. TIGNER	3/12/01	1"=30'	D	6040-288 SH. NO. 2 CONT. ON FIN	

6040-288 SH. NO. 2 CONT. ON FIN REV.

5.2 Technical Systems
5.2.1 Electron Source

We will employ a DC photoemission electron gun as the electron source for the prototype. This source has three major elements - the DC electron gun structure; the photocathode; and the laser which illuminates the photocathode. Each of these elements is described, below, along with the reasons for choosing a photoemission type gun.

The primary reasons for choosing a photoemission gun are the high beam brightness provided by a photoemission cathode, and the great flexibility in beam time structure which results from coupling a linear photoemitter with the ease of generating optical pulse patterns with lasers and electro-optic components. The principal reason photoemission cathodes produce high beam brightness is that these cathodes can support very high instantaneous current density. In addition, certain photocathodes provide very low thermal emittances. We have selected this type of cathode.

The first point to realize in using a photoemission cathode is that for the ERL application, the photocathode must offer a high quantum efficiency. For any linear photoemitter, the following relation is true:

$$i[\mathrm{mA}] = \frac{\lambda[\mathrm{nm}]}{124} \bullet P_{laser}[\mathrm{W}] \bullet Q.E.[\%].$$

This expression can be integrated over time to give an equivalent relationship between the bunch charge in nanocoulombs and the laser pulse energy in microjoules. There are three families of high quantum yield photoemitters: the alkali antimonides; the alkali tellurides; and the III-V semiconductors. The first two of these families have positive electron affinity, while the third has negative electron affinity. We will discuss the importance of this distinction later. In table 5.2.1-1 we give for each of these three cathode types the typical operating wavelength and the product of laser power and quantum efficiency necessary to support the 100 mA average current requirement of the ERL.

Table 5.2.1-1 Photocathodes

Cathode Type	Typical Operating Wavelength [nm]	P x Q.E. product to support 100 mA [W - %]
Alkali Antimonide (K_2CsSb)	527	23.5
Alkali Telluride (KCsTe)	266	46.6
NEA semiconductor (GaAs)	780	15.9

It should be noted that in Table 5.2-1 it is assumed that every laser photon and every photoemitted electron is useful. Thus, the laser power must be provided with the correct time structure (i.e. suitably short duration optical pulses at a 1300 MHz repetition rate). In addition, if a Gaussian transverse laser profile is truncated to provide a more uniform spatial profile, more laser power will be required.

Photocathodes of each type with initial quantum efficiencies of 10% or greater have been made. Thus, to produce 100 mA electron beams for the ERL, lasers delivering several watts with appropriate time structure are necessary. Presently, only one laser has demonstrated the necessary optical power and RF time structure. This is an optically pumped Ti:sapphire laser which is locked to the accelerator RF by gain modulation. The gain modulation is produced by a simple diode laser driven at a subharmonic of the fundamental accelerator frequency. At JLAB, a laser of this type has produced 2.5 W of near infrared light at 499 MHz. It is practical to produce the same optical power at 1300 Mhz (Hovater 1998). A version of this laser has been in routine service on the CEBAFaccelerator since August, 2000. This laser has proved exceptionally stable in operation. It has no active feedback loops to stabilize any parameter - including the cavity length. We anticipate that with straightforward development, a laser of this type providing 10 W at 1300 MHz and 780 nm will prove practical practical. We also note that high average power amplification of a high frequency optical pulse train from a Ti:sapphire laser has been demonstrated at the 5.77 W level (Liu 2000). Because of its long wavelength, this laser is only suitable for driving a GaAs photocathode.

No photoemission electron source delivering 100 mA average current for operationally useful periods of time has ever been demonstrated. A 433 MHz RF gun with an alkali antimonide photocathode has produced 32 mA average current (128 mA instantaneous current with 25% duty factor) with a cathode operational lifetime of about 2 hours (Dowell 1993). The JLAB IRFEL operates a GaAs cathode in a ~335 kV DC gun and delivers 5 mA average current with long cathode operational life (Sinclair 1992; Engwall 1997; Siggins 2000). The JLAB nuclear physics injector operates with GaAs cathodes, and has shown reproducible cathode lifetimes of 2×10^5 Coulombs/cm^2. The cathode lifetime is limited only by the effects of ion back-bombardment. Clearly operational lifetime improvements of about an order of magnitude are desirable for the ERL application. The approach for achieving this is detailed, below.

The thermal emittance of the beam produced by a photoemission cathode is an issue of fundamental importance in applications such as the ERL. The normalized rms emittance of a beam produced by photoemission from a uniformly illuminated spot of radius r is:

$$\varepsilon_{n,rms} = \frac{r}{2}\sqrt{\frac{E_{thermal}}{mc^2}},$$

where $E_{thermal}$ is the effective thermal energy of the emitted electrons. In the case of a thermionic emitter, the above relation is known to give a good description of the normalized emittance. In this case, $E_{thermal} = kT$, and T is the physical cathode temperature.

For the GaAs photocathode, Dunham et al. have reported measurements of $E_{thermal}$ for several wavelengths (Dunham 1995). They demonstrated that for a range of wavelengths close

to the fundamental absorption edge of GaAs, $E_{thermal}$ was about 35 meV (n.b. room temperature is 25 meV). Measurements of similar quality for the thermal emittance of alkali antimonide and alkali telluride cathodes have not been reported. $E_{thermal}$ values between 200 and 600 meV have been reported for alkali antimonide cathodes, and between 200 and 300 meV for alkali telluride cathodes. However, these numbers are not based on measurements as careful as those of Dunham et al.

It is clear that the basic thermal emittance of the GaAs photocathode is significantly superior to the alkali antimonide and alkali telluride photocathodes. This is a consequence of the fact that GaAs is a negative electron affinity photoemitter, while the other cathodes have positive electron affinity. The negative affinity and relatively low optical absorption of the GaAs photocathode allow photoexcited electrons to relax to the bottom of the conduction band prior to emission. In the case of positive electron affinity cathodes, electrons must be emitted prior to relaxation to the conduction band minimum. To obtain a high quantum efficiency with the positive electron affinity photoemitters, the photon energy must be several hundred meV above the work function. Thus, one expects the photoemitted electrons to have an effective thermal energy of this order. It is worth noting that in the future, the thermal emittance from GaAs photocathodes might be further reduced by lowering the cathode temperature. While the thermal emittance at reduced temperature has not been measured, the energy spread has shown the expected narrowing at low temperature (Feigerle 1984; Drouhin 1985).

In any high brightness, bunched-beam electron source, it is important that the external field applied to the cathode be large compared to the fields generated within the bunch itself. The fields within the bunch cause bunch lengthening, energy spread, and transverse emittance growth. In the case of a DC electron gun, the static electric field at the cathode produces a surface charge density on the cathode. The condition that the external field be large compared to the self field of the bunch requires that the charge per unit area extracted from the cathode in a single bunch be small compared to the charge per unit area stored at the cathode surface by the applied field. The allowable thermal emittance of the beam determines the maximum radius of the illuminated area on the cathode, and thus directly determines the cathode electric field required. In this respect, the GaAs cathode, with its small thermal emittance, permits a large illuminated area on the cathode, and thus the lowest cathode field requirement.

In a DC electron gun, the maximum field strength that can be supported on the cathode is limited by field emission from the cathode electrode structure and its supporting elements. This emission has three detrimental effects. First, field emitted electrons may strike the ceramic insulator that holds off the gun high voltage and thus build up a concentration of charge within the insulator. If this charge is not drained off, the field strengths created may become large enough to cause a mechanical “punch through” of the ceramic, creating a vacuum leak. Second, field emitted electrons striking the vacuum walls cause desorption of gases, which may either chemically poison the cathode, or provide a source of ions which damage the cathode through ion back bombardment. Third, some field emitted electrons can form dark beam contrast and halo in the accelerator.

Two recent advances allow a much higher field strength to be used in DC electron guns. The first is the discovery that the uniform implantation of the ceramic insulator with metal ions creates a uniform sheet resistance on the implanted surface. This sheet resistance can be made

appropriate to drain off the charge delivered by field emission. This technique has been very successfully applied on the DC photoemission electron gun of the JLAB IRFEL. (Liu 1997). The second and more recent advance is the discovery that metallic electrodes implanted by nitrogen ions show dramatically reduced field emission. Test electrodes have been operated with uniform DC fields of 30 MV/m over a 100 cm^2 area, and showed field emission currents between 0.5 and 1.8 pA/cm^2. These tests were done with high voltage (125 kV), finite gap (4 mm), and for extended duration (~ 8 hours/test) (Sinclair 2001). These results give confidence that a DC gun structure operating with a cathode field of 15 to 20 MV/m can be reliably operated.

In the JLAB GaAs photoemission guns, the cathode lifetime is limited only by ion back bombardment. The ion back bombardment flux is directly proportional to the average beam current and to the vacuum pressure in the cathode-anode gap. Thus, rather than quoting a cathode operational lifetime in terms of clock hours, it makes much more sense to quote the lifetime as the number of coulombs delivered per unit illuminated area. The injector of the JLAB CEBAF accelerator was designed to minimize the vacuum in the cathode-anode gap. Initial operation of the 100 kV electron gun in this injector gave cathode 1/e lifetimes of over 10^4 coulombs/cm^2 (Sinclair 1999) . Two of these guns are now in routine operation. As the vacuum conditions have slowly improved with time, the operational 1/e lifetime has steadily improved, and values above 10^5 coulombs/cm^2 are now standard. Presently, the vacuum in these guns is predominantly hydrogen, with a small amount of methane. The pressure, as measured by an extractor gauge, is in the mid-10^{-12} torr range. Further vacuum improvements are practical, and can be expected to provide further increases in cathode operational lifetime.

One advantage of DC photoemission guns is the relative ease with which excellent vacuum pressures can be produced. In contrast to the RF gun, the DC gun has no restrictions on the materials which can be used for the vacuum walls; no restriction on the geometry of the vacuum walls, and no practical restrictions on the size and location of ports in the vacuum chamber. In RF guns, the vacuum walls must be made of high electrical conductivity metal; they must have a size and shape restricted by the need to create a resonant cavity; and they may only have ports located symmetrically with respect to the beam axis and of a size limited by the RF frequency. These restrictions make it much more difficult to achieve a truly excellent vacuum pressure in a RF gun. It should be noted that the cathode degrading effects of ion back bombardment are likely to be significantly less in an RF gun. However, all high quantum efficiency photocathodes are highly sensitive to chemical poisoning by certain chemically active gases (e.g. H_2O, CO_2). When operated with high average power, as would be necessary in any RF gun for the ERL application, it is generally noted that the vacuum pressure rises, and this is likely to impact the cathode lifetime adversely. Finally, it should be noted that to date, all high quantum efficiency photocathode RF guns have shown reduced cathode life in an operating RF cavity.

Parameters for a DC photoemission gun with a GaAs cathode to deliver 100 mA average current at 1300 MHz for the Phase I ERL.

We assume that we must deliver a rms normalized thermal emittance of ≤ 0.5 μm. We further assume that the effective cathode temperature is 51 meV, a value conservative by a factor of over 1.4 based on Dunham's measurements. This allows us to use a cathode radius of 3.16 mm. We choose a 2.5 mm radius, giving a cathode illuminated area of 0.196 cm^2. We assume that we achieve the demonstrated 1/e operational lifetime of $2x10^5$ coulombs/cm^2, to give 0.393 x 10^5 coulombs cathode 1/e life. We assume an initial cathode QE of 10% at 780 nm, and assume that we begin with a laser able to deliver 2 W to the photocathode, and with appropriate 1300 MHz time structure. The laser beam will be truncated at ± 1 σ transversely, so it will provide about 3 W of raw power in a Gaussian beam profile. Since we need 15.9 W-% to maintain the necessary 100 mA, we have a factor of 1.26 excess laser power, allowing us to operate for 0.2296 e-folding times. This will deliver $9x10^3$ coulombs, or 25 continuous hours at 100 mA before the cathode is unusable. If we assume that we have a cathode of 2.5 cm diameter, and plan to use six separate 5 mm diameter spots, well away from the edge of the cathode, we could in principle operate for nearly 150 hours before needing to take some action to restore the cathode. At JLAB, we have been able to almost completely repair the QE damage from ion back bombardment by a heat treatment and cathode reactivation – a process conducted in situ in the electron gun, and requiring a few hours.

At 1300 MHz, each bunch contains 77 pC. With a cathode illuminated spot of 0.196 cm^2, this corresponds to a surface charge density of 3.92 μC/m^2. To establish this charge density requires a cathode field strength of only 0.443 MV/m. Based on the very promising field emission developments noted above, we plan to operate the DC gun initially at or above 10 MV/m at the cathode – a factor of 22.6 above that necessary to establish the surface charge density. Thus, the effects of space charge on the bunch as it traverses the gun structure are expected to be tolerable. This example illustrates that it is quite plausible to operate a DC photoemission gun with a GaAs photocathode to meet the performance required by the ERL prototype, using parameters which have all been demonstrated in practice.

5.2.2 Injector

5.2.2.1 Booster & Control

The booster subsystem of the overall photoinjector performs the function of accelerating the bunches from the electron source to relativistic speed (e.g., 5 MeV) with minimal emittance dilution. The booster calls for five 3-cell cavities, each providing one MV acceleration. The values quoted in the parameter list (section 4.2) are estimates based on an initial design; final design values will be completed during the early engineering stages of the Phase I project. We anticipate the need to open the beam pipe aperture to achieve stronger coupling necessary to deliver 100 kW of beam power per cavity. Injector cavities will be built with the same technology as for the main linac cavities. Each cavity will be equipped with a high power input coupler, two HOM couplers on each end, a beam line HOM coupler on each end, integrated helium vessel, mechanical and piezo tuners.

The input couplers for injector cavities must deliver 100 kW each. With TTF couplers successfully tested to 1.5 MW traveling wave power at one percent duty factor (TELSA 2001), we anticipate using the basic TTF input couplers design for ERL injector cavities with modifications to improve cooling and implement variable coupling An empty symmetrizing coupling port will be added to the cavity to avoid dipole kicks.

The injector cavity parameters are given in Phase I ERL Parameter List (Section 4.2). An injector cavity concept is shown in Figure 5.2.2.1-1.

5.2.2.2. Merging Optics

The merging optics comprise 4 quadrupoles and three dipoles. The quadrupoles are needed for matching the injector lattice functions into the main linac. The beam dump optics is the mirror image of the injection merge except for the beam dispersal lenses needed to minimize the beam power density at the dump. Preliminary merger layout and quadrupole specifications are presented in section 4.8.8.

The primary criterion for the merging dipoles is that their bending angle be as small as practical to minimize the influence of CSR on the beam emittance. The quadrupole and dipole fields and lengths are given in Table 5.2.4-1 and the needed quality in the parameter list for the Phase I ERL to be found in section 4.2. Note that the technical parameters are modest so that these magnets can be ordered from industry as required.

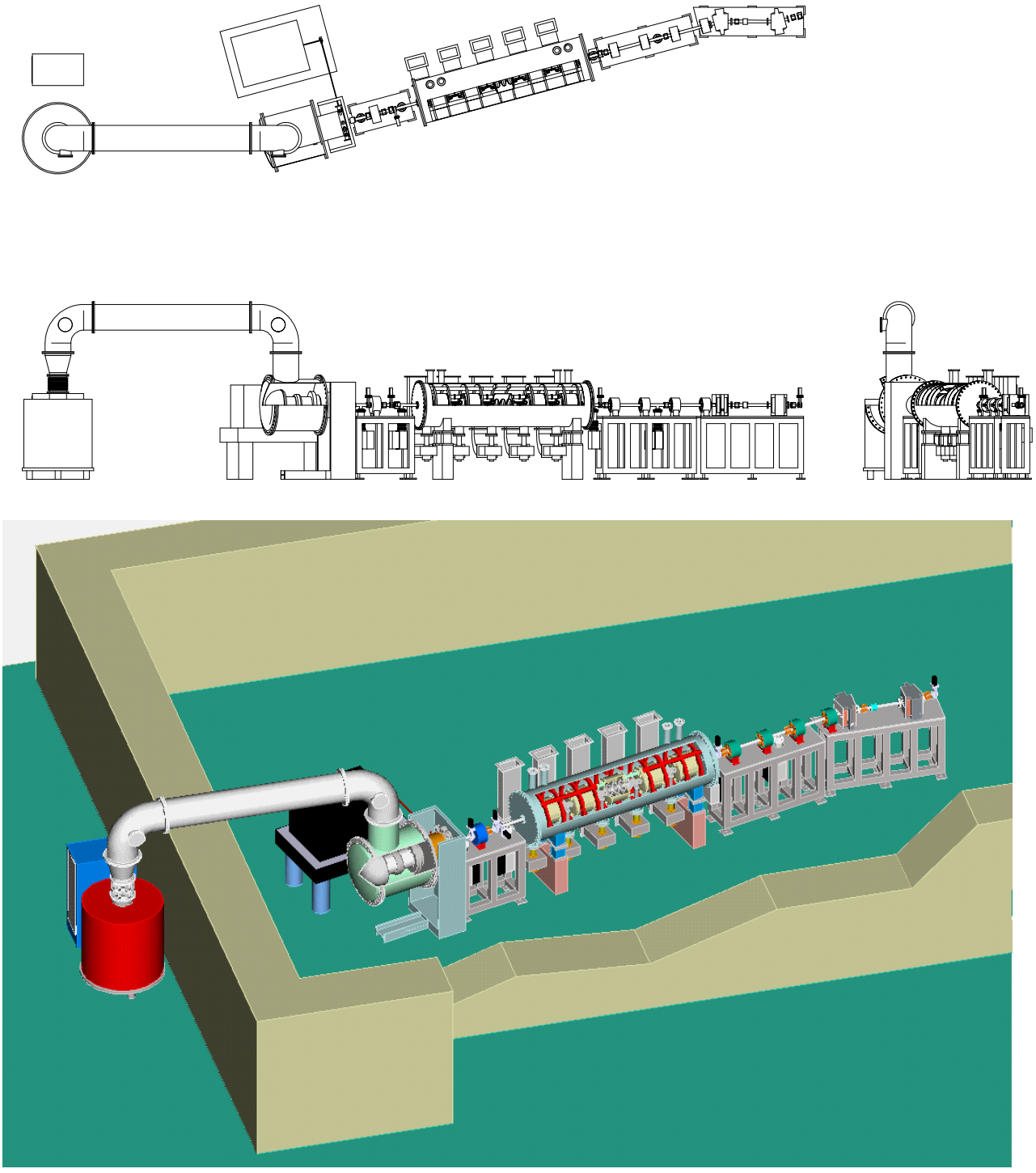

Figure 5.2.2.1-1. Layout of the injector. From left to right: The high voltage supply is connected by an insulated conduit over the shielding wall to the laser driven photocathode assembly. This feeds the cylindrical SRF booster linac which is connected, via electron optics to the main ERL linac (not shown).

5.2.3 Main Linac
5.2.3.1 SRF Cavities and HOM Structures

General remarks

Rapid advances in the performance of superconducting cavities have made RF superconductivity a key technology for accelerators fulfilling a variety of physics needs: high energy particle physics, nuclear physics, neutron spallation sources, storage ring light sources and free electron lasers. New applications are forthcoming in each of these arenas. New areas are also opening up for radioactive isotope accelerators, as well as muon sources for neutrino factories and the muon collider.

More than one kilometer of superconducting cavities have been installed in accelerators around the world providing more than 5 GV of acceleration. For a review, see (Padamsee 1998). The two largest installations are CEBAF at JLAB and LEP-II at CERN. Over its operating period starting in 1995, CEBAF has upgraded the in-line accelerating gradient from the design value of 5 to 7.5 MV/m. From 1996 to 2000, LEP upgraded operating gradients from 6 to 7.5 MV/m. Eight cavities prepared for the IRFEL at JLAB operate at 12 MV/m.

Considerable gradient advances have been made in anticipation for the needs for TESLA (TeV Energy Superconducting Linear Accelerator). Niobium cavities now routinely exceed 25 MV/m. Improved understanding of the physics of RF superconductivity, together with technology advances are responsible for increases in performance. Cornell has been the home for many of these developments. The original CEBAF cavities were Cornell designs. Presently, CESR operates entirely with SRF cavities. In the formative stages of the international TESLA collaboration, three 5-cell 1300 MHz cavities were built at Cornell and tested to accelerating fields of 26 - 28 MV/m. (Figures 5.2.3.1-1, 2, 3 & 6 are all, with permission, from the TESLA Technical Design Report (TELSA 2001)).

All the techniques used at Tesla Test Facility (TTF) will be adopted to achieve the highest possible gradients to provide adequate performance safety margin. Briefly, these techniques include the use of high purity niobium (RRR > 600), eddy current scanning to exclude defects from starting material, chemical etching for removing surface defects, high pressure rinsing and clean room assembly to avoid field emission. In case of accidental dust contamination due to final cavity assembly into the cryomodule or the accelerator, high pulsed power processing will be available for ERL and the prototype. This capability puts special demands on the input coupler (see input coupler section below).

For the TTF more than 50 1-meter long cavities were fabricated at various companies, prepared at DESY and tested to gradients above 25 MV/m. Figure 5.2.3.1-1 shows the results for one production series. Each cavity (Figure 5.2.3.1-2) is a one meter long 9-cell unit, RF frequency 1300 MHz. Twenty-four of these cavities were installed at TTF in three cryomodules and operated with beam at an average gradient of 20 MV/m. The highest average accelerating gradient measured for a complete module was 22 MV/m. The TTF linac has been operated for more that 5000 hours.

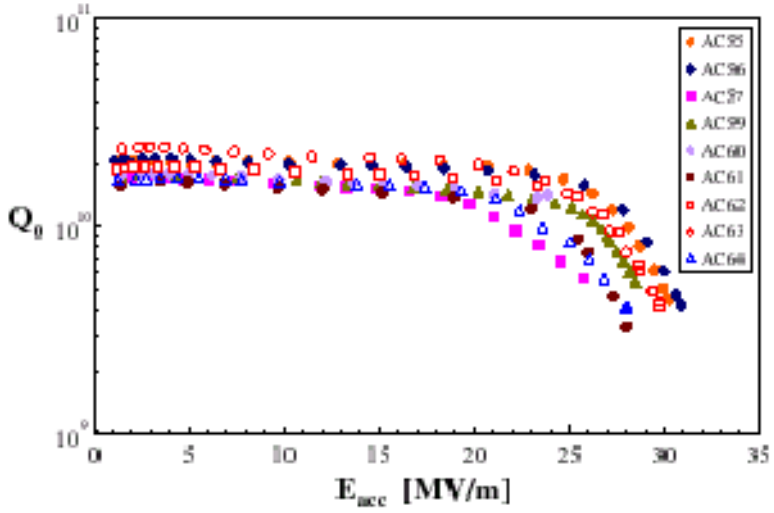

Figure 5.2.3.1-1: TTF cavity results (TELSA 2001).

Based on these successes, both the Phase I and the Phase II ERLs will be centered on TESLA SRF technology. There will be some significant differences, however, and these will be discussed by comparison to the TESLA design. For example, TESLA is envisioned as a pulsed machine with one percent duty cycle. Because of x-ray user requirements, the ERL will run CW. SRF cavities excel in applications requiring continuous wave (CW). However, for high gradients, a major impact of the CW choice is that refrigeration becomes a significant cost component. Another important difference is that each cavity will be powered by individual klystrons to control accelerating and energy recovering beams in precise balance. Powering by individual klystrons allows the flexibility to operate each cavity at its highest gradient to make up for cavities that run at lower gradients.

With our tight coupling to the TESLA community, we aim to take advantage of cost and performance improvement programs from cavity to cryomodule including RF control and operating systems. For example, one promising possibility is seamless Nb cavity production; another is electropolishing to replace standard dunk chemical etching procedures. Also, there have been major developments in digital RF control systems with feed-forward techniques.

Linac Cavities

The TESLA cavity is a 9-cell standing wave structure of one meter length, fabricated from sheet niobium by sheet metal forming and electron beam welding techniques (Fig. 5.2.3.1-2). The cavity is reinforced with Nb stiffening rings to reduce Lorentz Force detuning. The RF magnetic field in the cavity interacts with the RF wall current to result in a Lorentz force which causes a small (μm) deformation of the cavity shape that shifts the resonant frequency. Each cavity has a coaxial RF input power coupler, pick up probe to monitor the field level, HOM couplers to extract the beam induced HOM power, and a coarse mechanical tuning system augmented by fast piezoelectric fine tuner. As discussed in the HOM sections below, it will be

necessary to increase the number of HOM coupler ports at each of the cavity from one to two. Niobium-Titanium end flanges with surface hardness equivalent to stainless are welded at beam ports and coupler ports. O-ring type aluminum gaskets provide superfluid He seals.

Fig. 5.2.3.1-2. TTF 9-cell 1300 MHz cavity (TESLA 2001)

Injector Booster Cavities

The injector needs five 3-cell cavities, each providing one MV acceleration, chosen to keep the beam power delivered by the input coupler to be 100kW. These cavities will be fully designed during the prototype engineering stage. We anticipate the need to open the beam pipe aperture to achieve stronger coupling necessary to deliver 100 kW of beam power per cavity. Injector cavities will be built with the same technology as for the main linac cavities. Each will be equipped with a high power input coupler, two HOM couplers on each end, a beam line HOM coupler on each end, integrated helium vessel, mechanical and piezo tuners.

Input Couplers

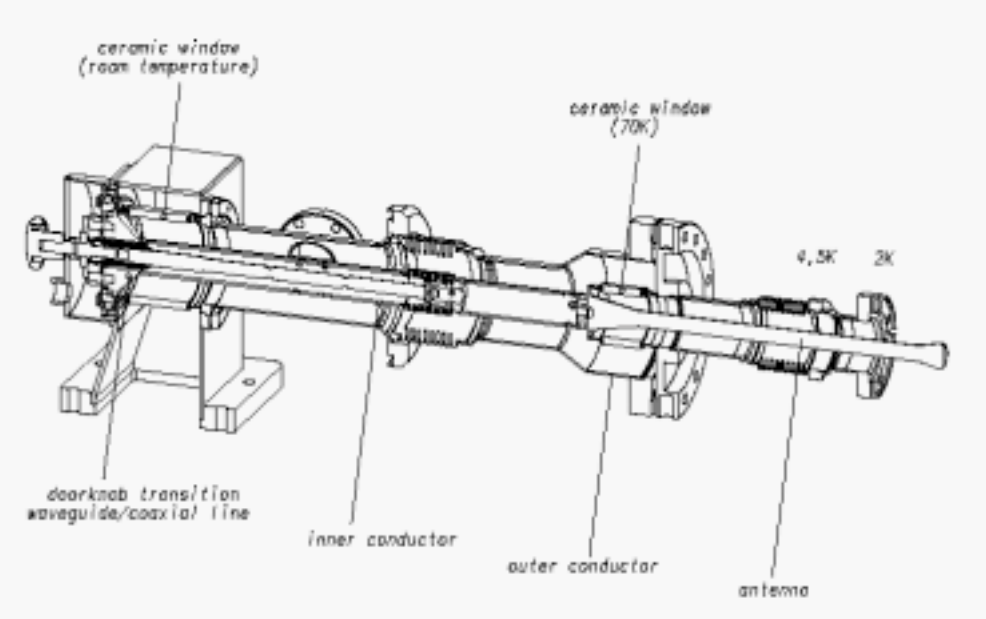

Fig. 5.2.3.1-3. TTF Input coupler, latest design (TELSA 2001).

The input coupler (Fig. 5.2.3.1-3) is of coaxial design chosen to be insensitive to multipacting resonances. Stainless steel inner and outer conductor pipes are plated with 10 - 20 μm copper to minimize both conduction losses and RF losses. Alumina windows are coated with titanium-nitride to reduce secondary electron emission. Possible multipacting in the window region can be suppressed by a 5 kV bias, successfully used at CERN. Bellows in the inner and outer coaxial line allow for a few mm motion between the 2 K cold mass of the cavity/helium vessel and vacuum vessel.

The coupler is designed in two sections to keep the cavity clean and to protect against window failures. The cold section of the coupler is mounted on the cavity in a clean room and closed by a cold ceramic window. The warm section is sealed against the air side by a second ceramic window. The transition from coaxial to waveguide is evacuated by an additional vacuum system. The coupler is equipped with standard diagnostics for vacuum, gas species, temperature and light monitoring. Vacuum and light levels can be used to trip the RF in case of an arc.

Couplers have been tested at TTF to transmit up to 1.6 MW for 0.5 ms pulse length and in the traveling wave mode (TELSA 2001). For the ERL the required power capability is 15 kW in CW and 1.5 MW in pulsed mode for high pulsed power (HPP is used to process the cavities – see below).

For the injector cavities the couplers must deliver 100 kW each. An empty symmetrizing coupling port will be added to the cavity to avoid dipole kicks. With TTF couplers successfully tested to 1.5 MW traveling wave power at one percent duty factor, we anticipate using TTF input couplers for ERL injector cavities.

The dynamic heat leak of the TTF coupler at 100 kW CW is expected to be less than one watt at 2 K. The heat load to the 5 - 8 K cold gas intercept is expected to be less than 5 watt per coupler, and 250 W at 70 K. From TESLA studies, the design static heat loads of the input coupler are 0.06 watt at 2 K, 0.5 W at 5 K, and 6 W at 70 K per coupler.

To minimize RF power for the ERL, the input coupler Q_{ext} will be 2.6×10^7 as compared to $Q_{ext} = 3 \times 10^6$ for TTF which is designed to be matched to TESLA beam power. The coupling change is easily accomplished by attaching the coupler in a position slightly withdrawn from the cavity. The design of the coupler allows Q_{ext} to be increased by a factor of 6 *in situ*. This will facilitate HPP to eliminate field emission that may arise from accidental contamination.

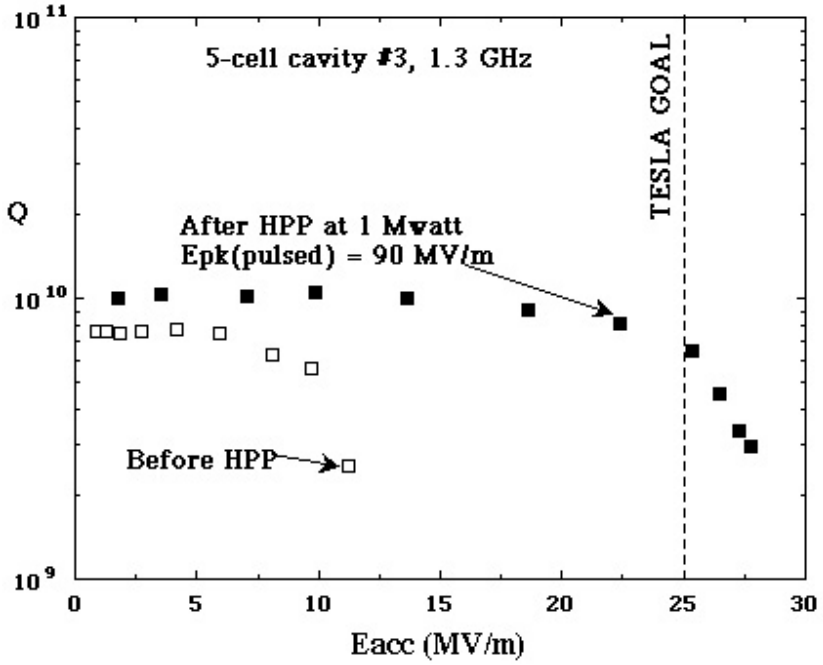

Fig. 5.2.3.1-4. High Pulsed Power Processing (HPP) improves gradient of deteriorated cavity by eliminating field emission (Crawford 1995).

Studies at Cornell show that it is possible to eliminate field emission and improve the cavity Q by applying short pulses of high peak power (HPP). Figure 5.2.3.1-4 shows results on a 5-cell 1300 MHz cavity which was processed to 90 MV/m peak electric field using one MW pulses of 200 μsec width (Crawford 1995). Extensive HPP studies show that to operate field emission free at E_{acc} = 20 MV/m it is necessary for the cavity to reach E_{pk} = 80 MV/m during pulsed processing. Figure 5.2.3.1-5 shows the pulsed field level accessible with 1.5 MW and 250 μs pulse length. Clearly the Q_{ext} needs to be variable. The TESLA input coupler design has a built in adjustability of a factor of 6 and can be augmented by another factor of three by the use of three stub wave guide transformers present in the RF distribution system.

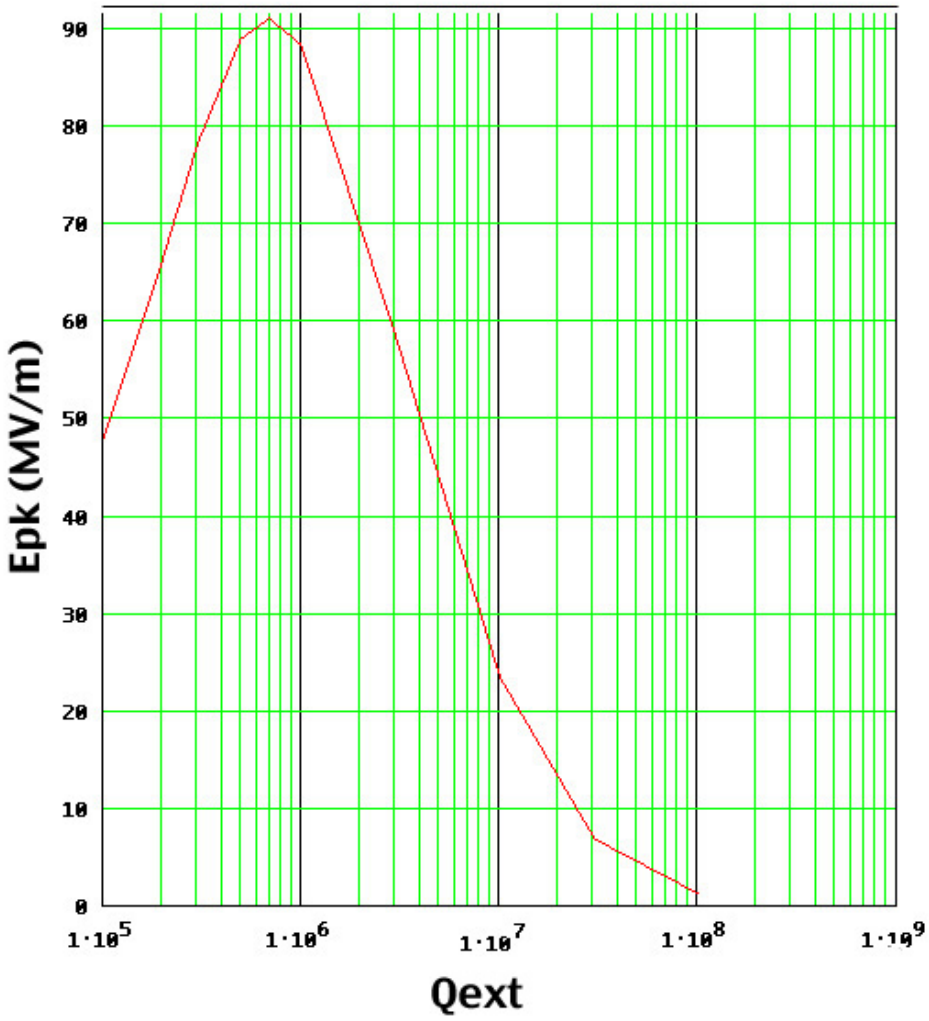

Fig. 5.2.3.1-5. Peak electric field reachable with 1.5 MW of RF power and pulse length of 250 μs as a function of the setting of the input coupler Qext. HPP experience shows that after reaching 90 MV/m peak field, a cavity will operate free of field emission at Eacc = 22.5 MV/m.

HOM couplers

Higher Order Modes (HOMs) are extracted via couplers mounted on beam pipe sections. Cavity end cells are slightly asymmetric to push low group velocity HOMs towards cavity end cells. The two polarization states of dipole modes require two orthogonal couplers. The TESLA cavity has one coupler (Fig. 5.2.3.1-6) on each side of a cavity mounted orthogonal to each other. A tunable 1.3 GHz notch filter suppresses power extraction from the accelerating mode to less than 50 mW at 23.4 MV/m. TTF tests have shown this design is well cooled and insensitive to bombardment from field emission electrons and x rays.

Bench and beam measurements show that most modes have Q values between 10^4 and 10^5 (TELSA 2001). ERL and its prototype will use two HOM couplers at each end of the cavity to ensure adequate damping of dipole modes as well as efficient extraction of monopole modes. Furthermore, one or more of the cells in each 9-cell structure may need to be polarized (Padamsee 1991) to get best coupling to dipole modes. This is accomplished by introducing a slight (5%) azimuthal asymmetry in the cell shape.

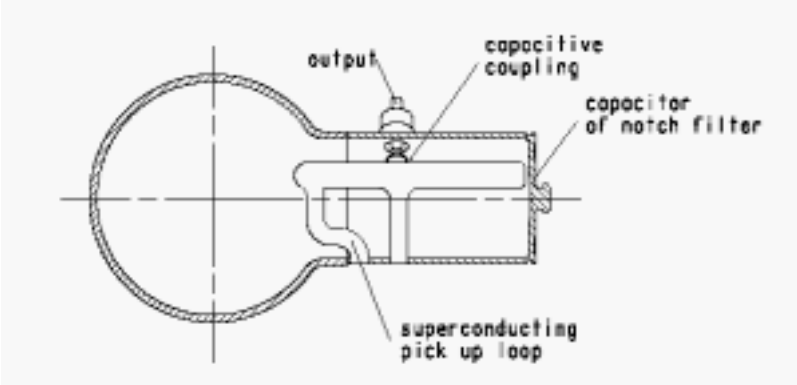

Fig. 5.2.3.1-6. The TESLA HOM coupler (TELSA 2001).

At 100 mA average beam current the HOM power excited by the beam will be much higher in ERL (162 watt/m) than in TESLA (2 watt/m). We anticipate that 5% of the HOM power will be deposited at 2 K. HOM couplers will extract the other 95%. A large fraction of HOM power will be in modes above the cut-off frequency of the beam pipe (3.2 GHz). At 0.3 mm bunch length for TESLA, the anticipated fraction is 0.5, but for 0.7 mm bunch length in ERL, we expect less HOM power propagating out the beam pipe. To intercept this power there will be special beam-pipe HOM absorbers consisting of a pipe of absorbing material integrated into the connection between adjacent cavity units. HOM power dissipated in these beam pipe absorbers will be intercepted by a stream of cold gas at 70 K. Candidate absorber materials are silicon carbide in an aluminum nitride matrix, a ceramic, like MACOR, or ferrite as used in CESR superconducting cavities.

Tuner

The Phase I and Phase II ERL injector cavity tuners will be based on the TESLA design. The TESLA tuner is driven by a stepping motor with gear box and double lever arm. The tuning range is ±300 kHz with resolution of 1 Hz. The 9-cell cavity tuning coefficient is 315 Hz/mm.

A piezo electric fine tuner augments the mechanical tuner to help compensate Lorentz force detuning and counteract microphonics. Piezoelectric compensation of Lorentz force detuning has been demonstrated to 100 Hz in pulsed operation at TTF (TELSA 2001), but will need further development for routine operation in the ERL.

5.2.3.2 RF Power System

The peak RF power needed for one superconducting cavity depends on the gradient, loaded Q (Q_L), intrinsic Q (Q_0) and the detuning tolerance from microphonics. At the TTF the maximum peak to peak microphonics observed was 10 Hz. Figure 5.2.3.2 -1 shows the RF power required to achieve 20 MV/m in the presence of detuning extent of 15 Hz and 25 Hz. If we choose a conservative detuning value of 25 Hz, the optimum Qext will be 2.5 $x10^7$ and the power required is 8 kW per cavity. With 20% for control margin and waveguide losses plus allowance for phase drift (see Table 3.1.9-1) a 13 kW klystron is needed.

For the Phase I ERL we need the additional reserve to allow for good phase and amplitude control. Due to possible large fluctuations in beam loading we need flexible control over amplitude and phase, and large reserve power. The baseline tolerance on cavity amplitude is 10^{-4} and on the phase is 0.5 degree.

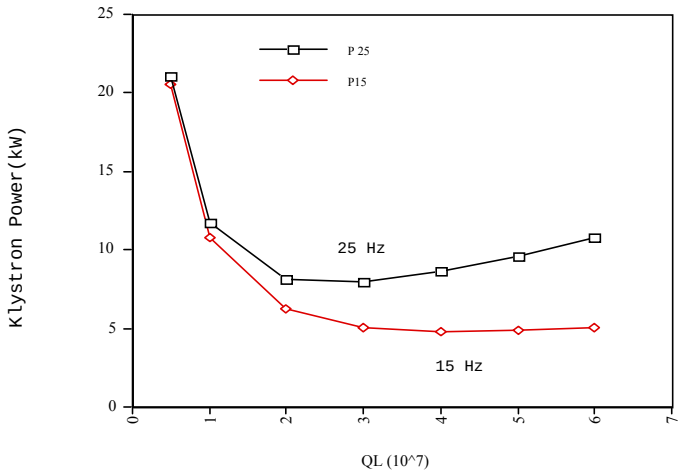

Fig. 5.2.3.2-1. RF power requirements as a function of Q_L for two different detuning tolerance values.

Using one klystron per cavity will provide the greatest simplicity of operation, the best RF stability, and the greatest flexibility for continued operation in the event of a single RF failure. A circulator and full power load will be installed on the output of each klystron to protect the klystron from reflections. One HV supply will power several klystrons. In the RF power distribution system, phase shifts due to thermal expansion will be compensated by wave guide

transformers installed between circulator and cavity. These provide ±50 deg phase adjustment, as well as impedance matching for Q_{ext} adjustment over a factor of 10. Experience at TTF shows a 20% variation in Q_{ext} setting; an adjustment method is necessary. Each tuning stub is equipped with a motor controlled by the low level RF system. The stub tuner can also be used to reduce the effective Q_{ext} by a factor of 3 for HPP.

The injector calls for a total of 500 kW of CW RF power. Development proposals for the needed tube are in hand.

The RF system must be robust against variations in system parameters such as beam loading and klystron gain. The major sources of field perturbations that must be controlled by low level RF system are fluctuations of cavity resonance frequency due to mechanical vibrations, gradient dependent Lorentz force detuning, and fluctuations of beam loading caused by inadequate balance between accelerated and energy recovering beams. Slow changes can be corrected by the mechanical tuner, while fast changes must be taken care of by amplitude and phase modulation of the incident RF power. Feed forward is added to improve regulation, as for example to compensate Lorentz force detuning while ramping up the cavity field.

The low level RF system is modeled after the TTF digital system and includes low RF power control circuitry, tuner control and RF interlocks. The system controls the amplitude and phase of the fields and protects the cavity and klystron from fault conditions. In TTF, using feedback and feed forward the rms errors in amplitude are less that $1x10^{-3}$ and $5x10^{-2}$ degrees in phase for pulsed operation. Repetitive components of residual fluctuations are dealt with by adaptive feed forward. The CW conditions in the machine will ensure adequate performance.

RF system interlocks protect against consequences of RF window arcs, RF window overheating, RF coupler multipacting, RF breakdown, low cryogen level, tuner position error, bad cavity vacuum, cryogen pressure error and similar phenomena.

5.2.4 Transport System

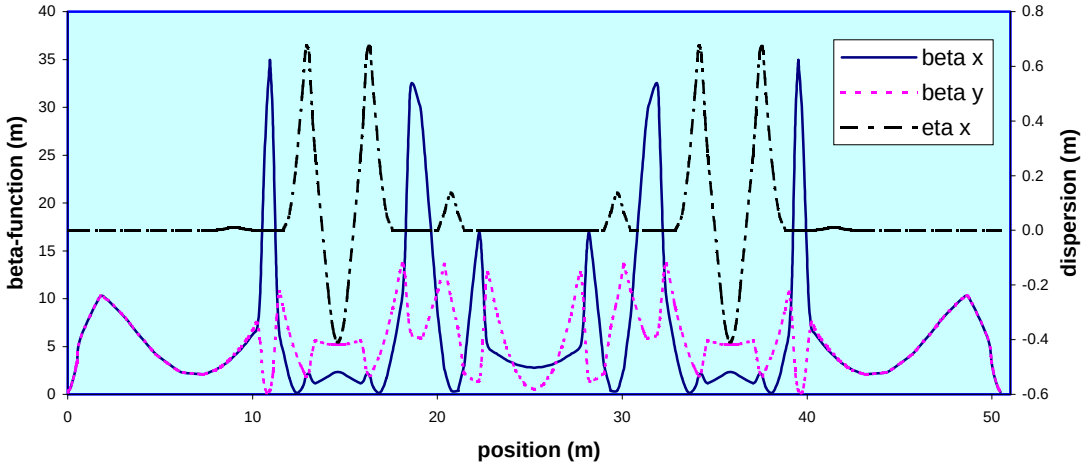

Fig. 5.2.4-1. An example of beta-functions and dispersion in the Phase I ERL from the point of injection to the dump.

The ERL is essentially a transport line between source and dump, making provision for the necessary acceleration and deceleration (treated under 5.2.2 and 5.2.3), beam confinement and central orbit needed to serve the experimental functions of the machine. The magnetic elements of the transport line comprise mostly dipoles and quadrupoles with a few sextupoles for chromatic corrections. The layout of the elements is displayed in Fig. 5.1-1. The beta-functions and dispersion is shown in Figure 5.2.4-1. High momentum acceptance (≤ 2 %) of the transport line is required to accommodate bunches run substantially off-crest in the main linac, which are necessary for successful compression to sub-picosecond bunch lengths. TBA sections, and quadrupole telescopes with a sufficient number of lenses to manipulate dispersion and betatron functions will provide the necessary flexibly for study of various emittance dilution effects as well as matching between the various sub-systems. The work on the final complete transport line design is in progress and will be completed during the early engineering stages of the Phase I project.

5.2.4.1 Magnet System

Table 5.2.4.1-1 contains the principal magnet parameters. Note that the strengths are modest so that standard iron and copper construction techniques will suffice. Field quality and stability requirements are given in the parameter list, (see section 4.2). These requirements are also well within the range of standard technology. For example, standard electron storage ring requirements are typically an order of magnitude more demanding in field quality and comparable in stability needs.

Steering corrector magnets are needed for precise control of the orbit position in the transport lines and must be placed often enough to allow centering in the focusing elements. The needed strength is given in the parameter list, (see section 4.2). Window frame construction of combined horizontal and vertical steering units will suffice.

The double chicane array of dipoles in the return leg of the transport line will be used as a bunch compressor and de-compressor for the study of very short bunches.

Table 5.2.4.1 – 1 Optics Parameter List

Notation:

Q – quadrupole : length; $k = (B_0/a)(1/\rho B)$

D – dipole magnet: Bend radius; Bend angle
1st pole rotation angle; 2nd pole rotation angle

A – Merger (*kinetic energy = 5 MeV*)

A-Q1 : 15 cm; 0.99 m^{-2}
A-Q2 : 15 cm; 0.48 m^{-2}
A-Q3 : 15 cm; 3.26 m^{-2}
A-Q4 : 15 cm; -7.66 m^{-2}
A-D1 : 1 m; 15 deg
0 deg; 0 deg – *sector magnet*
A-D2 : 1 m; 15 deg
-21 deg; -21 deg

kinetic energy = 100 MeV
A-D3 : 20 m; 1.5 deg
0 deg; 0 deg – *sector magnet*

C – matching section to / from TBA (*kinetic energy = 100 MeV*)

C-Q1 : 15 cm; -16.02 m^{-2}
C-Q2 : 15 cm; 6.37 m^{-2}
C-Q3 : 15 cm; 14.07 m^{-2}
C-Q4 : 15 cm; -17.66 m^{-2}

D – isochronous triple bend achromat (TBA) (*kinetic energy = 100 MeV*)

D-Q1 : 15 cm; 19.90 m^{-2}
D-Q2 : 15 cm; -9.49 m^{-2}
D-D1 : 1 m; 60 deg
0 deg; 0 deg – *sector magnet*

E – straight section in the recirculator (*kinetic energy = 100 MeV*)

E-Q1 : 15 cm; -9.20 m^{-2}
E-Q2 : 15 cm; 8.81 m^{-2}
E-Q3 : 15 cm; 3.18 m^{-2}
E-Q4 : 15 cm; 14.47 m^{-2}

E-Q5 : 15 cm; -15.08 m^{-2}

Chicane

E-D1 : 1 m; 20.49 deg
0/20.49 deg ; 20.49/0 deg – *rectangular magnet (35 cm long)*

E-D2 : 1 m; 40.98 deg
20.49 deg ; 20.49 deg – *rectangular magnet (70 cm long)*

F – achromat to the dump (*kinetic energy = 5 MeV*)

F-D1 : 50 cm; 90 deg
0 deg; 0 deg – *sector magnet*

F-Q1 : 15 cm; -5.39 m^{-2}

F-Q2 : 15 cm; 16.50 m^{-2}

5.2.4.2 Vacuum System

The transport line beam pipe is a 5 cm inner diameter stainless steel tube with some rectangular sections in dipoles where dispersion widens the beam. While a residual gas pressure of 10^{-8} Torr will suffice over most of its length there are three particularly sensitive locations requiring substantially lower pressure: The photogun, the main linac cryomodule and the injector cryomodule.

In the main runs, lumped ion pumps will suffice to maintain the needed pressure. As shown in the layout Fig. 5.1-1 each section has a metal seal valve for roughing down using a portable turbo station with leak detector as well as metal sealed, RF shielded beam line valves for section isolation.

In the vicinity of the photogun the pressure requirements are particularly stringent to avoid gun poisoning and special measures are called for (see section 4.2.1). Near the cryomodules it will be necessary to maintain pressures below 10^{-9} Torr to avoid breakdown enhancement due to adsorbed gas in the superconducting cavities. There, closely spaced ion pumps plus NEG pumping units will be used to maintain sufficient pumping speed for H_2 as well as the gases pumped well by the ion pumps.

5.2.4.3 Feedback Systems

In order to achieve high average brightness from the undulators, it is necessary that beam position and angle fluctuations at the undulator be smaller than the beam size and angular size, as computed by the emittance. There is relatively little decrease in the brilliance as long as the rms position fluctuation is smaller than 10% of the beam size, and the rms angle fluctuation is less than 10% of the angular beam size. Quantitatively, this means that the position fluctuation should be at the 5 micron level, and the beam angle fluctuation should be less than 1 μrad.

The position fluctuations in the JLAB CEBAF beam and the JLAB IRFEL have been measured. In the IRFEL case, the uncorrected fluctuation level is several hundred microns in position and about 10 μrad in angle, the noise being concentrated in the first three harmonics of

line frequency. Similarly, in the CEBAF machine the uncorrected position fluctuation level is about 100 microns rms. At the beam delivery points in CEBAF a 2 kHz sample rate feedback system is installed which corrects the position fluctuations to about 10 micron rms and the angular fluctuations to 1 μrad (Lebedev 1999; Krafft 2000) at 10-100 μA beam current.

The VME-based feedback system utilizes CEBAF standard input/output control computers and signals from the standard beam position monitoring system. Because the ERL will operate at currents approaching 100 mA, and therefore the BPM signals will be much higher, it is anticipated that no new developments will be required to use feedback to achieve the stability required to maintain the brilliance. It is further anticipated that a similar feedback system will be installed and tested on the prototype.

5.2.4.4 Beam Dump

After deceleration, the low emittance beam will emerge from the main linac section with about 500 kW. While defocusing the beam with permanent magnet lenses will help to lower the power density, it is likely that the density will be too high for absorption of the energy in a standard collector. For this reason we anticipate use of a beam excited decelerating length of copper L-band accelerating waveguide to convert beam kinetic energy to field energy which can be easily dissipated in the water cooled waveguide walls. The decelerator section can then safely be followed by a standard klystron type collector to dissipate the remaining beam kinetic energy.

5.2.5 Controls and Diagnostics

5.2.5.1 Operational Control

The functions of the control system are to set the operating point of all controllable elements in the Phase I ERL, to monitor the various sensors and provide the operations and machine physics staff with information in a useful form on the current state of the accelerator, and to archive and retrieve historical data.

The Phase I ERL control system design is based on the EPICS architecture. Originating at the Los Alamos and Argonne National Laboratories, EPICS is a toolkit of software components and corresponding device interfaces. It forms the basis of the system that provides a connection between the operators in the control room and the accelerator hardware. To reduce the software effort, whenever possible the control system will, in addition to utilizing higher level EPICS software components, incorporate software and design elements from control systems at other facilities (and, in particular, JLAB).

The control system will consist of three primary workstations for operation, experimentation and software development. One of the workstations will act as a server for the remote IOCs (input/output controllers), providing their bootable code images. There will be 6 IOCs. One will be dedicated to RF control; the other 5 will be geographically distributed and handle control and monitoring of nearby equipment. The number and types of control points are:

RF System
- 10 - RF Drive Power (input /output)
- 10 - RF Drive Phase (input /output)
- 10 - Cavity Field (input /output)
- 10 - Cavity Phase (input /output)

Beam Instrumentation
- 20 - BPM (input)
- 5 - Bunch Length (input)
- 5 - Beam Size (input)
- 5 - Beam Phase (input)
- 5 - Beam Intensity (input)

Magnet Supplies
- 30 - Quadrupole Current (input /output)
- 20 - Dipole Current (input /output)
- 20 - Horizontal Steering (input /output)
- 20 - Vertical Steering (input /output)

Vacuum
- 8 - Pressure (input)
- 1 - RGA (input)
- 10 - Ion Pumps
- 7 - Gate Valves

Machine Monitoring
- 70 - Thermometer (input)
- 3 - Flow Meter (input)
- 5 - Halo Monitor (input)
- 10 - Refrigerator (input)

5.2.5.2 RF Control

The ERL RF control system is modeled after the digital system now being employed in the TESLA system (Simrock 1999). Digital I/Q detectors are used for the cavity field probe signal and the incident and reflected waves. The RF signals are converted to an intermediate frequency of 250 kHz and sampled at a rate of 1 MHz (i.e. two consecutive data points describe the I and Q of the cavity field). The I and Q components are multiplied by 2 x 2 rotation matrices to correct the phase offsets and to calibrate the gradients of the individual cavity probe signals. The vector sum (in the case of the injector cavities) is calculated and corrected for systematic measurement errors. Finally the set point is subtracted and the compensator filter is applied to calculate the new actuator setting (I and Q control inputs to a vector modulator).

In the ERL injector cavities, with the relatively low loaded Q, microphonics and Lorentz force detuning are not expected to be issues. The primary issue will be beam loading control. If

feedback control is to be used for beam loading corrections, then the integrator pole should be set so that the loop gain is 1 at approximately 1 kHz, given that the cavity bandwidth is at approximately 10 kHz. Therefore the feedback gain at 10 Hz will be limited to ~100, which could be inadequate unless beam current fluctuations are sufficiently small. The magnitude and frequency spectrum of the beam current fluctuations must be measured and understood in order to determine whether feedback is adequate or whether feed-forward must be added. Feed-forward (together with a klystron linearizer) for beam loading control could be implemented with the use of a beam current measuring device that feeds the signal directly into the feed-forward block. Feedback could be used in addition to correct slow drifts such as thermal fluctuations. This scheme is envisioned for both the injector and the main linac cavities. Finally, RF voltage turn on in the main linac cavities, at the nominal gradient of 20 MV/m with loaded Q at the 10^7 level, is challenging due to Lorentz force detuning which is expected to be equal to several cavity bandwidths. Piezo tuners will be stepped at a rate consistent with the rise time of the RF to compensate for the cavity detuning. The operation of the linac RF systems will be highly automated by the implementation of a finite state machine which has access to high level applications including the adjustment of the loop phase, calibration of individual cavity gradients (in the main linac) or vector sum (in the injector), frequency and wave guide tuner control and exception handling. The elements of the systems are shown in Figures 5.2.5.2-1 to -4.

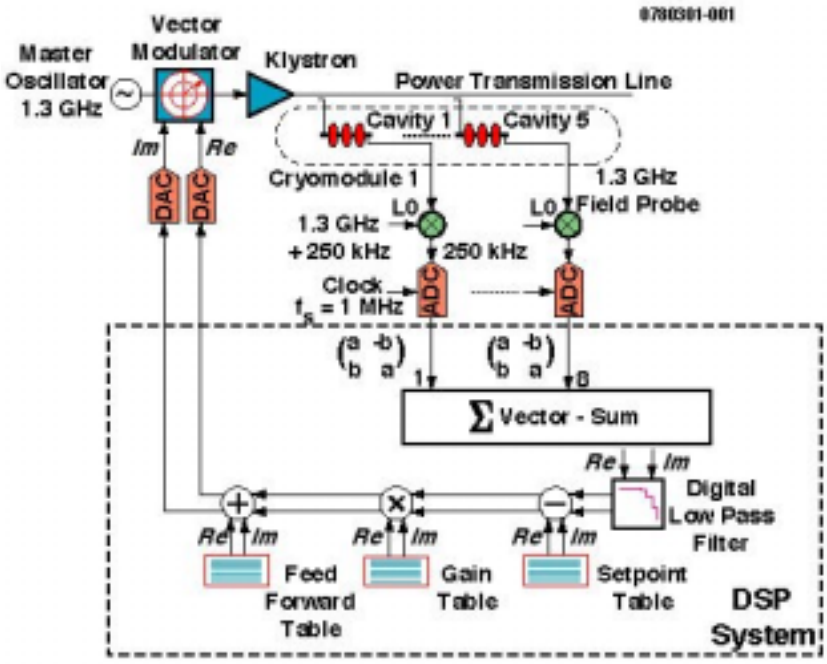

Figure 5.2.5.2-1: Digital RF control system concept for injector cavities. One klystron will feed several cavities.

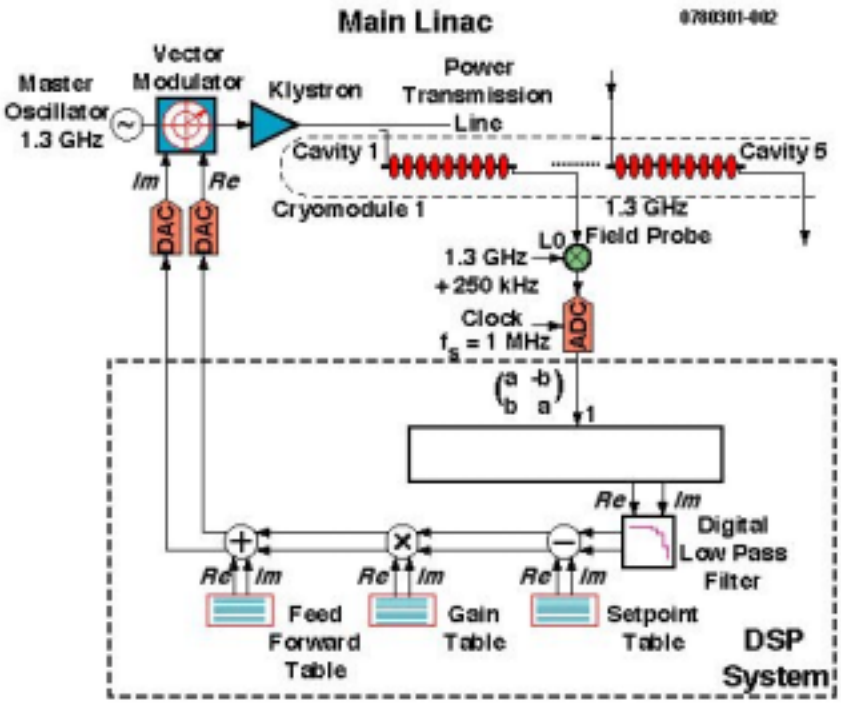

Figure 5.2.5.1.-2: Digital RF control system concept for main linac cavities. One control system is needed for each cavity.

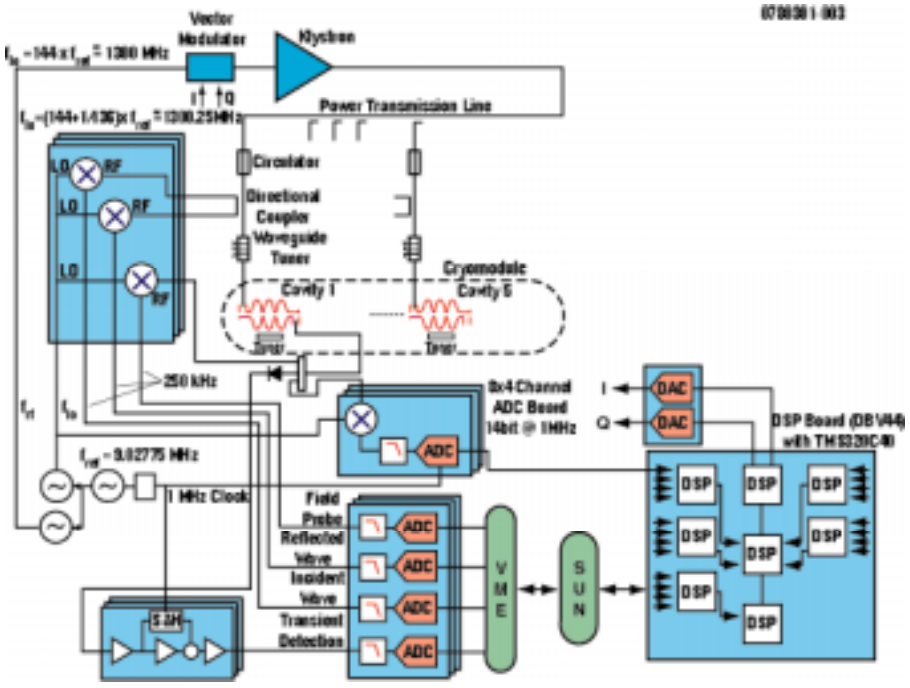

Figure 5.2.5.2.- 3: Low level digital RF control system components and layout for injector cavities.

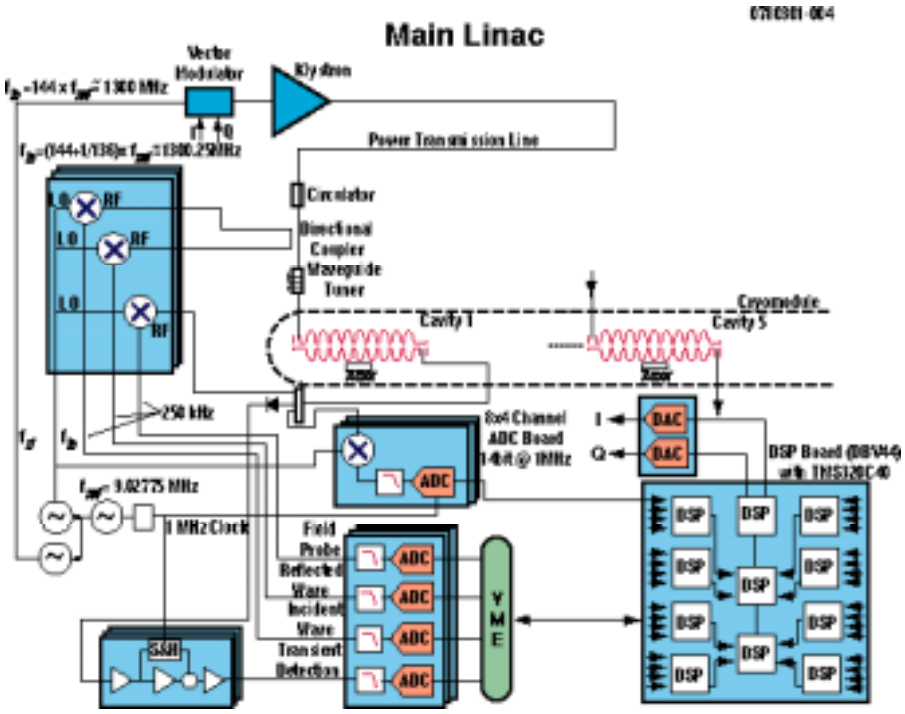

Figure 5.2.5.2.- 4: Low level digital RF control system components and layout for main linac cavities.

5.2.5.3 Diagnostics

The function of the Phase I ERL is to measure the influences of source characteristics, space charge, coherent synchrotron radiation, single bunch and multi-bunch wake effects (BBU thresholds), HOM extraction efficiency and other emittance dilution effects. Adequate diagnostics for measuring these effects play a central role in the outfitting of the Phase I machine. In addition, appropriate operational control of the system also demands corresponding instrumentation with ability to monitor and log key variables.

5.2.5.3.1 Variables to be Measured and Logged

A list of variables to be measured and logged follows. The asterisk (*) indicates the signal is to be logged. The number in parenthesis is the number of monitoring points in the machine:

Thermometers (70)*

BPM (20)
Bunch Length (5)
Beam Size (5)
Beam loss monitors
RF Drive Power (10)*
RF Drive Phase (10)*
Cavity field (10)*
Cavity Phase (10)*
Beam Phase (5)*
Beam Intensity (5)*
Vacuum Pressure (8)*
RGA (1)
Flow meters (3)*
Halo monitor (5)
Q-pole currents (30)*
D-pole currents (20)*
H-steering currents (20)*
V-Steering currents (20)*
Refrigerator temperatures and pressures(10)*
Gun voltage (1)*
Gun current (1)*
Gun solenoid current(1)*
Laser pulse length
Laser power (1)*
Laser rep rate and time pattern (1)*

5.2.5.3.2 Performance Evaluation

In order to understand the influences mentioned above, beam and cavity signals need to be measured at each stage of the beam path, gun exit, capture section exit, main linac entrance, main linac exit and at several points along the return path. Particularly important will be the transverse and longitudinal beam distribution functions needed for emittance and bunch length determination.

Transverse Beam Distribution

In general we will need nonintercepting methods of determination owing to the very high power and power density of the beam at full current. For crude measurements at very low average beam intensities, fluorescent screens will be provided for tune-up and trouble shooting. For halo analysis at all beam intensities, wire scanners followed by bremsstrahlung detectors will be used.

At high intensities and at energies well below 100 MeV, microchannel residual gas ion profile monitors based on microchannel plates will be used (Krider 1989; Zagel 1997). The ion current collected from a 10 cm length of beam line at full current will be about 30 pA. If the

gain of the microchannel plate is 5000, which is reasonable, then the output current onto the collector strips will be about 0.2 μA giving considerable dynamic range. In this regime the beam sigma are of order 1 mm in size so that achieving sufficient resolution will not be difficult.

For energies ~ 100 MeV, synchrotron radiation image formation on a CCD device can give adequate resolution. At 100 MeV and 1 m bending radius $\varepsilon_c = 2.2\,\text{eV}$ or ~5600 Å. Taking synchrotron light of the right polarization in a 10% band about 10,000 Å and forming an image will yield a resolution of about 10 μm (Hofmann 1998) to be compared with the approximately 200 μm beam size at the entrance to the TBA beyond the main linac. This method will be used in the return line to observe emittance dilution engendered by CSR should it be significant.

Longitudinal Beam Distribution

The bunch length will vary by large factors in passing from the gun, through the capture section and into the main linac and then through the bunch compressor in the return leg of the path. The bunch length will be several 10's of ps out of the gun. At that stage, a sampling oscilloscope connected to the BPM will give adequate measurement of the bunch longitudinal shape. After bunching, it is anticipated that we will be operating with bunches of 2 to 5 ps sigma. In this regime, a far infrared (FIR) spectrum of the CSR emitted in a dipole can be used to measure the longitudinal distribution function (Lai 1998). In the section between bunch compressor and decompressor, the bunch length may be one tenth of that outside. The FIR spectrum can also be used but with optics suited for the shorter wavelengths.

Impedance Influences

It is expected that the main source of impedance will be the main linac and the most important consequence the possible support of BBU and the conversion of beam kinetic energy into electromagnetic energy potentially to be deposited at low temperature. Other effects to be examined are single bunch wakes and their potential for energy spread enlargement and bunch tilting which can result in projected emittance enlargement. These latter can be measured via beam size measurements vs. bunch current in regions of high beta and high dispersion respectively and with the streak camera sliced image of the beam in synchrotron radiation.

Measurement of BBU threshold may be straightforward if the threshold is below the operating current of 100 mA. By lowering the beam energy by a factor of 2, we can increase our range somewhat. If these are not sufficient, a transfer function measurement using a broad band kicker and sensitive pickups can extend the range considerably (Sereno 1994).

Another important measurement will be the assessment of HOM power deposited at low temperature. A global measurement by calorimetry on the main linac cryostat will be carried out as will an inventory in which the power and power spectrum of the HOM coupled out by the HOM couplers and the total power coupled out by HOM beam line absorbers. In the case of the HOM couplers bolometry and spectrum analysis can be used. In the case of the beam line absorbers, individual thermal loops for these devices will be used so that sensitive calorimetry will be possible.

5.2.5.3.3 Operational Diagnostics

Beam Position and Optical Function Measurement

To assure the possibility of observing very high frequency beam motions there will be broad band BPM's placed frequently around the circuit. In most places these will be of the four button, HOM damped, equally spaced azimuthal type (Hinkson 1998) such as used in CESR (Billing 1993). At the 100 MeV peak beam energy minimum beam sizes will be in the 200 micron range so that resolutions of, say, 20 micron will normally be sufficient. As one of our purposes is to demonstrate fine control of beam position in selected places, however, some BPM's will be outfitted with electronics capable of micron resolution and stability (Palmer 2001). These can then be used as pickups for a feedback system, the H and V correctors being the feedback transducers. The BPM's will be used not only for centering the orbit but also for measuring the optical functions and correcting them (Rice 1998). Dispersion can be determined by varying the linac phase and thus the beam energy and measuring beam displacements around the circuit.

Beam Current

It will be important to measure the beam current in several places. Stainless steel 1300 MHz cavities, temperature regulated and calibrated by Faraday cup at low current can be used for comparison. A "DC Current Transformer" can be used for absolute measurement of the average current.

Phase Transfer Monitor

In order to achieve maximum performance in the main linac, one needs to be sure that the longitudinal phase space has been properly manipulated during the bunching process. The bunching process is optimized when both linear and parts of the non-linear distortions in longitudinal phase space are properly measured and corrected. In the CEBAF nuclear physics accelerator and the JLAB IRFEL such measurements are accomplished with the phase transfer monitor system (Abbott 1992).

Fundamentally, the phase transfer monitor system includes:

(1) a longitudinal pickup that produces an RF wave that is highly sensitive to the time-of-arrival of beam bunches;
(2) A mixer that is operated as a precision phase detector,
(3) A phase modulater that acts to change the RF phase of the beam formation region with respect to all other RF phases in the accelerator; and
(4) Data acquisition and display hardware and software.

Through such measurements, which are roughly the longitudinal equivalent to measuring the longitudinal dispersion and longitudinal chromaticity, one may

(1) Determine the proper beam recirculation phase with high precision;
(2) Calibrate the phases and amplitudes of the RF cavities in the bunching regions of the accelerator;

(3) Verify that the longitudinal setups in the accelerator correspond to performance calculations; and
(4) Monitor day-to-day changes in the accelerator due to thermal drifts and similar phenomena.

This final application is especially important in the machine commissioning phase, where obtaining information on RF drifts is particularly important for stabilizing the performance of the accelerator in the long term. The systems installed on CEBAF and the JLAB IRFEL have performed at very high precision with far smaller beam current than will be present in the ERL. Some detailed applications of the phase transfer systems at JLAB are discussed in (Krafft 1995; Piot 2000).

For the Phase I ERL, we expect to build one fundamental mode pickup cavity for testing, and the mixer and modulation hardware. Time-of-flight information can be obtained from the RF signals of any BPM, with the disadvantage during the Phase I machine that the signal levels will depend on the beam position, a situation that will be unacceptable for normal operations in the Phase II machine.

5.3 Phase I Infrastructure

5.3.1 Building.

The site selected for the Phase I ERL is the existing HV Laboratory building that is located about 1 mile from the main campus and from Wilson Laboratory. This building has been used by Cornell Engineering faculty members to investigate high voltage engineering issues. The building contains about 9,000 sq ft of space on the ground floor level. The limited office space in the building is supplemented by the office space available in a 10’ x 50’ trailer attached to the back of the building. Space at the site is tight for the task, but workable. We have very recently become aware of the possibility of a slightly larger site which may become available when the present tenant relocates. We will continue to evaluate this alternative site, should it become available, to see if it is advantageous. In the mean time we are assured of the availability of the HV laboratory. The layout of the Phase I ERL in the HV laboratory building is shown in Figure 5.3.1-1.

Although the Phase I ERL is only a 100 MeV machine, at 100 mA this still is beam power 10 MW. The refrigeration, RF system and beam dump will also dissipate significant power, necessitating a 2 MW evaporative cooling unit, as well as an adequate electrical feed substation. Moreover, 0.1 A @100 MeV is sufficient to produce copious neutrons if the beam strikes matter; therefore, safety considerations require heavy shielding. A large cryogenics/He refrigeration/compressor unit is also required.

Figure 5.3.1-1. (Next page) Layout of the Phase I ERL on the floor of the HV Lab building.

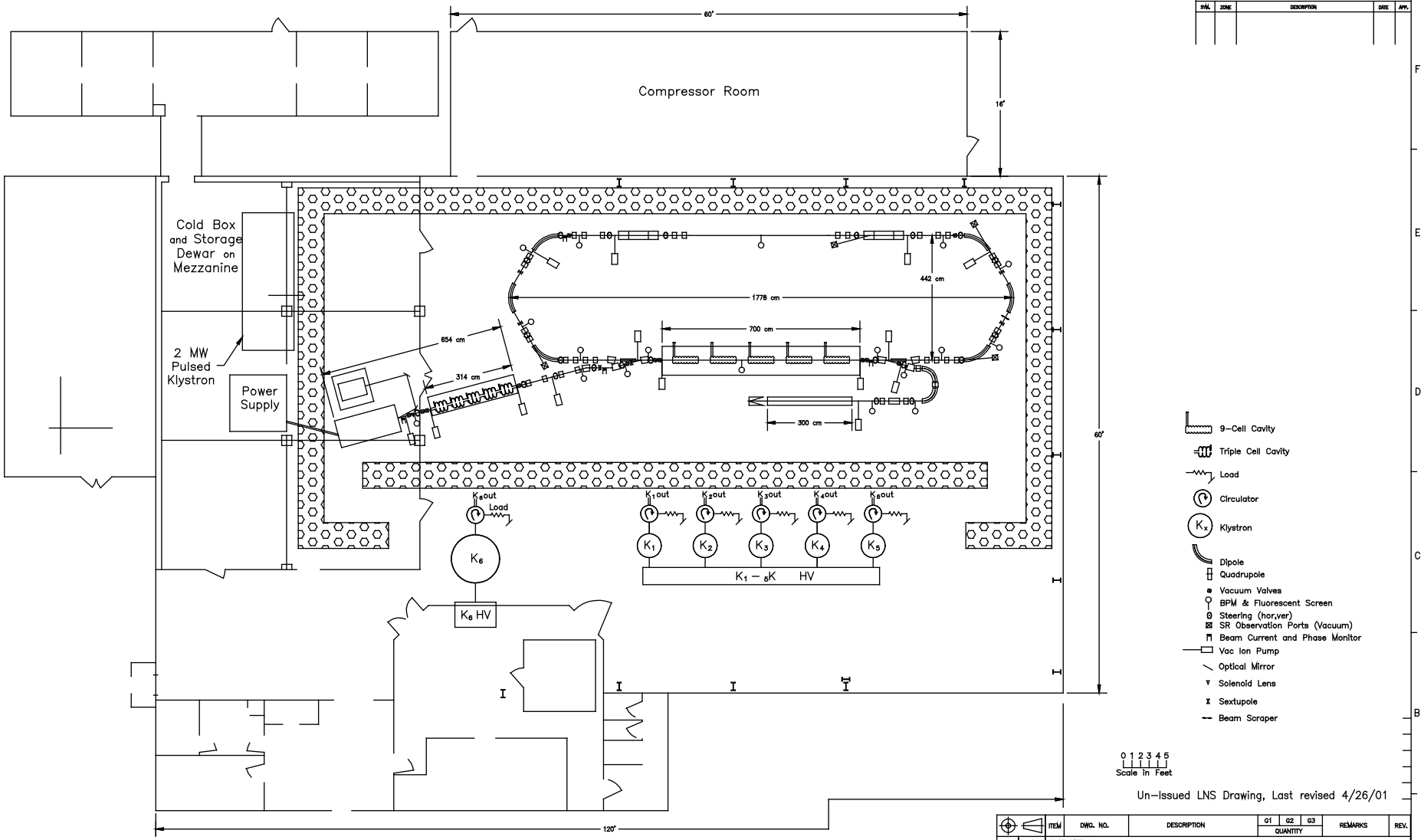

Un-Issued LNS Drawing, Last revised 4/26/01

REVISIONS				
SHT.	ZONE	DESCRIPTION	DATE	APP.

ITEM	DWG. NO.	DESCRIPTION	QUANTITY G1	G2	G3	REMARKS	REV.

PRINT DISTR. CR-1

PLOT DATE APRIL 30, 2001
CAD FILE NAME D-6040-288-01

UNLESS OTHERWISE SPECIFIED
DIMENSIONS ARE IN INCHES
TOLERANCES ON:
.XX ± .010
.XXX ± .005
FRACTIONS ± 1/64
ANGLES ± 0.5°
ALL SURFACES

CHECKED BY
APPROVED BY

Cornell University
Floyd R. Newman Laboratory of Nuclear Studies – Ithaca, NY 14853

HIGH VOLT LAB.
ENERGY RECOVERY LINAC LAYOUT

DRAWN BY	DRAWN FOR	DATE	SCALE	SIZE	DWG. NO.	REV.
J. LACEY	M. TIGNER	3/12/01	1"=60'	D	6040-288 SH. NO. 1 CONT. ON 2	

6040-288 SH. NO. 1 CONT. ON 2 REV.

5.3.2 Cryosystem

The cryogenic system for the ERL machine is designed to supply 500 watts of cooling at 2 K to support operation of the machine for up to 8 hour running period at full heat load. It must then be subsequently operated in a recovery mode to refill the liquid helium reservoir in a 16 hour long recovery period. Thus the cryogenic system will be able to support full machine operations an 8 hour period each 24 hour day. This combination has been chosen to provide the lowest cost system, while allowing a sufficiently long run of operation for the machine to assume steady state conditions for a reasonable period of time.

Figure 5.3.2-1 shows a schematic outline of a closed circuit helium system that starts with helium stored under pressure in a 15,000 gallon, 250 psig tank. The cooling system is built around a refrigerator cold box that continually produces liquid helium into a 2,000 liter liquid helium dewar that is a part of the system. The estimated warm gas liquefaction capacity of the refrigerator is 90 liters/hr. (This is the capacity based on liquification of warm helium gas feed from gas storage with no refrigeration loads present.) Refrigeration at the 80 K level is provided by liquid nitrogen from a 6,500 gallon LN2 tank located outside the building. An expansion engine operating between 18.6 and 1.15 atmospheres provides the refrigeration at the 10 K level. Colder refrigeration at 2 K is provided by Joule-Thompson expansion. The 2K cold stream feeds two cryomodules, one for the injector and one for the linac.

A few numbers can be given to help illustrate the capability of the cryogenic machinery. During ERL operations, liquid helium is withdrawn from the storage dewar at a rate of 24 g/s. During the recovery phase, an estimated 2.7 g/sec of liquid helium is used to hold the SRF cavities at 4 K while the liquid helium in the dewar is refilled. As with most of these complex refrigeration systems, most of the power consumed in the plant must be dissipated as heat from the compressors, etc. The total horse power of all the compressors and motors is 1,120 HP. The cooling water flow rate expected is 277 gallons/min with a 20 F temperature rise. This power will be dissipated into an evaporative cooling tower.

The TTF 8-cavity cryomodule (see Figure 3.1.8-2) static heat load was measured to be 4W at 2K, 13W at 4.5K, and 78W at 70K. We adopt the same numbers for both the ERL main linac cryomodule and the injector booster cryomodule. The total heat load for the Phase I ERL, including overhead, is 400W at 2K and 240W at 4.5K. Since the Phase I ERL is primarily a machine studies entity, the dynamic heat load (260W) will not be present all the time. In the interests of cost, a duty cycle of 33% will be used: During the 16 hours when the beam and RF are off, the refrigerator will fill a 200 liter storage dewar.

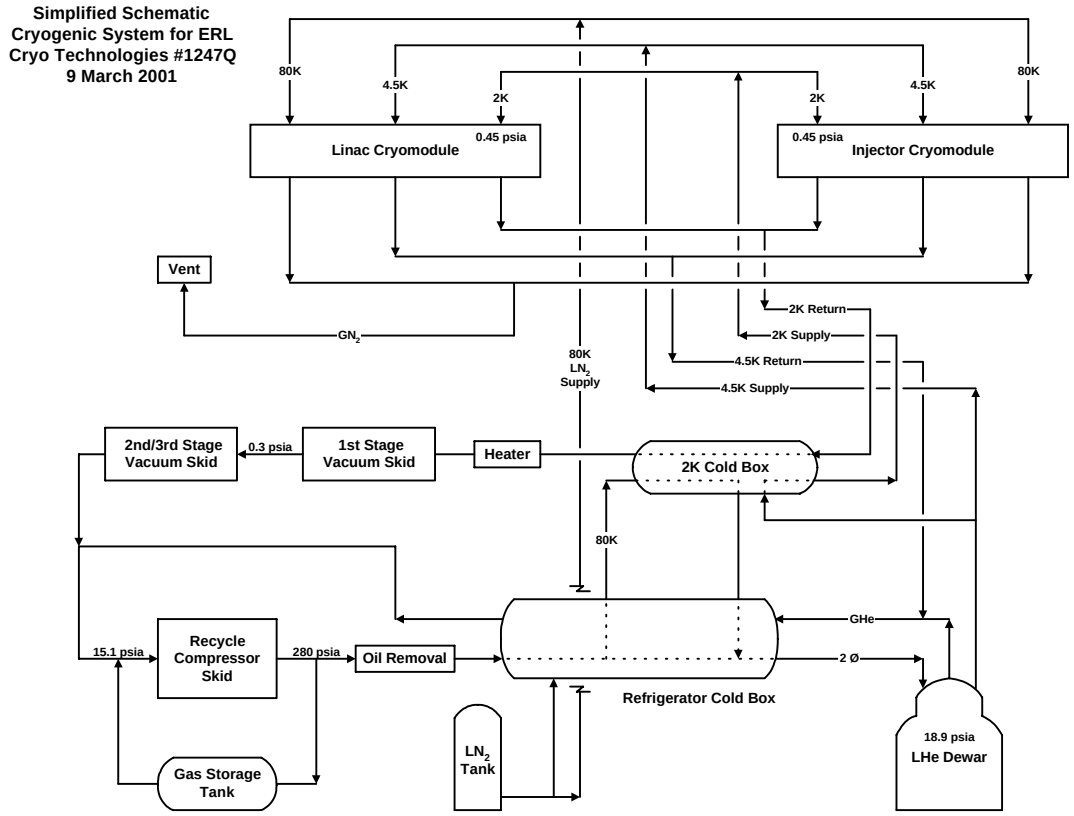

Figure 5.3.2-1. Schematic outline of the closed circuit helium system for the Phase I ERL.

5.3.3 Electrical Power

The power required by the Phase I ERL, given safety factors, is 2 MW. This will entail running 2000 ft. of new utility line to the nearest adequate electrical feed. Building transformers, switch-gear and primary panels and sub-panels will be installed to handle the power. Power will distributed by new feeders and conduit to the laboratory equipment, and new convenience receptacles and new lighting will be installed.

5.3.4 Evaporative Cooling Tower

An evaporative cooling tower will be installed to provide up to 2 MW of process cooling. This facility will house pumps, water sump, treatment equipment and controls in a building which is under the cooling tower.

5.3.5 Air Conditioning

The HV Laboratory is presently not air-conditioned. While extraordinary thermal stability is not expected to be required for the Phase I ERL, large thermal excursions on the support stands would result in unacceptable misalignments. We estimate that a temperature

stability of ± 2 C will be adequate. Accordingly, the building will be outfitted with 50 tons of refrigeration using direct expansion cooling with an air handler to be mounted outside the building or on the building roof.

5.3.6 SRF Infrastructure

Newman laboratory has extensive infrastructure for research, and development in RF superconductivity as well as for production, preparation and testing of superconducting cavities. These facilities have been used to build the prototype SRF cavities for CEBAF and TESLA, as well as for all the cavities that currently power the present storage ring at Wilson Laboratory (CESR).

Cavity production facilities include a 100 ton press for deep drawing niobium cavity cells, digital control milling machines for precise die machining, an electron beam welder large enough for TESLA scale cavities, and a large UHV furnace to purify cavity half cells at 1400 C.

Cleaning facilities include open and closed cavity etching systems that can handle TESLA type cavities, high purity water rinsing systems, and high pressure (100 atmospheres) water rinsing. There is a class 100 clean room for cavity assembly, and a smaller, class 100 area for attaching cavities to test set ups. There are several portable clean room set ups for critical assembly. We are in the process of procuring a 1000 sq ft Class 100 clean room.

Test setups include three radiation shielded pits, two of which can accommodate 1300 MHz cavities, several cryostats, and cryostat inserts to test cavities from 200 MHz to 3000 MHz, several 200 watt cw power sources and a 1.5 MW pulsed klystron for high pulsed power processing.

High power testing capabilities exist for windows at 500 MHz and HOM loads at 2450 MHz.

Research facilities include a rapid thermometry system for studying single cell 1500 MHz cavities, field emission apparatus, and a dedicated scanning electron microscope with energy dispersive analysis for element identification installed in a class 1000 clean room.

5.3.7 Ancillary Infrastructure

The ERL project is a cooperative venture between the Laboratory for Nuclear Studies (LNS) and the Cornell High Energy Synchrotron Source (CHESS). The LNS built and operates the 10 GeV synchrotron injector and CESR, a major high energy physics machine 0.8 km in circumference. CHESS built and operates 12 x-ray beam lines on CESR and is one of 5 major hard x-ray facilities in the U.S. Collectively, the LNS and CHESS employ about 200 people, including a full range of vacuum, electronics, machine shops and shop personnel necessary for an operation of the scope of CESR/CHESS. The Phase I ERL, which is expected to occupy roughly 15 people, is relatively minor by comparison. In addition, we have full access to the

resources of Cornell University, one of the nation's major science and engineering research universities, with additional shop capability and an extraordinary range of expertise. The ancillary infrastructure at the LNS, CHESS and Cornell University is adequate for the project being proposed.

5.3.8 Safety Systems

The Laboratory of Nuclear Studies and the Cornell High-Energy Synchrotron Source are located on the Cornell University Campus. Even though the Phase I ERL machine will be in a separate building located about a mile from the main campus, it too will operate under Cornell's Health and Safety Policy: "Cornell University strives to maintain a safe living, learning, and working environment. Faculty, staff, students, and other members of the Cornell community must conduct university operations in compliance with applicable federal, state, and local regulations, University Health and Safety Board requirements, and other university health and safety standards." As part of the implementation of this policy, the University has a Department of Environmental Health and Safety. Their staff provides substantial support to the Safety Programs of our laboratories.

The LNS operates with both a Safety Committee and a Safety Director. The Safety Director screens new installations and apparatus for compliance with health and safety regulations, for conformance to any safety standards that might apply, and for protection from any hazards these do not adequately address. Depending on the scale of the project or nature of the hazard, the Safety Committee or an ad hoc committee may be asked to conduct a formal review. Representatives from the Department of Environmental Health and Safety are invited to most Safety Committee meetings and reviews. CHESS has its own Safety Committee. The laboratories share portions of Wilson Laboratory and have fully coordinated safety programs. This includes participation of safety personnel of each lab in reviews of hazards in either lab.

The principal areas where ERL must be examined for safety are radiation and cryogenic safety.

5.3.8.1 Radiation Safety

Cornell University is licensed by the New York State Department of Health, by authority of 10NYCRR, Part 16 to operate the accelerators that make up and fill CESR. The University Radiation Safety Committee and the Cornell Radiation Safety Officer prepare and enforce rules that implement the requirements of these regulations. Radiological monitoring of CESR is done by employees of the Laboratory of Nuclear Studies and reviewed by Cornell's Department of Environmental Health and Safety. The laboratory's radiation safety program is administered by a laboratory Radiation Safety Officer, a Radiation Safety Technician and other laboratory personnel as needed and is reviewed by the LNS Safety Committee.

Cornell has an aggressive ALARA (As Low As Reasonably Achievable) program that seeks to minimize exposures to occupational workers (with an investigation trigger of one-tenth the whole-body dose allowed under federal and state regulations). The radiation badges worn by

LNS and CHESS personnel at the existing CESR facility show exposures much lower than ALARA levels and nearly all are less than the dose limits for the general public (<100 mrem/year).

The practices now in place at CESR/CHESS will be extended to the ERL. The radiations from the ERL are synchrotron x-rays formed in the bending magnets and electromagnetic shower products, such as gammas or neutrons, from lost particles either from circulating beam or the injector.

A system of shielding, gates and light beams isolate the high radiation areas from the rest of the facility. Entry can only be made by a system of access keys which, in hardware, either disable all or parts of the accelerator or enable local area monitor trip circuits (depending on the location of the particular area). Keys can only be released by the ERL Operator. Electronic radiation monitors are placed near the shielding around the perimeter of the ERL. Neutron and gamma levels are continually recorded by a computer. Hardware interlocks in each monitor trip the accelerator or injector if either level exceeds a threshold (usually 2 mrem /hr.) Inspection of similar graphs of the CESR machine history of similar monitors show average rates much less than the trip levels. Radiation survey badges are also placed around the building to monitor integrated doses near the accelerator. Personnel will wear radiation monitoring badges in monitored areas. All of the radiation levels from outside the controlled access areas are planned to be less than 2 mrem in one hour and less than 100 mrem/year.

In summary, we know how to safely operate the existing 5.3 GeV, 800 mA (electron and positron beams) CESR facility and this experience will be applied to the proposed 100 MeV, 100 mA ERL machine in an appropriate manner.

5.3.8.2 Cryogenic Hazards

The installation of superconducting RF system in the experimental hall raises the question of the safe use of liquid cryogens. Because of cryogens ability to displace air in a relatively limited volume, their use in a small space must be implemented with great care.

There are several precautions that will be observed. Supply rates and local inventories will be hardware limited to necessary amounts. The machine area will have a high ventilation rate to replace any accidental release of cryogens with fresh air. However, all normal exhaust of evaporated cryogens will be through an exhaust line out of the building. All reasonably anticipated events that might result in a venting of a cryogen will be engineered to vent outside the building. This would include quenches, simple vacuum failures, simple operational errors, warm ups. This will be accomplished by having a set of pressure relief systems that discharge into an appropriately sized and engineered vent line (which might also be the exhaust line). These measures are beyond the active or passive operational controls that serve to limit quench conditions or overpressures.

There will be a Safety Review of the detailed plans to ascertain that the final installation will be safe.

5.4 Section 5 References

Abbott, R., Bowling, B., Crofford, M., Fugitt, J., Hovater, C., and Krafft, G. (1992). "The CEBAF Injector RF Distribution and Bunch Length Measurement System". Proc. 1992 Intl. LINAC Conf.: 232.

Billing, M. (1993). "Introduction to beam diagnositcs and instrumentation for circular accelerators"., AIP Conference Proceedings **281**: 55.

Crawford, C., Graber, J., Hays, T., Kirchgessner, J., Matheissen, A., Moller, W. D., Padamsee, H., Pekeler, M., Schmuser, P. and Tigner, M. (1995). "High Gradients in Linear Collider Superconducting Accelerator Cavities by High Pulsed-Power to Suppress Field-Emission.", Particle Accelerators **49**(1): 1-13.

Dowell, D., . et al. (1993). "First Operation of a High Duty Factor Photoinjector". Proceedings of 1993 PAC, Washington DC, May: 2967.

Drouhin, H. J., Hermann, C. and Lampel, G. (1985). "Photoemission from Activated Gallium-Arsenide .1. Very-High- Resolution Energy-Distribution Curves.", Physical Review B **31**(6): 3859-3871.

Dunham, B. M., Cardman, L.S. and Sinclair, C.K. (1995). "Emittance measurements for Illinois/CEBAF polarized electron source". Particle Accelerator Conference, Dallas, IEEE, New York: 1030-1032.

Engwall, D., Bohn, C., Cardman, L., Dunham, B., Kehne, D., Legg, R., Liu, H., Shinn, M. and Sinclair, C. (1997). "A high-voltage GaAs photoemission gun: transvers emittance and momentum spread measurements". PAC 97, Vancouver, B.C., Canada, 12-16 May 1997.

Feigerle, C. S., Pierce, D. T., Seiler, A., Celotta, R. J. (1984). "Intense Source of Monochromatic Electrons - Photoemission from Gas.", Applied Physics Letters **44**(9): 866-868.

Hinkson, J. A. (1998). Beam position monitors. Handbook of Accelerator Physics and Engineering. A. W. a. T. Chao, M. (World Scientific, NJ. pp. 555-557).

Hofmann, A. (1998), "Diagnostics with Synchrotron Radiation, in CERN Accelerator School on Synchrotron Radiation and Free Electron Lasers", CERN, CERN 98-04.

Hovater, C., Poelker, M. (1998). "Injection mode-locked Ti-sapphire laser with discretely variable pulse repetition rates to 1.56 GHz.", Nuclear Instruments & Methods in Physics Research Section A **418**(2-3): 280-284.

Krafft, G., et al. (1995). "Proc. of Microbunches Workshop". AIP Conference Proc.**367**: 46.

Krafft, G. A., et al. (2000). "Measuring and Controlling Energy Spread at CEBAF". Proc. of the 2000 Int. LINAC Conf.: 721.

Krider, J. (1989). "Residual-Gas Beam Profile Monitor.", Nuclear Instruments & Methods in Physics Research Section A **278**(3): 660-663.

Lai, R., Schneider, G. and Sievers, A.J. (1998). Measuring longitudinal distribution of electron bunches with coherent synchrotron radiation. Handbook of Accelerator Physics and Engineering. A. W. Chao, and Tigner, M. (World Scientific, NJ. pp. 557-559).

Lebedev, V. A., Musson, J., and Tienfenback, M.G. (1999). "High-precision beam-based RF pahse stagilization at Jefferson Lab". PAC 99, New York, NY: 1183-1185.

Liu, F., Brown, I., Phillips, L., Biallas, G., and Siggins, T. (1997). "A method for producing very high resistivity surface conduction on ceramic accelerator components using metal ion implantation". PAC 97, Vancouver, B.C., Canada: 3752-3755.

Liu, Z. L., Murakami, H., Kozeki, T., Ohtake, H. and Sarukura, N. (2000). "High-gain, reflection-double pass, Ti : sapphire continuous- wave amplifier delivering 5.77 W average power, 82 MHz repetition rate, femtosecond pulses.", Applied Physics Letters **76**(22): 3182-3184.

Padamsee, H. (1991). "Crab cavity development for the Cornell B-factory". PAC 1991: 2423.

Padamsee, H., Knobloch, J., and Hays, T. (1998). RF Superconductivity for Accelerators. NY, John Wiley & Sons, NY.

Palmer, M. A., et al. (2001). "An upgrade for beam position monitoring system at the Cornell Electron Storage Ring". PAC 2001.

Piot, P., Douglas, D.R. and Krafft, G. (2000). 2000 European Part. Accel. Conference: 1543.

Rice, D. (1998). Orbit and lattice function measurements. Handbook of Accelerator Physics and Engineering. A. W. a. T. Chao, M. (World Scientific, NJ. pp. 264-267).

Sereno, N. (1994), Experimental studies of multipass beam break-up and energy recovery using the CEBAF injector linac, (Ph.D. Thesis, University of Illinois at Urbana-Champaign, Urbana-Champaign).

Siggins, T., Sinclair, C., Bullard, D., Douglas, D., Grippo, A., Gubeli, J., Krafft, G.A., Yunn, B.C. and Bohn, C. (2000). "Performance of a DC GaAs Photocathode Gun for the Jefferson Lab FEL". Proceedings of the FEL 2000 Conference, Durham, NC, August, 2000.

Simrock, S. (1999). "LA-13782-C". 9th Workshop on RF Superconductivity, Los Alamos Natl. Lab., Santa Fe, NM.

Sinclair, C. K. (1992). "A 500 kV photoemission electron gun for the CEBAF FEL.", Nuclear Instruments & Methods in Physics Research A **318**(1-3): 410-414.

Sinclair, C. K. (1999). "Recent advances in polarized electron sources". PAC 99, New York, NY: 65-69.

Sinclair, C. K., Dylla, H., Siggins, T., Manos, D., Venhaus, T. and Wu, L. (2001). "Dramatic Reduction of DC Field Emission from Large Area Electrodes by Plasma-Source Ion Implantation". Proceedings of 2001 PAC, Chicago, June.

TELSA (2001), "Technical Design Report", March, 2001, DESY, Hamburg, Germany, DESY 2001-011, http://tesla.desy.de/new_pages/TDR_CD/start.html.

Zagel, J., et al (1997). "Fermilab main ring ion profile monitor system". PAC97: 2166.